論文 / 著書情報
Article / Book Information

題目(和文)	
Title(English)	Liquefaction-induced Deformation of Embankments on Non-homogeneous Foundation
著者(和文)	マハルジャンモニカ
Author(English)	Manika Maharjan
出典(和文)	学位:博士（学術）, 学位授与機関:東京工業大学, 報告番号:甲第9898号, 授与年月日:2015年3月26日, 学位の種別:課程博士, 審査員:高橋　章浩,北詰　昌樹,時松　孝次,竹村　次朗,佐々木　栄一
Citation(English)	Degree:, Conferring organization: Tokyo Institute of Technology, Report number:甲第9898号, Conferred date:2015/3/26, Degree Type:Course doctor, Examiner:,,,,
学位種別(和文)	博士論文
Type(English)	Doctoral Thesis

Liquefaction-induced Deformation of Embankments on Non-homogeneous Foundation

Manika Maharjan

Tokyo Institute of Technology

2015

Liquefaction-induced Deformation of Embankments on Non-homogeneous Foundation

Manika Maharjan

DISSERTATION

submitted in partial fulfillment of the requirements for the degree of

DOCTOR OF PHILOSOPHY

at

TOKYO INSTITUTE OF TECHNOLOGY

2015

Acknowledgements

I would like to express my sincere gratitude to my supervisor Professor Akihiro Takahashi for his continuous support and guidance during this thesis work. His patience, knowledge, and encouragement have provided the indispensable support throughout the course of my study. He constantly inspires me with innovative ideas and valuable advices. The role he plays in this thesis can never be overemphasized, and I must say that I could not have finished it without him. I am also grateful for the critical insights he has put into my work.

I am also grateful to the committee members Professor Kohji Tokimatsu, Professor Masaki Kitazume, Associate Professor Jiro Takemura, and Associate Professor Eiichi Sasaki for their suggestions and helpful comments.

I would like to extend my special thanks to our lab technician, Mr. Sakae Seki for his support and guidance during experiments. The successful completion of experiments would not have been possible without his sincere efforts. I am also obliged to my lab mates Dr. Ke Lin, Sawada, and Horikoshi for helping me with my experiments and valuable suggestions. My sincere gratitude goes to all the Nepalese friends of Tokyo Tech who always inspired and motivated me to complete the beautiful journey of my study. I am indebted to the Ministry of Education, Culture, Sports, Science and Technology (MEXT), Japan for granting me a Monbukagakusho scholarship. I am also grateful to The work presented is a part of the research and development project on safety measures for levees, commissioned by the Ministry of Land, Infrastructure, Transport and Tourism, Japan.

Finally, I would like to thank my dear family, my parents, Mr. Gyan Lal Maharjan and Mrs. Sarita Maharjan for teaching me to believe in myself, their love, guidance and moral support and my brother Manish for being my true sunshine, his support, care and indispensable love. I would also like to extend a special thanks to Maharjan family whose love and blessings have always ruled over me. Lastly, but not the least, I would like to thank Deepak for not only providing the support and encouragement, but always inspiring me with the most creative ideas and solutions and his unconditional and immense love, and putting a smile on my face after the most frustrating days during my study.

Abstract

Liquefaction has been reported as a cause of severe damage to foundations of buildings, bridges and other structures, as well as to ports and buried lifelines during past major earthquakes. While most of the earlier physical model tests on liquefaction problems have dealt with uniform clean sand, most recent studies have employed horizontally layered soil (with uniform properties within distinct soil layers). However, the mechanism of liquefaction in non-homogeneous soil when the relatively impermeable layer consists of discontinuities of higher permeability is not well understood. The modeling of liquefaction in real soil profile is very complicated because of various uncertainties and non-uniformities in stratigraphic details and geological non-uniformities.

During earthquakes, saturated sandy soils are characterized by a substantial rise in excess pore water pressure (Δu), leading to dramatic loss of strength and stiffness. When this excess pore water pressure reaches a value equal to the initial effective stress, soil particles do not support each other, a phenomenon referred to as zero effective stress condition—a state of initial liquefaction. Previous studies that initiated following the observations from liquefaction-related damage during several past devastating earthquakes, have provided significant insights into the liquefaction phenomenon and associated failures. Initially studies were only focused on assessing the triggering factors for liquefaction in clean sandy soils. As the years passed, physical model studies on layered soil deposits evolved. It is noted that the real soil profile is complex and a soil deposit is neither uniform nor consists of continuous layers. The actual soil profile characterized by various patterns of layering and lensing is very complex, which may have a great effect on geotechnical engineering problems at a site. Earthquake induced liquefaction has become a major problem to soil embankments such as river dykes, levees, road embankments and earth dams, supported on a cohesionless foundation soil. Previous studies have shown that the widespread damage to such embankments occurred mainly due to the liquefaction of foundation soil, resulting in cracking, settlement, slumping and lateral spreading. Previous studies have investigated the dynamic response of embankments by mainly considering uniform sand foundation and a single earthquake event. However, the foundation of an embankment consists of many sublayers of soil from liquefiable sand to relatively impermeable layer, and during earthquakes a mainshock may trigger numerous aftershocks within a short time which may have the potential to cause additional damage to soil structures. Therefore, my research is focused on investigating the effects of non-homogeneity and mainshock-aftershock sequence of ground motions on liquefaction mechanism in embankments.

The research was carried out in three phases. The first phase is focused on the

liquefaction of non-homogeneous leveled ground. The objective is to gain understanding of the liquefaction mechanism in non-homogeneous soil deposits. The study was carried out by a series of dynamic centrifuge tests and finite element analyses. Four types of model tests were conducted: one model test involved a uniform soil deposit; one involved continuous layered soil deposit; and two involved discontinuous layered soil deposits. Non-homogeneity in the tests was incorporated by including periodically distributed discontinuous silty sand patches. It was found that, in non-homogeneous soil deposits, the pore water was trapped beneath or within less permeable silty sand patches due to the local migration of pore water and difference in permeabilities of the soils. The less permeable silty sand layer acts as a barrier and restricts the seepage of pore water. This indicated that the pore water found a path to drain from the high pore pressure region to the low pressure region, which revealed that the presence of the discontinuous less permeable layer could have substantial effects on the pore pressure dissipation mechanism and drainage. It was found that more excess pore water pressure (Δu) remains for a longer period of time in the discontinuous region in non-homogeneous soil deposits compared with the continuous layered and uniform soil deposits. The generation of pore water pressure ceased the supply of a new mass of water after seismic excitation; therefore the dissipation of Δu became the dominant factor for settlement after seismic excitation. The rapid dissipation of Δu through the discontinuous part in the non-homogeneous soil deposits manifested as a larger settlement in the discontinuous part, causing non-uniform settlements.

Since most of the embankments lie on the non-homogeneous foundation, and during earthquakes a mainshock may trigger numerous aftershocks within a short time, i.e., before the major dissipation of excess pore water pressure, which may have the potential to cause additional damage to soil structures. In the second phase, the deformation mechanism of embankments lying on non-homogeneous soil deposits under mainshock and sequential ground motion was investigated. Accordingly, the investigation of liquefaction-induced deformation of earthen embankments on various liquefiable foundation conditions under mainshock-aftershock sequential ground motions was carried out by a series of dynamic centrifuge tests and finite element analyses. The liquefiable foundation included uniform sand foundation, a multi-layered sand/silty sand foundation, and a non-homogeneous multi-layered discontinuous sand/silty sand foundation. Effects of various foundation conditions on embankment deformations were compared and analyzed. In the non-homogeneous foundation, the dissipation of pore water from the underlying layer was concentrated at the discontinuous region below the embankment, inducing the larger excess pore water pressure ratios. From the results, it was found that the embankment resting on non-homogeneous soil deposits suffered more damage compared to the uniform sand foundation of the same relative density. The results also suggested that the sequential ground motions had a significant effect on the accumulated deformation of embankment.

The stratification of non-homogeneous foundation is complex and the discontinuity in low-permeability layer may lie at any location below the embankment. Therefore, the third

phase investigated the effects of position of non-homogeneity on the deformation of embankment. Parametric studies were carried out by changing the position of non-homogeneity in order to determine the critical position of non-homogeneity using finite element analysis. The position of non-homogeneity varied from the discontinuity lying exactly below the center of embankment to the toe of embankment. The position of discontinuity was changed towards the left embankment toe by 1 m in each model configuration. The parametric studies showed that larger excess pore water pressure ratio were found below the toe region for the cases where the discontinuity lay below the embankment toe. This caused the liquefaction of soil at the free field and toe region, which decreased the confining stress of foundation soil below the embankment. This might have allowed the lateral stretching of the soil below the embankment towards the free field, leading to the larger lateral deformation in the free field and toe region for the cases where discontinuity lay below the embankment toe. Furthermore, the crest settlement was found to be even and uniform when the discontinuity lay exactly below the center of embankment. However, uneven settlements occurred at the embankment crest when the discontinuity was located at the position other than the center of embankment.

Table of contents

List of figures

List of tables

Chapter 1
Introduction

1.1 Liquefaction

Liquefaction, which involves substantial loss of strength and stiffness of saturated sandy soils, has been reported as a cause of severe damage to foundations of buildings, bridges and other structures, as well as to ports and buried lifelines during past major earthquakes. If loose saturated sand is subjected to earthquake loading, it tends to compact and decrease in volume. Under undrained condition, if the pores of the soil are filled with water that is prevented from escaping, then the pore water pressures will increase when the soil skeleton attempts to contract, and decrease when the soil skeleton attempts to dilate. The diminution of volume tends to build-up the pore water pressure, which involves substantial loss of strength and stiffness of soils. This phenomenon is primarily, but not exclusively, associated with saturated cohesionless soils (National Research Council, 1985). During an earthquake shaking, the generation of excess pore water pressure plays a key role in all liquefaction-related phenomena (Kramer, 1996). Under undrained conditions, the build-up of excess pore water pressure reaches a value equal to the total stress, soil particles do not support each other, referred as a zero effective stress condition; a state of initial liquefaction (National Research Council, 1985; Fiegel and Kutter, 1994; Brennan and Madabhushi, 2005; Ishihara and Yoshimine, 1992). Some of the liquefaction-induced ground failures are sand boils, lateral spreading, differential settlement, flow slides etc. (Kramer, 1996; Adalier and Elgamal, 2004). The consequences of liquefaction vary for level ground and slope. Level ground sites undergo ground oscillations accompanied by cracks and fissures and settlements (National Research Council, 1985). Moreover, the surface manifestations of level ground include failure of superstructures by loss of bearing capacity; differential settlement, sand boils, and slumping etc. (see Figs.1.1-1.5).

The destructive effects of soil liquefaction causes loss of billions of dollars due to structural damage, yet the casualties of human lives is immeasurable. The Niigata and Alaska earthquakes in 1964 are the events that focused world attention on the phenomenon of soil liquefaction, illustrating the significance and damage caused by the liquefaction. Significant number of researches have been conducted so far in understanding the liquefaction phenomenon since last five decades. Liquefaction was the cause of much of the damage to the port facilities and structures near waterfront in Kobe due to the 1995 Kobe

Figure 1.1. Sand boils during 1989 Loma Prieta earthquake (University of Washington, 2000).

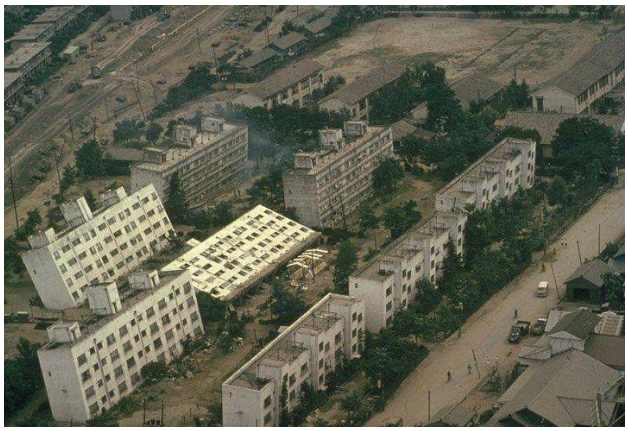

Figure 1.2. Collapse of buildings due to loss of bearing capacity during 1964 Niigata earthquake (University of Washington, 2000).

Figure 1.3. Depression behind quay wall at Kashima port (EERI, 2011).

Figure 1.4. Liquefaction induced differential movements around buried tanks of a water treatment plant in Kashima City during 2011 Great East Japan Earthquake (EERI, 2011).

Figure 1.5. Tilting of gas tank and damage to port facilities during 1995 Kobe earthquake (University of Washington, 2000).

earthquake. Soil liquefaction is also a major design problem for large sand structures such as mine tailings, impoundments and earthen dams. Earthquake induced liquefaction has become a major problem to soil embankments such as river dykes, levees, road embankments and earth dams, supported on a cohesionless foundation soil. Figures 1.6-1.8 show the widespread damage of embankments during past earthquakes due to liquefaction of foundation ground. Previous studies have shown that the widespread damage to such embankments occurred mainly due to the liquefaction of foundation soil, resulting in cracking, settlement, slumping and lateral spreading (Institute, 1997; Koga and Matsuo, 1990; Matsuo, 1996; Adalier et al., 1998; Tani, 1991). About 1200 levees were distressed during 2011 Great East Japan Earthquake due to liquefaction of foundation ground.

Figure 1.6. Lateral spreading at Raqui 2 bridge during 2010 Maule Earthquake in Chile (Yen et.al 2011).

Figure 1.7. Embankment failure due to liquefaction on the Pan-American Highway during 2007 Peru earthquake (MCEER, 2007).

Figure 1.8. Views of slumped Hinuma River Levee and cracks induced by liquefaction (GEER, 2011).

While most of the earlier physical model tests on liquefaction problems have dealt with uniform clean sand, most recent studies have employed horizontally layered soil (with uniform properties within distinct soil layers) (Liu and Qiao, 1984b; Dobry and Liu, 1992; Fiegel and Kutter, 1994; Kokusho, 1999, 2000c). However, real soil profile is complex and the soil layer is never uniform or continuous in case of layered soil. Most of the natural soil deposits not only vary in vertical direction but also vary in the horizontal direction as shown in Fig. 1.9. Recently, the liquefaction mechanism of heterogeneous soil deposits consisting of loose pockets of same sand with lower relative density had been studied by Chakrabortty and Popescu (2012). However, the stratification is not only limited to soft layers involving one type of soil material; it consists of many discontinuous layers ranging from highly permeable liquefiable to impermeable non-liquefiable layers, which will be referred as non-homogeneity hereafter. The presence of impermeable layer within liquefiable sand is of great significance as earthquake induced liquefaction can cause loosening of soil below impermeable layer (i.e., void redistribution), which is one of the mechanisms of flow failures in liquefied cohesionless soils during an earthquake. Moreover, during liquefaction, pore water flows from high pore water pressure zone to other zones with low pore water pressures, loosening the soil in combination with cracking which is another mechanism of flow failure (National Research Council, 1985). The importance of void redistribution and redistribution of excess pore water pressure and their effects have been identified and studied individually since last two decades. However, limited studies have been carried out under the combination of both mechanisms, i.e., void redistribution and redistribution of excess pore water pressure. Nevertheless, the presence of discontinuous impermeable layer focuses both localized loosening of the soil below the impermeable layer and flow of pore water from high pore pressure zone to other zones with

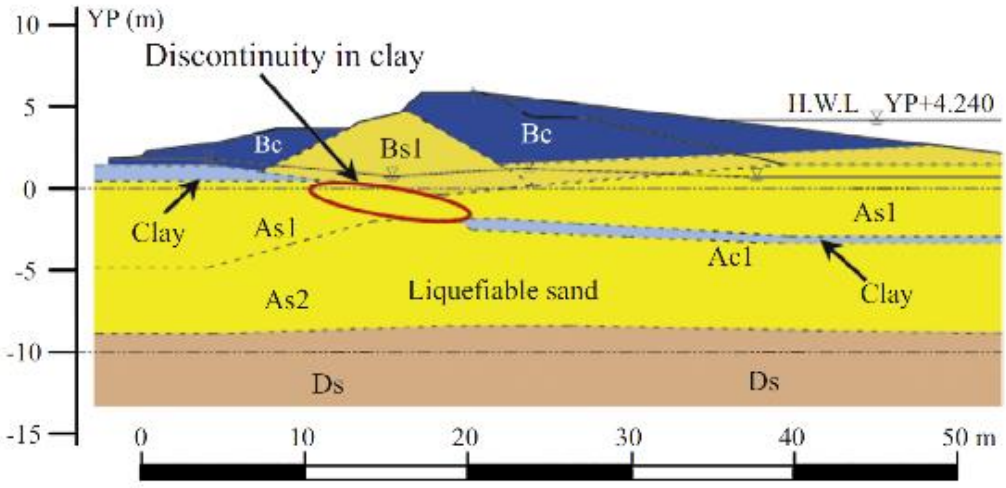

Figure 1.9. Soil profile along a levee in Tone river (Left levee at 32.3 km) (courtesy of Kanto Regional Development Bureau of Ministry of Land, Infrastructure, Transport and Tourism, Japan).

low pore water pressures. There are many unknown factors regarding the behavior of liquefiable soil with the discontinuous impermeable layers during an earthquake.

Regardless of the numerical and experimental approaches, the modeling of liquefaction induced localizations in the field is complicated by uncertainties in defining the spatial distribution and regularity of stratigraphic details that affect the continuity, extent, and hence influence of such localizations. In order to systematically predict the earthquake response of saturated porous media it is essential to correctly simulate the generation, redistribution, and dissipation of excess pore water pressure during and after earthquake shaking, which are the major mechanisms in case of real soil profile (Taiebat et al., 2010). To the best knowledge of the author, numerical or experimental studies related to presence of discontinuous less permeable layer in the liquefiable soil have not been carried out. Therefore, liquefaction potential of non-homogeneous soil profile is not well understood, though many liquefaction case histories exist. Neglecting the non-homogeneity of soil profile can underestimate the liquefaction potential of the soil. Despite the extensive research and development of remedial measures to prevent the large deformation of soil structures, embankments have suffered severe damage during past earthquakes. During 2011 Great East Japan Earthquake, Japan's Ministry of Land, Infrastructure, Transport, and Tourism (MLIT) documented that more than two thousand locations of levee suffered some level of damage (GEER, 2011; Oka et al., 2012). The minor to major damage was attributed due to the liquefaction of foundation soil. This event elucidates the further need to understand the deformation behavior of embankment resting on non-homogeneous liquefiable foundations.

1.2 Previous physical model tests on liquefaction in layered soil deposits

Natural sand deposit normally consists of many sublayers with different soil particles and properties, ranging from soft sand lenses to dense cohesive clay and coarse sand layers. The patterns of layering and lensing in an actual soil profile can be extremely complex and have great effect on geotechnical engineering problems at a site (National Research Council, 1985). In the present studies, most of the studies are dealt with continuous layered soil, which will be referred as homogeneous continuous layered soils hereafter. However, real soil profile is complex and the soil layer is never uniform or continuous in case of layered soil. Most of the natural soil deposits not only vary in vertical direction but also vary in the horizontal direction as shown in Fig. 1.10. Figure 1.10 displays the stratified soil which consists of thin layers of silt and clay sandwiched within liquefied sand, yet the layers are not continuous, which is referred as non-homogeneous soils hereafter.

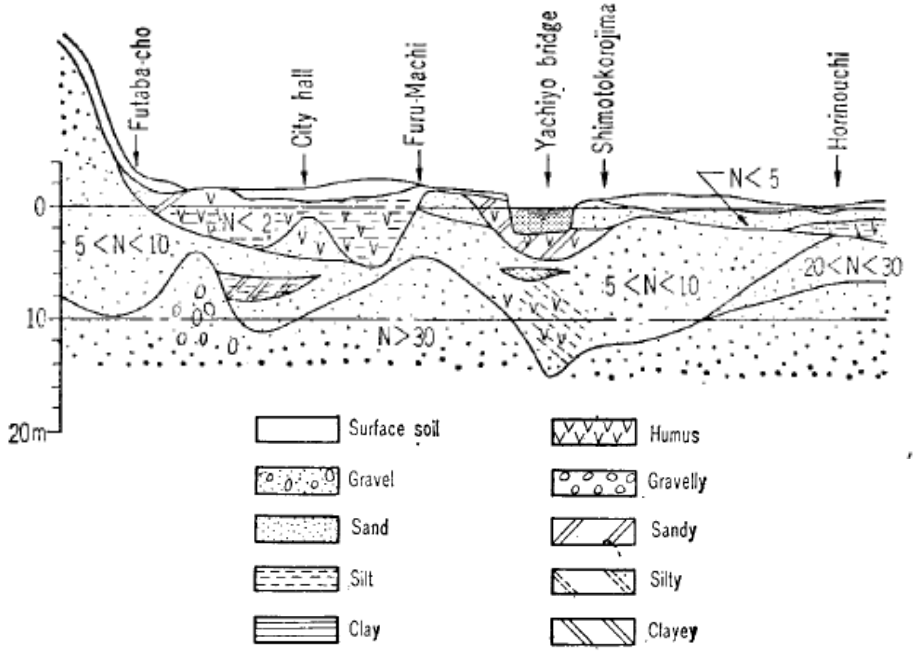

Figure 1.10. Subsoil condition of Niigata City (Kishida, 1966).

1.2.1 Homogeneous layered soil deposits

Following the two devastating earthquakes of 1964, the 1964 Niigata and 1964 Great Alaska Earthquakes, many geotechnical earthquake engineering research programs on liquefaction were initiated in Japan and North America. These have provided researchers with better insight into the liquefaction phenomenon and associated failures. Initially, the study was only confined to assess the triggering of liquefaction in clean, sandy soils. As the years passed followed by the devastating earthquakes like 1995 Kobe earthquake, 1999 Turkey earthquake, 1999 Chi Chi earthquake, physical model studies on layered soil deposits evolved. As a first known published work on formation of water film underneath the impermeable layer, Scott and Zuckerman (1972) studied the mechanism of liquefaction in stratified soil deposits of varying permeability, where the formation of water film was observed. Various experimental studies based on the physical model tests, such as one dimensional column tests (Kokusho, 1999; Kokusho and Kojima, 2002; Scott and Zuckerman, 1972; Tohumcu Özener et al., 2008; Liu and Qiao, 1984b), shaking table tests (Liu and Qiao, 1984b; Kokusho, 1999), and centrifuge model tests (Fiegel and Kutter, 1994; Kulasingam et al., 2004; Dobry and Liu, 1992; Brennan and Madabhushi, 2005; Balakrishnan and Kutter, 1999; Arulanandan and Scott, 1994), site investigation (Kokusho and Fujita, 2002; Kishida, 1966; Ishihara and Koga, 1981; Elgamal et al., 1996a) and numerical research efforts (Seid-Karbasi and Byrne, 2007; Yoshida and Finn, 2000; Lu and Cui, 2010) have been incorporated to examine the liquefaction in stratified sands and its effects.

1.2.1.1 Physical model tests

- Shaking table tests

Liu and Qiao (1984a) conducted shaking table tests on homogeneous deposits and horizontally stratified deposits in the presence or absence of a model foundation (Fig. 2.14). A sinusoidal excitation of 3-5 Hz frequency was applied to the models and continued until evidence of liquefaction was observed. The sinusoidal motion applied to the stratified models had a 0.3 g acceleration. In homogeneous sand deposits, the pore pressure of different locations at the same elevation was nearly identical. The small horizontal fissures filled with water were appeared symmetrically or asymmetrically when the pore pressure increased. The fissures grew rapidly to form water interlayer or water lens as the vibration continued. The further build-up of pore pressure interconnected the water lens located at the same elevation to form a long water interlayer. Moreover, the ground surface was uplifted with the increment in thickness of water interlayer. Once the thickness of water interlayer reached its maximum thickness, the water burst out with a noise and sand boiling occurred. Kokusho (2000a, 1999) conducted a 1 G shaking table for a two dimensional slope model with an arc of silt within a saturated sand. The author considered the silt sublayers to be continuous and the effect of the impermeable layer was studied. The tests showed the formation of water film beneath a silt seam in slope in short time after liquefaction which can possibly drive the soil mass with gentle slope. The continuous formation of water film along a potential slip surface, upper soil will deform discontinuously along the water film. It was found that the water film had a significant role in lateral spreading or slope failure in liquefied sand. The breakage of the silt seam enabled the upward flow of trapped water, which can trigger re-liquefaction and lateral flow deformation.

- Centrifuge model tests

Dobry and Liu (1992) presented two centrifuge tests results conducted on layered soil deposits. In the first test, Nevada sand was placed at a relative density of 40% with a silt layer on top. Based on the pore pressures and accelerations measured in these tests, they inferred four stages of behavior, which included the formation of a water interlayer (Fig. 1.11). The first stage lasted 2 seconds where generation of pore water pressure took place and the upward flow of pore water occurred (Fig. 1.11(a)). During the shaking or shortly after shaking, initial liquefaction had occurred at the upper part of the sand layer and the water film started to develop (Fig. 1.11(b)). As the shaking stopped, it was seen that the excess pore water pressure is constant for a certain period of time below the silt layer with zero hydraulic gradient (Fig. 1.11(c)). After this water film got dissipated and coupled consolidation of the two layers took place (Fig. 1.11(d)). This clearly explained the mechanism of liquefaction in layered soils. The second test had a model with a very similar two-layer horizontal soil deposit with a shallow foundation on the soil surface. The relative density of the sand was 45%. A water interlayer was formed in this test as well. The

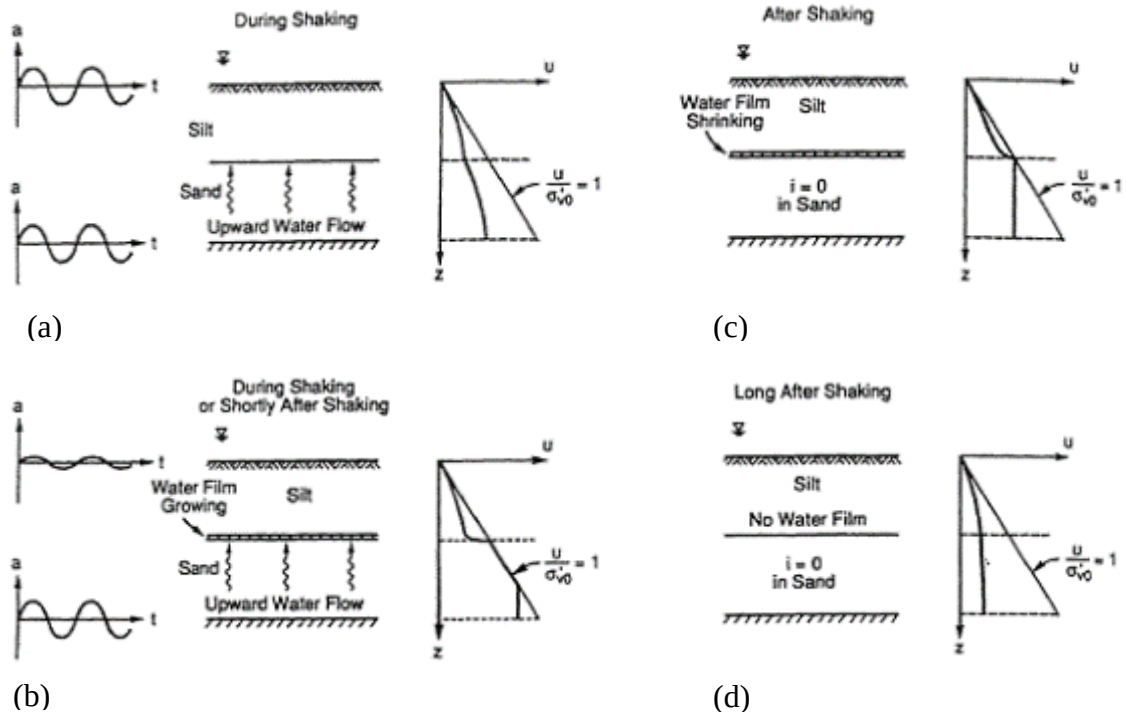

Figure 1.11. Four stages observed in centrifuge test of two-layer deposits (Dobry and Liu, 1992).

thickness of the water interlayer was found to be larger in the free field than under the structure, since the weight of the structure was forcing the water out towards the free field.

Fiegel and Kutter (1994) described the mechanism of liquefaction in layered soil deposits. The water interlayer was generated beneath the silt layer during liquefaction in centrifuge tests. Balakrishnan and Kutter (1999) investigated the remediation required to control the settlement and lateral sliding of liquefiable sand overlain by clay floodplains. A series of centrifuge model tests were conducted on loose sand deposits and improved sand which was densified to higher relative density. The results also showed the restriction of upward flow of water due to presence of an impermeable clay layer, caused a weak zone with shear resistance much less than the undrained residual strength. Also, it was found that densification of sand deposit was effective in reducing the extent of liquefaction. Adalier and Elgamal (2002) studied the behavior of dense sand surrounded by liquefied loose sand by conducting a series of dynamic centrifuge tests. Tests were performed on saturated side-by-side dense-loose sand column model in a laminar container. The tests results showed that the development of high pore water pressure in the liquefied zone could degrade the strength of dense sand due to migration of pore water pressure towards the dense sand column from the loose sand column. Kulasingam et al. (2004) conducted several centrifuge tests in homogeneous sand slope and sand slope with incline silt plane to study the void redistribution effects on sand slope with low permeability silt interlayer. The tests

demonstrated that the void redistribution developed at the interface between sand and silt layer causes the strain localizations and associated large deformations in liquefied soil. Brennan and Madabhushi (2005) investigated liquefaction and drainage in stratified soil by conducting several centrifuge tests in liquefiable sand overlain by a silt graded rock flour paste, also consisting of vertical drains installed through the soil profile. The tests also gave the evidence supporting the development of water films at the interface between the saturated sand and low permeability fines. Moreover, the results suggested that vertical drains could be an effective measure to reduce the formation of water film around the vicinity of drains.

- One dimensional model tests

Kokusho (1999) conducted one dimensional model tests in loose saturated sand sandwiched by a seam of silt to investigate the detail mechanism of water film formation and related postliquefaction behavior (Fig. 1.12(a)). This 1D sand layer was instantaneously liquefied by a shock given by a steel hammer. After 35 s of the shock, the water film of about 8 mm was formed by a migration of pore water from underlying sand layer (Fig. 1.12(b)). The model tests also showed that the thickness and duration of a water film are inversely proportional to the density of sand. This water film can act as a sliding surface in horizontally layered deposit, resulting in flow failure and lateral spreading (Kokusho, 2000a; Kokusho and Kojima, 2002). Amini and Sama (1999) compared the behavior of stratified and homogeneous sand-silt-gravel composites during seismic liquefaction for various silt and gravel contents in cyclic triaxial tests, based on the method of sample preparation. The moist tamping method represented homogeneous soil conditions and the wet pluviation method represented stratified soil conditions. It was concluded that the liquefaction resistance of layered and homogeneous sand-silt-gravel composites were not significantly different. The effects of silt content were quite similar for both homogeneous and layered soil conditions. Tohumcu Özener et al. (2008) conducted the shaking table model tests to investigate the generation of pore water pressure and liquefaction mechanism in layered and silt interlayered sand deposits with different relative densities subjected to different input excitations. A water film was developed beneath the silt seam as soon as the shaking started, as the silt layer prevents the upward flow of pore water lowering the excess pore water pressure above the silt layer. It was also observed that the thickness of water film increased with the intensity of shaking and lowering of relative density. However, the stable water film could not be observed under strong shaking due to turbulences induced by high hydraulic gradient.

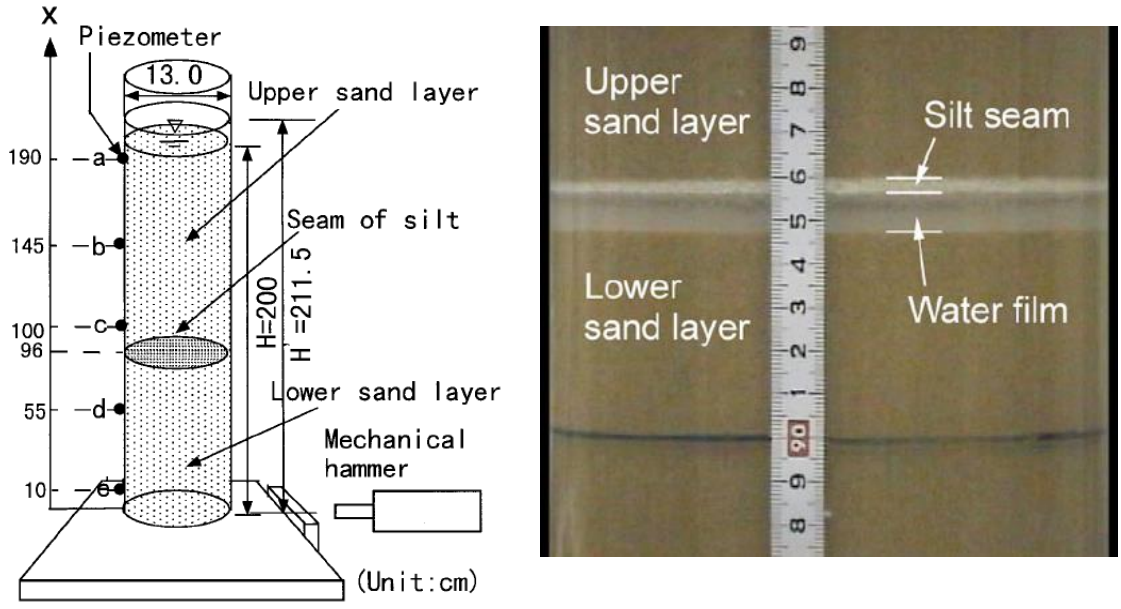

(a) (b)

Figure 1.12. (a) 1D saturated loose sand model liquefied by hammer and (b)Formation of water film beneath silt seam (Kokusho, 1999).

1.2.1.2 Site investigations

Kokusho and Fujita (2002) examined the involvement of water films in lateral flow failure during earthquake based on site investigation data obtained from borehole logs in two areas in Niigata city where large flow displacements took place. The authors reviewed case histories of flow failures in liquefied sandy deposits in Niigata city during the 1964 earthquake from the point of view of formation of water film beneath the relatively impermeable sublayers. The boring data revealed the presence of continuous and discontinuous sublayers of fine soil near the ground surface. It was found that the presence of continuous or discontinuous sublayers of fine soil near the ground surface might have developed the water films beneath the fine soil, resulting in large lateral flow in liquefied soil deposits.

1.2.1.3 Numerical studies

Naesgaard et al. (2005) numerically simulated the liquefaction induced displacements and flow failures observed in the centrifuge tests using UBCSAND model and prescribed the methods for mitigating the effects of void redistribution. The authors explained the three zones, i.e. a lower contractive zone, an upper expansive zone and a thin very expansive interface layer at the top developed in loose sand underlying a low permeability barrier (Fig 1.13). The thin very expansive interface layer could play an important role in lateral displacement of the overlying layer. Drainage was recommended as an effective means of mitigating low permeability barrier induced flow sliding.

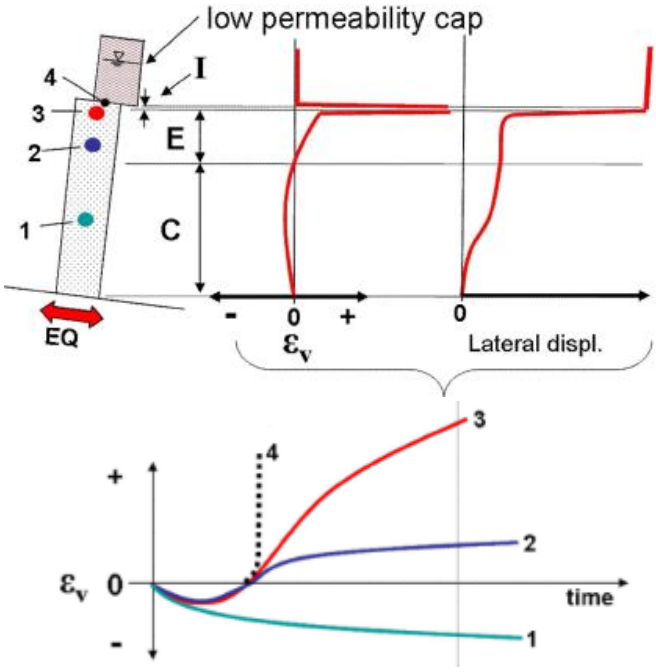

Figure 1.13. Schematic of mechanism for void redistribution with a low permeabilitylayer over loose sand (Naesgaard et al., 2005).

Seid-Karbasi and Byrne (2007) investigated the effects of a low permeability barrier layer on ground deformations by using an effective stress coupled stress-flow dynamic analyses based on elastic-plastic constitutive model (UBCSAND). The presence of low permeability layer caused the contraction of loose sand at the base of sand layer and expansion at the upper layer due to redistribution of pore pressure. The expansive zone developed beneath the low permeability layer during seismic loading with very high void ratio or water interlayer zones had very low to nearly zero shear strength, which was responsible for flow failures. Moreover, the migration of excess pore water pressure even from high pore pressure region might cause a larger deformation even after the cessation of earthquake. Yoshida and Finn (2000) proposed a joint element to study the effect of impermeable layer on liquefiable sand. The element was incorporated in a finite element program, which can simulate the interface behavior of layered soils. Yang and Elgamal (2002) numerically investigated the influence of soil permeability on liquefied soil. Several numerical simulations were conducted in an inclined (4^o) saturated soil profile which consists of liquefiable soil stratum of different permeabilities, uniform clean sand in first case, sandy gravel interlayered by silt in second case, and clean sand interlayered by silt in third case. Flow failure occurred in second case as soon as the shaking stopped due to the loss of shear below the silt interlayer, whereas delayed flow failure occurred in third case after the end of shaking. The authors highlighted the role of relatively impermeable seams in the possible development of a flow failure mechanism. One of the major

observations was the potential significance of permeability in liquefaction-induced shear deformations. Therefore, the study related to overall site permeabilities profiles and site investigations of liquefiable natural as well as man-made soil deposits are of prime importance. Kamai and Boulanger (2011) numerically analyzed the effects of void redistribution in layered soil profiles on residual strength of a liquefied soil. The two dimensional finite difference simulations of a centrifuge test with mildly-sloping ground concluded the potential of void-redistribution to induce shear-strain localization and delayed flow-slide was also observed.

1.2.2 Non-homogeneous soil deposits

Natural soil profile not only varies in the vertical direction but they could also vary in the horizontal direction. It may consist of loose pockets which can affect the seismic response of the liquefied soil. When the seismic waves travels through the soil medium, the soft layer prevents the incident waves from travelling freely in the soil medium by reflecting most of them downwards. Ghosh et al. (2005) performed a series of centrifuge tests to analyze the effects of localized loose sand in a dense sand deposit subjected to seismic loading followed by numerical simulations. It was found that the soft layer has significant influence on the overall response of the layered strata. The soft layer beneath the structure affected the post-earthquake stability and settlement of the existing structure. Moreover, it was found that the excess pore water pressure reached the value equal to the overburden pressure at the soft layer, indicating the full liquefaction in soft layer. The shear wave velocity in soft layer considerably decreased. The presence of the localized loose patch diffracts the shear waves around the corners of the patch, increasing the accelerations below the surface. Popescu et al. (2006) investigated the variation of excess pore water pressure in heterogeneous soil deposits by numerical analysis. He concluded that a larger amount of excess pore water pressure was generated in a heterogeneous soil than in the corresponding uniform soil having similar geomechanical properties. Chakrabortty and Popescu (2012); (Chakrabortty et al., 2008) also conducted a series of centrifuge tests on homogeneous and heterogeneous soil deposits followed by numerical simulation to investigate the behavior of liquefaction in heterogeneous soils. The heterogeneous model consisted of sixteen loose pockets of same sand with lower relative density of 35%.The results showed more excess pore water pressure is generated in a heterogeneous soil deposits of average relative density 64% than in corresponding homogeneous soil of relative density 55%, which supported the previous findings by Popescu et al. (2006). The excess pore water pressure generated in the loose zone migrated to the dense zone, reducing the shear strength in dense sands. This study emphasized the effects of soil heterogeneity on water migration in spatially variable soils.

1.3 Liquefaction-induced settlement during earthquakes

Large lateral ground deformations including settlement, which induce severe damage to

various infrastructure and lifelines, are the major geotechnical hazards following liquefaction during earthquakes. The permanent deformation in the form of settlements had been observed during the past and recent earthquakes during liquefaction. When the pore water pressures build-up during liquefaction, start to dissipate mainly towards the ground surface, some volume changes occur in the sand deposits which is manifested on the ground surface as settlements (Ishihara and Yoshimine, 1992). Nevertheless, due to the geological non-uniformities and uncertainties in stratigraphic profile, the rate of dissipation of pore water pressure changes at respective locations, accounting differential settlements in the surface (Ishihara and Yoshimine, 1992). Past laboratory experiments suggested that large deformation often occurred after sand liquefaction, in most cases when the effective stress in sand reduced to zero (Shamoto et al., 1997). Many past studies have focused mainly on the pre-liquefaction (i.e. the initiation of liquefaction) while several studies of post liquefaction and case histories have confirmed the occurrence of large post-liquefaction deformation (Vaid and Thomas, 1995; Sento et al., 2004; Yoshida et al., 1987) . For instance, an apartment building in Kawagishi-cho overturned after several minutes and deformed continuously after the end of shaking during 1964 Niigata earthquake (Kawakami and Asada, 1966).

Scott (1986) studied the solidification and consolidation of a liquefied sand to examine the settling out of the suspended sand grains, and dissipation of pore pressures. The author pointed out that the sand particles were in suspension in liquefied zone and began to settle out when the shaking stops or when the intensity diminished. The settling particles accumulated to form a solidified zone which increased with time, followed by dissipation of excess pore water pressure. Nagase (1988) studied the settlement phenomena following the liquefaction of the ground during earthquake by using the simple shear device. The test results showed that the volume change taking place during reconsolidation was equal to the amount of excess pore water pressure which had been generated during the application of irregular shear stress. The settlement of the specimen is accompanied by the volume change during reconsolidation. Ishihara and Yoshimine (1992) studied the volumetric strain in sand deposits during dissipation of pore water pressures developed as a results of application of cyclic shear stress. The pore water pressure dissipated towards the ground surface, accompanied by some volume change of the sand deposit which is manifested on the ground surface as settlement. The authors concluded that the volumetric strain of sand during liquefaction was uniquely correlated with the amount of pore water pressure developed, no matter what types of irregular loads were used.

Boulanger and Truman (1996) studied the response of sand in an infinite slope under post-earthquake loading conditions by triaxial tests and described a mechanism for void redistribution within a confined layer of sand. Tokimatsu et al. 2001 studied shear deformation behavior under arbitrary water drainage conditions using torsional hollow cylinder shear tests and found that shear stress tends to decrease due to pore water migration from the lower liquefied layer. Sento et al. (2004) examined the postliquefaction flow failure

mechanism, in which shear strain developed due to seepage upward flow during redistribution of excess pore water pressure after an earthquake by performing triaxial tests. The authors concluded the possibility of postliquefaction flow failure due to redistribution of excess pore water pressure from lower liquefied layers. The continuous flow of pore water pressure from lower layers developed large shear strain inducing larger horizontal and vertical deformation. Tsukamo and Ishihara (2010) examined the procedure to evaluate the settlement of saturated soil deposit following liquefaction during earthquake. The authors also concluded that the settlement of saturated soil deposits following the liquefaction was equivalent to the volume changes of saturated soil specimens caused by the drainage of excess pore water following either undrained cyclic triaxial tests or shear tests.

1.4 Mechanism of postliquefaction failure due to seepage

During liquefaction, excess pore water pressure develops in respective sand layers under earthquake loadings. As soon as the cyclic loading stops, the excess pore water pressure tries to dissipate towards the ground surface. Figures 1.14 and 1.15 explain the mechanism of postliquefaction failure due to seepage. Pore water pressure would redistribute in the following ways (Sento et al., 2004) (Fig. 1.14). (a) Pore pressure in lower sand layer is higher than that in the upper layer at the end of earthquake(t_o), (b) Excess pore water pressure in the upper sand layer increases until it becomes equal to effective overburden pressure (i.e. t_1 second after shaking stops). (c) Upward seepage flow continues until t_2 second after earthquake stops, when the hydraulic gradient becomes zero. (d) The sand layer continues to consolidate until the excess pore water pressure dissipates in all layers. Figure 1.15 depicts the schematic diagrams of stress path and volumetric and shear strain relationship. Path A→B indicates the undrained cyclic shearing process. Path B→D

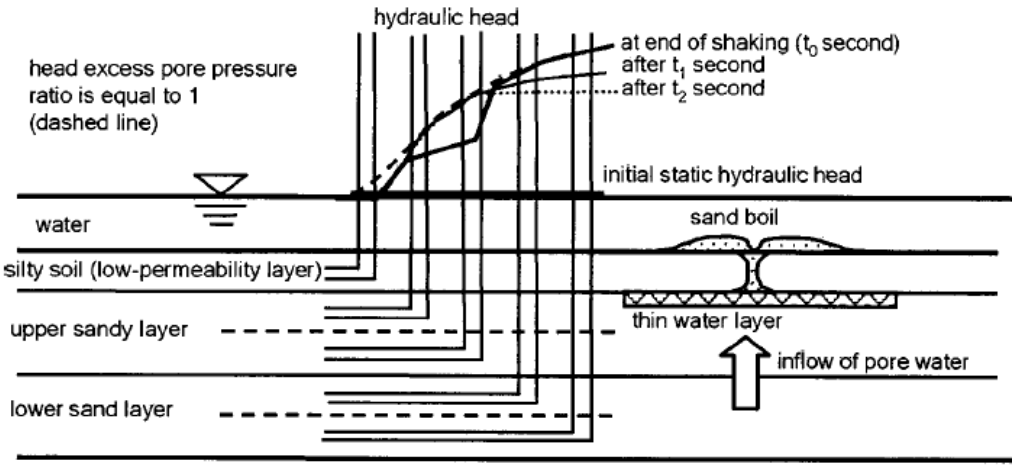

Figure 1.14. Schematic diagram to explain the flow failure mechanism of ground (Sento et al., 2004).

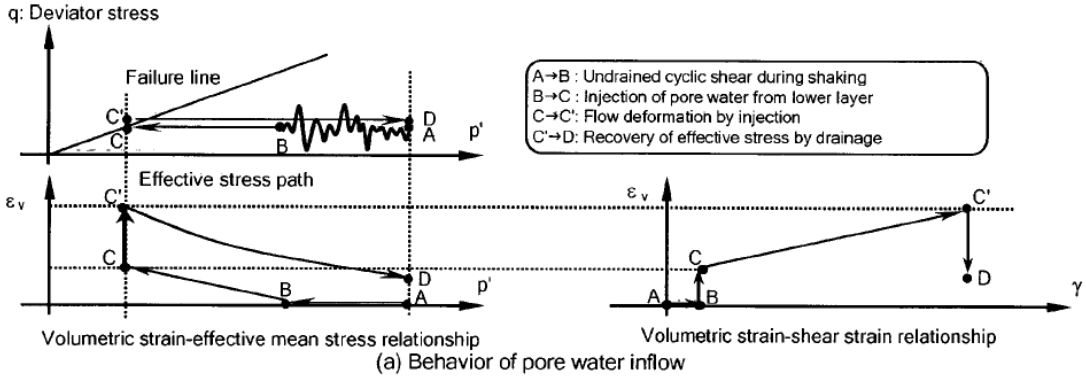

Figure 1.15. Schematic diagram to explain the flow failure mechanism due to seepage (Sento et al., 2004).

indicates the dissipation of excess pore water pressure after earthquake. Path B→C represents the dissipation of excess pore water due to inflow which corresponds to period from t_o to t_1. Path C→C' corresponds to continuous pore water inflow from period t_1 to t_2. Reconsolidation occurs dissipating the excess pore water pressure from path C'→D.

1.5 Seismic response of embankments

Many earth embankments worldwide are located in seismically active areas (Marcuson and Silver, 1987). Many of these embankments are founded on liquefiable soils, which may have the potential hazardous impact during earthquakes. The past major seismic events such as Loma Prieta 1989, the Hyogoken-Nanbu 1995, the Great East Japan 2010 Earthquakes continued to demonstrate the associated deformations and damaging effects of embankments. Earthquake induced liquefaction has become a major problem to soil embankments such as river dykes, levees, road embankments and earth dams, supported on a cohesionless foundation soil. Previous studies have shown that the widespread damage to such embankments occurred mainly due to the liquefaction of foundation soil, resulting in cracking, settlement, slumping and lateral spreading (Seed, 1968; Koga and Matsuo, 1990; Matsuo, 1996; Adalier et al., 1998; Tani, 1991).

Several experimental studies and numerical analyses have been conducted previously to examine the behavior of embankments resting on uniform clean cohesionless soil during earthquakes (Adalier et al., 1998; Koga and Matsuo, 1990; Aydingun and Adalier, 2003; Adalier and Sharp, 2004). Koga and Matsuo (1990) conducted a series of shaking table tests on earthen embankment founded on saturated sand ground and found out that the ground beneath the embankment did not liquefy, whereas the ground in the free ground liquefied and the slumping and cracking of embankment is due to the softening of the underlying ground associated with pore water pressure generation. Previous studies that proposed

various techniques for mitigation of liquefaction-induced damage in uniform ground have also been reported (Adalier et al., 1998; Adalier and Sharp, 2004). Adalier and coworkers conducted a series of centrifuge tests and numerical analysis to assess the earthquake performance of mitigation techniques for a liquefiable uniform foundation under an embankment (Adalier, 1998; Aydingun and Adalier, 2003; Adalier and Aydingun, 2003). The embankment foundation system was first studied without and then with the following four different liquefiable countermeasure techniques: densification, cement deep-soil-mixing, gravel berms, and sheet-pile enclosure. It was found that the implemented countermeasures reduced the embankment vertical deformations by a maximum of 50%. Moreover, the retrofit techniques constrained the lateral outflow of the underlying foundation soil below the embankment, reducing the deformation of embankments.

Adalier and Sharp (2004) investigated the effects of foundation densification and found out that there might be an optimum depth of densification treatment beneath an earth dam beyond which the reduction of the earthquake-induced deformations are relatively minor. Sharp and Adalier (2006) investigated the effects of the location of a liquefiable layer in the foundation by a series of dynamic centrifuge tests. The foundation consists of two dense sand layers and a loose sand layer. Tests were carried out by changing the position of loose sand layer.

It is noted however, that natural sand deposit normally consists of many sublayers with different soil particles and properties, ranging from soft sand lenses to stiff cohesive clay and coarse sand layers. Kokusho and coworkers (Kokusho, 1999, 2000c) have studied the formation of water film beneath the thin impermeable silt due to difference in permeability in layered sand and its role in the extent of lateral deformation in the sloping surface. Malvick and coworkers (Malvick et al.; Kulasingam et al., 2004) conducted centrifuge tests to demonstrate the shear localization due to void redistribution and its consequences on large postshaking deformations in a sand slope with continuous embedded silt layers. Nonetheless, most of the embankments rest on non-homogeneous liquefiable soil profiles, which consist of thin layers of discontinuous low permeability layers like silty sand or clay. Oka et al. (2012) performed numerical modeling of river embankments on a foundation with various soil profiles and ground water tables, including a clayey soil layer. However, most previous studies have only investigated the dynamic behavior of embankments resting on uniform sand. Thus, the dynamic behavior of earthen embankments on a liquefiable non-homogeneous foundation, consisting of discontinuous low permeability layers of silt or clay at different depths is not well understood. Despite the extensive research and development of remedial measures to prevent the large deformation of soil structures, embankments have suffered severe damage during past earthquakes. During 2011 Great East Japan Earthquake, Japan's Ministry of Land, Infrastructure, Transport, and Tourism (MLIT) documented that more than two thousand locations of levee suffered some level of damage (GEER, 2011; Oka et al., 2012). The minor to major damage was attributed due to the liquefaction of foundation soil. This event elucidates the further need to understand the deformation

behavior of embankment resting on non-homogeneous liquefiable foundations.

1.6 Sequential ground motions

Repeated ground-motion sequences occurring after short intervals of time, resulting from mainshock-aftershock earthquakes, have been observed during many earthquakes (Zhang et al., 2013). For instance, Fig. 1.15 shows the series of sequential ground motions consisting of mainshock followed by aftershock after some interval of time period during the past earthquakes. Many researchers based on the centrifuge tests concluded that lateral ground deformation in lateral spreads in mildly sloping ground stopped as soon as the shaking ended. Moreover, they even pointed out that even if the soil continued to liquefy for some time after the end of shaking, lateral deformation stopped as soon as shaking ended, which indicated that there was no any lateral displacement without shaking (Towhata et al., 1988; Dobry et al., 1995; Dobry and Abdoun, 1998). However, these phenomena did not

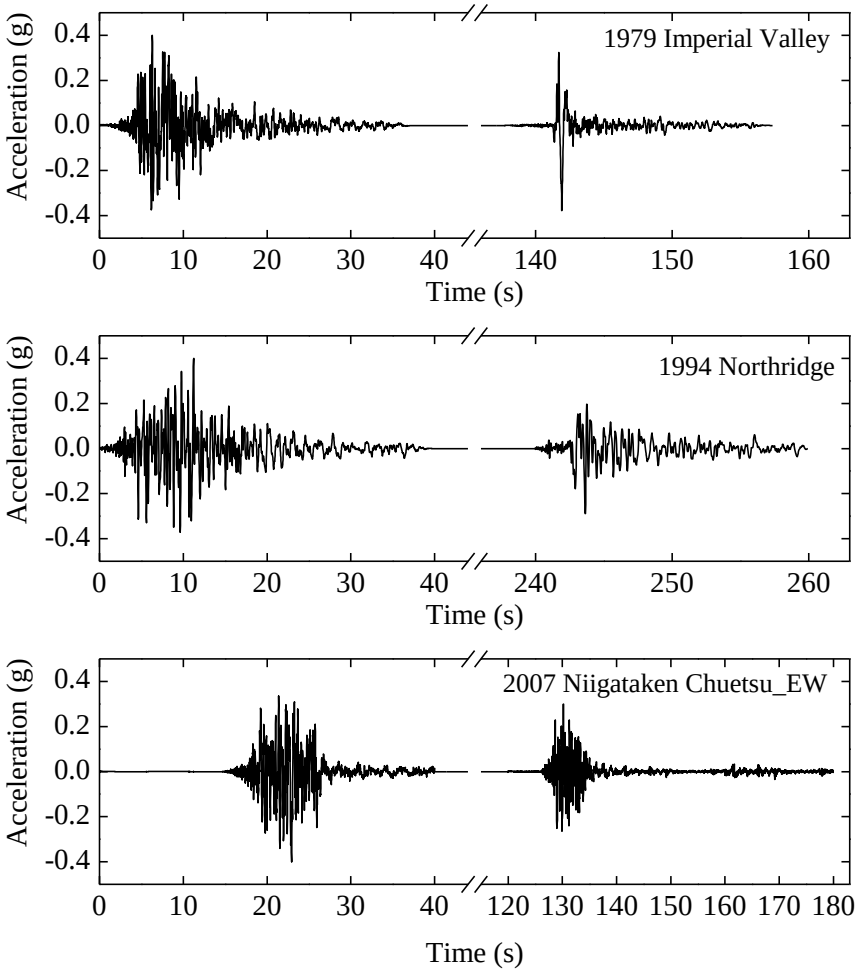

Figure 1.16. Sequential ground motions.

incorporate to a liquefied layer under an impermeable layer due to the potential of void redistribution inducing shear localization (Fiegel and Kutter, 1994; Kokusho, 1999; Kulasingam et al., 2004). These would contradict with the permanent deformation reported by eye witnesses during 1964 Niigata earthquake (Kawakami and Asada, 1966). Previous studies have pointed out that the low-amplitude aftershock can accumulate large lateral deformation and continue for several minutes on the liquefied soil (Okamura et al., 2001; Meneses-Loja et al., 1998; Ishihara and Cubrinovski, 1998). According to Dobry et al. (1995), the continued deformation might have been caused by small vibration after main shaking or aftershocks with the small vibration or weak aftershocks not felt by the witnesses on the ground surface. According to the Japan Meteorological Agency, many aftershocks occurred few seconds or minutes after the main shaking during 1964 Niigata earthquake and 1995 Kobe earthquake, including 2011 Great East Japan earthquake.

Okamura et al. (2001) conducted centrifuge tests by applying the shaking consisting of main shock followed by two aftershocks separated by a time interval of 4 seconds. The pore pressure ratio remained equal to 1 during the main shock and also throughout the aftershocks. Moreover, the lateral displacement stopped as soon as the main shock ended but the displacement increased with the excitation of aftershocks. This provides strong evidence to the hypothesis that weak aftershocks after the main shock can drastically increase the rate of displacement. Ye et al. (2007) conducted shaking table tests and numerical analyses on saturated sandy soil to investigate the mechanical behavior of liquefiable foundations during repeated shaking and consolidation. Xia et al. (2010) presented numerical analysis of an earth embankment on liquefiable foundation soils under repeated shake-consolidation process. During 2011 Great East Japan Earthquake, the liquefaction-vulnerable structures continued to shake after the onset of soil liquefaction for more than two minutes. Moreover, during the reconnaissance survey after 2011 Great East Japan Earthquake, Sasaki and his team (Sasaki et al., 2012) found that the more severe deformation and subsidence of levees was due to the occurrence of aftershock, 30 minutes after the mainshock. Moreover, the gap between mainshock and aftershock is the primary factor during earthquakes. It has been pointed out by many researchers that the occurrence of aftershock before the major dissipation of excess pore water pressure causes more severe damage to the superstructures. However, in most of the previous experimental and numerical studies seismic performance of soil structures is investigated by applying only a single earthquake, ignoring the influence of repeated earthquake phenomena. Moreover, no previous study has examined the effects of repeated earthquakes on embankments lying on non-homogeneous soil deposits. Therefore, to understand the deformation mechanism of embankments lying on non-homogeneous soil deposits under mainshock and sequential ground motion is of great importance.

1.7 Objectives and scope of the study

Regardless of the numerical and experimental approaches, the modeling of liquefaction in the field is complicated by uncertainties in defining the spatial distribution and regularity of stratigraphic details that affect the continuity, extent, hence influence of shear localizations, void redistribution, and dissipation of excess pore water pressure. Accounting for geological non-uniformities are very hard to evaluate but this study modeled the features of actual liquefiable soil profiles with discontinuous low permeability layers to provide new insights into the drainage path for dissipation of excess pore water pressure in various ground conditions and compared the liquefaction-induced deformation of embankments on different foundations. To this end, a series of dynamic centrifuge tests were conducted on saturated uniform, continuous silt interlayered sand, and discontinuous silt interlayered sand, referred as non-homogeneous soil profile specimens. Tests were also conducted with embankments on different foundation grounds. Finite element analyses were also carried out to simulate the experimentally observed behavior and to conduct parametric studies for generalization of the findings of the study. The main objectives of this study are as follows:

1. Model the multi-layered soil profile consisting of discontinuous thin layers of low permeability based on observations of several damage sites during recent earthquakes to improve the ability to account for them in practice.

2. Enhance the understanding of the complicated mechanisms of liquefaction in non-homogeneous soil deposits following earthquake loading

3. Investigate the liquefaction-induced deformation of embankments resting on non-homogeneous foundation and compare that with uniform and continuous layered foundations.

4. Explore the effects of different aftershocks occurring before the major dissipation of excess pore water pressure.

5. Determine the critical position of non-homogeneity and assess the effects of non-homogeneity on liquefaction-induced deformation of embankments on non-homogeneous soil deposits.

1.8 Outline of dissertation

This dissertation is composed of 6 additional chapters. Below is a short description of the six chapters that encompass the main body of the research work. The corresponding acknowledgements and references sections were combined and are presented at the beginning and at the end of this dissertation, respectively.

Chapter 2 presents the results of dynamic centrifuge model tests conducted to investigate the liquefaction mechanism in non-homogeneous soil deposits. Four types of model tests were conducted: one model test involved a uniform soil deposit; one involved continuous layered soil deposit; and two involved discontinuous layered soil deposits. Non-homogeneity in the tests was incorporated by including periodically distributed discontinuous silty sand patches.

Chapter 3 presents the results of dynamic centrifuge tests conducted on different foundation conditions: one involving a uniform foundation; one involving a continuous silty sand layer foundation; and three involving non-homogeneous discontinuous silty sand layer foundations. The liquefaction-induced deformation of embankments resting on different foundations under mainshock and sequential ground motion are compared.

Chapter 4 simulates centrifuge model tests to understand the liquefaction mechanism of non-homogeneous soil deposits and dynamic behavior of embankments resting on non-homogeneous foundation, using finite element analyses. The numerical results are compared with experimental results for the validation of numerical model used.

Chapter 5 presents the numerical results of embankments resting on different liquefiable foundation under different sequential ground motions. The sequential ground motions consist of mainshock followed by different aftershocks, where the peak ground acceleration and duration of aftershock is varied. The effects of aftershock on deformation of embankments are compared.

Chapter 6 presents the numerical results of parametric studies conducted to compare the deformation of embankment under different position of non-homogeneities. The position of non-homogeneity is varied in order to determine the critical position.

Conclusions and recommendations of this study are presented in *Chapter 7.*

Chapter 2

Liquefaction-induced settlement and pore water migration in non-homogeneous soil deposits

This chapter presents the results of dynamic centrifuge model tests conducted to investigate the liquefaction mechanism in non-homogeneous soil deposits. Four types of model tests were conducted: one model test involved a uniform soil deposit; one involved continuous layered soil deposit; and two involved discontinuous layered soil deposits. Non-homogeneity in the tests was incorporated by including periodically distributed discontinuous silty sand patches. The records of all the transducers are not shown here for brevity. Therefore, in this chapter, the liquefaction mechanism in non-homogeneous soil deposits are investigated. Effects of non-homogeneity on dissipation of excess pore water pressure, a significant phenomenon after seismic loading and settlement induced by seepage flow are discussed in depth. Comparison of the results of these tests after shaking allowed investigating the influence of non-homogeneity on reconsolidation settlement. The entire results are presented and discussed in prototype scale units, unless indicated otherwise.

2.1 Seismic response of uniform soil deposits

Previous studies that initiated following the observations from liquefaction-related damage during several past devastating earthquakes, have provided significant insights into the liquefaction phenomenon and associated failures. Initially studies were only focused on assessing the triggering factors for liquefaction in clean sandy soils. As the years passed, physical model studies on layered soil deposits evolved. Besides site investigations (Kokusho and Fujita, 2002) and numerical analyses (Seid-Karbasi and Byrne, 2007; Yoshida and Finn, 2000; Lu and Cui, 2010), several experimental studies based on physical model tests, such as one-dimensional column tests (Kokusho, 1999; Kokusho and Kojima, 2002; Scott and Zuckerman, 1972; Tohumcu Özener et al., 2008), shaking table tests (Liu and Qiao, 1984b; Kokusho, 1999), and centrifuge model tests (Fiegel and Kutter, 1994; Kulasingam et al., 2004; Dobry and Liu, 1992; Brennan and Madabhushi, 2005; Balakrishnan and Kutter, 1999; Malvick et al., 2008b), have been conducted to examine the effects of liquefaction in stratified sands. Previous studies indicate that the presence of a relatively impermeable layer (e.g., silt) within a liquefiable sand deposit results in the formation of a water film beneath it because of the trapping of pore water squeezed from

the liquefied sand. This plays a key role in the extent of lateral deformations in the sloping surface (Kokusho, 1999, 2000b; Kokusho and Kojima, 2002).

It is noted that the real soil profile is complex and a soil deposit is neither uniform nor consists of continuous layers. Natural sand deposits normally consist of many sublayers with different soil particles and properties, ranging from soft sand lenses to stiff cohesive clay and coarse sand layers. The actual soil profile characterized by various patterns of layering and lensing is very complex, which may have a great effect on geotechnical engineering problems at a site (National Research Council, 1985) . The recent seismic events of March 11, 2011 in Japan elucidate the further need to understand the complex behavior in a stratified soil profile during liquefaction. However, with the exception of the work by Malvick et al. (2008b), Ghosh et al. (2005), and Chakrabortty and Popescu (2012), other physical model tests on liquefaction problems have dealt with uniform clean sand and more recently horizontally layered soil (with uniform properties within distinct soil layers). Malvick et al. (2008b) conducted a centrifuge test to demonstrate the distribution of pore water during dissipation of earthquake-induced Δu in a sand slope with continuous embedded silt layers and large postshaking deformations. Ghosh et al. [20] performed a series of centrifuge tests to investigate the effects of localized loose sand in a dense sand deposit subjected to seismic loading. It was found that the presence of loose sand has significant influence on the overall response of the layered strata. Chakrabortty and Popescu (2012) conducted centrifuge tests and numerical simulations on homogeneous and heterogeneous soil deposits consisting of loose pockets of Fraser river sand of relative density 35% surrounded by dense sand of relative density 75%. The results showed that more Δu is generated in a heterogeneous soil deposit than that in homogeneous soil deposit. Nonetheless, these studies (Ghosh et al., 2005; Chakrabortty and Popescu, 2012; Malvick et al., 2008b) did not discuss the potential effects of pore water dissipation after shaking on non-uniform settlements as observed in several damage sites during last earthquakes. The conclusions of these studies are not applicable to soil profiles, where the stratification is not only limited to loose and dense sand layers of same material and continuous silt planes. Liquefiable soil deposits consist of thin layers of discontinuous low permeability layers like silt or clay imbedded in sand. To the best knowledge of the authors, numerical or experimental studies related to the presence of discontinuous low permeability layers of silt or clay in liquefiable sand which represents the actual soil profile, have not been carried out. Therefore, the liquefaction potential of a non-homogeneous soil profile is not well understood, though many liquefaction case histories exist.

This chapter presents the results of four dynamic centrifuge model tests, conducted to investigate the liquefaction-induced settlement and pore water migration during dissipation of earthquake-induced Δu in non-homogeneous soil deposits. Two of the model tests were conducted on non-homogenous soil deposits. Non-homogeneity was incorporated by including periodically distributed silty sand patches with a lower permeability than the liquefiable soil specimen. The other two tests were conducted on a uniform soil deposit and

a continuous layered soil deposit for comparison purposes. Laminar containers were used in all the tests to properly simulate the boundary conditions. The main objective of the chapter is to understand the liquefaction mechanism in non-homogenous soil deposits by systematically investigating the effects of non-homogeneity on the amount of excess pore water pressure dissipation, drainage path, and settlement.

2.2 Centrifuge model testing program and conditions

Four dynamic centrifuge model tests were conducted on a 2.45-m-radius Tokyo Tech Mark III centrifuge (Takemura et al., 1999) at a centrifugal acceleration of 40g. The model configurations and the entire test results are presented and discussed in prototype scale units, unless indicated otherwise.

2.2.1 Soil and pore fluid

Toyoura sand and Silica sand No.8 were used in the tests conducted in this study. Table 2.1 presents the index properties of both soils. Shown in Fig. 2.1 is the particle size distribution curves of Toyoura sand and Silica sand No. 8. According to Unified Soil Classification System under ASTM standard, soil with particle size between 75 μm and 0.425 mm is classified as fine sand and particle size less than 75 μm is classified as silt (ASTM, 2013). Thus, Toyoura sand, falling under the first category, is referred to as fine sand, was deposited at a relative density D_{R1}≈50%. Silica sand No. 8 consists of 30% silt and 70% sand, hence referred to as silty sand, was deposited at a relative density D_{R2}≈55%. Silica sand No. 8, being ten times less permeable than Toyoura sand, was employed to create the relatively impermeable layer in layered soil profiles.

The models were saturated with a viscous fluid, i.e., a mixture of water and 2% Metolose (Hydroxypropylmethyl cellulose from Shin-Etsu Chemical Company) by weight of water, to achieve a viscosity of about 40 times the viscosity of water. Previous studies have shown that this type of viscous fluid neither disturbs nor adversely affects the dynamic properties of cohesionless soil (Okamura et al., 2001). The density and surface tension of this viscous fluid is practically identical to that of water. Also, the viscous fluid simulates the actual prototype permeability of soil.

Table 2.1. Index properties of soils.

Property	Toyoura sand	Silica sand No. 8
Specific gravity, G_s	2.65	2.65
D_{50} (mm)	0.19	0.10
D_{10} (mm)	0.14	0.041
Maximum void ratio, e_{max}	0.973	1.333
Minimum void ratio, e_{min}	0.609	0.703
Permeability, k (m/s) at Dr=50%	2×10^{-4}	2×10^{-5}
Sand %	100%	75%
Silt%		25%

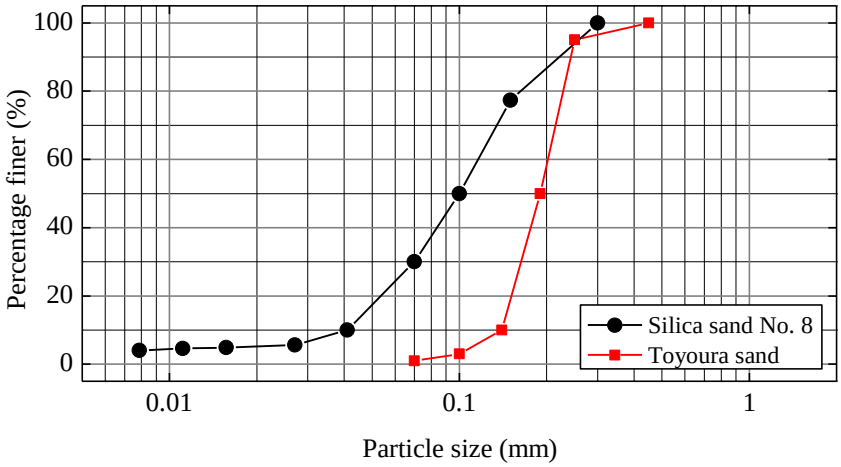

Figure 2.1. Particle size distribution curves of Toyoura sand and Silica sand No. 8.

2.2.2 Test conditions

The four different model geometries (Models 1–4) of soil thickness 9.8 m with the water table 0.8 m below the surface are depicted in Fig. 2.2. The model details are presented in Table 2.2. Model 1 is a homogeneous uniform sand profile, consisting of fine sand only (Fig. 2.2(a)); Model 2 is a non-homogeneous soil deposit with continuous silty sand layers consisting of three layers of fine sand and two continuous sandwiched silty sand layers of thickness H_s = 1.0 m (Fig. 2.2(b)); Model 3 and Model 4 are non-homogeneous soil profiles consisting of fine sand layers with two discontinuous silty sand layers of thickness 1.0 m (Fig. 2.2(c) and (d)). In Model 3, the lower silty sand layer has one 5.0-m-long discontinuous layer of fine sand, i.e., the length is 5.0 m, dividing the silty sand layer into two equal portions of length 7.5 m each, and the upper silty sand layer consists of two discontinuities at the quarter-line of length 2.5 m each (Fig. 2.2(c)). In Model 4, the lower and upper silty sand layers consist of only one 5.0-m-long discontinuity in each layer at the edge near the left and right boundary, respectively (Fig. 2.2(d))..,

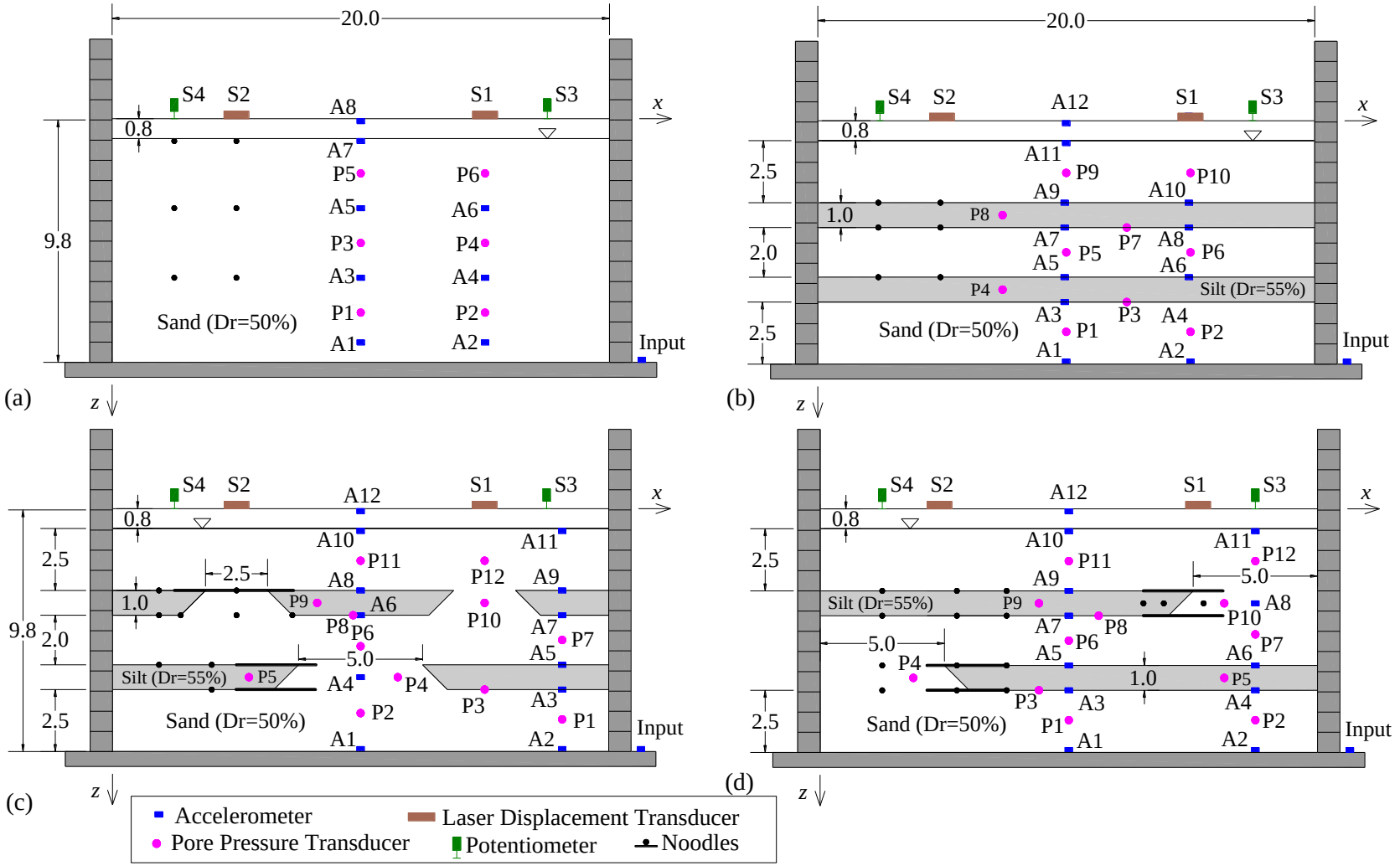

Figure 2.2. Model configurations. All the units are in meters in the prototype scale. (a) Model 1, (b) Model 2, (c) Model 3, and (d) Model 4.

Table 2.2. Model configurations.

Test code	Model series	Model details
Model 1	Uniform sand	D_{r1}=50–55%
Model 2	Continuous silty sand layered model	D_{r1}=50–55% D_{r2}=55–60%, H_s = 1 m No discontinuity
Model 3 and Model 4	Discontinuous silty sand layered models	D_{r1}=50–55% D_{r2}=55–60%, H_s = 1 m Drainage length = 5 m

2.2.3 Model preparation

Models were constructed in a flexible laminar container with dimensions of 500×200×315 mm in length, width, and height, respectively. The top, front, and side views of the laminar box is shown in Fig. 2.3. The box is composed of 15 aluminum alloy, rectangular rings separated by linear roller bearings, arranged to permit relative movement between rings with minimal friction. The outer size of each lamina is 540×240×21 mm in length, width, and height, respectively and the inner size is 500×200×21. Each lamina has a mass of 1.7 kg. The rings allow the container to move with the soil, which minimizes the side effects, creating a flexible boundary and ensuring the uniform distribution of dynamic shear stresses within the soil.

The models were prepared by air pluviation method, where soil was poured from a constant falling height, using a hopper which was manually moved back and forth along the longest dimension of the box. During the preparation of non-homogeneous soil deposits, Toyoura sand was deposited first with the help of two lightweight blocks placed on both sides (Fig. 2.4). The angle of the lightweight blocks were 45^o and the Toyoura sand was filled in a way to form an angle of 45^o. However, due to the cohensionless behavior of Toyoura, it was difficult to obtain the required angle. Nevertheless, the actual angle was less than 45^o. Then, the remaining parts were filled with Silica sand No. 8 by air pluviation method. Natural soil deposits consist of geological uncertainties with thin seams of less permeable layers (silt and clay) tapered at the end, as a result of successive erosion, transportation, and deposition (Atkinson, 2007; Kishida, 1966). Therefore, trapezoidal silty sand patches were chosen to model the non-homogeneous soil profile. The soils were first poured such that total model depth is kept to 225 mm in model scale. Then the de-aired Metolose solution was dripped slowly from the top of the container under a vacuum of 760 mmHg until the solution level reached the ground surface. The saturation process for all the tests required approximately 30 hours. After saturation, the sand was again poured by air pluviation method to make the total height equal to 245 mm in model scale, so that the water

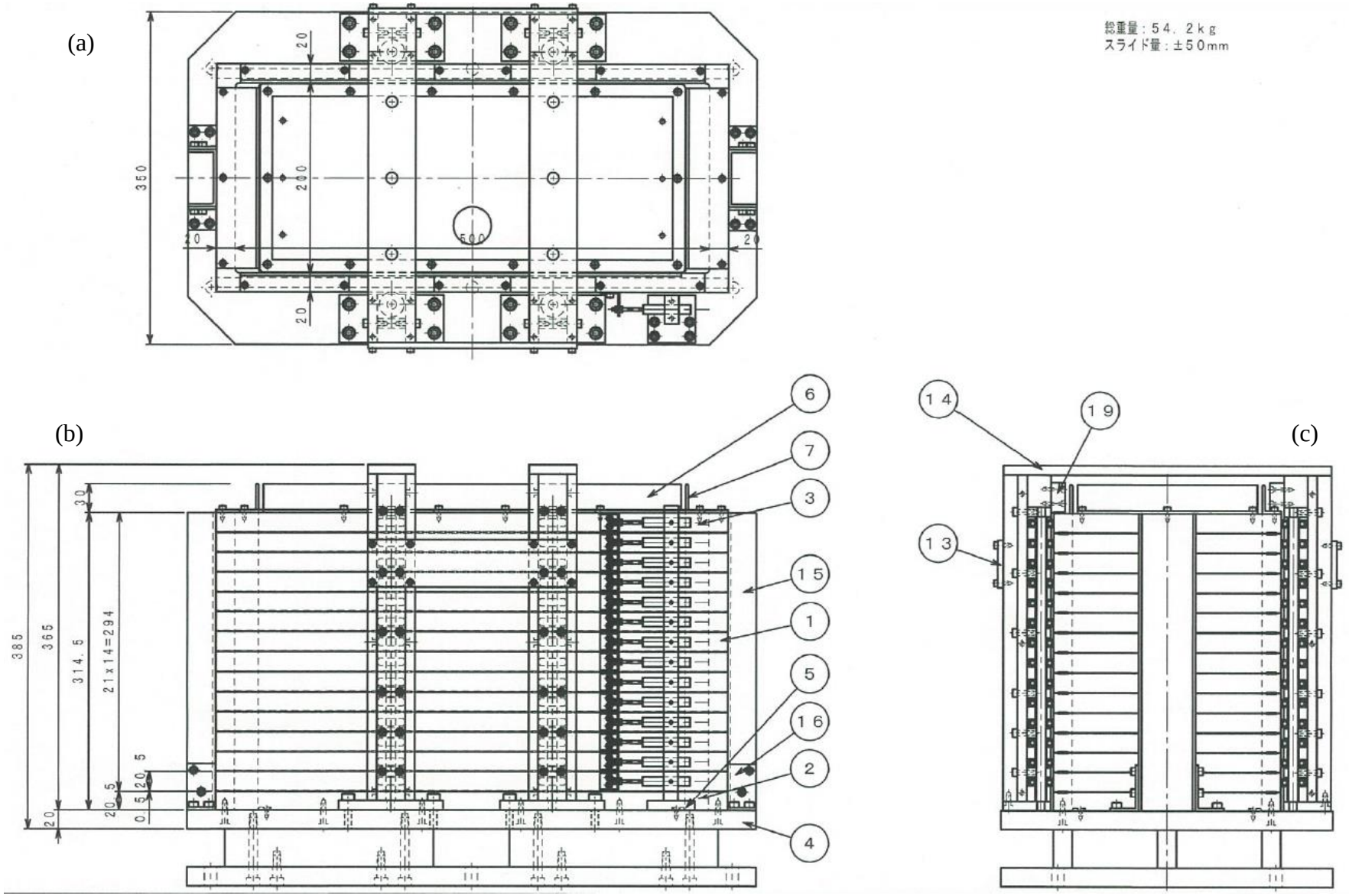

Figure 2.3. Details of laminar container: (a) Top view, (b) Front view, and (c) Side view.

table was 20 mm below the surface in model scale. As soon as dry sand was placed on the saturated ground, it might absorb the Metolose from the saturated ground due to capillary action, partially saturating the dry sand and ground water table might increase to some extent. The model was rotated in a centrifuge as soon as possible. During the rotation at larger centrifugal acceleration the pull of gravity is stronger than the capillary action; thus, maintaining the ground water table as before. The ground water table calculated from the back calculation using the measured pore water pressure at different locations also showed that the original ground water table was maintained. It is noted that the soil layers in all the models were leveled and horizontal. Considering the rotational direction, the ground surface has to be curved in the plane parallel to the y-direction in Fig. 2.2 by 3 mm from the edges of the container. However, since there was no obvious spreading on the ground in the y-direction due to shaking, its effects were neglected.

Accelerometers and pore pressure transducers (PPTs) were installed at the desired locations during model preparation (Table 2.3) to measure the accelerations and pore water generated during dynamic loading, respectively. The accelerometers are the piezoelectric type of Sekonic, 111BW with a dimension of 4x12x4 mm and a mass of 2 g. The PPTs are SSK sensors with a diameter of 6 mm, a height of 12 mm, and a mass of 1.5 g, fitted with a porous element to isolate the fluid pressure. The laser displacement transducers are LB-60 manufactured by Keyence. Colored noodles (soumen) were placed at the interface between fine sand and silty sand to trace the deformation pattern. Laser displacement transducers (LDTs) and potentiometers were placed on the surface (Table 2.3) to measure settlements.

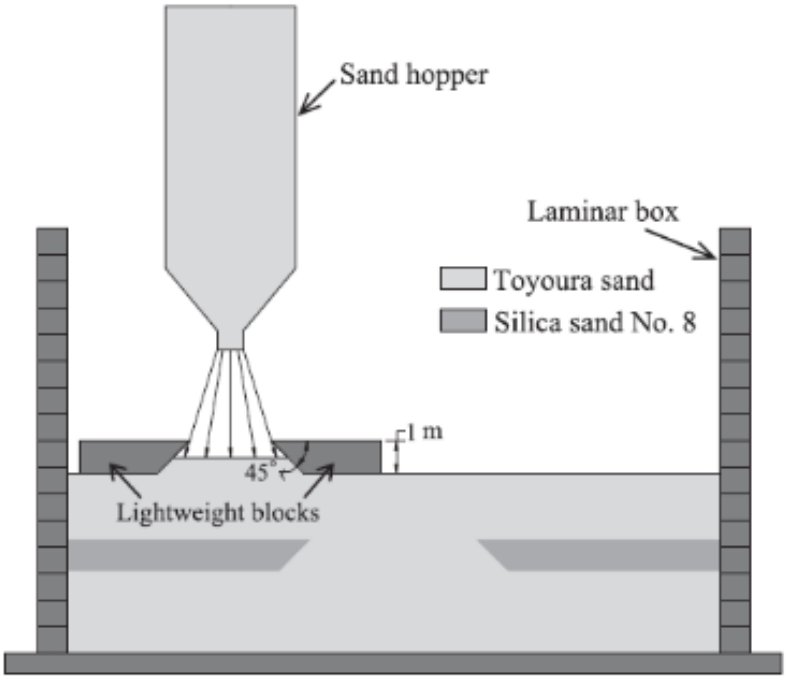

Figure 2.4. Model preparation of non-homogeneous soil deposits.

2.2.4 Testing procedure

For the entire centrifuge model tests, the earthquake ground motion recorded at the Hachinohe Port during the 1968 Tokachi-Oki earthquake (NS component) was applied at the base of the model parallel to the long sides of the container (Fig. 2.5). In Fig. 2.5, the ground motion applied to the shaker is plotted with a dotted line, and the input motions recorded at the base of the laminar container for each test are plotted with solid lines. As shown in the figure, the waveform simulated by the shaker is not identical to that of the Tokachi-Oki earthquake, but similar in the time domain and agrees fairly well in the frequency domain. Repeatability of applied earthquake motion for all cases was satisfactory.

2.3 Test results and discussions

2.3.1 Effect of non-homogeneity on excess pore water pressure responses

The excess pore water pressure, Δu upon reaching a value equal to the initial vertical effective stress (VES), indicates the occurrence of liquefaction, i.e., a state of initial liquefaction. The time histories of excess pore water pressure for all the Models 1-4 during shaking are presented in Figs. 2.6-2.7. Excess pore water pressure generates rapidly at all depths, causing liquefaction during 13-15 s of shaking. Acceleration time histories recorded during the tests are presented in Figs. 2.8-2.9. The acceleration time histories at the bottom strata (A1and A3 in Models 1-4) followed the applied input motion but at shallow depth, the acceleration responses followed the imparted input motion for the first short time and attenuates for the remaining event, indicating the soil had totally liquefied. The acceleration responses after the initial liquefaction at the bottom strata appeared nearly identical in all the models. Hence, no concrete conclusions could be drawn from the acceleration responses. Nonetheless, the observed excess pore water pressure responses appeared completely different for each models and thus, the responses are compared and interpreted for further analyses.

The Δu isochrones at the centerline during and after shaking for Models 1 and 2 are shown in Figs. 2.10 and 2.11, respectively. Similarly, the Δu isochrones PPTs located at the centerline and the quarter-line after shaking for Models 3 and 4 are shown in Figs. 2.12 and 2.13. Also shown in Figs. 2.11–2.13 are the positions of silty sand layers with dashed lines. The Δu generated rapidly, reaching liquefaction in 13–15 s at all the depths in all the tests. In the case of the uniform homogeneous profile, the Δu dissipated rapidly in 400 s, shown by changes in EPWP isochrones for PPTs P1, P3, and P5 aligned at the centerline in Fig. 2.10. In the case of continuous and discontinuous layered soils ,the Δu beneath the upper silty sand layer remain equal to the initial effective stress for a longer time even after the cessation of dynamic motion, indicating the trapping of pore water as shown by PPT P7 for Model 2 and PPT P8 for Models 3 and 4 (Figs. 2.11–2.13). It can be seen that the Δu

Table 2.3. Location of transducers (All the units are in meters in the prototype scale).

Transducer	Model 1		Model 2		Model 3		Model 4	
	x	z	x	z	x	z	x	z
A1	10	9	10	9.8	10	9.8	10	9.8
A2	15	9	15	9.8	18	9.8	17.5	9.8
A3	10	6.4	10	7.3	18	7.3	10	7.3
A4	15	6.4	15	7.3	10	6.8	17.5	7.3
A5	10	3.6	10	6.3	18	6.3	10	6.3
A6	15	3.6	15	6.3	10	4.3	17.5	6.3
A7	-	-	10	4.3	18	4.3	10	4.3
A8	-	-	15	4.3	10	3.3	17.5	3.8
A9	-	-	10	3.3	18	3.3	10	3.3
A10	-	-	15	3.3	10	0.8	10	0.8
A11	-	-	10	0.8	18	0.8	17.5	0.8
A12	-	-	10	0.1	10	0.1	10	0.1
P1	10	7.8	10	8.5	18	8.5	10	8.5
P2	15	7.8	15	8.5	10	8.5	17.5	8.5
P3	10	5	12.5	7.3	15	7.3	10	7.3
P4	15	5	7.5	6.8	11.5	6.8	3.75	6.8
P5	10	2.2	10	5.3	5.5	6.8	16.25	6.8
P6	15	2.2	15	5.3	10	5.3	10	5.3
P7	-	-	12.5	4.3	18	5.3	17.5	5.3
P8	-	-	7.5	3.8	10	4.3	11.2	4.3
P9	-	-	10	2.1	8.25	3.8	8.8	3.8
P10	-	-	15	2.1	15	3.8	16.25	3.8
P11	-	-	-	-	10	2.1	10	2.1
P12	-	-	-	-	15	2.1	17.5	2.1
S1	2.5	0.0	2.5	0.0	2.5	0.0	2.5	0.0
S2	4.8	0.0	4.8	0.0	4.8	0.0	4.8	0.0
S3	15.2	0.0	15.2	0.0	15.2	0.0	15.2	0.0
S4	17.5	0.0	17.5	0.0	17.5	0.0	17.5	0.0

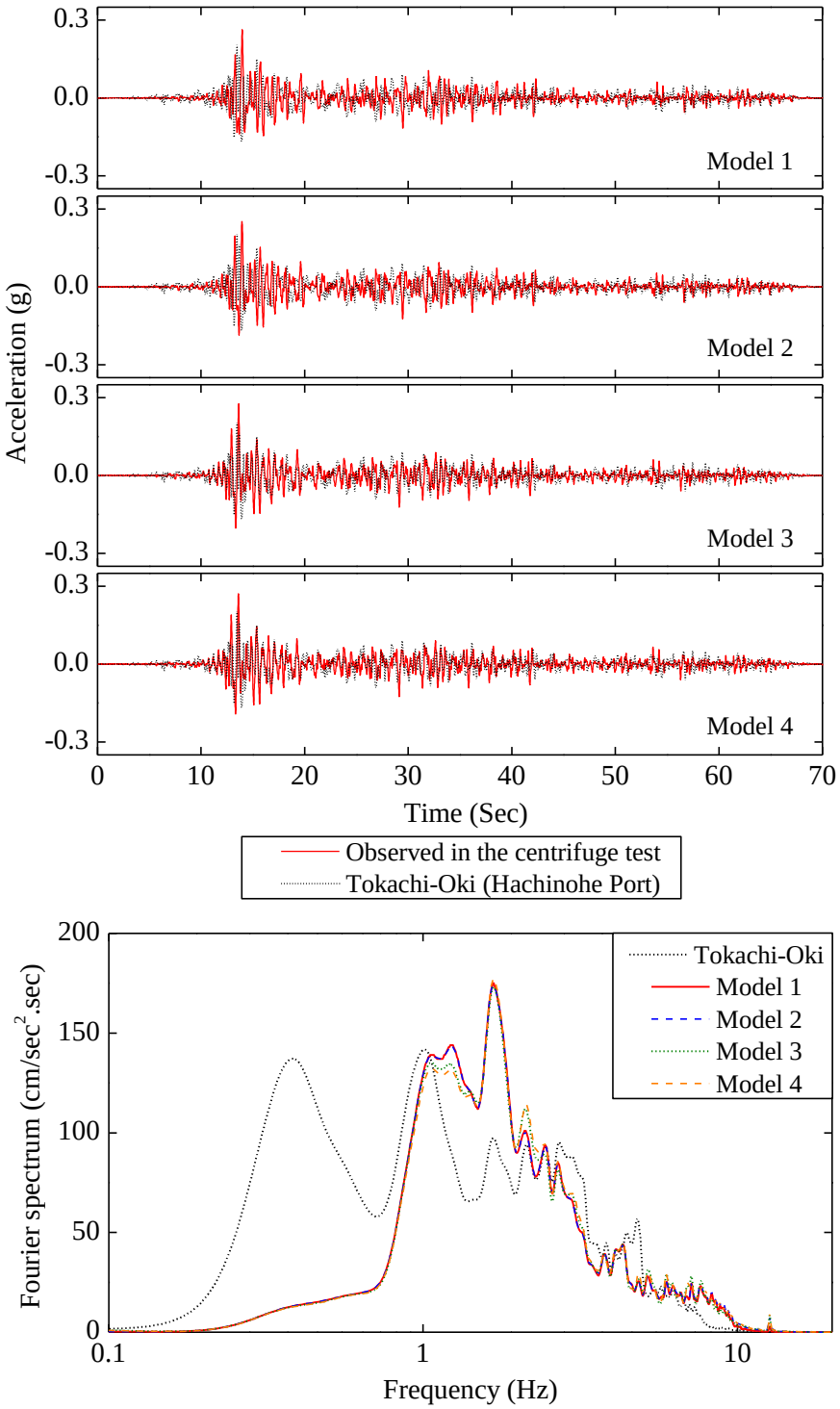

Figure 2.5. Acceleration time histories and Fourier spectra of input waves for Hachinohe Port record of 1968 Tokachi-Oki earthquake (NS component).

measured below the upper silty sand layer have nearly the same rate of dissipation after a certain time, which is about 400 s for continuous layered and 300 s for discontinuous layered soils (Figs. 2.11–2.13). The faster dissipation in discontinuous layered soils might be due to the presence of Discontinuity in the silty sand layer, allowing the pore pressure in the high pore pressure region to easily find a path to be drained out and transmitted to the low pore pressure region.

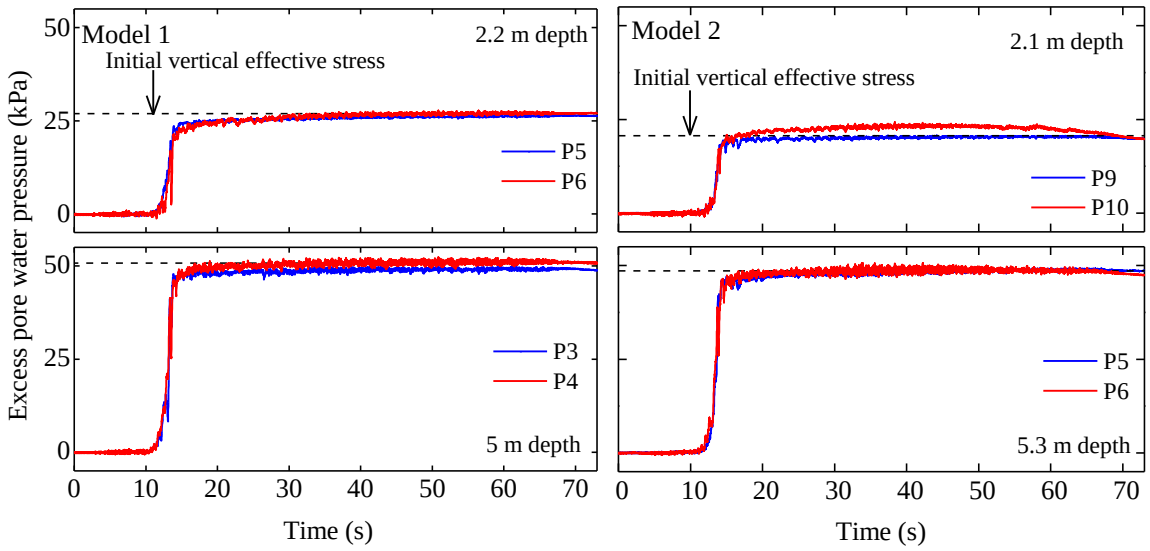

Figure 2.6. Time histories of excess pore water pressure at several depths during shaking in Model 1 and Model 2.

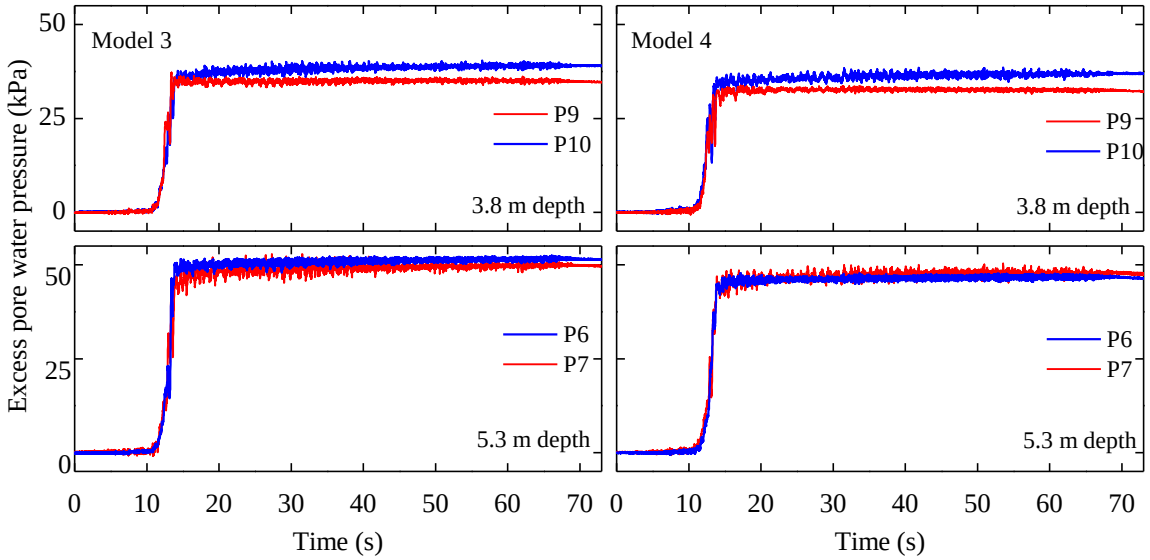

Figure 2.7. Time histories of excess pore water pressure at several depths during shaking in Model 3 and Model 4.

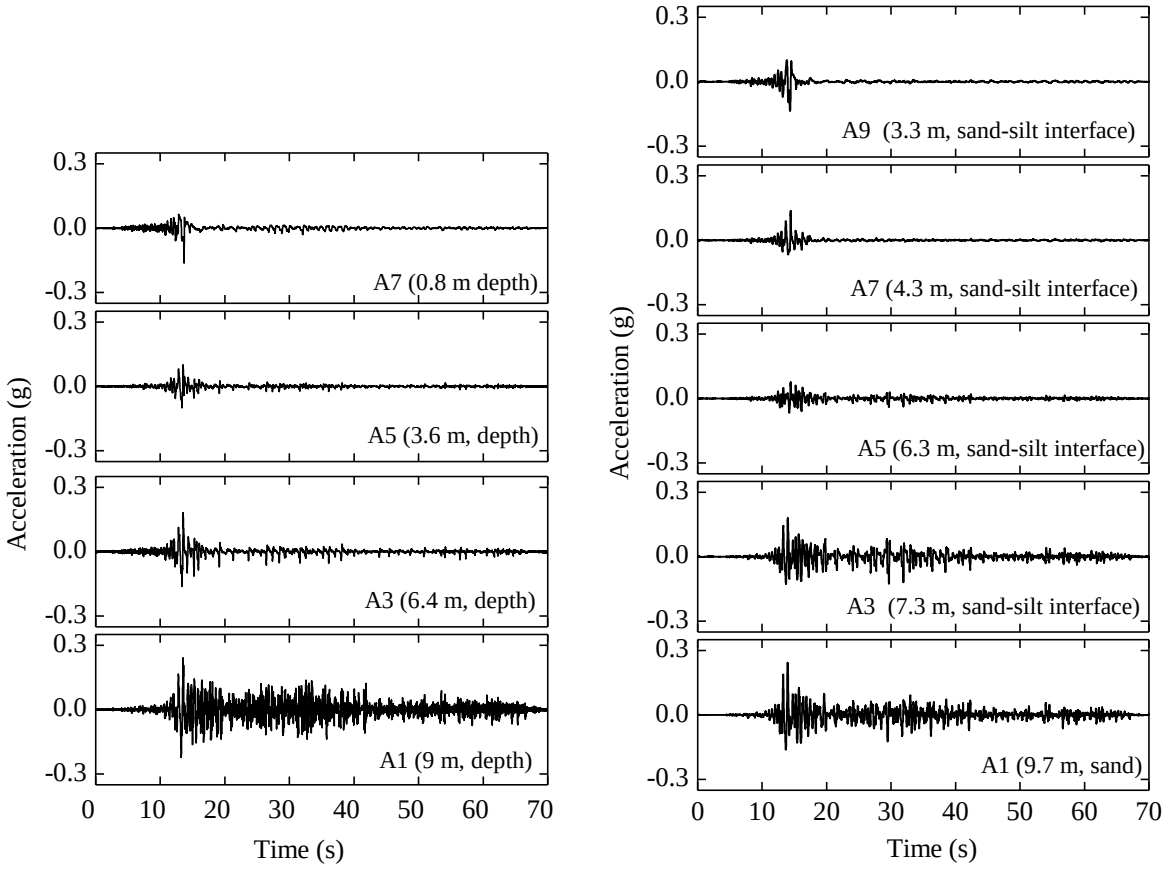

Figure 2.8. Time histories of acceleration at several locations in Model 1 and Model 2.

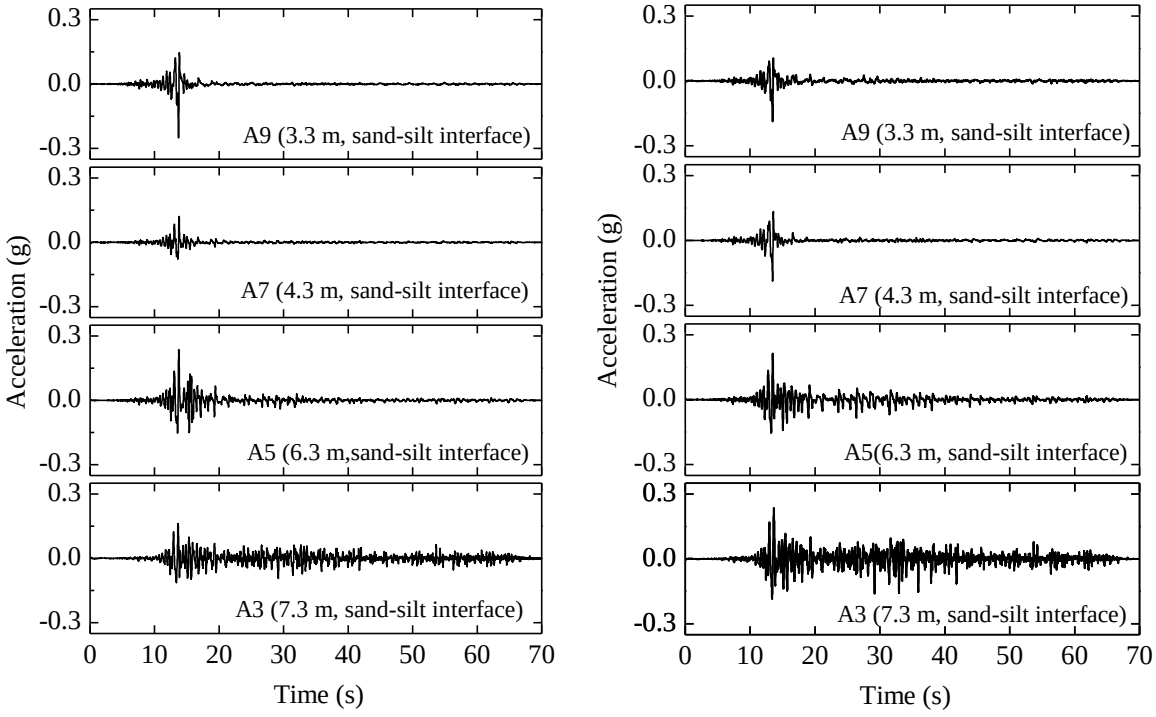

Figure 2.9. Time histories of acceleration at several locations in Model 3 and Model 4.

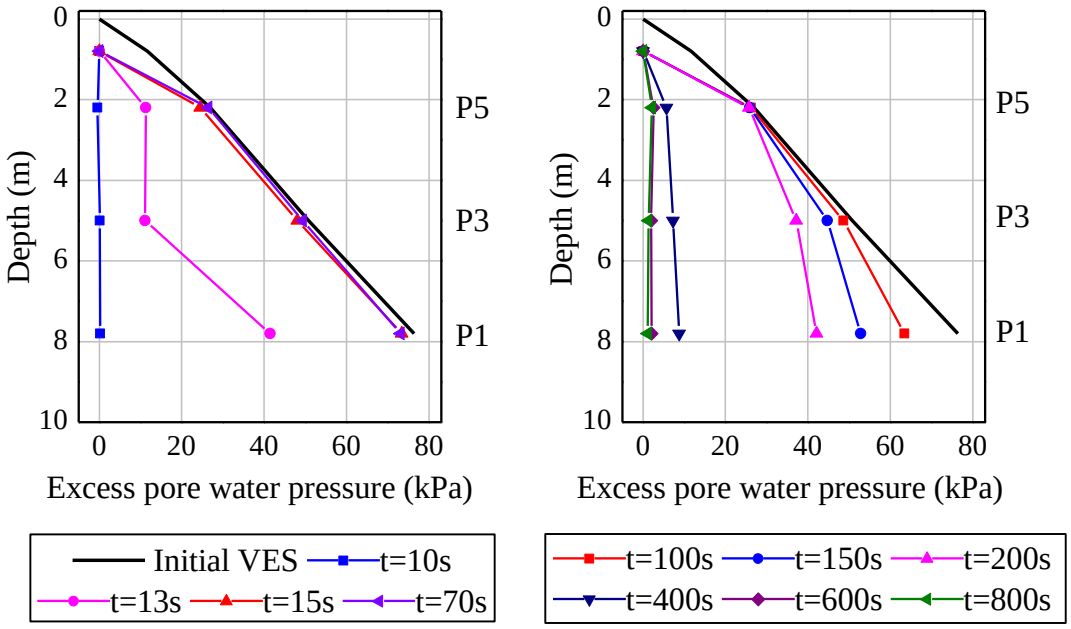

(a) During shaking (b) After shaking

Figure 2.10. Excess pore water pressure isochrones measured on centerline in Model 1.

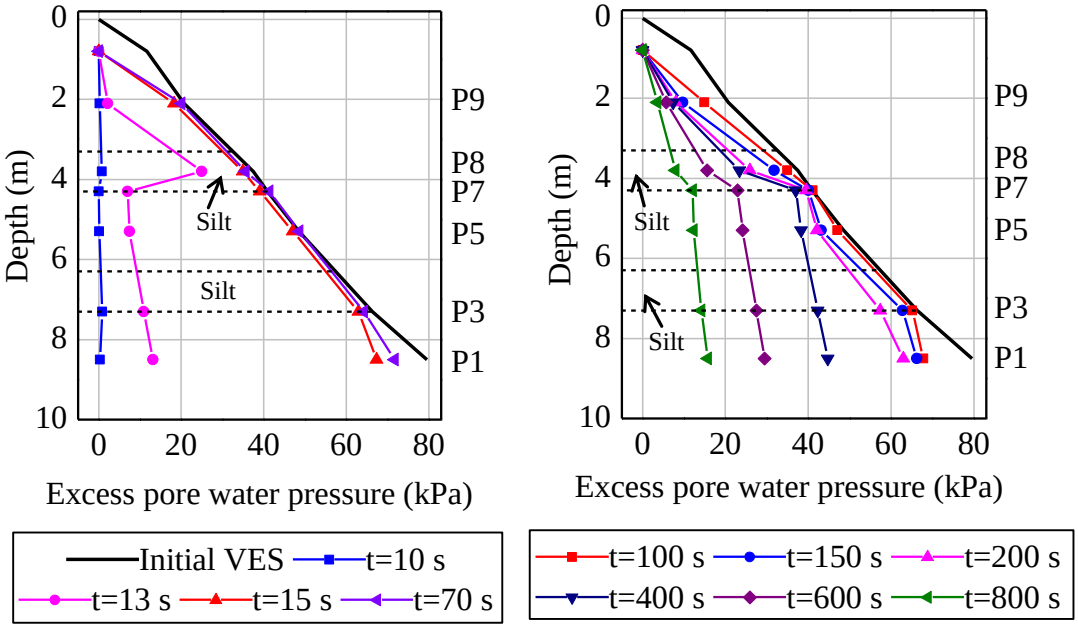

(a) During shaking (b) After shaking

Figure 2.11. Excess pore water pressure isochrones measured on centerline in Model 2. Dotted lines distinguish the sand and silt layers in the model.

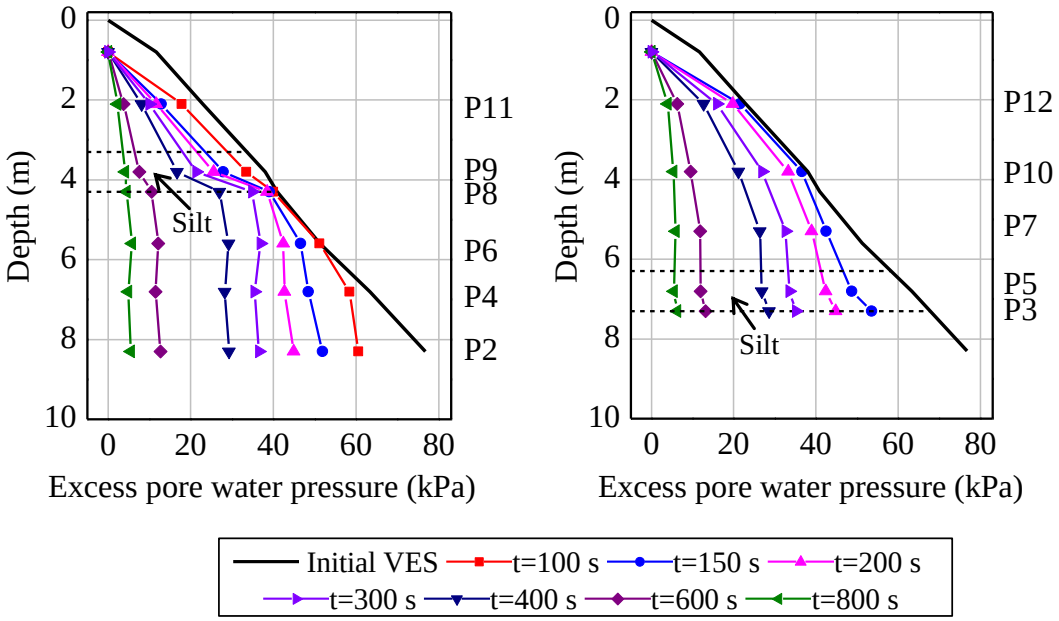

(a) Centerline (b) Quarter line

Figure 2.12. Excess pore water pressure isochrones measured in Model 3 after shaking.

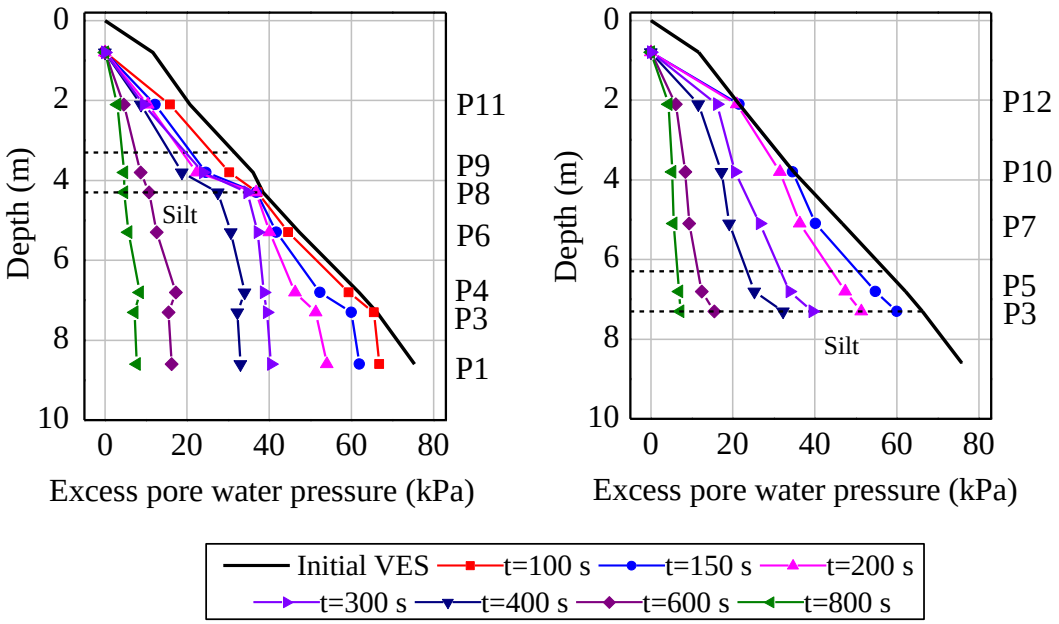

(a) Centerline (b) Quarter line

Figure 2.13. Excess pore water pressure isochrones measured in Model 4 after shaking.

When the pore water pressures build up during shaking, dissipation starts mainly towards the ground surface through the shortest possible path (Ishihara and Yoshimine, 1992). The silty sand layer, being relatively impermeable, hinders the upward movement of pore water. Thus the possible shortest drainage path is the path through P4, P6, P10, and P12 for Models 3 and 4 (see Figs. 2.2(c) and 2.2(d)) and finally towards the ground surface. A comparison be1 tween EPWP for PPTs lying along the drainage path (i.e., P6, P10, and P12) and those lying away from the drainage path (i.e., P7, P9, and P11) for Models 3 and 4 is shown in Fig. 2.14. The Δu is larger for PPTs lying along the drainage path than that for PPTs away from the drainage path, especially at shallow depths (for example at 2.1 m in Fig. 2.14). The difference in Δu around the discontinuous region and below the upper silty sand layer creates a hydraulic gradient pointing towards the discontinuous region, which led to the migration of pore water towards the discontinuity region. This concentrates the dissipation of Δu only through the discontinuity region, increasing the rate and total time of dissipation. As a result, for Models 3 and 4, the EPWP responses at P12, which lies above the discontinuity at 2.1 m depth, are larger than that at P11 above the silty sand layer at the same depth (Figs. 2.12–2.14). However the Δu during and after shaking at the same depth (P5 and P6 in Model 1 and P9 and P10 in Model 2) appears almost identical in contrast to

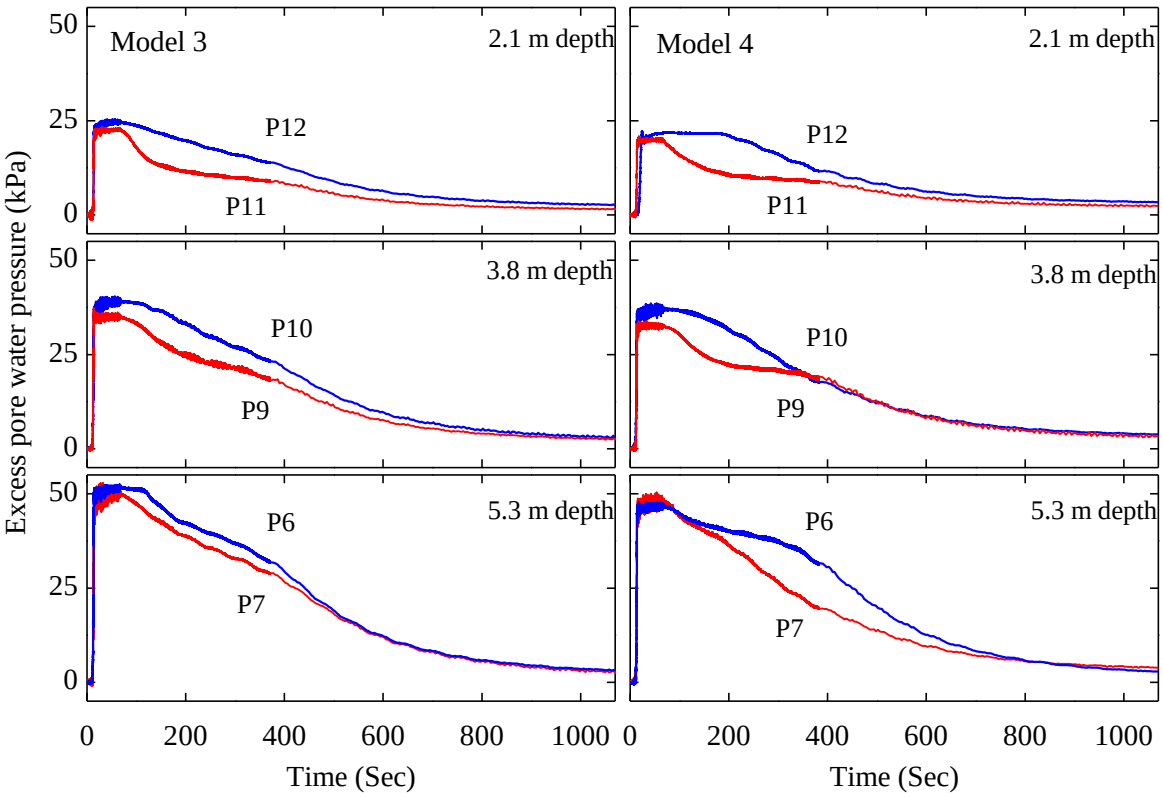

Figure 2.14. Time histories of excess pore water pressure measured at several depths in Model 3 and Model 4.

that observed at the same depth in non-homogeneous soil profile (i.e., Models 3 and 4), as shown by the time histories of excess pore water pressure at several depths in Model 1 and 2 in Fig. 2.15. The pore water tends to dissipate vertically rather than concentrating at certain definite locations in uniform and continuous soil profile.

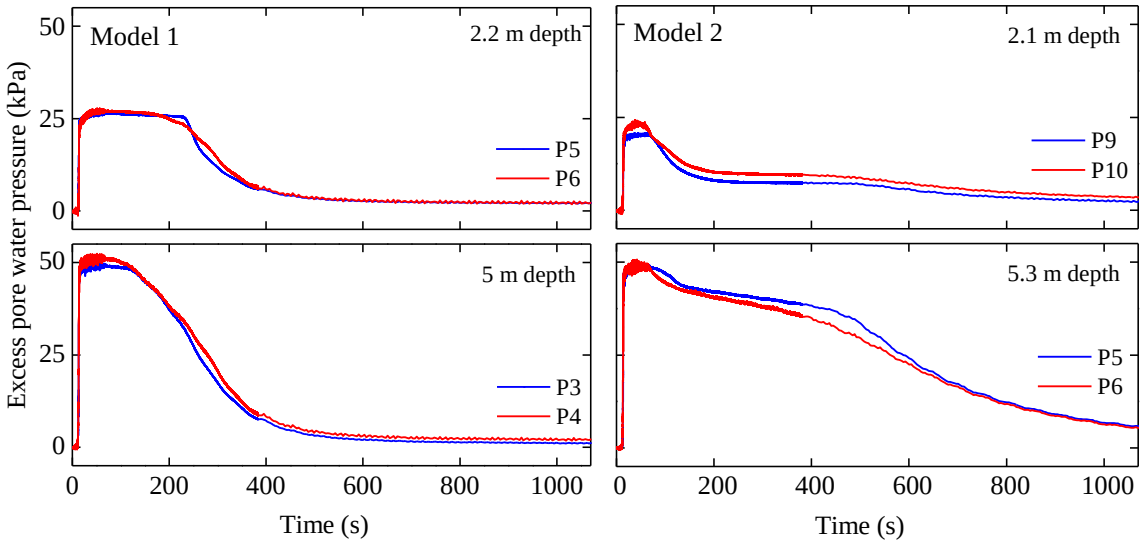

Figure 2.15. Time histories of excess pore water pressure measured at several depths in Model 1 and Model 2.

The effect of non-homogeneity is illustrated in Fig. 2.16 by comparing the time histories of EPWP ratios (r_u) for non-homogeneous soil models containing continuous silty sand layers (Model 2) and discontinuous silty sand layers (Models 3 and 4). The excess pore water pressure ratio (r_u) is the ratio of Δu to the initial vertical effective stress. The pore water remains for a longer period of time beneath and in the silty sand layers in the non-homogeneous soil model containing continuous silty sand layers (P5 and P7 Model 2), compared to that in discontinuous silty sand layers (P6 and P8 for Models 3 and 4). However, the pore water above the discontinuous higher permeability region is larger for models containing discontinuous silty sand layers at shallow depths (P12 for Models 3 and 4). The dissipation of Δu after shaking at P9 and P10 for Model 2, and that at P11 for Models 3 and 4, which are above the upper silty sand layer, are at about the same rate (Fig. 2.15). The relatively less permeable layer, acting as a barrier, retards the escape of pore water, resulting the faster rate of dissipation above the upper silty sand layer. The EPWP ratio reduces to half of the initial value (i.e., r_u = 0.5) by the first 150 s at P9 and P10 (Model 2) and P11 (Models 3 and 4), but r_u = 0.9 at 150 s at P12 for Model 3 and r_u = 1 at 150 s at P12 for Model 4.

The effect of distribution of the silica sand pockets was studied for Models 3 and 4. The EPWP response is almost the same for both tests except the response at shallow depth, P12. Nonetheless, as seen in Fig. 2.16, the value of r_u at P12 for Model 4 is nearly equal to

1 until 200 s, while the value is about 0.8 for Model 3. Moreover, the r_u is extensively larger until 400 s for Model 4 than that for Model 3. This is due to the effect of length and number of discontinuities in the silty sand layer. Model 4 consists of only one discontinuity in the silty sand layer at the right part of length 5 m in the upper silty sand layer, while Model 3 consists of two discontinuities in the upper silty sand layer of length 2.5 m each. It is evident that the presence of several discontinuities can accelerate the rate of dissipation. The excess pore water can be easily transmitted from the liquefied sand beneath the silty sand layer (high pore pressure region) to the upper sand layer through the highly permeable discontinuities in the silty sand layer (i.e., both drainage layers) due to seepage flow or migration of pore water.

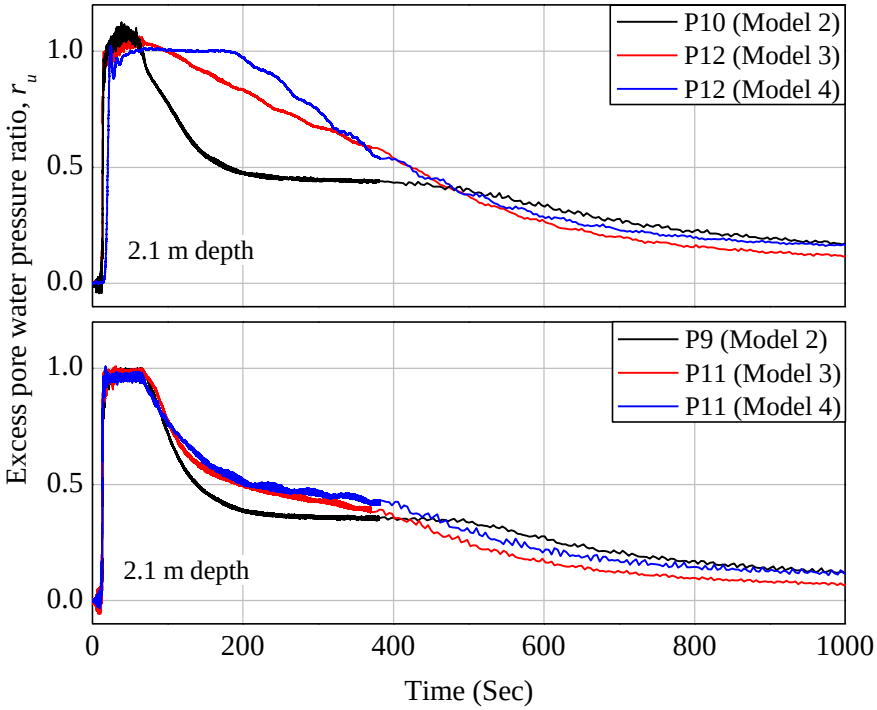

Figure 2.16. Time histories of excess pore water pressure ratio (r_u) for Models 2, 3, and 4.

2.3.2 Effect of non-homogeneity on settlement responses

Settlement time histories at the surface measured by laser displacement transducers (LDTs) and potentiometers for all the tests are presented in Fig. 2.17. An acrylic base plate was used as a target for LDTs so that they would not sink into the liquefied sand. Similarly, plexiglass was used to support the potentiometers. The potentiometers for Models 1 and 4 malfunctioned; therefore, the records are not presented. Potentiometer S3 indicates a very large noise in settlement time histories (Fig. 2.17). Displacement at S3 was measured by a contact-type linear position transducer. When the ground settlement is measured using this type of sensor, one end of a rod contacts the ground surface through a plate and the other end of the rod is connected to a sliding contact that forms an adjustable voltage divider

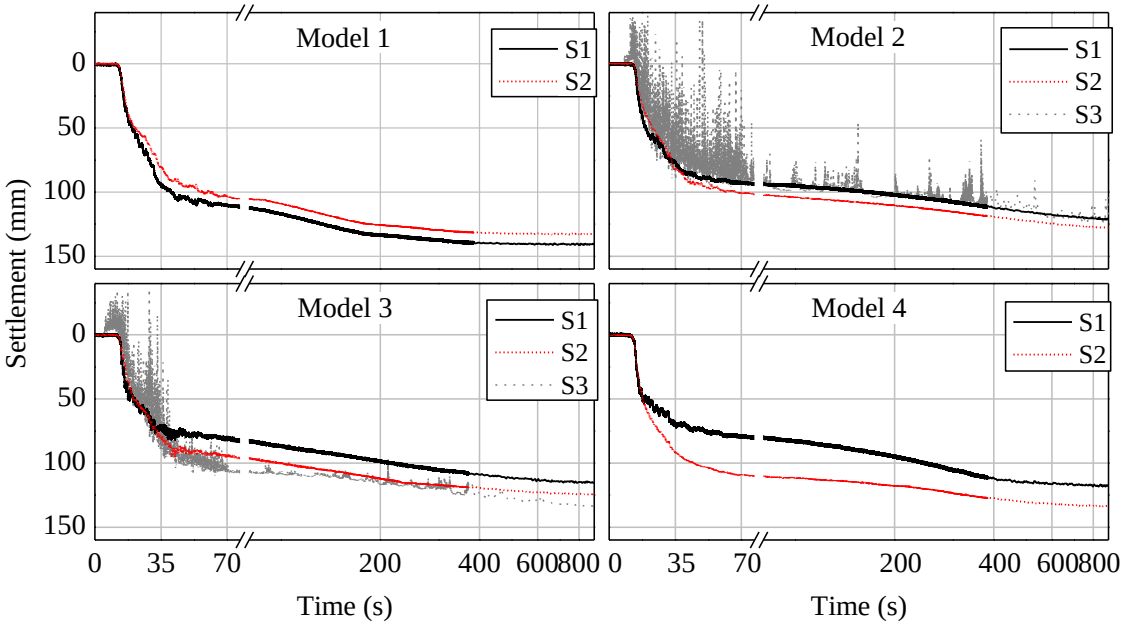

Figure 2.17. Settlement time histories for all the model tests.

in a housing. Since the rod bounces due to the dynamic interaction between the rod and ground surface during shaking, a relatively large noise, i.e., jumps in the record, is observed. However, as seen in Fig. 2.17, the lower envelope of the record coincides with those obtained using the LDT, i.e., noncontact transducer, in Model 2 in which the uniform settlement is expected. This fact indicates that the lower envelop of the record obtained using the contact-type linear position transducer gives useful information even though it comes with the upward spiky noise.

A significant part of the settlement takes place in all the tests during the initial process of pore pressure build-up, at the time when seismic shaking is applied (up to 70 s). Nonetheless, a part of the settlement during seismic shaking might also be due to compression of dry sand and penetration of target base plates, which was observed during the tests. It is noted that soil settlement is incorporated by the increment in the amount of pore pressure generation and drainage. The dissipation of Δu becomes the dominant mechanism after seismic loading as the pore pressure generation ceases the supply of a new mass of water, which is manifested as settlement. Therefore, the settlement induced during dissipation of Δu after shaking is of great importance for assessing the uneven settlement induced by non-homogeneity of soil deposits and so is further compared in terms of rate of settlement. The variation in rate of settlement for all the models for different time windows is presented in Figs. 2.18 and 2.19. In the case of uniform sand and continuous silty sand interlayered soil profiles, the rate of settlement is nearly the same at different locations for different time windows, revealing that the settlement is uniform (see for example S1 and S2, Figs. 2.18(a) and (b)). In the case of non-homogeneous soil deposits containing discontinuous silty sand layers for Model 3, the rate of settlement is larger at S1 and S2

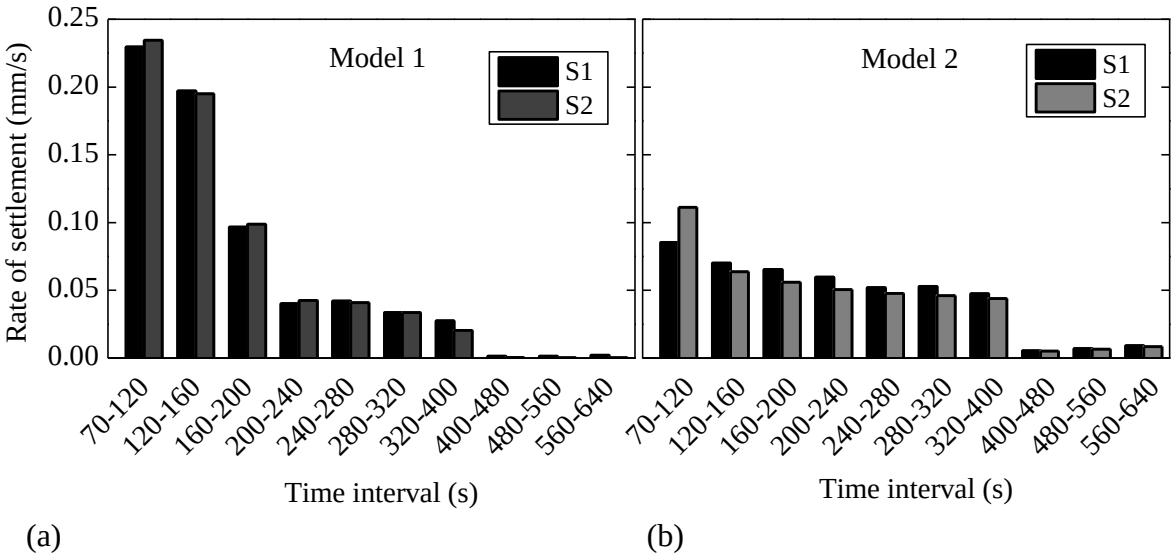

Figure 2.18. Variation in rate of settlement: (a) Model 1 and (b) Model 2.

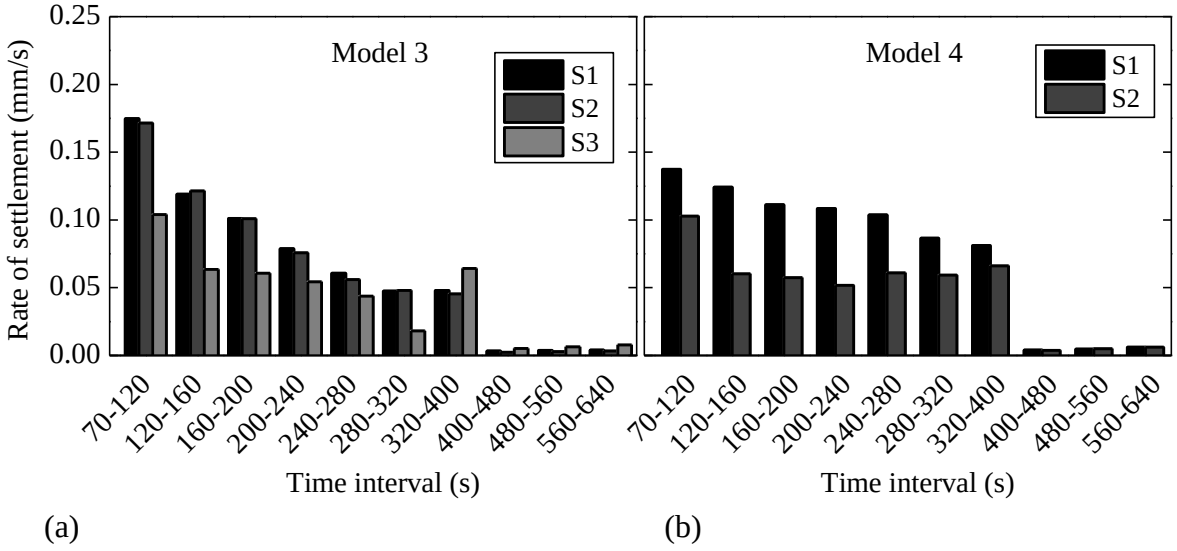

Figure 2.19. Variation in rate of settlement: (a) Model 3 and (b) Model 4.

(which lie above the discontinuity region) than that at S3 (which is above the upper silty sand layer), with few exceptions (Fig. 2.19(a)). Furthermore, in Model 4 the rate of settlement at S1, which is above the discontinuity part, is extensively larger than at S2, which is above the upper silty sand layer for all time windows (Fig. 2.19(b)).

The total settlement induced by seepage flow after the shaking at S1, S2, and S3, lying on the ground surface for all models, is presented in Table 2.4. The settlements at S1, S2, and S3 for Models 1 and 2 indicate uniform settlement. The larger settlements at S1 and S2 for Model 3 and S1 for Model 4 and the smaller settlement at S3 for Model 3 and S2 for

Table 2.4. Settlement induced by seepage.

Test code	S1 (mm)	S2 (mm)	S3 (mm)
Model 1	30.6	30	
Model 2	29	28.3	30.2
Model 3	35	32	27
Model 4	39.5	24.9	

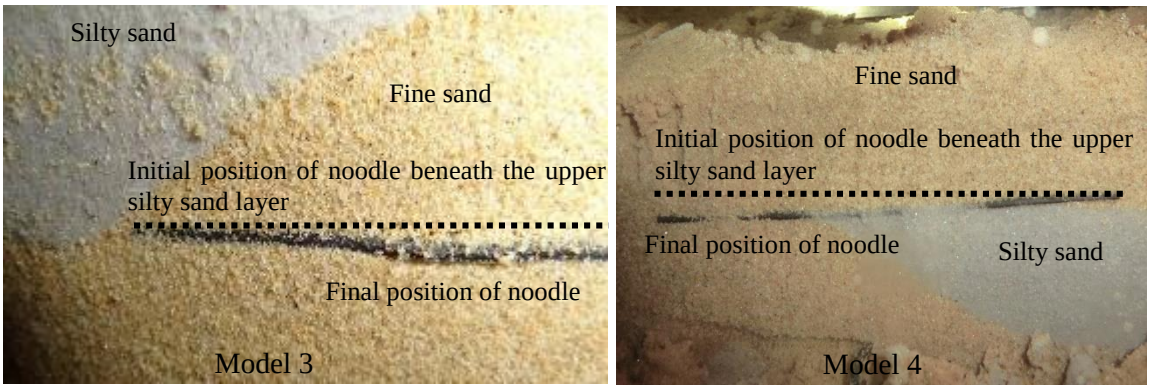

Figure 2.20. Settlement pattern at the interface between fine sand and silty sand layers: (a) Beneath the upper silty sand layer in Model 3 and (b) above the upper silty sand layer in Model 4.

Model 4 indicate uneven settlement. Figures 2.20(a) and (b) indicate the deformation of the noodles imbedded just beneath the upper silty sand layer in Model 3 and just above the upper silty sand layer in Model 4. This was observed during the dissection of the models. Pore water pressure remains larger for a longer period of time in the discontinuous region, causing enough time for the soils to settle. The figures also suggest that more deformation and a larger local settlement occurred in the discontinuous region than in the silty sand layer. These results reveal that the settlement is not uniform in non-homogeneous soil deposits, causing differential settlement of the soil surface.

Figure 2.21 compares the rate of settlement after shaking at S1 for different time windows. It can be seen that the rate of settlement is presumably greater in Model 1 until 160 s and the rate is larger for Models 3 and 4 after 160 s. EPWP dissipates rapidly within a shorter period of time in Model 1 due to the large value of permeability of Toyoura sand. Consequently, more settlement is induced during a short period of time (70–160 s) in Model 1. The continuous dissipation of EPWP in Models 3 and 4 for a longer period of time causes the rate of settlement to be larger for a longer period of time. Moreover, the rate of settlement for Models 3 and 4 is extensively larger for all the time windows than for Model 2. This results show a contrast between dissipation of EPWP and rate of settlement (Figs. 2.16 and 2.21). The rate of settlement for Model 2 after 200 s remains nearly constant as the EPWP ratio at P10 is also nearly constant until 400 s. In Models 3 and 4, the seepage flow or

migration of pore water from the surrounding soil of high pore pressure to discontinuous part for a longer period of time (P12, Fig. 2.16) causes the rate of settlement to be greater at S1 in Models 3 and 4. The rate of settlement for Models 3 and 4 is nearly the same until 200 s, while it is substantially larger after 200 s for Model 4 than for Model 3, indicating the larger rate of dissipation of Δu at P10 in Model 4 (Figs. 2.16 and 2.21). This shows that, in Model 4, the Δu is forced to drain through only one discontinuity layer, increasing the rate and time of dissipation, inducing the larger settlement in the discontinuity region. While in Model 3, the excess pore water is drained out through two discontinuities, reducing the volume of dissipation and inducing the smaller settlement.

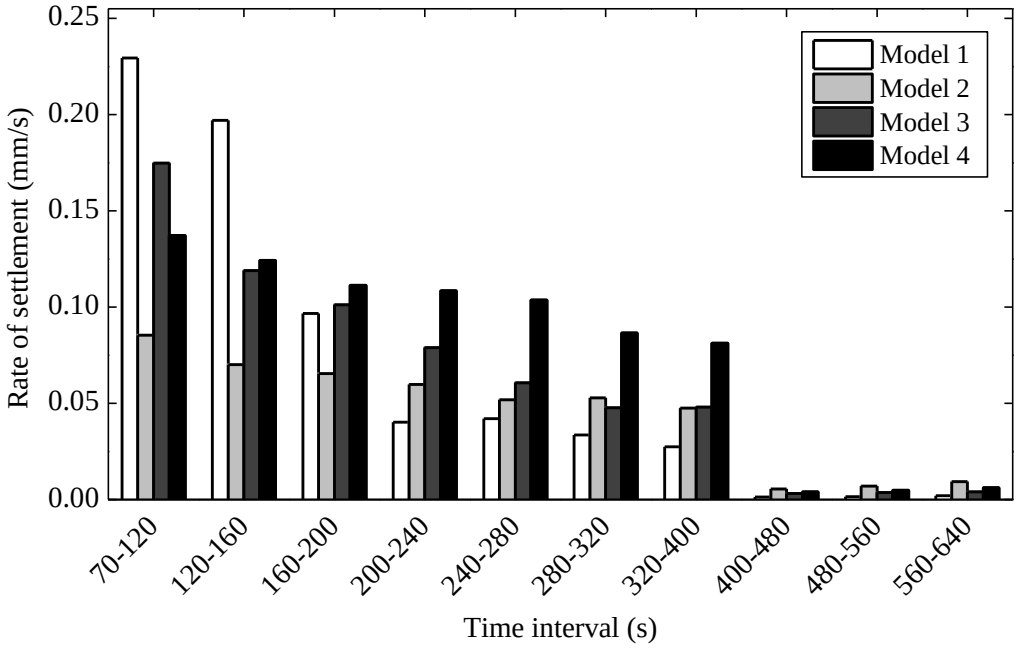

Figure 2.21. Variation in rate of settlement at S1 for all the model tests.

2.4 Summary and conclusions

This study investigated the liquefaction mechanism in non-homogeneous soil deposits by conducting dynamic centrifuge model tests. In particular, two model tests were conducted on non-homogenous soil deposits, where non-homogeneity was incorporated by including periodically distributed discontinuous silty sand patches with lower permeability than the surrounding soil. For comparison purposes, tests were also conducted on a model for continuous layered soil deposit and a model for uniform soil deposit.

This study was focused on modeling of realistic liquefiable soil profile with discontinuous low permeability layers to properly simulate the generation, redistribution, and dissipation of excess pore water pressure during and after shaking. It was found that, in non-homogeneous soil deposits, the pore water was trapped beneath or within less

permeable silty sand patches due to the local migration of pore water and difference in permeabilities of the soils, restricting its upward movement. This indicates that the pore water finds a path to drain from the high pore pressure region to the low pressure region, which reveals that the presence of the discontinuous less permeable layer can have substantial effects on the pore pressure dissipation mechanism and drainage. It is determined that the presence of discontinuity of higher permeability in the less permeable soil layer can act as the drainage layer. This concentrates the dissipation of excess pore water pressure mainly through the discontinuity region, increasing the rate and total time of dissipation after shaking, inducing the larger settlement in the discontinuity region. Excess pore water pressure was accumulated for a longer period of time after shaking in non-homogeneous soil deposits compared with the uniform and continuous layered soil deposits, especially at shallow depths. The settlement induced by seepage at the surface above the discontinuity part was found to be larger than that above the silty sand layer, resulting in non-uniform settlements. The work presented in this study provides new insights into the dissipation of excess pore water pressure and the potential causes of non-uniform settlements in realistic non-homogeneous soil deposits.

Chapter 3

Deformation of earthen embankments on non-homogeneous soil deposits under sequential ground motions

Damage of embankments during earthquakes is widely attributed to the liquefaction of foundation soil. Previous studies have investigated the dynamic response of embankments by mainly considering uniform sand foundation and a single earthquake event. However, the foundation of an embankment consists of many sublayers of soil from liquefiable sand to relatively impermeable layer, and during earthquakes a mainshock may trigger numerous aftershocks within a short time which may have the potential to cause additional damage to soil structures. Therefore, in this chapter, the liquefaction-induced deformation of earthen embankments on various liquefiable foundation conditions under mainshock-aftershock sequential ground motions are investigated. The liquefiable foundation includes uniform sand profile, continuous layered soil profile, and non-homogeneous soil profiles. Furthermore, effects of various foundation conditions on embankment deformations are compared and analyzed.

3.1 Embankments in uniform foundation

Earthquake induced liquefaction has become a major problem to soil embankments such as river dykes, levees, road embankments and earth dams, supported on a cohesionless foundation soil. Previous studies have shown that the widespread damage to such embankments occurred mainly due to the liquefaction of foundation soil, resulting in cracking, settlement, slumping and lateral spreading (Seed, 1968; Koga and Matsuo, 1990; Matsuo, 1996; Adalier et al., 1998; Tani, 1991).

Several experimental studies and numerical analyses have been conducted previously to examine the behavior of embankments resting on uniform clean cohesionless soil during earthquakes (Adalier et al., 1998; Koga and Matsuo, 1990; Aydingun and Adalier, 2003; Adalier and Sharp, 2004). Previous studies that proposed various techniques for mitigation of liquefaction-induced damage in uniform ground have also been reported (Adalier et al., 1998; Adalier and Sharp, 2004). It is noted however, that natural sand deposit normally

consists of many sublayers with different soil particles and properties, ranging from soft sand lenses to stiff cohesive clay and coarse sand layers, referred to as non-homogeneous soil deposits (Fig. 3.1). Malvick and coworkers (Malvick et al.; Kulasingam et al., 2004) conducted centrifuge tests to demonstrate the shear localization due to void redistribution and its consequences on large postshaking deformations in a sand slope with continuous embedded silt layers. In a previous study (Maharjan and Takahashi, 2013b; Maharjan and Takahashi, 2013a) we conducted centrifuge model tests and numerical analyses to investigate the liquefaction mechanism in non-homogeneous soil deposits. Non-homogeneous soil deposits were modeled based on the features of actual soil profile with discontinuous low permeability layers in multi-layered sand deposits. Non-homogeneity in foundation was incorporated by including periodically distributed silty sand patches of a lower permeability than the liquefiable sand. It was found that excess pore water pressure remains for a longer period of time at discontinuous regions in non-homogeneous soil deposits compared with the continuous layered and uniform soil deposits, manifesting a larger settlement at that corresponding region causing non-uniform settlements. Nonetheless, most of the embankments rest on non-homogeneous liquefiable soil profiles, which consist of thin layers of discontinuous low permeability layers like silty sand or clay. Oka et al. (2012) performed numerical modeling of river embankments on a foundation with various soil profiles and ground water tables, including a clayey soil layer. However, most previous studies have only investigated the dynamic behavior of embankments resting on uniform sand. Thus, the dynamic behavior of earthen embankments on a liquefiable non-homogeneous foundation, consisting of discontinuous low permeability layers of silt or clay at different depths is not well understood. Despite the extensive research and development of remedial measures to prevent the large deformation of soil structures, embankments have suffered severe damage during past earthquakes. During 2011 Great East Japan Earthquake, Japan's Ministry of Land, Infrastructure, Transport, and Tourism (MLIT) documented that more than two thousand locations of levee suffered some level of damage (GEER, 2011; Oka et al., 2012). The minor to major damage was attributed due to the liquefaction of foundation soil. This event elucidates the further need to understand the deformation behavior of embankment resting on non-homogeneous liquefiable foundations.

Repeated ground-motion sequences occurring after short intervals of time, resulting from mainshock-aftershock earthquakes, have been observed during many earthquakes (Zhang et al., 2013). Previous studies have pointed out that the low-amplitude aftershock can accumulate large lateral deformation and continue for several minutes on the liquefied soil (Okamura et al., 2001; Meneses-Loja et al., 1998; Ishihara and Cubrinovski, 1998). Ye et al. (2007) conducted shaking table tests and numerical analyses on saturated sandy soil to investigate the mechanical behavior of liquefiable foundations during repeated shaking and consolidation. Xia et al. (2010) presented numerical analysis of an earth embankment on liquefiable foundation soils under repeated shake-consolidation process. However, in most of the previous experimental and numerical studies seismic performance of soil structures is investigated by applying only a single earthquake, ignoring the influence of

repeated earthquake phenomena. During 2011 Great East Japan Earthquake, the liquefaction-vulnerable structures continued to shake after the onset of soil liquefaction for more than two minutes. Moreover, during the reconnaissance survey after 2011 Great East Japan Earthquake, Sasaki and his team (Sasaki et al., 2012) found that the more severe deformation and subsidence of levees was due to the occurrence of aftershock, 30 minutes after the mainshock. Moreover, no previous study has examined the effects of repeated earthquakes on embankments lying on non-homogeneous soil deposits. Therefore, to understand the deformation mechanism of embankments lying on non-homogeneous soil deposits under mainshock and sequential ground motion is of great importance.

This chapter presents the results of dynamic centrifuge tests conducted on different foundation conditions: one involving a uniform foundation; one involving a continuous silty sand layer foundation; and three involving non-homogeneous discontinuous silty sand layer foundations. The work presented herein compares the liquefaction-induced deformation of embankments resting on different foundations under mainshock and sequential ground motion.

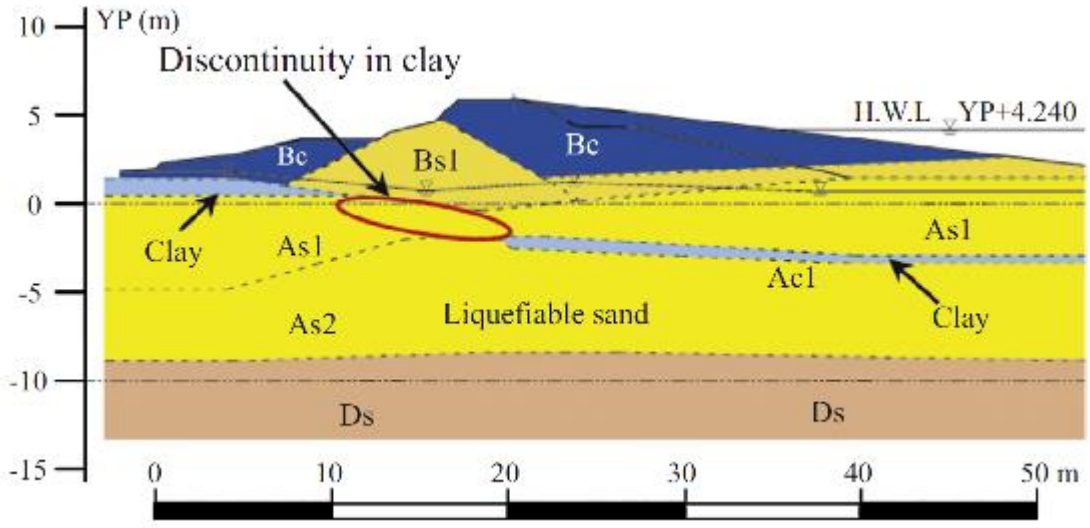

Figure 3.1. Non-homogeneous soil profile along levee in Tone River (Left levee at 32.3 km) (courtesy of Kanto Regional Development Bureau of Ministry of Land, Infrastructure, Transport, and Tourism).

3.2 Centrifuge testing program

Five dynamic centrifuge tests were conducted on three different liquefiable foundations utilizing the Tokyo Tech Mark III centrifuge of radius 2.45 m, at a centrifugal acceleration of 40g. The model configurations and the entire test results are presented and discussed in prototype scale units, unless indicated otherwise. All tests simulated a prototype soil deposit of 8.4 m depth and embankment of 1.2 m height. Toyoura sand and Silica sand No. 8 was used in the tests to model the foundation (Table 3.1). It is noted that Toyoura sand, also referred to as fine sand, was deposited at a relative density Dr ≈ 50%. Silica sand No. 8, also referred to as silty sand, was deposited at a relative density Dr ≈ 55%, and used to create the relatively impermeable layer in layered soil profiles. DL clay, which consists of 90% silt and 10% clay, was mixed with 22% silicon oil by weight to build the embankments, with 1:2 slopes having a unit weight of 16 kN/m3. The model configurations are shown in Table 3.2 and Fig. 3.2: Model NHG1 and Model NHG2 simulate non-homogeneous foundations consisting of fine sand layers with two discontinuous silty sand layers of thickness 1.0 m (Fig. 3.2(a) and (b)); Model UG simulates homogeneous uniform sand foundation consisting of only Toyoura sand (Fig. 3.2(c)); Model CG simulates non-homogeneous soil deposit with continuous silty sand layers (Fig. 3.2(d)). An additional test, Model NHG1-MS was also conducted, which consists of the same non-homogeneous foundation as Model NHG1, but only having a mainshock applied.

A flexible laminar container with inner dimensions of 500×200×450 mm in length, width, and height, respectively was used to build the models. The box is composed of 20 aluminum alloy rectangular rings which allow the container to move with the soil, creating a flexible boundary and ensuring the uniform distribution of dynamic shear stresses within the soil. The foundation was prepared by air pluviation to a depth of 210 mm in model scale. The sand was poured from a hopper which was manually moved back and forth along the longest dimension of the box, while the falling height was kept constant to obtain the desired relative density. During the preparation of non-homogeneous soil deposits, Toyoura sand

Table 3.1. Index properties of soils.

Property	Toyoura sand	Silica sand No. 8
Specific gravity, G_s	2.65	2.65
D_{50} (mm)	0.19	0.10
D_{10} (mm)	0.14	0.041
Maximum void ratio, e_{max}	0.973	1.333
Minimum void ratio, e_{min}	0.609	0.703
Permeability, k (m/s) at Dr=50%	2×10^{-4}	2×10^{-5}
Sand %	100%	75%
Silt%		25%

Table 3.2. Summary of model configurations.

Test code	Model series	Peak acceleration of input motion (g)	
		Mainshock	Aftershock
Model NHG1	Non-homogeneous foundation with discontinuity below the center of embankment at shallow depth	0.433	0.24
Model NHG2	Non-homogeneous foundation with discontinuity below the toe of embankment at shallow depth	0.37	0.16
Model UG	Uniform sand foundation	0.434	0.27
Model CG	Continuous silty sand layered foundation	0.434	0.28

was deposited first and then, the remaining parts were filled with Silica sand No. 8 (Fig. 3.2(c) and (d)). Trapezoidal silty sand patches were chosen to model the multi-layered soil profile consisting of discontinuous thin layers of low permeability observed in many damaged sites during past earthquakes (Atkinson, 2007; Kishida, 1966). After the foundation was constructed, the embankment was built of a mixture of DL clay and silicon oil with 1:2 slopes. The models were saturated with a viscous fluid, i.e., a mixture of water and 2% Metolose (Hydroxypropylmethyl cellulose from Shin-Etsu Chemical Company) by weight of water, to achieve a viscosity of about 40 times the viscosity of water. The density and surface tension of this solution is practically identical to that of water (Okamura et al., 2001). Also, the viscous fluid simulates the actual prototype permeability of the soil. The de-aired Metolose solution was dripped slowly from the top of the container under a vacuum of 760 mmHg which slowly moves downwards. In this process, the water table rises from the bottom. The saturation was continued until the solution level reached the elevation of 210 mm in model scale, i.e., the water table is at the free field surface. The saturation process for all the tests required approximately 30 hours. It is noted that the soil layers in all the models were leveled and horizontal. Considering the rotational direction, the ground surface has to be curved in the plane parallel to y direction (the direction perpendicular to the embankment section) in Fig. 3.2 and the elevation at the center should be 2.8 mm lower than that at the edges of the container. However, since there was no obvious spreading on the ground in the direction perpendicular to the embankment section due to shaking, its effects were neglected.

Accelerometers and pore pressure transducers (PPTs) were installed during model preparation to measure the accelerations and excess pore water pressure (Δu) generated at three regions representing different stress states: (1) free field; (2) under the toe of the embankment where static shear stress exists; and (3) under the center of embankment where

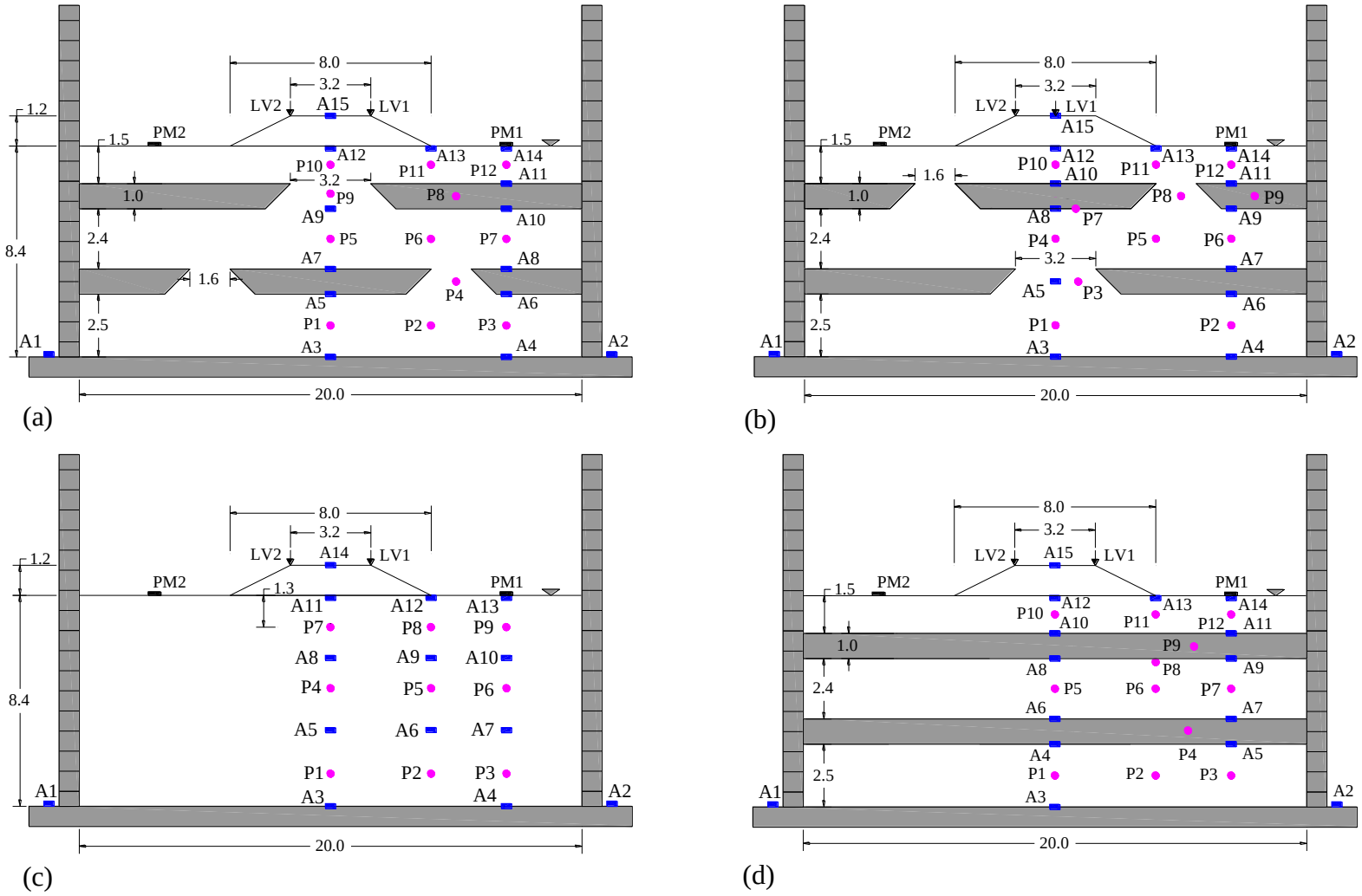

Figure 3.2. Model test configurations: (a) Model NHG1, (b) Model NHG2, (c) Model UG, and (d) Model CG (All the units are in meters in the prototype scale).

large effective stress exists. Colored noodles were placed both vertically and horizontally at several locations to trace the deformation pattern within the foundation layer. The horizontal noodles were placed at the sand-silt interface. The vertical noodles of 1.5 cm were placed at several locations (1.2, 3.6, 6, 7.2, 9.5 m) along the x-axis at several depths as shown in Table 3.3. Also, markers made up of small nails were aligned at the center on the ground surface and several locations on embankment to map the deformations. Finally, laser displacement transducers (LDTs) and potentiometers were placed at the embankment crest and free field surface. The locations of accelerometers, PPTs, LDTs, and potentiometers are indicated in Fig. 3.2. All the models except NHG1-MS were subjected to the same sequential earthquake ground motion, consisting of a mainshock and aftershock, recorded at the Moorpark-Fire station (EW component) during 1994 Northridge earthquake (PEER., 2013), normalized to maximum PGA equal to 0.4 g (for the mainshock). Table 3.2 indicates the peak acceleration of input motion observed in centrifuge test for all the models. A gap of 100 s is applied between two consecutive seismic events. This gap has zero

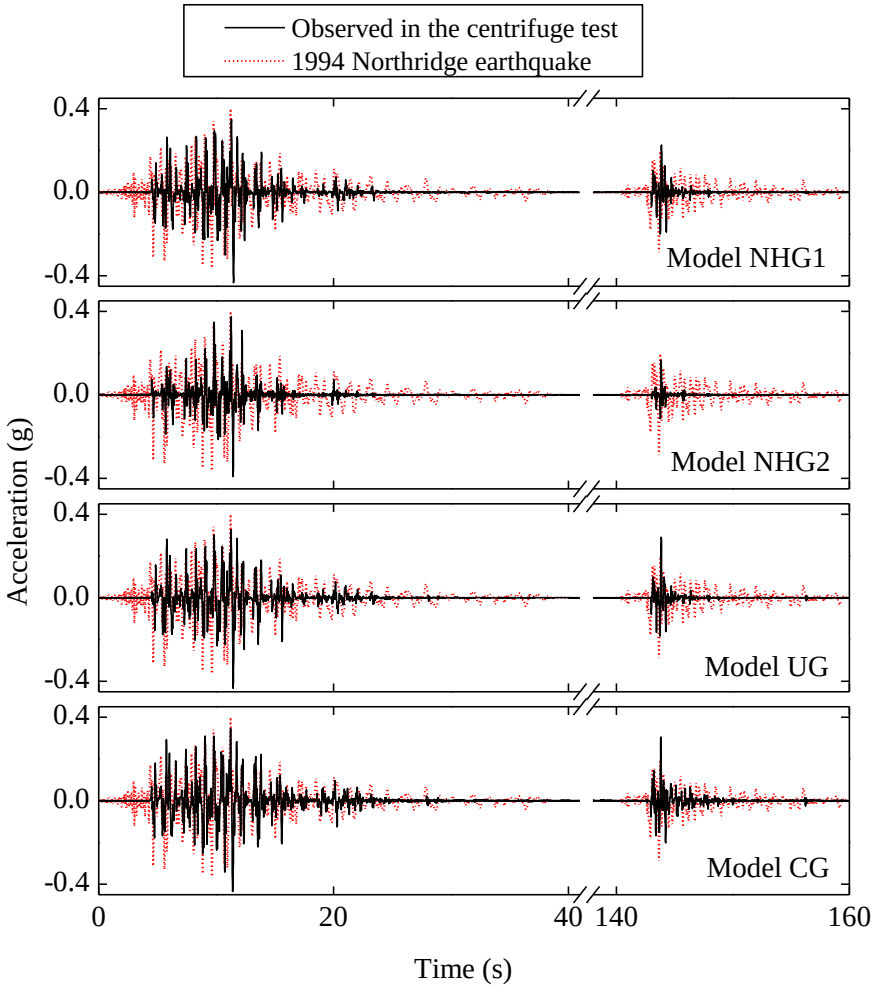

Figure 3.3. Acceleration time histories of input base motion.

acceleration ordinates. In Fig. 3.3, the ground motion applied to the shaker is plotted with a dotted line, and the input motions recorded at the base of the laminar container for each test are plotted with solid lines. Figure 3.4 depicts the Fourier spectra and Arias intensity of the input base motions. The waveform simulated by the shaker is not identical to that of the Northridge earthquake, but similar in the time domain (Fig. 3.3) and agrees fairly well in the frequency domain as shown by Fourier spectra in Fig. 3.4, except for Model NHG2. Also, the Arias intensity of all the input motions appear to be similar. Repeatability of applied earthquake motion for all cases was satisfactory, except for the test NHG2, where the intensity of applied input motion was less than other tests.

After completion of the tests, the final locations of markers aligned on the ground surface and embankments were carefully measured. Dissections of models were also carried out to measure the final locations of the noodles placed at different positions (Table 3.3), accelerometers, and PPTs. The post-test deformed shapes of the model cross section were then obtained by carefully mapping the measured coordinates of noodles, markers, and transducers. Selected response records in prototype units will be presented in following sections.

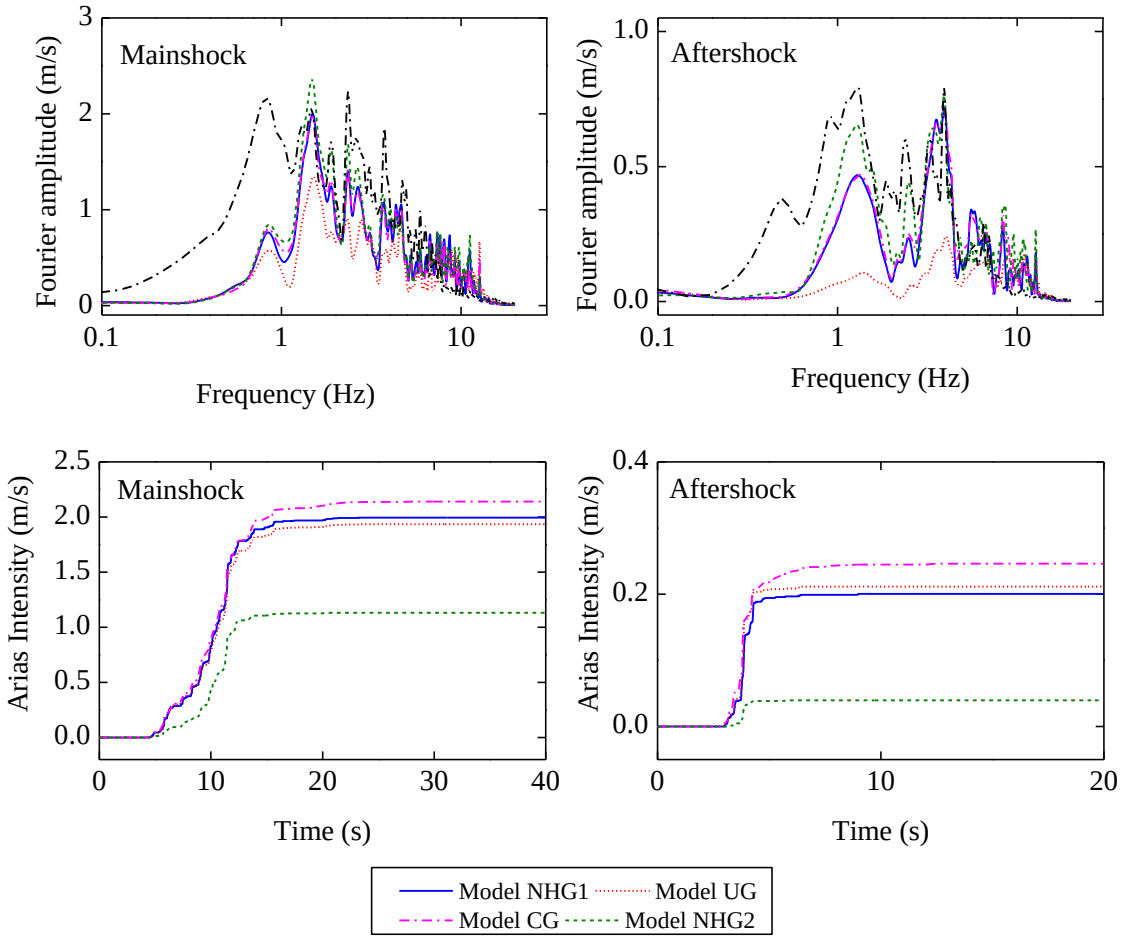

Figure 3.4. Fourier spectra and Arias intensities of input base motion.

Table 3.3. Coordinates of noodles before and after the test (All the units are in meters in prototype scale).

NHG1				UG				CG				NHG2			
Before		After		Before		After		Before		After		Before		After	
x	y	x	y	x	y	x	y	x	y	x	y	x	y	x	y
1.2	-7.15	1.2	-7.16	1.2	-7.15	1.2	-7.16	1.2	-7.15	1.2	-7.16	1.2	-7.15	1.2	-7.16
3.6	-7.15	3.56	-7.16	3.6	-7.15	3.58	-7.16	3.6	-7.15	3.56	-7.16	3.6	-7.15	3.58	-7.16
6	-7.15	5.94	-7.16	6	-7.15	5.96	-7.16	6	-7.15	5.96	-7.16	6	-7.15	5.96	-7.16
7.2	-7.15	7.16	-7.2	7.2	-7.15	7.18	-7.16	7.2	-7.15	7.16	-7.2	7.2	-7.15	7.18	-7.18
9.5	-7.15	9.5	-7.22	9.5	-7.15	9.5	-7.2	9.5	-7.15	9.5	-7.22	9.5	-7.15	9.5	-7.2
1.2	-5.4	1.16	-5.4	1.2	-5.4	1.18	-5.44	1.2	-5.4	1.16	-5.4	1.2	-5.4	1.2	-5.4
3.6	-5.4	3.5	-5.36	3.6	-5.4	3.56	-5.44	3.6	-5.4	3.5	-5.36	3.6	-5.4	3.54	-5.42
6	-5.4	5.88	-5.4	6	-5.4	5.92	-5.36	6	-5.4	5.84	-5.44	6	-5.4	5.9	-5.38
7.2	-5.4	7.08	-5.44	7.2	-5.4	7.14	-5.44	7.2	-5.4	7.08	-5.44	7.2	-5.4	7.12	-5.44
9.5	-5.4	9.46	-5.54	9.5	-5.4	9.48	-5.48	9.5	-5.4	9.46	-5.54	9.5	-5.4	9.5	-5.5
1.2	-3.7	1.14	-3.7	1.2	-3.7	1.16	-3.76	1.2	-3.7	1.14	-3.7	1.2	-3.7	1.18	-3.7
3.6	-3.7	3.5	-3.6	3.6	-3.7	3.54	-3.72	3.6	-3.7	3.5	-3.64	3.6	-3.7	3.54	-3.72
6	-3.7	5.84	-3.7	6	-3.7	5.9	-3.68	6	-3.7	5.84	-3.74	6	-3.7	5.86	-3.66
7.2	-3.7	7.08	-3.78	7.2	-3.7	7.1	-3.78	7.2	-3.7	7.08	-3.78	7.2	-3.7	7.12	-3.76
9.5	-3.7	9.44	-3.92	9.5	-3.7	9.46	-3.84	9.5	-3.7	9.44	-3.92	9.5	-3.7	9.48	-3.86
1.2	-2	1.1	-2	1.2	-2	1.16	-2.08	1.2	-2	1.1	-1.96	1.2	-2	1.18	-2
3.6	-2	3.44	-1.88	3.6	-2	3.52	-2.04	3.6	-2	3.44	-1.92	3.6	-2	3.5	-2.06
6	-2	5.64	-2	6	-2	5.84	-2	6	-2	5.64	-2.08	6	-2	5.84	-2
7.2	-2	6.96	-2.12	7.2	-2	7.06	-2.1	7.2	-2	6.96	-2.12	7.2	-2	7.06	-2.08
9.5	-2	9.4	-2.3	9.5	-2	9.44	-2.2	9.5	-2	9.4	-2.28	9.5	-2	9.42	-2.2
1.2	-0.76	1.1	-0.72	1.2	-0.76	1.14	-0.86	1.2	-0.76	1.1	-0.72	1.2	-0.76	1.14	-0.76
3.6	-0.76	3.42	-0.6	3.6	-0.76	3.5	-0.8	3.6	-0.76	3.42	-0.66	3.6	-0.76	3.5	-0.82
6	-0.76	5.6	-0.76	6	-0.76	5.8	-0.76	6	-0.76	5.6	-0.8	6	-0.76	5.8	-0.76

7.2	-0.76	6.96	-0.96	7.2	-0.76	7.04	-0.88	7.2	-0.76	6.96	-0.92	7.2	-0.76	7.04	-0.88
9.5	-0.76	9.38	-1.12	9.5	-0.76	9.42	-1.04	9.5	-0.76	9.38	-1.08	9.5	-0.76	9.44	-1
1.2	0	1.1	0.04	1.2	0	1.14	-0.1	1.2	0	1.1	0.06	1.2	0	1.14	0
3.6	0	3.4	0.2	3.6	0	3.5	-0.04	3.6	0	3.4	0.1	3.6	0	3.5	-0.1
6	0	5.6	0	6	0	5.8	0	6	0	5.6	-0.1	6	0	5.8	-0.08
7.2	0	6.92	-0.2	7.2	0	7.04	-0.14	7.2	0	6.92	-0.16	7.2	0	7.04	-0.12
9.5	0	9.36	-0.4	9.5	0	9.4	-0.32	9.5	0	9.36	-0.352	9.5	0	9.44	-0.24

3.3 Test results and analyses

3.3.1 Model NHG1

Figure 3.5(a) depicts the mapped post-test deformed shape of Model NHG1. The performance of soil structures such as embankments, levees, and dams is investigated mainly by the movement of structures and the ground supporting it during and after the earthquake. The deformation of embankment in this study is basically investigated and estimated in terms of lateral spreading and crest settlements. The time histories of displacements at LV1 and PM1 and accelerations at A12 and A13 (see Fig. 3.2 for locations of these points) for the model NHG1 are presented in Fig. 3.6. Here a crest settlement of 0.5 m (about 40% of the embankment height) was observed of which about 0.34 m was measured during the mainshock shaking (Figs. 3.5(a) and 3.6). Slumping of embankment sides and the lateral spreading of 0.4 m at the toe portion were observed, where the ground surface was observed to heave upward by as much as 0.2 m (Fig. 3.5(a)). The lateral outflow of underlying foundation soil toward the free field, shear deformation of embankment, and contractive volume change of loose sand under embankment are largely responsible for the larger crest settlement. The lateral deformation may be associated with an average normal tensile strain of about 10% along the embankment base. In addition, tension cracks occurred at the crest and side of the embankment in the direction perpendicular to the embankment section, which might be due to the extension of the embankment as the lateral spreading of underlying foundation soil occurred. Major cracks of width 0.3 m were observed at the crest and cracks of width 0.1 m at the embankment sides (Fig. 3.5(a)).

A significant amount of crest settlement took place during mainshock shaking, presumably larger during 8-20 s with a heave of about 0.12 m at PM1 as shown in Fig. 3.6. When the excess pore water pressure, Δu reaches a value equal to the initial vertical effective stress, σ' i.e., excess pore water pressure ratio, r_u approaches unity, $r_u = \Delta u / \sigma'$) liquefaction occurs. Initial vertical effective stresses due to embankment loadings were calculated based on the influence values assuming the foundation ground to be elastic semi-infinite as proposed by Osterberg (1957). Pore water generated rapidly in a few cycles at all depths (Fig.3.7). The maximum r_u values at all depths are included in Fig. 3.7. The r_u values were largest at the free field and lowest below the embankment throughout the shaking. The rapid liquefaction in the free field might have reduced the confinement of the soil below the embankment and might have allowed the lateral stretching of the soil below the embankment towards the free field. Under nearly undrained condition, this tensile strain mechanism suppressed the increase of excess pore water pressure in the soil below the embankment. This effect was more prominent near the center line as the embankment and its foundation ground was symmetric, causing lower r_u values below the embankment. Also, the r_u was limited to lesser values due to the presence of initial shear stress in the soil

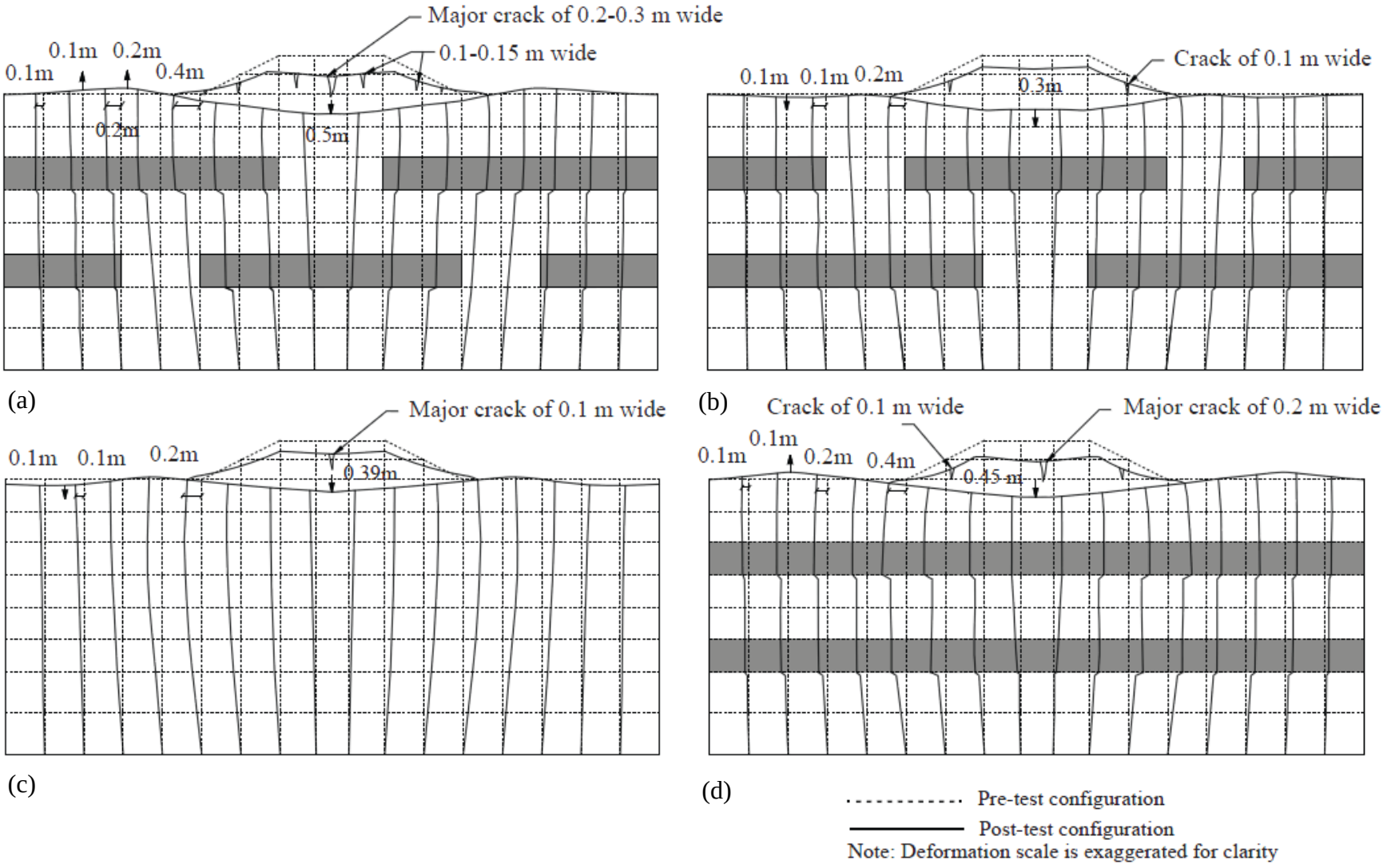

Figure 3.5. Deformed shape of (a) Model NHG1, (b) Model NHG2, (c) Model UG, and (d) Model UG.

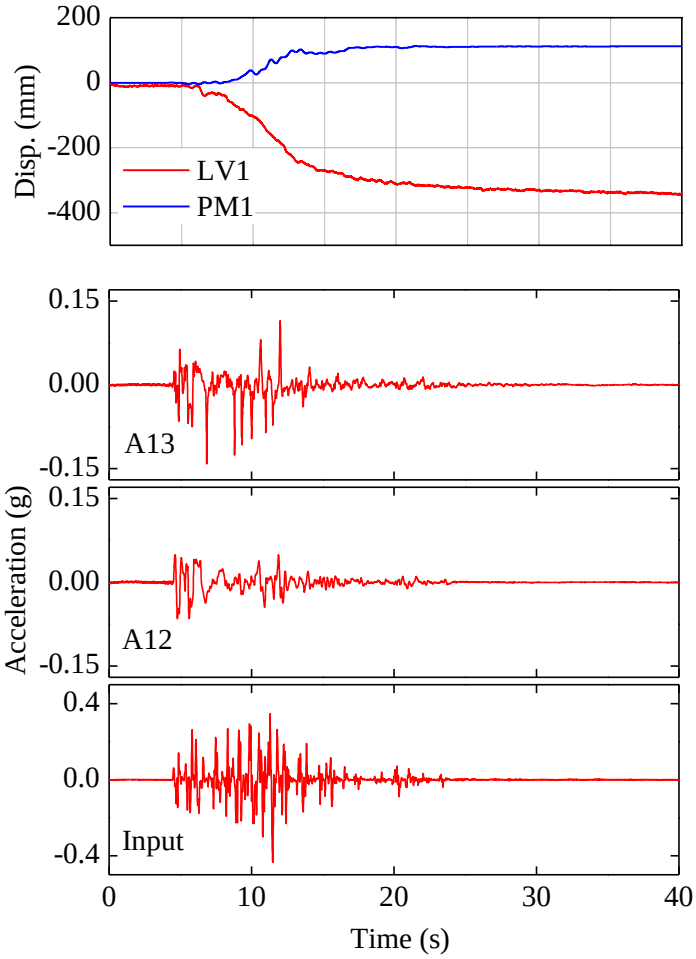

Figure 3.6. Time histories of displacements and accelerations in Model NHG1.

below the embankment (Boulanger and Seed, 1995; Ishihara and Yamazaki, 1980). Such lower r_u values below the embankment were also reported by (Dobry and Liu, 1992; Koga and Matsuo, 1990; Adalier et al., 1998; Idriss and Boulanger, 2003). As the r_u value was larger at the bottom stratum, the accelerations were highly attenuated relative to the base input. In the free field, the attenuation of acceleration was significant after a few cycles due to the loss of soil stiffness and strength. However, some asymmetric acceleration spikes appeared below the embankment toe at A13, where high initial static shear stress existed (Fig. 3.6). Such asymmetric spiky acceleration responses has been investigated by many researchers (Dobry et al. (1995), Elgamal et al. (1996b)) which depict the occurrence of cyclic downslope deformations towards the free field, further suggesting the maximum shear strain at the toe region. Moreover, large strains were attained near the toe region and relatively small strains below the embankment centerline. Figure 3.8 indicates the maximum shear strain amplitude observed in the centerline at different depths during mainshock and aftershock. Shear strain amplitude at several locations during shaking was calculated by

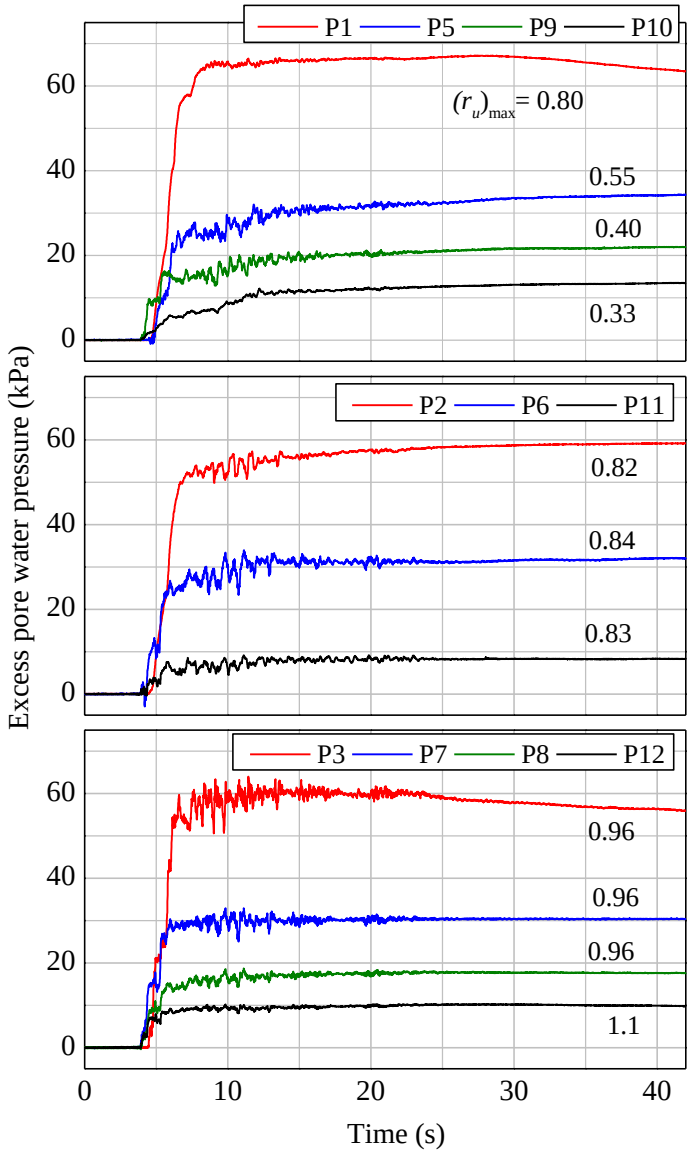

Figure 3.7. Time histories of excess pore water pressure at selected locations during mainshock in Model NHG1 (The numbers on figures represent the maximum r_u values).

using acceleration time histories, based on the method by Koga and Matsuo (1990) and Elgamal et al. (1996b). The pore water was accumulated beneath the silty sand layer as the silty sand layer acted as the barrier for vertical dissipation of excess pore water pressure. As a result, formation of dilation zone beneath the low permeability silty layer might occur, isolating the silty layer and the lateral deformation was observed at the bottom of the silty sand layer. Shear strain amplitudes were larger at the bottom of the silty sand layer as seen in Figs.3.5 (a) and 3.8. It is noted that the middle sandy layer above the silty sand layer translated sideways without much internal shear deformation. However, the shear deformation was continuous as depth decreases at the bottom sand portion.

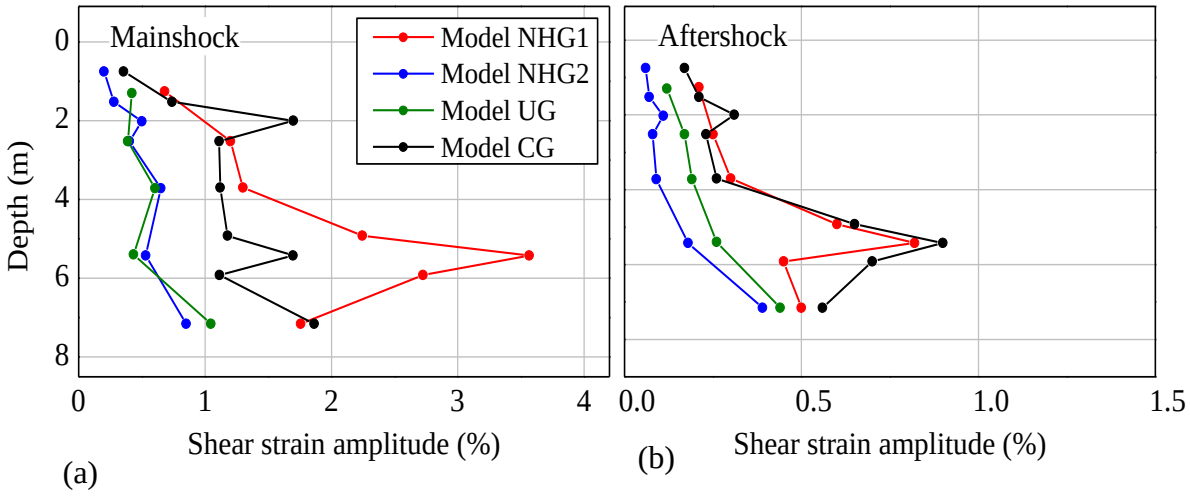

Figure 3.8. Maximum shear strain amplitude in centerline at different depths: (a) Mainshock and (b) Aftershock.

Shear deformation of embankment due to shear deformation of underlying liquefied sand is also a significant factor for crest settlement. Generally, the change in volume of embankments is expected to be small (Okamura and Matsuo, 2002). It is noted that no slope failure of the embankments was detected during the tests presented in this chapter. Assuming the volume change of the embankments due to shaking to be negligible, the vertical strain at the top of embankment becomes equal to the horizontal strain at the embankment base. Thus, the crest settlement due to shear deformation of embankment is expressed as the product of horizontal strain of embankment base and its height. For example, in Model NHG1, crest settlement due to shear deformation = 0.1 x 1.2 =0.12 m, where horizontal strain of embankment base =10% and height of embankment = 1.2m. The crest settlement due to shear deformation for all the model tests are summarized in Table 3.4.

Volumetric change due to pore water dissipation is also a factor for crest settlement along with the initiation of earthquake loading and generation of Δu and its dissipation. Closer examination of the recorded Δu during the mainshock shaking revealed the gradual

Table 3.4. Crest settlement due to shear deformation.

Model Code	Horizontal strain of embankment base (%)	Height of embankment (m)	Crest settlement due to shear deformation (m)
Model NHG1	10	1.2	0.12
Model NHG2	5	1.2	0.06
Model UG	5	1.2	0.12
Model CG	10	1.2	0.06

increment of Δu under the embankment, i.e., at P5, P9, and P10 (Fig. 3.7). The migration of pore water might also have taken place during shaking and this might have caused the continuous and gradual rise of Δu below the embankment centerline (i.e., at P5, P9, P10), contracting the soil. Nonetheless, such gradual increment was not observed in the free field and beneath the toe regions. Moreover, the settlement of PPTs might have contributed partly in the rise of Δu. Evidence of PPT settlement was visible in each of pore pressure plots where the Δu has not returned back to the zero value, i.e., there existed residual excess pore water pressure after dissipation, Δu_r. The calculated Δu_r and the location of PPTs measured after the test indicated that the PPTs below the embankment settled more than that at the free field. Compared to the other models, the r_u values were the largest below the embankment and below the embankment toe throughout shaking (Fig. 3.7). The larger r_u values were associated with the larger cyclic shear strain (Fig. 3.8) and tendency to contract, causing large crest settlement.

Shown in Fig. 3.9(a) are the recorded time histories of displacements at the crest and free field and Δu at 0.75 m depth. The rise in Δu further occurred under the application of small aftershock, re-liquefying the soil at free field, and causing some additional deformations. The shear strain amplitudes observed during aftershock at different depths

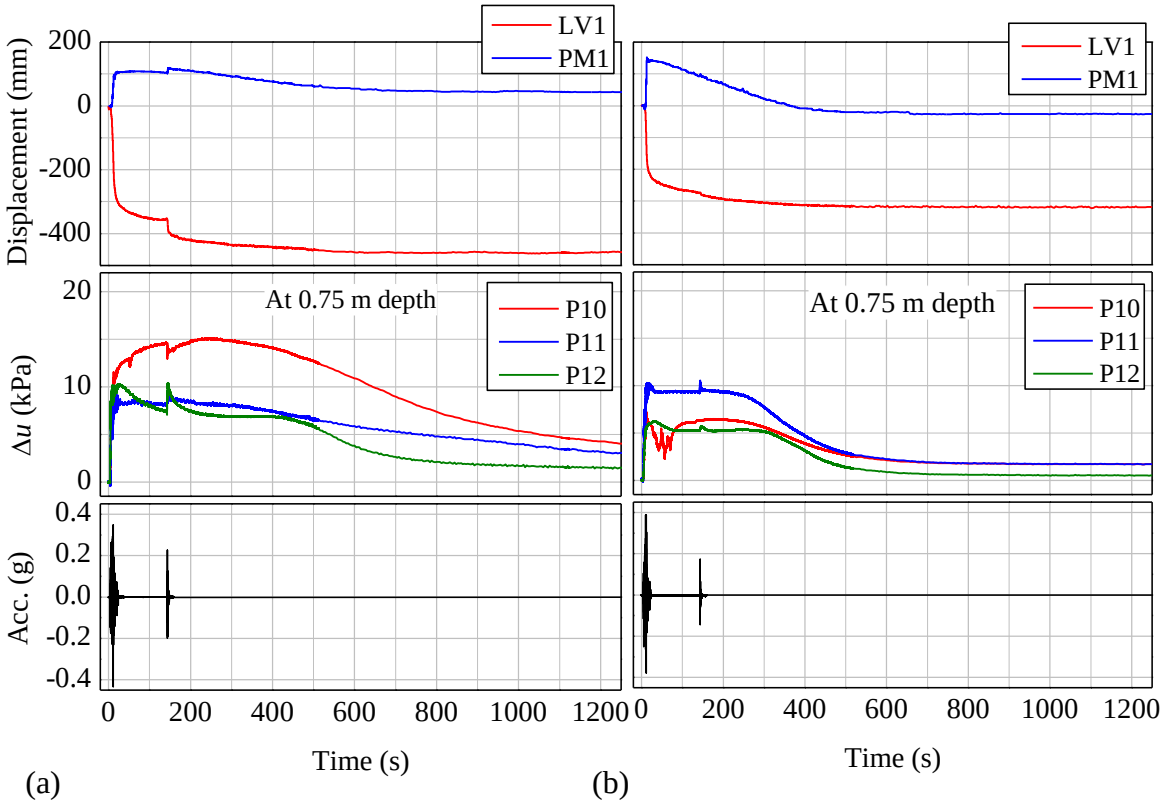

Figure 3.9. Time histories of input acceleration, excess pore water pressure (Δu), and displacement during and after shaking: (a) Model NHG1 and (b) Model NHG2.

were also larger for Model NHG1 (Fig. 3.8(b)). The deformation occurring after seismic excitation stopped was solely due to the dissipation of Δu. At P10, Δu continued to increase and was significantly larger for a longer period of time. The dissipation of pore water was concentrated through the discontinuity region below the embankment centerline and finally towards the ground surface, contracting the foundation soil below embankment and inducing additional settlement after shaking. As the pore water pressure was dissipated mainly through the discontinuity beneath the embankment in test NHG1, the complete dissipation took a longer period of time, about 1200 s. An additional crest settlement of 0.14 m was measured due to aftershock and dissipation of Δu. The heaving occurring during the mainshock shaking also settled down to a final heave of 0.1 m with the dissipation of Δu. No large deformations took place, but still the overall deformation was large compared to other tests.

3.3.2 Model NHG2

Figure 3.5(b) depicts the mapped post-test deformed shape of Model NHG2. Figure 3.10 shows the displacement time histories during the mainshock. As the intensity of the input motion for this test was comparatively smaller, the deformation was also reduced. A crest settlement of 0.35 m was observed of which about 0.25 m was measured during the mainshock shaking. Slumping of embankment sides and the lateral spreading of 0.2 m at the toe were observed. An average normal lateral tensile strain was about 5% along the embankment base.

A significant amount of settlement took place during 10-15 s as shown in Fig. 3.10 which is different from Model NHG1. This might be associated with the rate of Δu build-up. The build-up of Δu was somewhat slower with more cyclic excitation required for liquefaction (Fig. 3.11), which might be due to the slightly smaller input acceleration. Similar to test NHG1, the soil liquefied at the free field region. However, foundation soil below the embankment centerline was observed to have lower r_u values. i.e., at P10 the maximum r_u value is around 0.15, which is very small (Fig. 3.11). Also, the gradual decrement in Δu was observed at P10 during shaking, which might be due to the restriction of pore water dissipation through the silty sand layer. This might be attributed to a possible reduction in cyclic shear strain below the embankment (Fig. 3.8). Also the presence of the upper silty sand layer acted as a hindrance and the water dissipates through the discontinuous region under the toe. The smaller cyclic shear strain might have caused less amount of crest settlement.

Shown in Fig. 3.9(b) are the recorded time histories of displacements at the crest and free field and Δu at 0.75 m depth during and after shaking. The intensity of aftershock was also significantly reduced, so no big difference in Δu and displacement was observed. The shear strain amplitudes below the embankment centerline were also significantly smaller (Fig. 3.8(b)). Since P11 was above the discontinuous permeable region, Δu was incredibly

large at P11 compared to P10 and P12. This was associated with the hindrance of pore water to transmit through the upper silty sand layer, as the pore water drained through the discontinuous region under the toe. It is noted that the behavior of delayed seepage towards the discontinuity at P11 in Model NHG2 was different from that at P10 in Model NHG1. Despite being the location of both PPTs above the discontinuities, Δu at P11 in Model NHG2 was much lesser and dissipation was quite faster. This might be due to two possible reasons: (a) the presence of two discontinuities at the shallow depth distributes the outflow of water and (b) application of low intensity input motion. The total dissipation of Δu took about 700 s and the heaving occurred during mainshock was recovered.

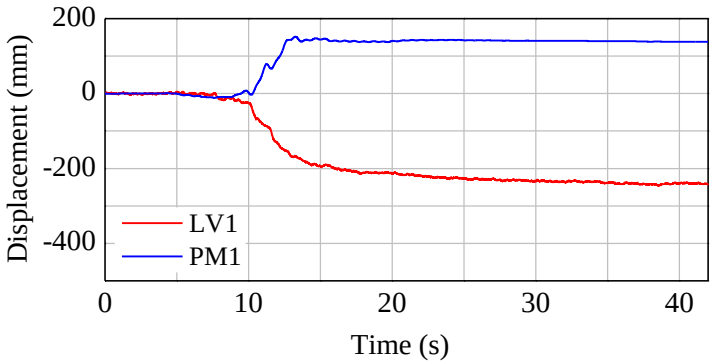

Figure 3.10. Displacement time histories at LV1 and PM1 in Model NHG2.

3.3.3 Model UG

Figure 3.5(c) depicts the mapped post-test deformed shape of Model UG. The time histories of displacement at LV1 and PM1, acceleration at A11 and A12 during mainshock are presented in Fig. 3.12(a). The pattern of deformation was considerably different from other models. The lateral deformation is found to increase continuously towards the ground surface as seen in Fig. 3.5(c). Nevertheless, the embankment and foundation deformations were reduced compared to other tests. A crest settlement of 0.39 m was observed of which about 0.28 m was measured during the mainshock shaking. The embankment toe was found to laterally spread on both sides towards the free field by 0.2 m. The average normal lateral tensile strain along the embankment base was about 5% which was less than that in Model NHG1. Surface cracking was much less with the largest crack only 0.1 m wide.

The time histories of Δu during the mainshock are presented in Fig. 3.13. As observed in Model NHG1, the gradual rise of Δu was not observed during the mainshock shaking. The maximum r_u values at P4 and P7 were much lowered compared to Model NHG1 (Figs. 3.7 and 3.13). The r_u value is about 0.17 at 10 s, which resulted in the reduced settlement during that period. The lower r_u value below the embankment centerline was associated with the possible reduction in shear strain amplitude (Fig. 3.8). Also the maximum r_u value after 10 s is 0.27, which is still lower , attributing to the smaller shear strain amplitude.

Moreover, the maximum r_u values below the embankment toe, i.e., at P8 is 0.68, which was the major cause for the reduced tendency for lateral deformation. Also, the less significant asymmetric spiky acceleration response at A12 (Fig. 3.12(a)) was attributed to the reduction in cyclic downslope deformation (Dobry et al., 1995; Elgamal et al., 1996b). The lateral outflow of less amount of foundation soil has further reduced the embankment settlement. Although attenuation was occurred, the acceleration just beneath the embankment (A11) was slightly higher than Model NHG1 (A12), attributing to the stiffer foundation (Fig. 3.12(a)). Moreover, to a small extent, the pore pressure generated at P7 showed a fluctuation or dip (Fig. 3.13). The appearance of dips has been explained as dilation of soil, indicating

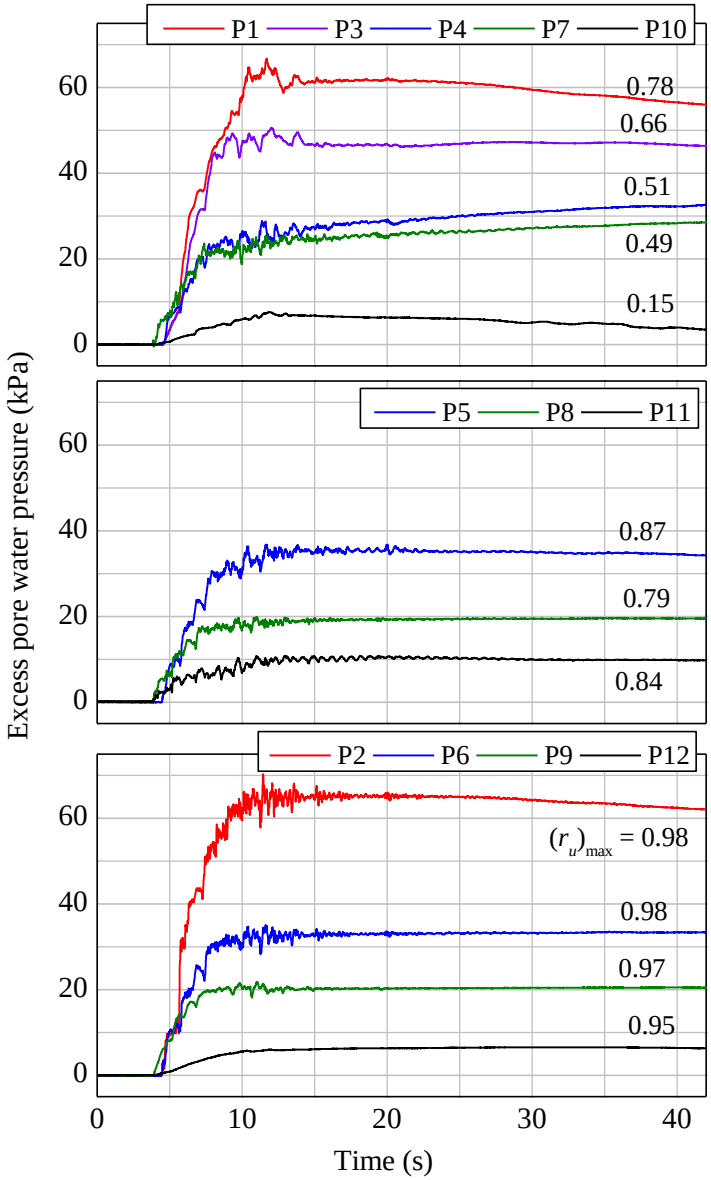

Figure 3.11. Time histories of excess pore water pressure at selected locations during mainshock in Model NHG2 (The numbers on figure represent the maximum r_u values).

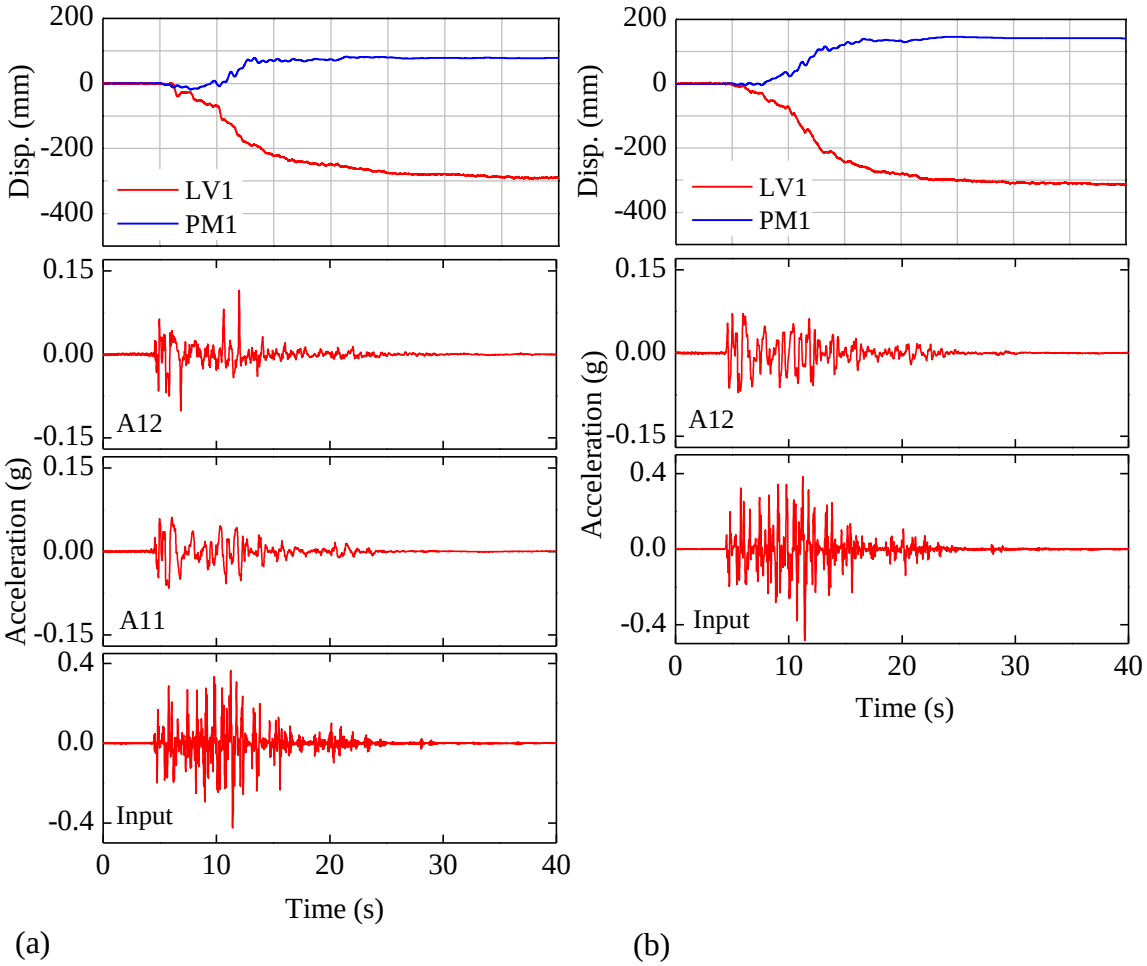

Figure 3.12. Time histories of displacement and accelerations: (a) Model UG and (b) Model CG.

a positive volume change, further decreasing the crest settlement (Dobry et al., 1995; Okamura and Matsuo, 2002).

Shown in Fig. 3.14(a) are the recorded time histories of displacements at the crest and free field and Δu at 0.75 m depth in Model UG. Similar to Model NHG1, aftershock caused an increase in Δu generation and an additional settlement with the smaller shear strains below the embankment centerline compared to other tests (Fig. 3.8(b)). Vertical dissipation took place in the free field and toe region and lateral dissipation occurred under the embankment, consolidating the liquefied soil. For instance, the Δu started decreasing at 200 s at P7, 250 s at P8, and 300 s at P9, which suggested the lateral dissipation mechanism. After shaking, Δu rose slowly below the embankment due to pore water dissipation from the underlying layer (Yang and Elgamal, 2003). As the permeability of Toyoura sand is large, Δu was fully dissipated in 600 s and the settlement also ceased after 500 s. The heaving of 0.1 m occurring during the mainshock shaking also settled down due to pore water dissipation. An additional crest settlement of 0.1 m was measured due to aftershock and dissipation of Δu.

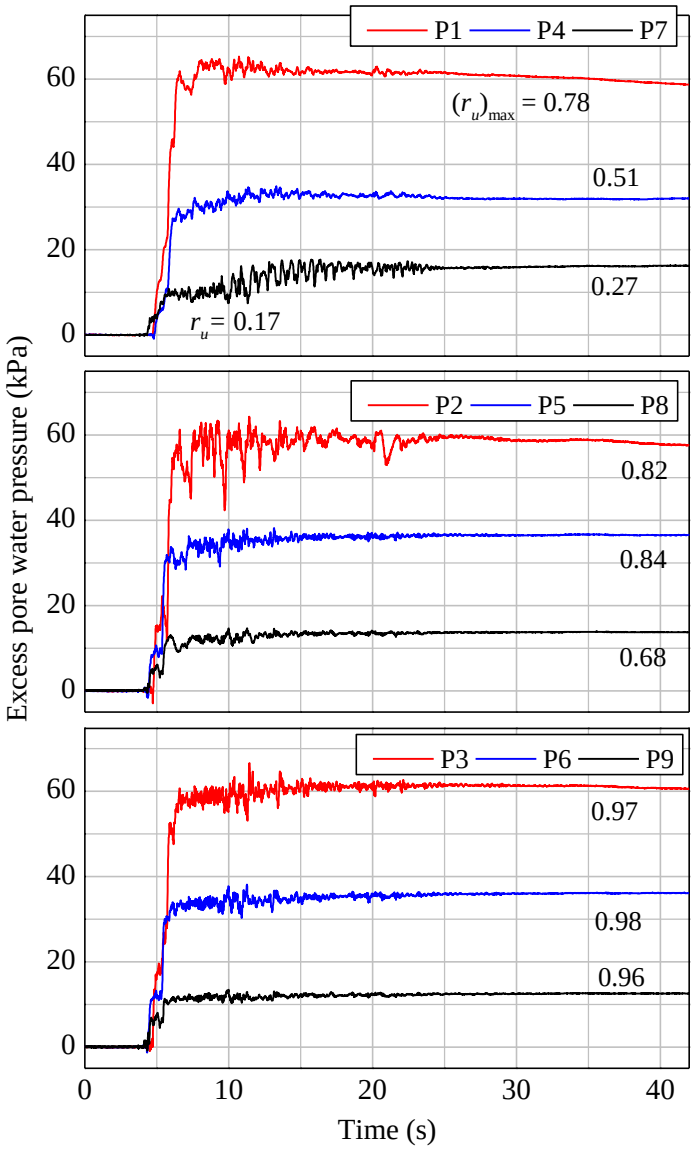

Figure 3.13. Time histories of excess pore water pressure at selected locations during mainshock in Model UG (The numbers on figure represent the maximum r_u values).

3.3.4 Model CG

Figure 3.5(d) depicts the mapped post-test deformed shape of Model CG. Figure 3.12(b) shows the time histories of displacement at LV1 and PM1, and acceleration at A12 during mainshock shaking. A crest settlement of 0.45 m was observed of which about 0.32 m was measured during the mainshock shaking. The embankment toe was found to laterally spread on both sides towards the free field by 0.4 m and the ground surface at free field was observed to heave upward by 0.1 m. The lateral deformation may be acquainted with an average normal tensile strain of about 10% along the embankment base. In addition, tension

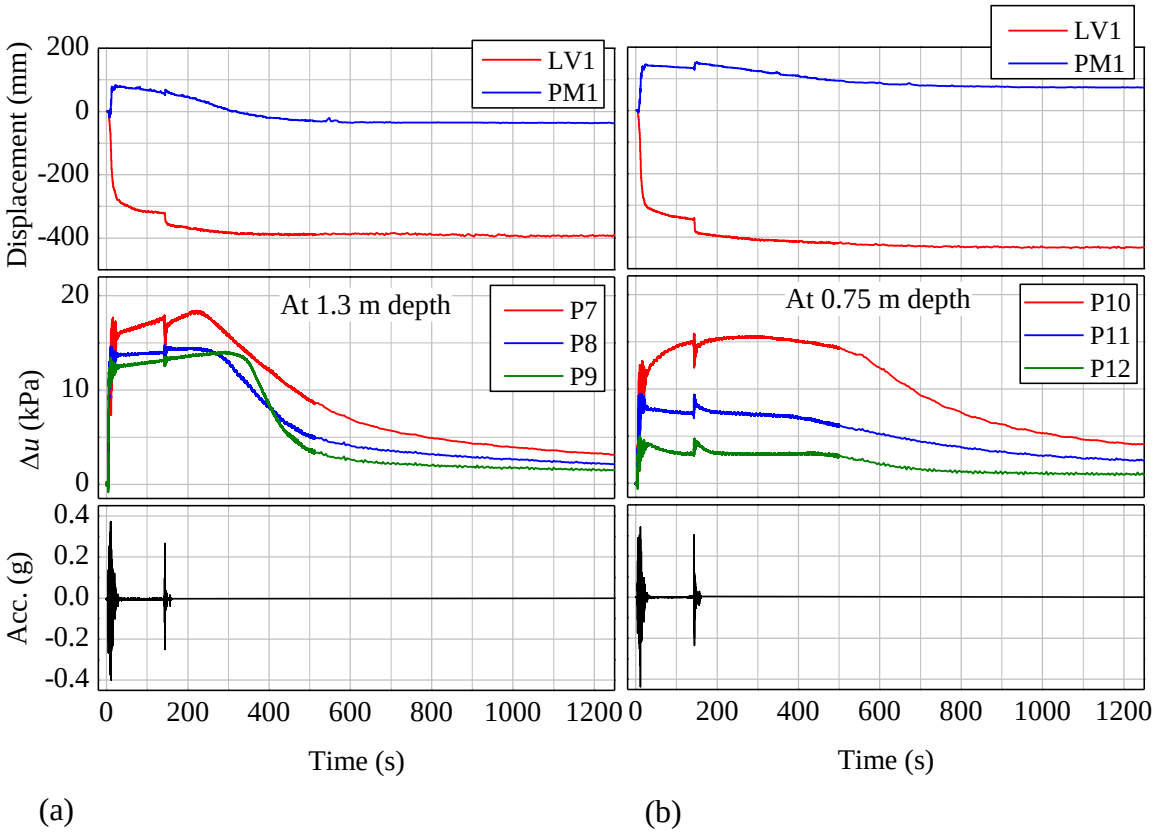

Figure 3.14. Time histories of input acceleration, excess pore water pressure (Δu), and displacement during and after shaking: (a) Model UG and (b) Model CG.

cracks occurred at the crest and side of the embankment in the direction perpendicular to the section of embankment, which might be due to the extension of the embankment as the lateral spreading of underlying foundation soil occurred. Major cracks of width 0.2 m were observed at the crest and cracks of width 0.1 m at the embankment sides.

Notable shear deformation occurred at the bottom of the silty sand layers. The middle sand layer translated sideways with no shear deformation (Fig. 3.5(d)). The top sand layer together with the embankment translated sideways. At P10, just below the embankment centerline, Δu increased in a few cycles consisting of several dips and fluctuation as that in Model UG (Fig. 3.15). At about 9 s, some large dips or fluctuation of pore pressure appeared. This signified dilative stress-strain response, causing a positive volume change which reduced the crest settlement (Dobry et al., 1995; Okamura and Matsuo, 2002). No gradual rise in Δu was monitored below the embankment centerline until 25 s of shaking. Also, the r_u value was significantly smaller at P12 in the free field region throughout the shaking, revealing the soil has not yet liquefied. The non-occurrence of liquefaction indicates the possibility of lack of pore water migration from the underlying layers. After 25 s, a gradual rise in Δu was observed at P10, which might possibly be due to the formation of cracks or vents in the upper silty sand layer around the centerline. Although large attenuation occurred,

the acceleration just beneath the embankment (A12) was slightly higher than Model NHG1, attributing to the stiffer foundation (Fig. 3.12(b)). Maximum lateral deformation of 0.4 m occurred, with equal lateral deformation as that of Model NHG1. As the large shear deformation occurred beneath the top and bottom silty layer, lateral deformation should also occur to a large extent. The lower r_u values at the shallow depth (i.e., above the upper silty layer) at the free field region suppressed the lateral outflow of foundation soil below the embankment.

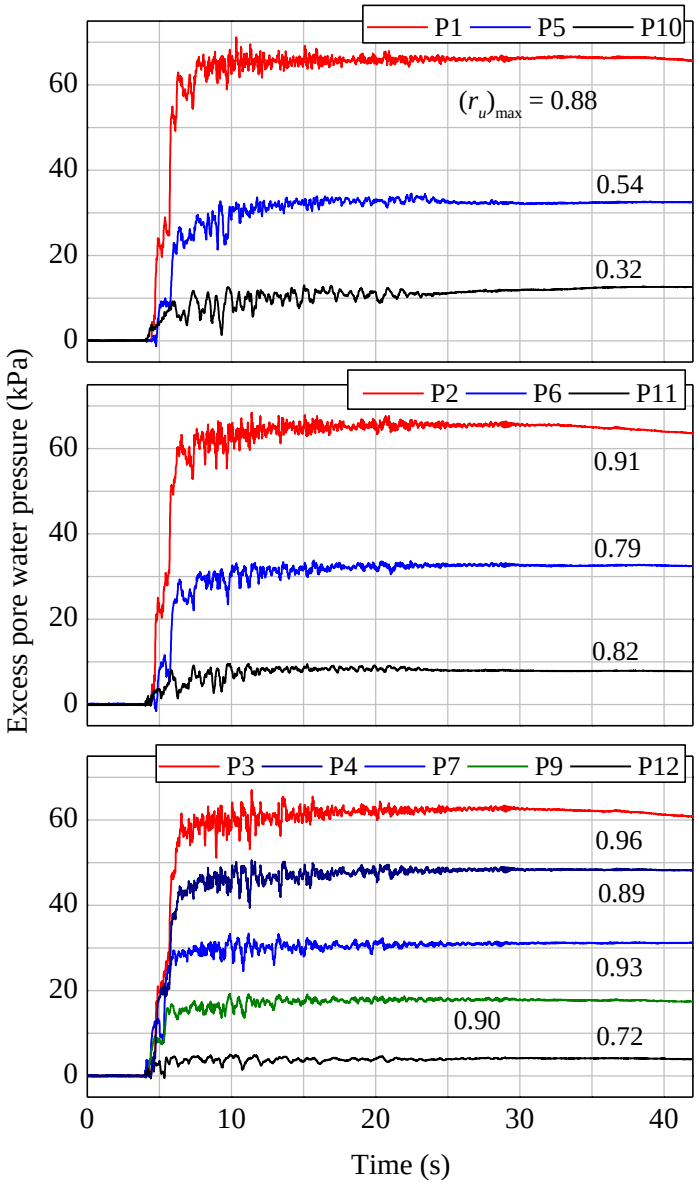

Figure 3.15. Time histories of excess pore water pressure at selected locations during mainshock in Model CG (The numbers on figure represent the maximum r_u values).

The recorded time histories of displacements at the crest and free field and Δu at 0.75 m depth during and after shaking in Model CG are presented in Fig. 3.14(b). A continuous increase in Δu at P10 was observed, similar to Model NHG1, due to the dissipation of pore water through the vent formed around the centerline of the upper silty sand layer. A small aftershock caused rapid increase in Δu, re-liquefying the sand at the free field and beneath the toe. At P10, Δu continued to increase and remained significantly larger until 400 s, while the Δu decreased instantly after the aftershock at P11 and P12. The total dissipation of Δu took about 1200 s and the settlement also continued until 1000 s at a slower rate. An additional crest settlement of 0.11 m was measured due to aftershock and dissipation of Δu.

3.4 Void redistribution

The presence of low permeability layers trap the pore water, leading to the formation of loosening or dilation zone beneath it during seepage of pore water due to the drainage restriction caused by the low permeability layer. Many researchers have investigated the occurrence of localized void redistribution due to the formation of dilation zone, leading to the shear strain localization in continuous layered soil profile. In order to depict the occurrence of void redistribution beneath the silty sand layer in non-homogeneous soil profile, Model NHG2 was considered. In Fig. 3.2(b), PPT P7 was placed below the silty layer, i.e., in the sand so that the trapping of pore water beneath the lower permeability layer could be observed. Figure 3.16 shows the excess pore water pressure isochrones for array (P1-P3-P4-P7-P10) of Model NHG2 during and after shaking. Δu just above the silty layer is extrapolated using the value of Δu at P10 and assuming $\Delta u = 0$ at the ground surface. The isochrones shown in Fig. 3.16 was computed by a least-squares fit to the data and boundary condition by a curve of the form as suggested by Malvick et al. (2008b).

$$\Delta u(z) = a_0 \exp(a_1 z) + a_2 z^2 + a_3 z + a_4 \tag{3.1}$$

where a_i are constants obtained from the least squares fit and boundary conditions.

The boundary conditions are:

$\frac{\partial(\Delta u)}{\partial z} = 0$ at $z = 0$, $\Delta u = 0$ at $z = 8.4$, and hydraulic gradient at the bottom of silt, $i_t = \frac{k_s i_s}{k_t}$

The hydraulic gradient at the bottom of silt, i.e., at the top boundary in the sand was calculated from the continuity equation across the boundary which is given by:

$$k_f i_f = k_s i_s \tag{3.2}$$

where, k_f = Permeability constant of silty layer,

i_f = Hydraulic gradient through silty layer

k_s = Permeability of Toyoura sand,

i_s = Hydraulic gradient at the top boundary of Toyoura sand

The hydraulic gradient through the silt, i_f can be calculated from the difference in excess pore water pressure above and below the silt: the difference in Δu at z = 5.9 m and 6.9 m.

The obtained curve fits the experimental data well with high correlation coefficient. The silt layer being less permeable than liquefied sand layer accumulates the pore water seeped upward. This trapping of pore water beneath the low-permeability layer leads to the formation of loosening (dilating zone) of sand at the top of liquefied layer and contraction zone in the lower part of the liquefied layer due to densification. The accumulation of pore water beneath the silty layer increases the pore water immediately during shaking compared to that above the silty layer, causing the larger hydraulic gradient though the silty layer during and after shaking as shown by isochrones in Fig. 3.16.

1-D flow method described by Malvick et al. (2008a) is used to compute the volumetric strains during and after shaking and consolidation analysis proposed by Kokusho (2000a) is

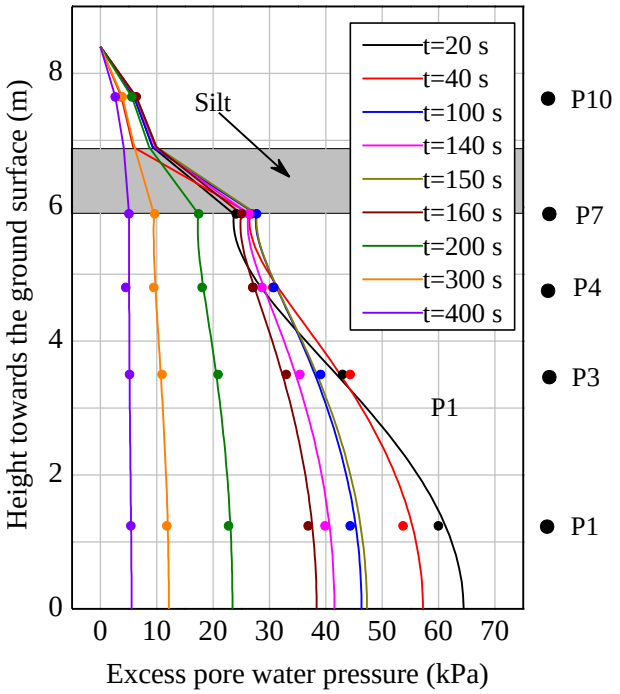

Figure 3.16. Excess pore water pressure isochrones at centerline for Model NHG2.

used to calculate the thickness of water film generated beneath the silty layer. The analysis is conducted for Model NHG2 because of availability of sufficient test data of excess pore water pressure.

1-D flow method

The values of excess pore water pressure were used to calculate the volumetric strains at the centerline by using a data analysis method described by Malvick et al. (2008b). Assuming one-dimensional flow, using Darcy's law to calculate flow velocity, the volumetric strain is calculated as

$$\frac{\partial \varepsilon_v}{\partial t} = \frac{k_s}{\gamma_w} \frac{\partial^2 \Delta u}{\partial z^2} \tag{3.3}$$

For this equation, k_s = permeability of Toyoura sand; γ_w = unit weight of water,

z = height towards the ground surface

The volumetric strains at different height during and after shaking were evaluated by double differentiating Eq. (3.1) with respect to z and integrating $\partial \varepsilon_v / \partial t$ over time. Figure R3 shows the volumetric strain below the upper silty layer of Model NHG2 for different time period. The negative ε_v represents contraction and positive ε_v represents dilation. Distinct zone of contraction and dilation can be seen in Fig. 3.17 until t = 300 s. The loosening zone formed even during shaking and started decreasing after shaking stopped (after 160 s).

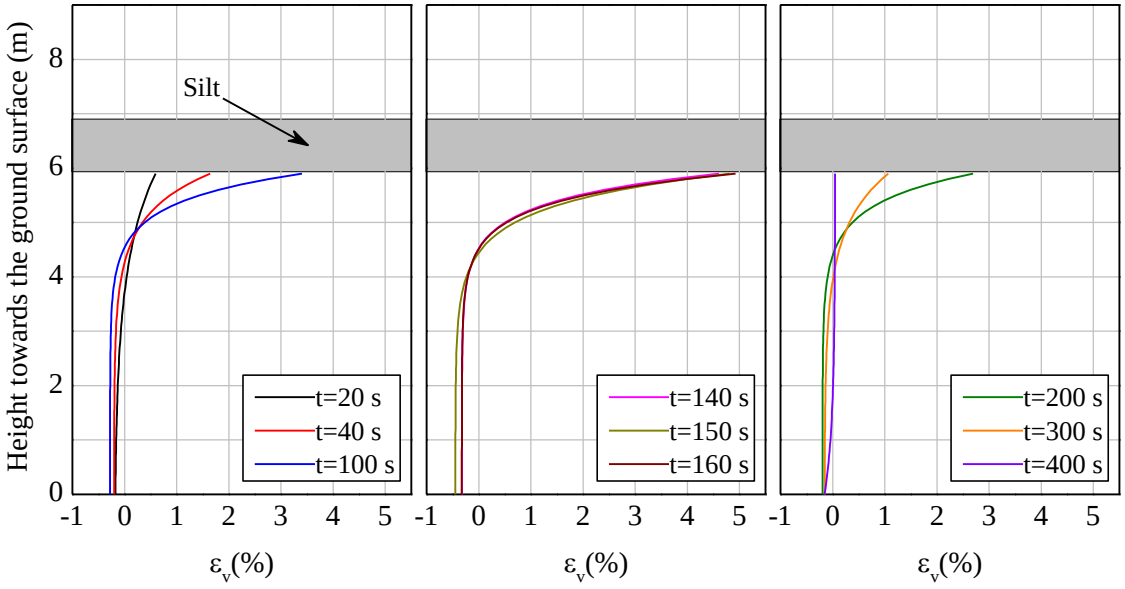

Figure 3.17. Volumetric strain calculated by 1D flow method for Model NHG2.

Consolidation analysis

Kokusho and his coworkers (Kokusho, 2000a, 1999) have demonstrated the formation of water film as a result of pore water trapped by a relatively impermeable layer. They conducted one-dimensional consolidation analysis to calculate the thickness of water film generated. The thickness of water film was calculated as the difference between the surface settlement below the silty layer, S_l and the seepage flow through the silty layer, q_s.

$$\begin{aligned} S_l &= m_{vl}\left\{\int_0^{H_l}\gamma_l'(H_l-z)dz-\int_0^{H_l}(\Delta u)\,dz\right\} \\ &= \frac{1}{2}m_{vl}\gamma_l' H_l^{\,2}\left[1-\frac{32}{\pi^3}\sum_{n=1}^{\infty}\frac{(-1)^{n+1}}{(2n-1)^3}\times\exp\left\{-\left(\frac{2n-1}{2}\pi\right)^2 T_l\right\}\right] \end{aligned} \tag{3.4}$$

where m_{vl} = compressibility coefficient; γ_l' = buoyant unit weight of lower sand layer; H_l = height of lower liquefied layer; T_l = time coefficient $= \left(c_{vl}/H_l^{\,2}\right)t$ in which c_{vl} is the consolidation coefficient given as $c_{vl} = (k_l/m_{vl}\gamma_w)$; k_l = the permeability constant; γ_w = unit weight of water

Seepage volume per unit area, q_s is expressed as

$$q_s = v_s t = k_f^{\,*} i_f t \tag{3.5}$$

where

$k_f^{\,*}$ = composite permeability coefficient through the silt and upper sand

$$= \frac{H_u + H_f}{H_u/k_u + H_f/k_f};$$

i_f is the hydraulic gradient through silt layer which is calculated from the test data

The volume compressibility coefficient, m_{vl} is determined from the final settlement below the silty sand layer using Eq. (3.4). The final settlement below the silty sand layer was measured during the post-test dissection of the model after the test. The final settlement of 0.24 m was observed below the upper silty sand layer in Model NHG2. Using this settlement, from Eq. (3.4), the volume compressibility coefficient, $m_{vl} = 1.6\times10^{-3}$(1/kPa). Using this value of m_{vl} the settlement at the surface of the lower liquefied layer was determined for different time period. Figure 3.18 compares the time dependent settlement at the surface of the lower liquefied layer with the seepage volume per unit area. The water film thickness is given by the gap between the two lines, and the water film diminishes when two lines intersect. Moreover, the chart suggests that the water film appears immediately during the shaking. The maximum thickness of water film generates at t=70 s and starts

decreasing after shaking.

Tables 3.5 and 3.6 summarize the analyses results of two methods proposed by Malvick et al. (2008b) and Kokusho (2000c) presented herein. 1-D flow method suggests the formation of dilating zone with increment in localized void ratio immediately after the onset of liquefaction. The volumetric strain in dilating zone decreases after shaking stops (after 160 s) and ceases after 300 s. Also, the consolidation analysis indicates the generation of water film immediately after the onset of liquefaction. The thickness of water film is the larger at t=70-80 s. In addition, the thickness of water film during shaking is significantly larger compared to that after shaking stops (after 160 s). The water film ceases after 300 s which is consistent with the diminishing of dilating zone after 300 s below the silty layer. This formation of dilating zone or water film during shaking might be the significant factor for the deformation of embankment.

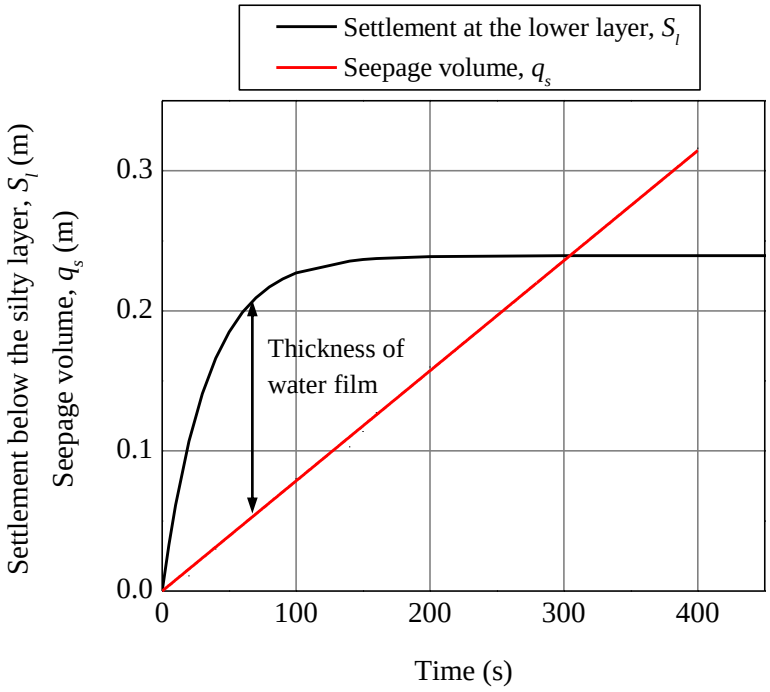

Figure 3.18. Comparison of settlement at lower liquefied layer and seepage volume.

Table 3.5. Summary of volumetric strain and thickness of dilating zone.

	Time					
	20 s	40 s	100 s	150 s	200 s	300 s
$\varepsilon_{v,c}{}^{a}$(%)	-0.18	-0.20	-0.28	-0.45	-0.19	-0.15
$\varepsilon_{v,d}{}^{b}$(%)	0.60	1.64	3.40	4.81	2.69	1.07
$h_d{}^{c}$(m)	2.1	1.6	1.3	1.3	1.5	1.9

[a]Volumetric strain in contracting zone
[b]Volumetric strain in dilating zone
[c]Thickness of dilating zone

Table 3.6. Thickness of water film with time.

Time (s)	$t_w{}^{a}$(m)	Time (s)	$t_w{}^{a}$(m)	Time (s)	$t_w{}^{a}$(m)
10	0.053	60	0.151	140	0.124
20	0.091	70	0.153	150	0.117
30	0.117	80	0.153	160	0.109
40	0.134	90	0.151	200	0.079
50	0.145	100	0.147	300	0.0

[a]Thickness of water film

3.5 Discussions

In the present study the performance of soil structures such as embankments, levees, and dams is investigated mainly by the movement of structures and the ground supporting it during and after the earthquake. Although, time histories of Δu may be governing factors to estimate the behavior of embankments during an earthquake, eventually the deformations are the most important aspects.

An additional test NHG1-MS was also conducted to investigate the effects of aftershocks on the deformation of embankments. The model configuration is the same as Model NHG1; the difference is that only mainshock shaking was applied. Table 3.7 indicates the crest settlement occurred in each model during various period of time. Figure 3.19(a) depicts the normalized crest settlements during the mainshock relative to Model UG. The crest settlement for Models CG and NHG1 was about 10% and 20% larger than that for Model UG. Also, it is noted that the crest settlement was nearly the same for Models NHG1 and NHG1-MS during the mainshock, which supports the repeatability of the experiment. Based on the theory proposed by Malvick et al. (2008b) and Kokusho (2000a), analyses were conducted to determine the formation of dilating zone/water film beneath the lower

Table 3.7. Crest settlement during various time stages.

Model	Crest settlement (mm)			
	0-40 s[a]	40-140 s[b]	140-160 s[c]	160-1400 s[d]
NHG1	341.7	30.7	49.3	65.0
NHG2	258.5	34.8	13.7	33.1
UG	280.0	29.1	41.3	30.2
CG	314.7	29.6	43.6	62.1
NHG1-MS	335.3		41[*]	

Time period:

[a]Mainshock event;

[b]Quite period between mainshock and aftershock;

[c]Aftershock event;

[d]After shaking until complete dissipation of pore water

[*]Crest settlement after mainshock, i.e., 40-1400 s

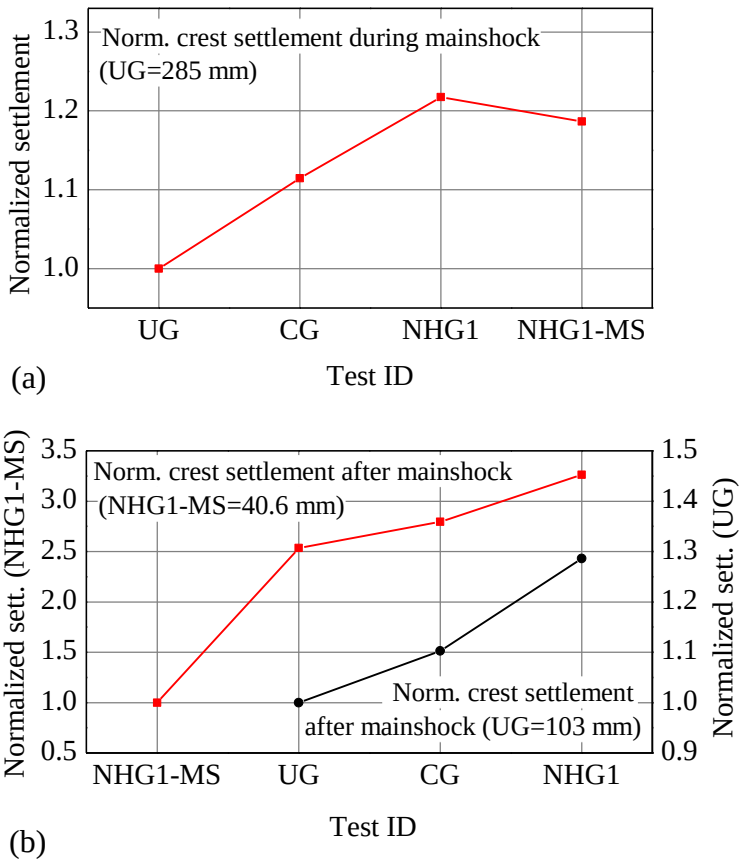

Figure 3.19. Normalized crest settlement: (a) During mainshock and (b) During aftershock and total dissipation of excess pore water pressure.

permeability silty sand layer. The analysis confirmed the possible formation of the dilating zone/water film beneath the silty sand layer even during shaking which started decreasing after shaking stopped. This might have caused the shear deformation at the bottom of embedded silty sand layer in non-homogeneous and continuous layered foundation, inducing the deformation of embankment. Moreover, the dissipation of pore water from the underlying layer was concentrated at the discontinuous region below the embankment, inducing larger r_u values at P10 in NHG1 (Fig. 3.7). The larger r_u values can be attributed to the larger shear strain at different depths below the embankment centerline in Model NHG1 (Figs. 3.7 and 3.8(a)). A large shear strain below the embankment in Model NHG1 (Fig. 3.8(a)) indicated the larger lateral outflow of foundation soils and consolidation of loose sand below the embankment. This type of response has been investigated by many researchers and highlighted as the prime factor to embankment settlement and lateral deformation (Dobry et al., 1995; Elgamal et al., 1996b; Okamura and Matsuo, 2002). The crest settlement of Model NHG2 was not compared with the other tests as the intensity of applied input motion was smaller than that for the other tests.

The settlement occurred during the quite period between mainshock and aftershock (40-140 s) was nearly the same for all the models except Model NHG2 (Table 3.7). Our previous study (Maharjan and Takahashi, 2013a) has shown that despite the fact that settlement during shaking was the same for different ground conditions, settlement induced by seepage after the shaking was found to be larger in non-homogeneous soil deposits. Figure 3.20 shows the displacement times histories at LV2 for Models NHG1 and NHG2. It is noted that the large difference in settlement during the mainshock (0-40 s) is due to the difference in the intensity of input motion. However, despite the application of low intensity input motion, the settlement induced by seepage after the mainshock (during 40-140 s) is larger in Model NHG2. Moreover, the settlement keeps increasing continuously with time during 40-140 s in Model NHG2 as shown in Fig. 3.20. Nonetheless, the settlement remains relatively constant for 110-140 s in Model NHG1. In addition, the Δu under the toe at P11 was larger during and after shaking in Model NHG2 than that in Model NHG1. The discontinuity in silty layer was below embankment toe (exactly below P11) in NHG2, causing larger Δu (Fig. 3.9). Had the intensity of input motion been the same for Models NHG1 and NHG2, the embankment settlement and lateral deformation at the toe in Model NHG2 might have been larger.

Similar to the mainshock, the crest settlement due to aftershock was also larger in Model NHG1 compared to other models (Table 3.6). In addition, the settlement induced due to seepage after shaking (160-1400 s) was significantly larger in Models NHG1 and CG compare to that in Model UG (Table 3.3). Figure 3.19(b) depicts the normalized crest settlements due to aftershock and complete dissipation of Δu for all the tests. The left vertical axis represents the normalized crest settlements relative to Model NHG1-MS and the right vertical axis represents the normalized crest settlements relative to Model UG. Dissipation of Δu became the major factor after the shaking stopped, which caused some

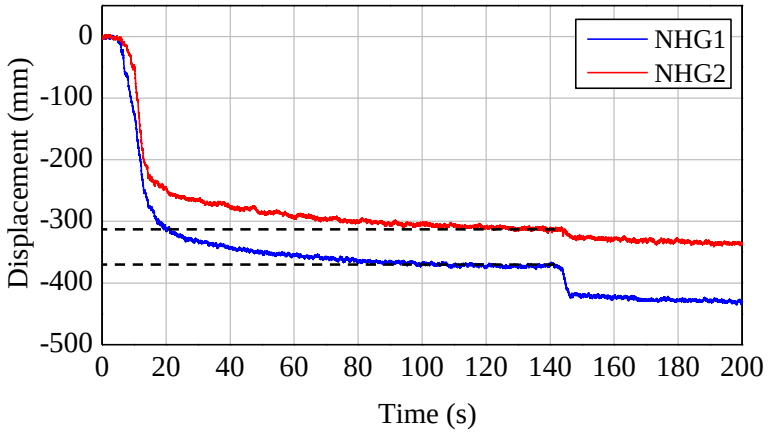

Figure 3.20. Displacement time histories at LV2 for Models NHG1 and NHG2.

additional settlement. The crest settlement induced by dissipation of Δu after shaking is about 0.04 m in Model NHG1-MS. The crest settlement due to small aftershock and dissipation of Δu after shaking for Models UG, CG, and NHG1 was about 2.5, 2.8, and 3.5 times more than that for Model NHG1-MS, respectively. A small aftershock generated the additional Δu and accumulated shear strain ultimately increasing the displacements of the embankment (Figs. 3.8(b), 3.9, 3.14). Also, the crest settlement due to aftershock and pore water dissipation after shaking for Models NHG1 and CG was about 30% and 10% larger than that in Model UG, respectively. Model UG, consisting of a high permeability Toyoura sand foundation has faster dissipation of pore water while the dissipation continued for a longer time period in Models CG and NHG1, accumulating delayed displacements (Figs. 3.9 and 3.14).

3.6 Summary and conclusions

A series of dynamic centrifuge tests was performed to investigate the seismic performance of earthen embankments resting on various liquefiable foundations. The liquefiable foundations include a uniform sand foundation, a multi-layered sand/silty sand foundation, and a non-homogeneous multi-layered discontinuous sand/silty sand foundation. The effects of repeated earthquake ground motions in the deformation of embankments were also studied by applying mainshock-aftershock sequential ground motions. The work presented in this study modeled the features of actual liquefiable soil profiles with discontinuous low permeability layers to provide new insights into the drainage path for dissipation of excess pore water pressure in various ground conditions and compared the liquefaction-induced deformation of embankments on different foundations.

Several conclusions can be drawn from the results of the model tests discussed in this paper. Clear shear straining was observed in the foundation and the embankments appeared to have settled into the foundation in all tests. The accumulation of pore water beneath the

low permeability silty sand layer induced large shear strain below the silty sand layer, resulting lateral spreading and excessive settlement in non-homogeneous foundation. In the non-homogeneous foundation, the dissipation of pore water from the underlying layer was concentrated at the discontinuous region below the embankment, inducing the larger excess pore water pressure ratios. No massive failures were observed in the embankments, but the overall deformation was still very large in the non-homogeneous foundation. Severe deformation patterns in the form of cracking, lateral spreading and slumping were observed. It was found that the sequential ground motions have a significant effect on the accumulated deformation of embankments. Moreover, the effects of aftershocks were more pronounced in the non-homogeneous liquefiable foundations, leading to the post-liquefaction delayed settlement. This study modeled the multi-layered soil profile consisting of discontinuous thin layers of low permeability based on observations of several damage sites during recent earthquakes to improve the ability to account for them in practice. The test results would be useful in the development of design guidelines, as well as in the calibration of numerical procedures.

Chapter 4

Numerical analysis of liquefaction in non-homogeneous soil deposits

The computational simulations are presented for a series of centrifuge tests conducted to investigate the liquefaction mechanism of non-homogeneous soils deposits and to understand the liquefaction-induced deformation of embankments on non-homogeneous liquefiable foundations. The experimental series includes: (i) centrifuge model tests in a levelled ground consisting of uniform, continuous layered and non-homogeneous ground and (ii) centrifuge model tests of earthen embankments on of uniform, continuous layered and non-homogeneous liquefiable foundation. The series of experiments documents a wide range of practical liquefaction responses. In order to numerically simulate the centrifuge tests described in Chapters 2 and 3, a finite element analysis code developed by Takahashi (2002), Takahashi and Takemura (2005) was used. Confidence in ability of the numerical tool, for the realistic behavior on embankments and saturated soils during dynamic loading events, relies heavily on proper verification and validation. Comparison of the numerical and experimental results were carried out to demonstrate the validation and limitations of the numerical model used.

4.1 Modeling assumption

Two dimensional finite element analyses were conducted under the plain strain condition (Takahashi, 2002). The constitutive model, extended sub-loading surface model proposed by Hashiguchi and Chen (1998), was adopted for the soil layers.

Material parameters on soil behavior

The material parameters of the soil layers are listed in Table 4.1. The detail procedure involved in determining the material parameter is explained in Appendix C. The parameters of λ and κ can be determined from the isotropic normal consolidation and swelling curves. G or ν may be determined from the shear modulus obtained by element tests. ϕ_{d} can be determined by phase transformation line in the undrained test. β_{ij0} can be determined by a stress path of anisotropic consolidation, i.e., the coefficient of earth pressure

at rest. $F_0/(-\sigma_{m0})$ represents an over consolidation ratio, where $p_0 \equiv -\sigma_{m0}$. The other parameters i.e. μ, ϕ, u_1, m_1, b_r, ϕ_b, c and s_{ij0} can be determined by trial and error so that the parameters can be fitted into the element tests. The details of parametric studies based on trial and error procedure carried out to determine the material parameters are explained in Appendix C. The cyclic undrained triaxial tests were conducted to determine the liquefaction resistance curves for Toyoura sand and Silica sand No. 8. Figure 4.1 illustrates the liquefaction resistance curves for Toyoura sand and Silica No. 8.

Table 4.1. Material parameters for numerical analysis.

Parameter	Toyoura Sand	Silica No. 8	DL Clay
G_S	2.65	2.65	2.675
e_0	0.791	0.98	0.8
κ	0.0013	0.0029	0.020
λ	0.0072	0.015	0.160
ν	0.33	0.33	0.30
ϕ	40^o	35^o	50
ϕ_d	25^o	27^o	25
μ	0.9	1	1.8
ϕ_b	30^o	27^o	40
b_r	100	100	70
u_1	4	8	1
m_1	1	1	1
c	30	30	25
K_0	0.7	0.7	0.7
$F_0/(-\sigma_{m0})$	1.2	1.2	1.2
s_{ij0}	$0.2\sigma_{ij0}$	$0.2\sigma_{ij0}$	0.3
k (m/s)	2.0×10^{-4}	2.0×10^{-5}	2.0×10^{-7}

4.2 Simulation of centrifuge model tests

The centrifuge model tests as described in Chapter 2 and Chapter 3 were numerically simulated. Two dimensional finite element analyses were conducted under the plane strain condition. The material properties of sand and pore fluid used in the centrifuge tests were determined, which are listed in Table 4.1. The liquefaction resistance curve for Toyoura sand

and Silica sand No. 8 are illustrated in Fig 4.1. The liquefaction resistance curve is a relation between the ratio of the cyclic shear stress to the initial confining stress and the number of loading cycles required to cause shear strain of 5% in the double amplitude. The soil model used, could not properly simulate the flat curves which causes the simulated values of cyclic stress ratio for both Toyoura sand and Silica sand No. 8 larger than those obtained from laboratory test results at the smaller number of loading cycles. However, the simulated values are closer to those obtained in the laboratory for larger number of loading cycles. In order to obtain the numerical solution, the differential equations were integrated along time. System damping was represented by stiffness- proportional damping, and the damping ratio used was 1% in the first mode of the free vibration of the system. The centrifuge model tests consisting of saturated liquefiable foundation and embankment were modeled using four-node quadrilateral elements using one-point intergration together with a classical hourglass control technique (Flanagan and Belytschko, 1981). A periodic boundary was considered to simulate the flexible boundary at the ends of both sides. Nodes at the both side ends were allowed to move freely in vertical directions.

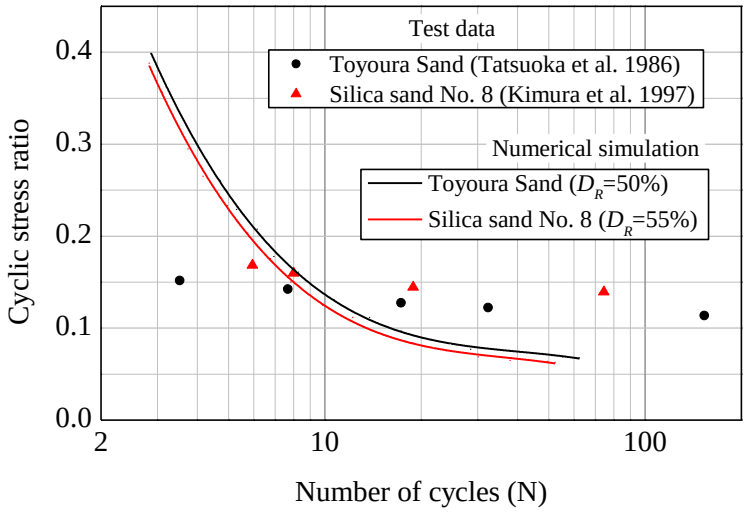

Figure 4.1. Liquefaction resistance curves for Toyoura sand and Silica sand No.8.

4.3 Numerical analysis and results

4.3.1 Seismic response of non-homogeneous soil deposits

Modeling and results of Model test 1 and 4 are discussed for brevity. Figure 4.2 shows the finite element model of the test specimens. The acceleration recorded during the centrifuge tests were applied as earthquake motion.

During the numerical simulations, acceleration time histories were sampled at A3, A5, and A7 locations for Model 1 and at A1, A3, A5, and A9 locations for Model 4, excess pore water pressure time histories were sample at P3, P4, P5, and P6 locations for Model 1 and

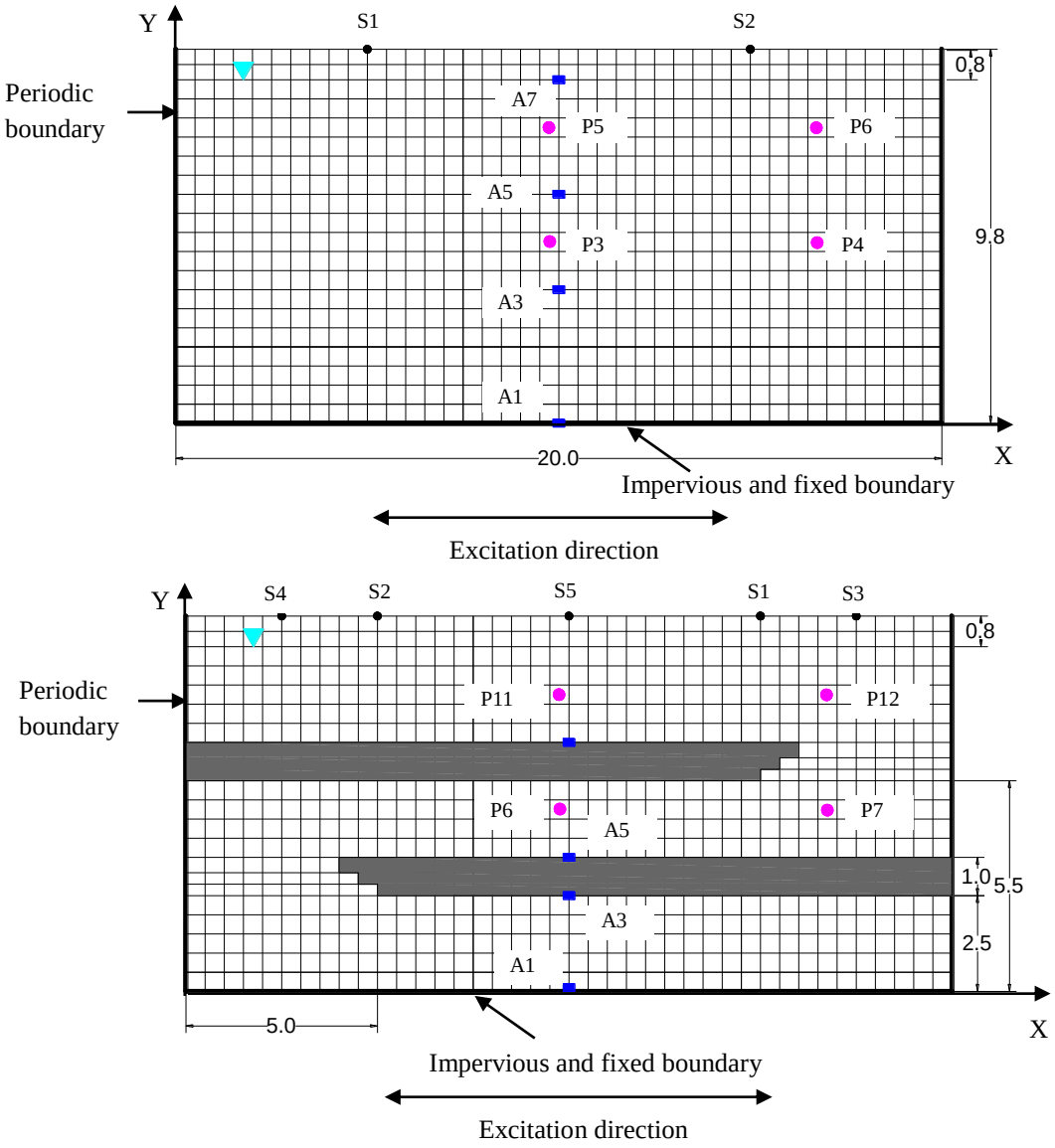

Figure 4.2. Finite element discretization and boundary condition of centrifuge model test: (a) Model 1 and (b) Model 4.

at P6, P7, P11, and P12 locations for Model 4 and settlement were sampled at S1 and S2 locations for Model 1 and at S1, S2, S3, S4, and S5 locations for Model 4 as shown in Fig. 3. P6, P7, and P12 were selected for Model 4 to observe the pore water pressure responses along the drainage path and are compared with the responses at P11, which lies far from the drainage path. At these key locations, computed accelerations, pore pressures and vertical settlement are compared to the corresponding experimental measurements.

Figure 4.3 shows the time histories of the acceleration for Model 1 and Model 4 at the selected locations in both the numerical analyses and the centrifuge model tests. Solid

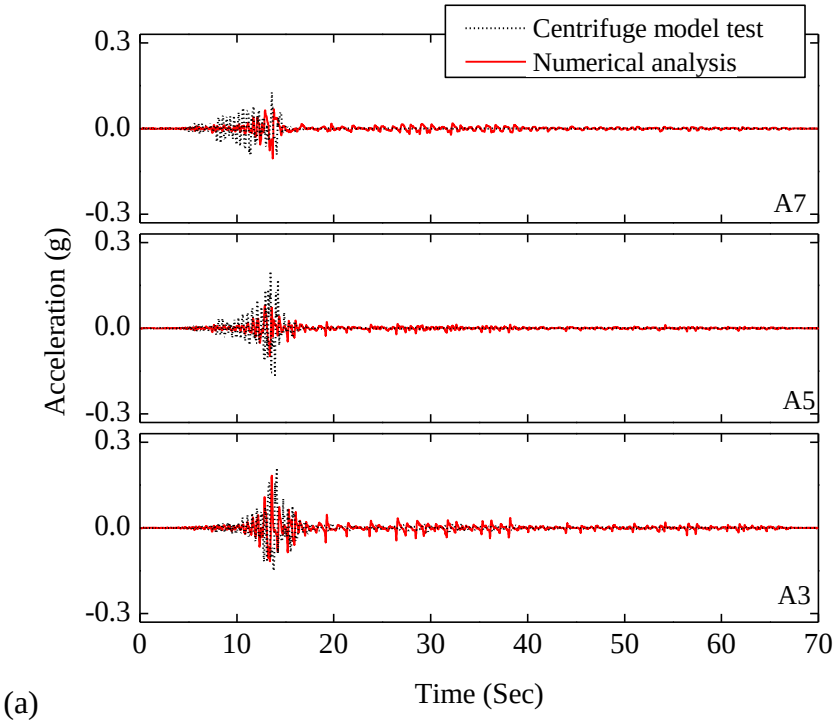

(a)

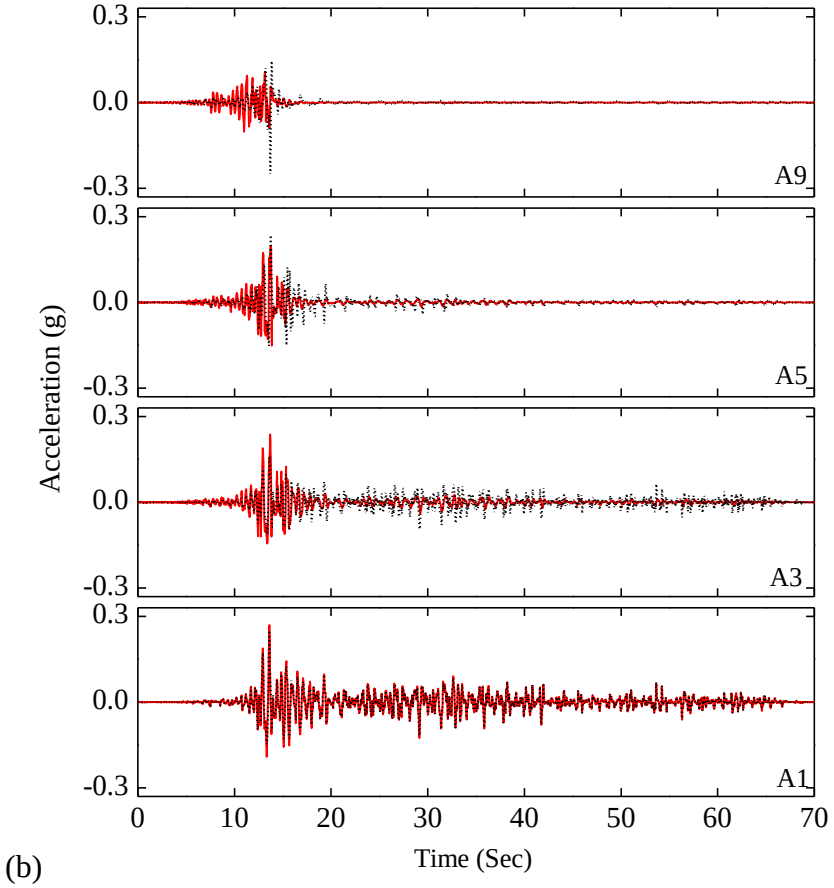

(b)

Figure 4.3. Acceleration time histories: (a) Model 1 and (b) Model 4.

lines represent the responses in the numerical analyses and dotted lines represent the responses in the centrifuge model tests. The calculated acceleration records fairly agree with that in the centrifuge model tests. Meanwhile, the computed acceleration records more or less agree with the centrifuge model tests in amplitude for the lower strata. The differences are observed in amplitude for the upper strata. Amplifications are observed at the upper strata in centrifuge model tests.

During liquefaction, a significant increase in soil permeability occurs by seismic excitation (Shahir et al., 2012; Taiebat et al., 2010). It is important to take an account of the permeability change in the course of simulation of liquefaction. However, such a change is not considered in the analyses code used. The actual variation of permeability incorporates the accurate simulation of excess pore water pressure generation and dissipation. In the physical model tests, it is quite difficult to measure the permeability of soil after initial liquefaction. Assuming a constant increased permeability is a common method for taking permeability variation into consideration in the process of liquefaction modeling (Shahir et al., 2012). Balakrishnan (2000) increased the permeability coefficient equal to 3.67 times the initial value for the simulation of the centrifuge experiment. (Taiebat et al., 2010) used an increased permeability coefficient, equal to four times of the initial value which gave the best fit to the centrifuge results. In order to determine the effects of permeability of sand on the responses of excess pore water generation and dissipation and consequent settlement during liquefaction in non-homogeneous soil deposits, several numerical analyses were conducted by varying the coefficient of permeability of both liquefiable soil and relatively impermeable soil. The coefficient of permeability ($k_{initial}$) of Toyoura sand and Silica No. 8 are 2×10^{-4} and 2×10^{-5} m/sec respectively. In order to evaluate the effect of permeability increase during pore pressure generation, and dissipation, three sets of results are presented, namely numerical simulations with constant permeability values of liquefaction of $k_{initial}$, 2.5 $k_{initial}$, 5 $k_{initial,}$ and 25 $k_{initial.}$

Figure 4.4 and 4.5 show the time histories of excess pore water pressures at the selected locations for both the tests in both the numerical analysis and the centrifuge model tests. Solid lines represent the responses in the numerical analyses and dotted lines represent the responses in the centrifuge model tests. The computed excess pore water pressures for all the permeabilities are similar to the centrifuge model tests in terms of the generation of excess pore water pressure, while the dissipation of excess pore water is quite different for different permeabilities. It can be seen that the dissipation of excess pore water pressure is quite faster with the increase in permeabilities. In Model 1, for P3-P6, the excess pore water pressure responses obtained when k=2.5 $k_{initial}$ agree very well with the centrifuge model tests. For P6 and P7 of Model 4, it is seen that the excess pore water pressure responses obtained when k=2.5 $k_{initial}$ agree very well with that in the centrifuge tests. While for P11 and P12, excess pore water pressure responses obtained when $k=k_{initial}$ agree well with that in the centrifuge tests until t=500 sec. The responses agree quite well with that obtained when k=2.5 $k_{initial}$ after t=500 sec.

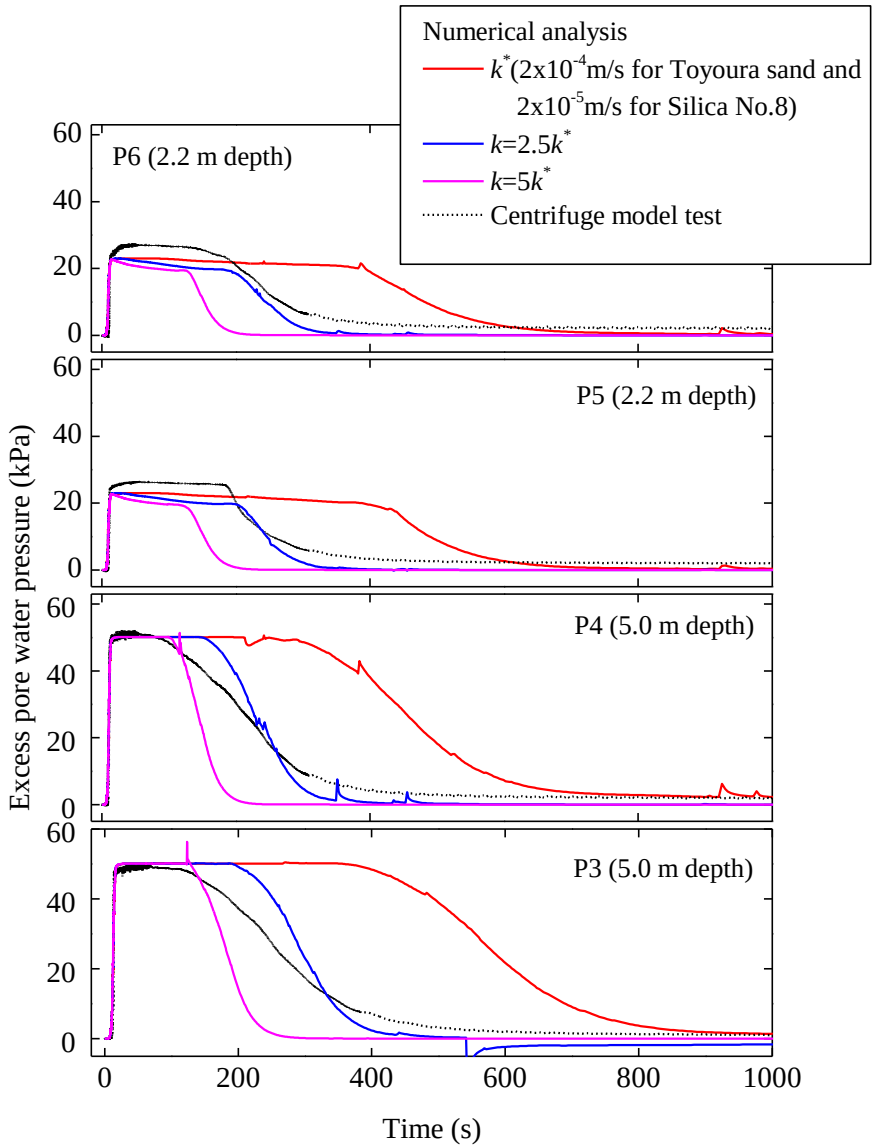

Figure 4.4. Time histories of excess pore water pressure for Model 1 for varying permeabilities of soils.

Figure 4.6 shows the time histories of the excess pore water pressure for P11 and P12 computed from numerical analysis when k=2.5 $k_{initial}$ and centrifuge model tests for Model 4. Both numerical analysis and centrifuge model tests indicate that the excess pore water pressure is significantly larger for longer period of time after shaking at the discontinuity part. The vertical displacements at the selected locations in the ground surface for the varying permeabilities of soils computed from the numerical analysis and the centrifuge model tests are also analyzed. The lower permeability of the soil is accompanied by slower rate of dissipation of excess pore water pressure, incorporating the settlement at the slower rate. It is seen that the computed results of excess pore water pressure and settlement are

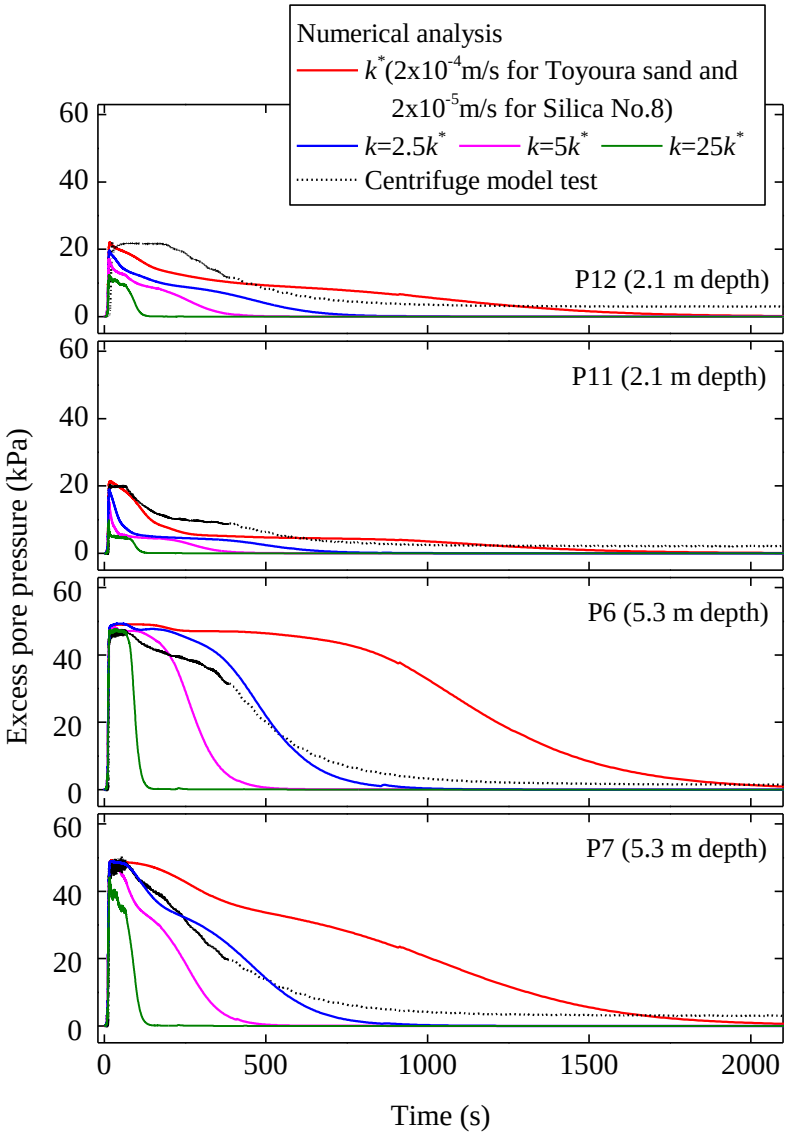

Figure 4.5. Time histories of excess pore water pressure for Model 4 for varying permeabilities of soils.

closer to the centrifuge test results when k=2.5 $k_{initial}$. Figure 4.7 shows the time histories of the vertical displacement at the selected locations for the numerical analysis when k=2.5 $k_{initial}$ and the centrifuge model tests for Model 4. The final settlement is larger at S3, which lies completely above the discontinuity region, while the settlement at S1, which is at the adjacent of the discontinuity region, is also larger than that above the silt layer (S2, S4, and S5).

Figure 4.8 shows the permanent deformations of the model ground for the numerical analysis along with the contours of excess pore water pressure distribution for Model 4. The deformation at the discontinuity part is larger than that in the silt layer at the sand silt

interface. The colored noodles placed at the sand-silt interface in the centrifuge model tests also showed the same deformation pattern. The permanent vertical displacement above the discontinuity part at the ground surface was found to be larger than that above the silt layer. Moreover, the contours of excess pore water pressure distribution shows the larger amount of excess pore water pressure above the discontinuity region.

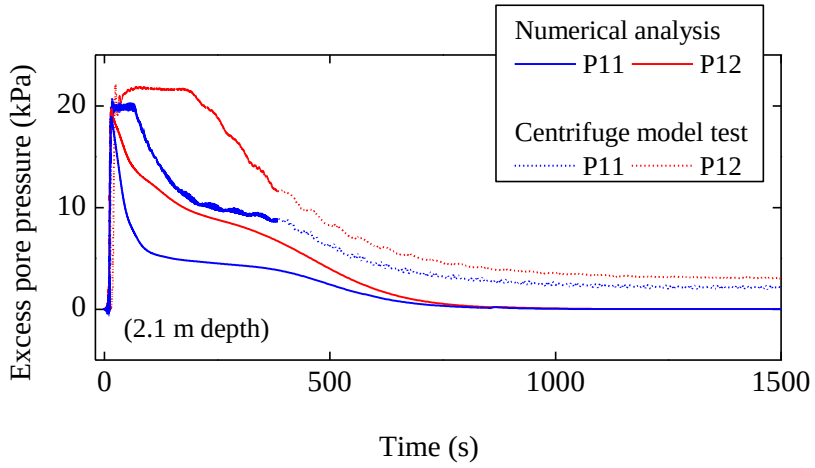

Figure 4.6. Excess pore water pressure time histories when $k=2.5\ k_{initial}$ for Model 4.

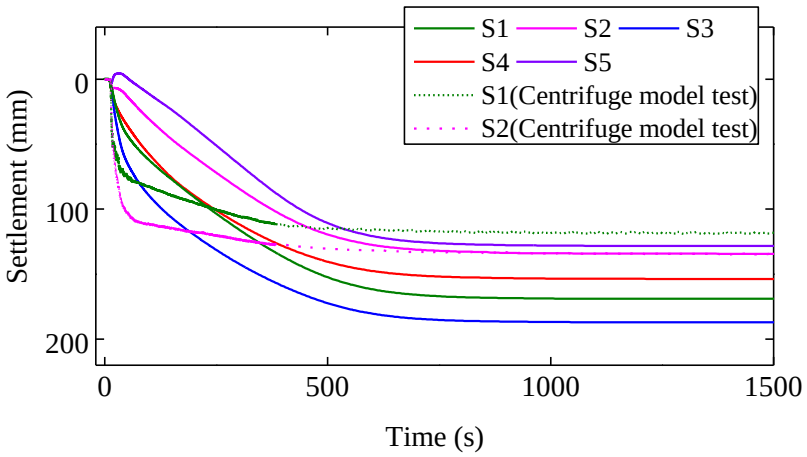

Figure 4.7. Time histories of displacement when $k=2.5\ k_{initial}$ for Model 4.

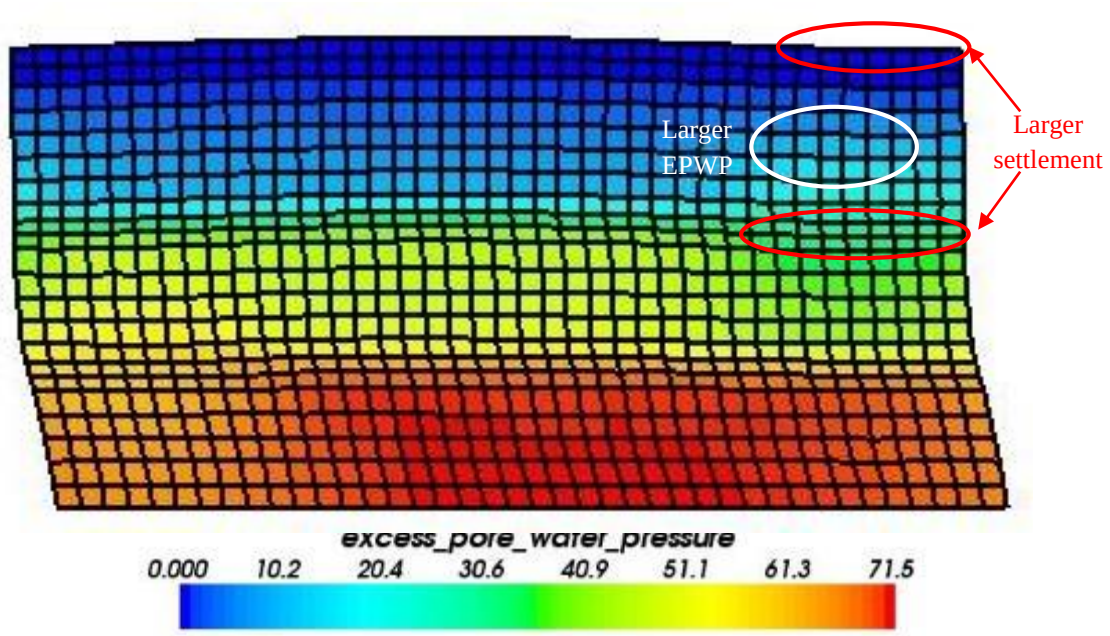

Figure 4.8. Permanent deformations of model ground with contours of excess pore water pressure distribution for Model 4.

4.3.2 Seismic response of embankments on liquefiable foundation

A series of centrifuge model tests were performed on a different foundations: non-homogeneous, continuous layered, and uniform ground foundations in a flexible laminar container at a gravitation acceleration of 40g as discussed in Chapter 3. The centrifuge models simulated a prototype clayey earthen embankment of 1.2 m height and 8 m wide, which is built of the mixture of DL clay and silicon oil with 1:2 slope, resting on a saturated liquefiable sand deposit of thickness 8.4 m. Figure 4.9 shows the finite element discretization of the centrifuge model tests, as described in Chapter 3. Non- homogeneous foundation ground (Models NHG1 and NGH2) comprises of Toyoura sand with two discontinuous silty sand layers of thickness 1.0 m. Non-homogeneity was incorporated by including periodically distributed silt patches. Uniform foundation ground (Model UG) comprises of only Toyoura sand, deposited at a relative density of 50%. Silica sand No. 8 was deposited at a relative density of 50% to create the relatively impermeable silty sand layer. The coefficient of permeability ($k_{initial}$) of Toyoura sand and Silica No. 8 are 2×10^{-4} and 2×10^{-5} m/sec respectively. As described in the preceding section, the excess pore water pressure and settlement obtained from computational analysis agreed fairly well with that obtained from experimental results when the coefficient of permeability of both soils were taken as 2.5 $k_{initial.}$ Hence, the coefficient of permeability of Toyoura sand and Silica sand No. 8 are taken as 5×10^{-4} and 5×10^{-5} m/sec respectively. The ground motion recorded at the Moorpark-Fire station (90^0 component) during 1994 Northridge earthquake, normalized.

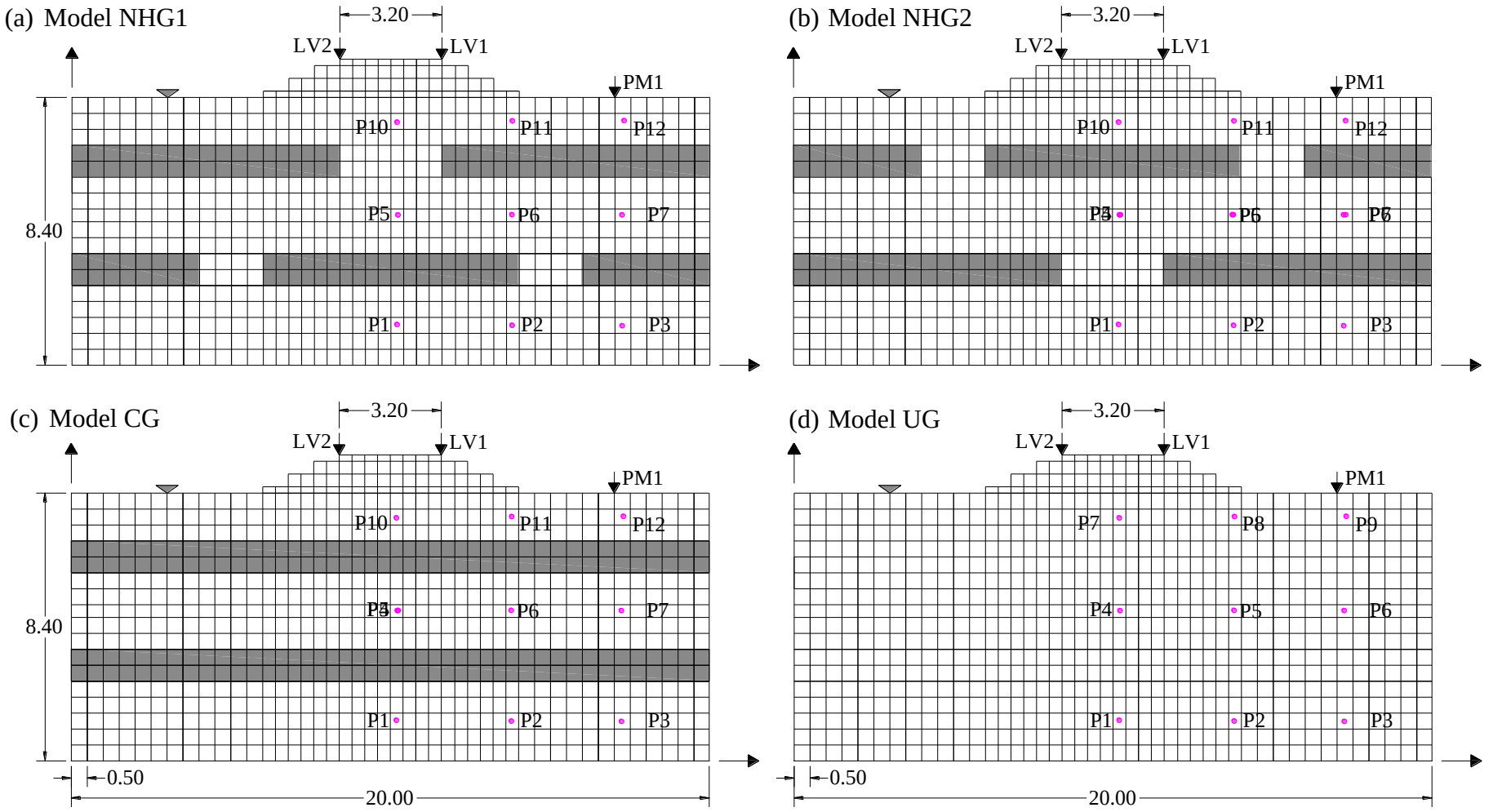

Figure 4.9. Finite element discretization: (a) Model NHG1, (b) Model NHG2, (c) Model CG, and (d) Model UG.

to maximum PGA equal to 0.4 g was applied along the base (Fig. 3.3). A numerical analysis of the centrifuge model tests were carried out by two dimensional finite element analyses under the plain strain condition (Takahashi, 2002).

Figure 4.10 shows time histories of EPWP during the shaking below the embankment and free field region for Models NHG1 and UG. Figure 4.11 shows the time histories of displacement at embankment crest and free field during the shaking. The solid lines represent the numerical results and the dotted lines represent centrifuge model tests results. The EPWP and displacement responses look similar during the large shock (0 to 12 s) in both foundation. A marked difference is observed after large shock (12-20 s); for instance, at P5 and P10 of Model NHG which are below the embankment, the increment in EPWP is larger compared to that at P4 and P7 of Model UG, respectively. This is due to the dissipation of EPWP through the discontinuous region. This difference causes a notable difference in settlement during 12-20 s. Embankment crest settled to 0.28 m in Model NHG1 and 0.24 m in Model UG during the first 20 s of shaking. Similarly Figures 4.12 and 4.13 show the time histories of excess pore water pressure and displacement during and after shaking until the total dissipation of pore water for Models NHG1 and UG. A good correlation is seen between experimental and numerical results both in value and pattern during and after shaking (Figs. 4.10-4.13). However, the experimental values of excess pore water pressure seem to be larger compared to the numerical values at shallow depths. This might be due to the settlement of pore pressure transducers during the experiments. Evidence of PPT settlement is visible in each of pore pressure plots where the EPWP has not returned to the zero value, i.e., there exists residual excess pore water pressure after dissipation, Δu_r. The location measured before and after shaking revealed that the PPTs did, in fact, settled during shaking, which is consistent to the settlement calculated from residual excess pore water pressure after dissipation (Table 4.2). The post-test inspection revealed the total amount of transducer settlement during the entire test. The calculated Δu_r and the location of PPTs measured after the test indicated that the PPTs below the embankment settled more than that at the free field.

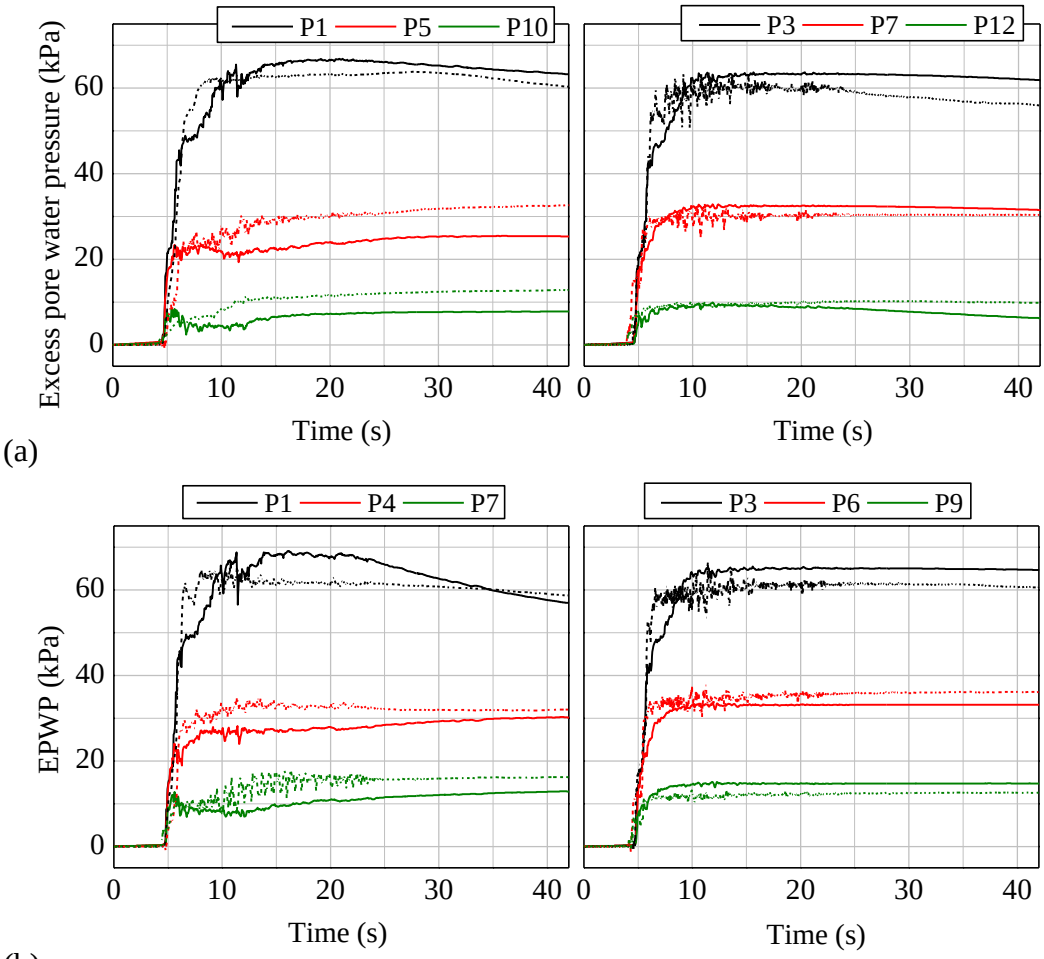

Figure 4.10. Excess pore water pressure time histories: (a) Model NHG1 and (b) Model UG.

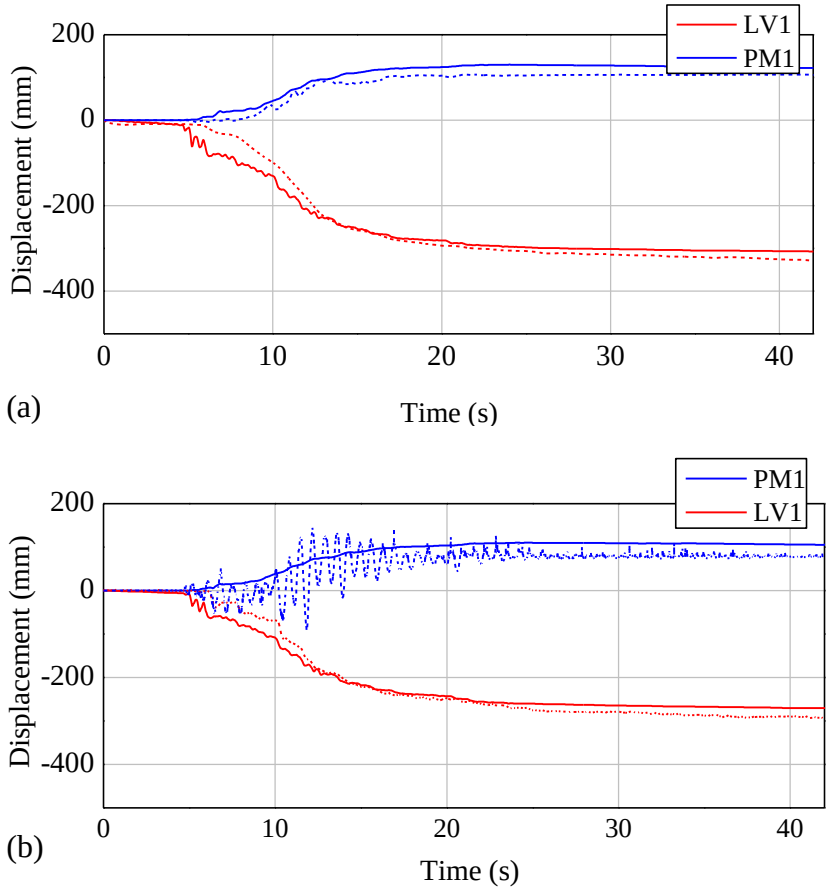

Figure 4.11. Displacement time histories: (a) Model NHG1 and (b) Model UG.

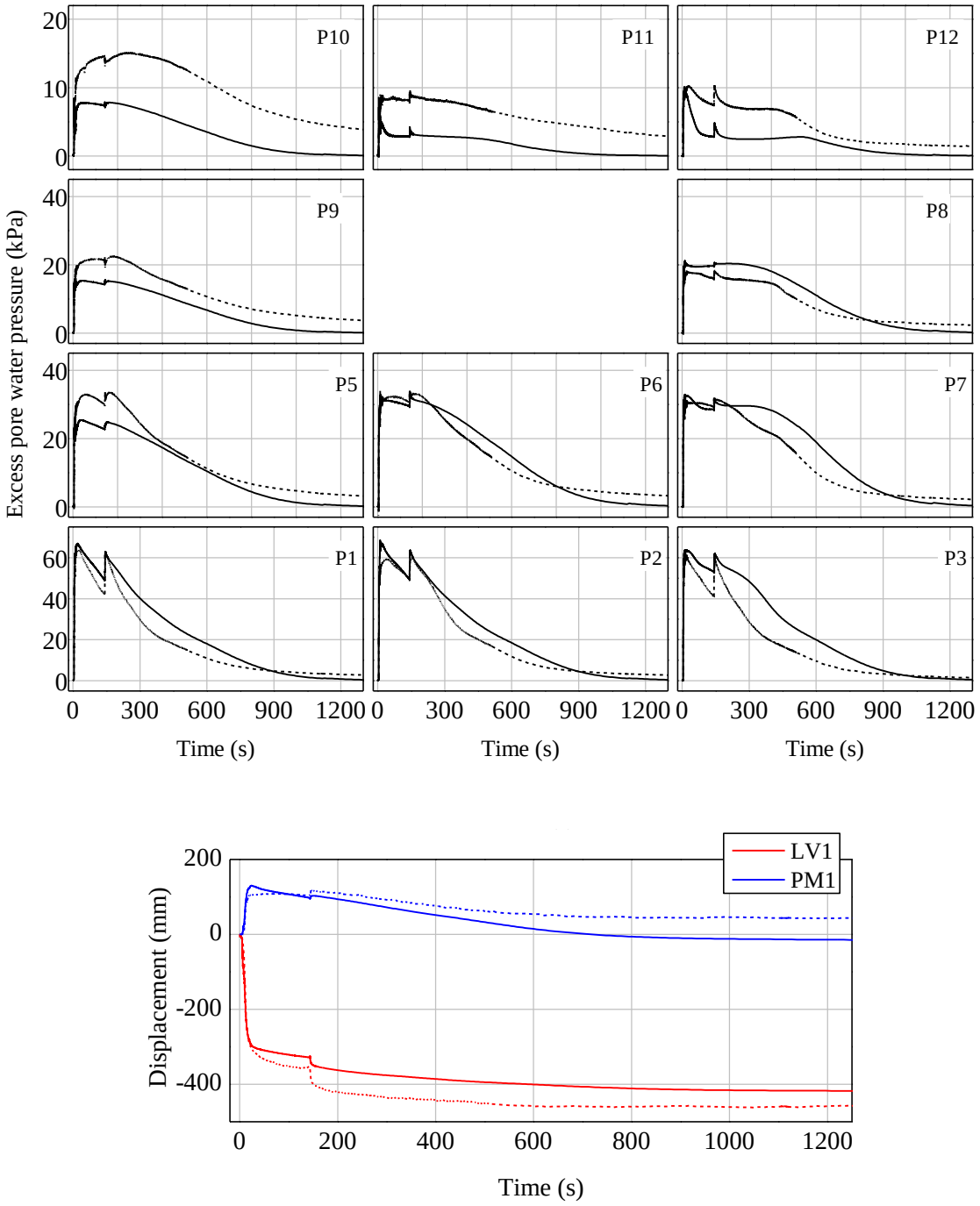

Figure 4.12. Time histories of excess pore water pressure and displacement for Model NHG1 during and after shaking.

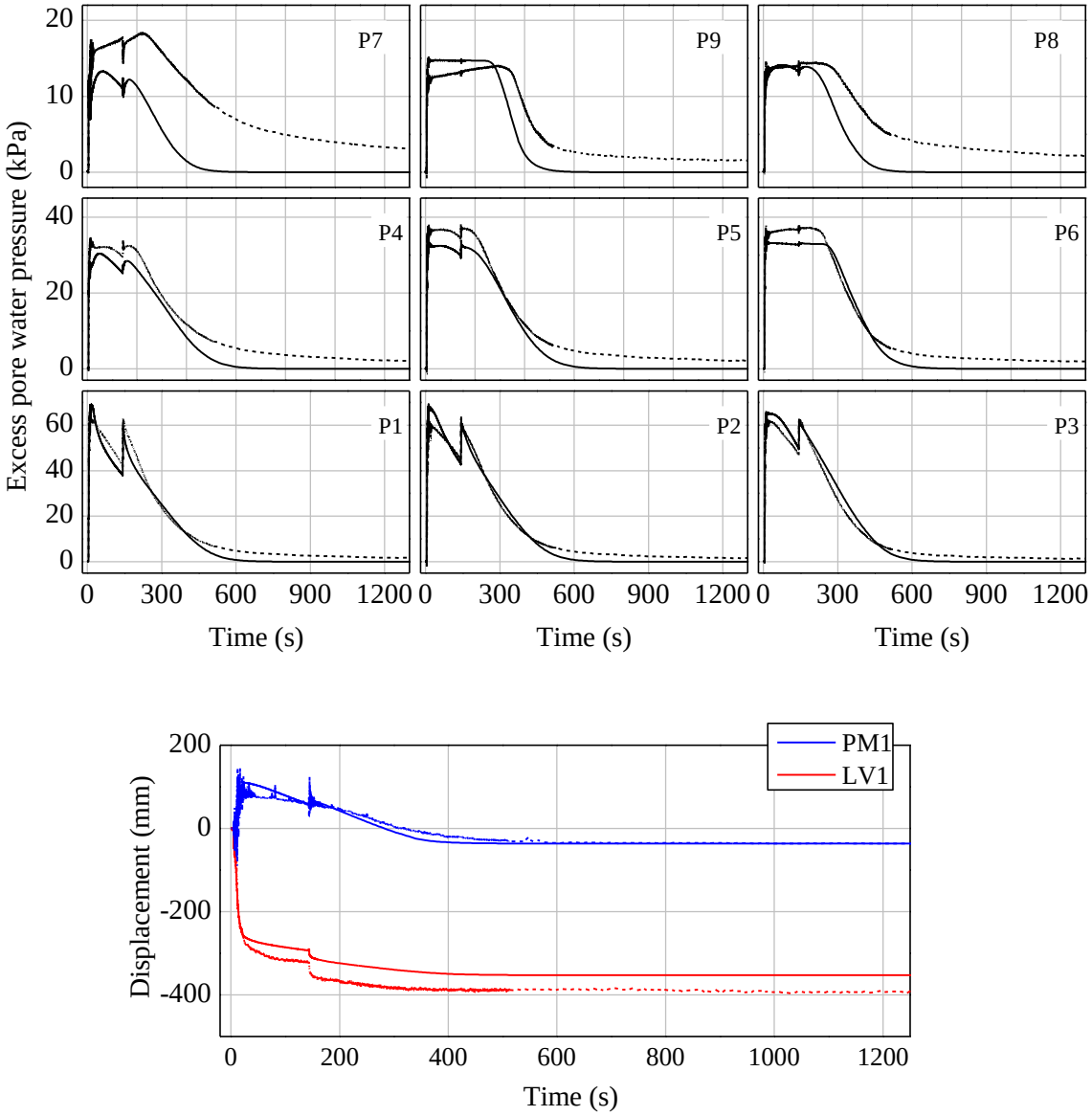

Figure 4.13. Time histories of excess pore water pressure and displacement for Model UG during and after shaking.

Table 4.2 Settlement of transducer in prototype scale.

PPTs at shallow depth	Residual EPWP, Δu_r (kPa)				Settlement of PPTs relative to water table (cm)			
	NHG1	NHG2	UG	CG	NHG1	NHG2	UG	CG
P10	3.10	1.71	2.53	3.20	31.62	17.45	25.76	32.62
P11	2.46	1.70	1.80	2.23	25.08	17.36	18.36	22.76
P12	1.39	0.52	1.32	0.93	14.19	5.25	13.50	9.53

4.4 Comparison between Model NHG1 and Model NGH2

As mentioned in Chapter 3, the strength of input motion in NHG2 was significantly less than that in other models. This creates difficultness in comparison between the results. Despite the application of low intensity input motion, the settlement induced during quite period (40-140 s) is larger than other tests, which has provided some fruitful information. Thus, it can be predicted that had the intensity of input motion had been the same as other models, the deformation of embankment would have been equal or larger than that in model NHG1. In order to verify this, numerical simulation of NHG2 was carried out by applying the input motion recorded during centrifuge test in NHG1.

Figure 4.14 compares the time histories of excess pore water pressure at different locations between Models NHG1 and NHG2. The Δu is larger from the early stage of shaking at P4 and P7 in Model NHG2 comapred to NHG1. The larger Δu at P7, which is just beneath the upper impermeable layer indicates that larger amount of pore water has

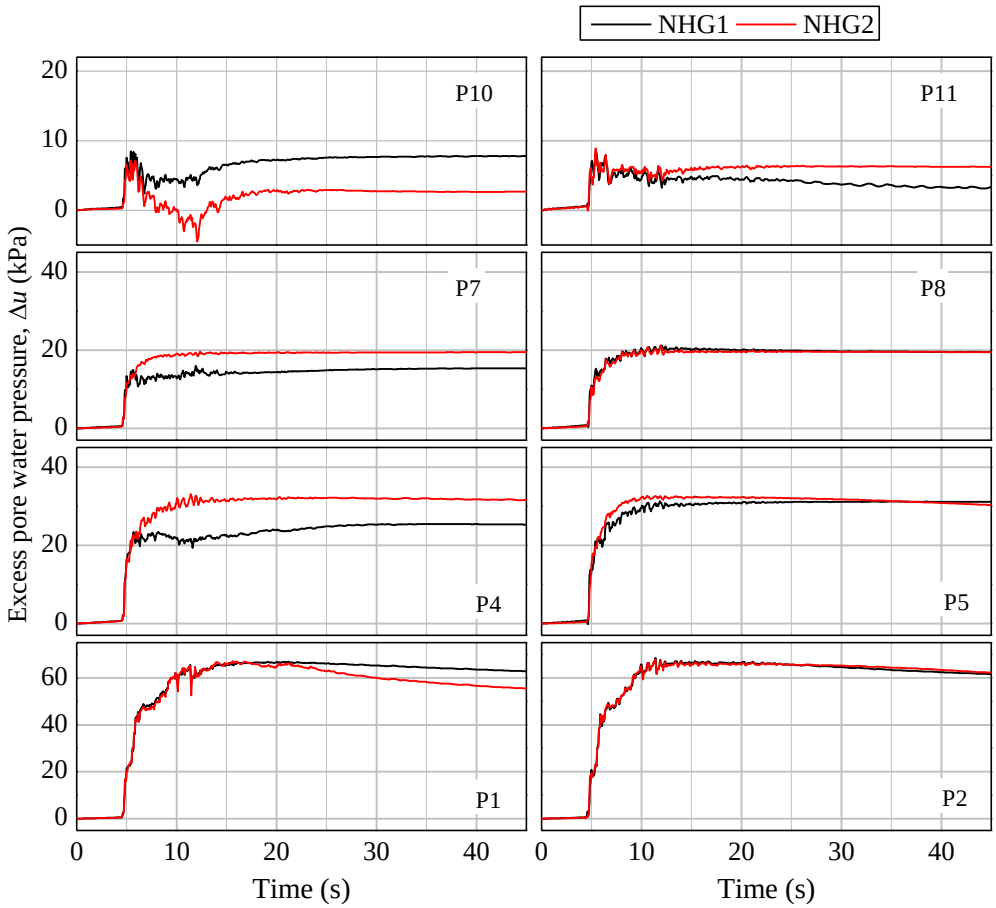

Figure 4.14. Comparison of time histories of excess pore water pressure at different location between NHG1 and NHG2.

started to accumulate from the early stage of shaking. This trapping of pore water beneath the upper impermeable layer causes the shear strain deformation, finally contributing to the larger deformation of embankments. Moreover, the Δu at P11, which is above the discontinuous region below the toe region, is larger after 12s of shaking in Model NHG2, allowing the soil beneath the toe region to reach the state of liquefaction. Thus, the liquefaction of soil under the toe region reduces the lateral restraint of foundation soil towards the free field region. In reality, this mechanism might have contributed a significant difference in the deformation of embankments, but in fact, the difference in the displacements of embankments in NHG2 is not very significant as shown in Fig. 4.15. At crest center, the settlement during mainshock is found to be more or less the same, while the settlements at crest edge and toe are slight larger in NHG2 than NHG1, causing a larger heave at the free field region. This might be due to the generation of negative excess pore water pressure at P10, above the upper impermeable layer (Fig. 4.14). The negative Δu is associated with the positive volume change due to the tendency of cyclic dilation, suppressing the deformation caused by lateral stretching of foundation soil towards the free field region to some extent. Figure 4.16 presents the time histories of horizontal displacement at toe. It can be seen that the lateral displacement is also larger in NHG2 than NHG, which is ultimately caused by the lateral stretching of foundation soil towards the free field.

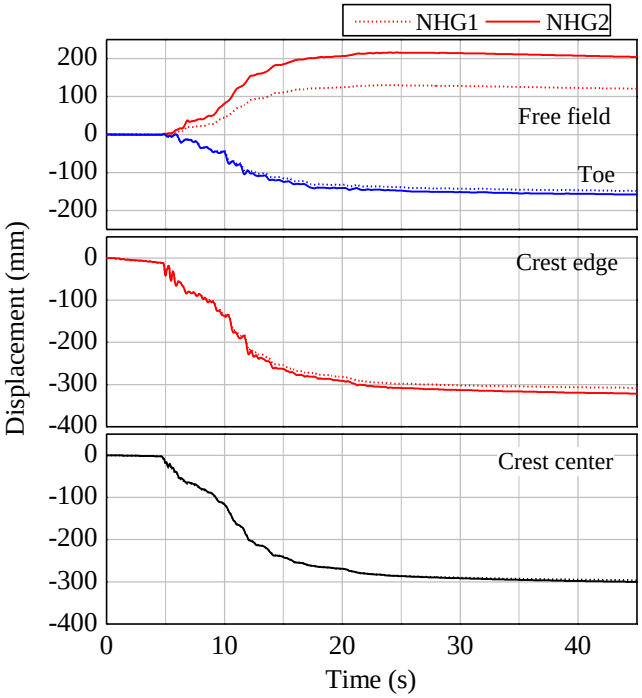

Figure 4.15. Comparison of time histories of displacement at different location between NHG1 and NHG2.

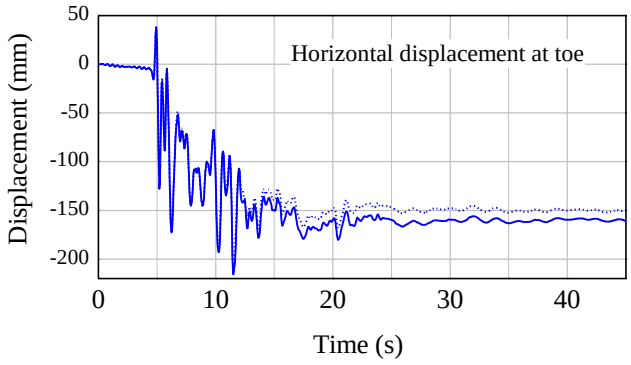

Figure 4.16. Comparison of time histories of horizontal displacement at toe between NHG1 and NHG2.

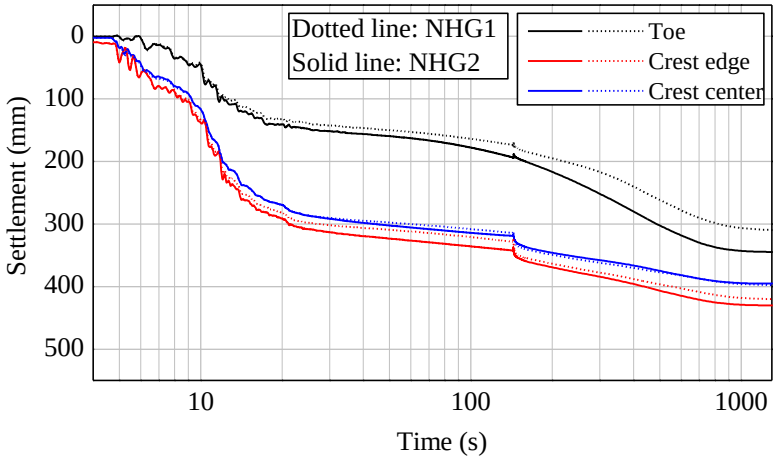

Figure 4.17. Comparison of time histories of settlement at different position of embankment between NHG1 and NHG2.

Also, shown in Fig. 4.17 is the time histories of settlement at different location of embankments during shaking and until the total dissipation of pore water. The dotted line represents the settlement observed in NHG1 and solid line in NHG2. At each location of embankment, the settlements are larger in NHG2 during mainshock and aftershock, and also after the shaking has stopped. This gives us an important insights on the impact of the location of discontinuous layer. The discontinuous impermeable layer at the shallow depth, with the discontinuous region lying below the toe of embankment on the liquefiable foundation soil layer, has more impact on the deformation of embankments.

4.5 Summary and conclusions

In this chapter, the computational simulations were presented for a series of centrifuge tests conducted to investigate the liquefaction mechanism of non-homogeneous soils deposits and to understand the liquefaction-induced deformation of embankments on non-

homogeneous liquefiable foundations. Confidence in ability of the numerical tool, for the realistic behavior on embankments and saturated soils during dynamic loading events, relies heavily on proper verification and validation. Overall, the presented investigations explored the capabilities and limitations of the computational formulations using a valuable series of centrifuge test results. Analyses have emulated the centrifuge model tests and can give important insight into both the behavior of embankments during mainshock and aftershock resting on different foundations. In all cases, computed excess pore water pressure responses were in good agreement with the recorded counterparts. Computed displacement responses were also realistic in pattern and amplitude. However, significant discrepancies existed between the computed and recorded acceleration responses. The computed one showed a large amount of amplification at the shallow depth. Overall, the good correlation between the experimental and numerical results validated the numerical model used. The implemented constitutive model was also verified and validated using the experimental data. It was also found that the deformation of embankment caused severe damage to some extent when the discontinuous region of impermeable layer at the shallow depth lay below the embankment toe.

Chapter 5

Effects of aftershock on deformation of embankments

Determination of earthquake-induced ground displacements is an integral part of seismic performance based design for embankments and slopes. The deformation observed during mainshock as well as aftershock is of major concern. After the confidence in ability of the numerical tool is achieved by verification and validation of the formulation and resulting implementation, the numerical tool is then applied to investigate the seismic performance of embankments under different ground motions where the aftershocks occur before the major dissipation of excess pore water pressure. As such a finite element analysis is used to emulate the deformation of embankments during mainshock and various aftershocks, and possibly capture pore water redistribution. This chapter first compares the liquefaction-induced behavior for different foundations during mainshock and later the comparison is made for aftershocks.

5.1 Sequential ground motions

After the numerical model was validated, it becomes prudent to predict the liquefaction-induced deformation of embankments under different other ground motions. It is noted that the ground motions applied in the previous chapters are the one obtained from the shaking table, where all the realistic characteristics, intensity, and frequency of ground motion could not be replicated. To this end, ground motions recorded during 1994 Northridge earthquakes are applied. The gap between mainshock and aftershock is chosen to be 100 s. The gap between mainshock and aftershock varies from short time period (say less than a minute to several minutes) and longer time period (say a day to several days). The gap of short time period indicates the occurrence of aftershock before the major dissipation of excess pore water pressure while the gap of longer time period indicates the occurrence of aftershock after total dissipation of pore water. The gap of 100 s, in this chapter represents the occurrence of mainshock before the major dissipation of excess pore water pressure. The aftershock before the major dissipation of excess pore water pressure re-liquefies the soil again, leading to the accumulation of larger deformations. The finite element mesh for embankment-foundation system and the model parameters as shown in Chapter 4 are considered. Three ground motions are selected which consists of same mainshock but

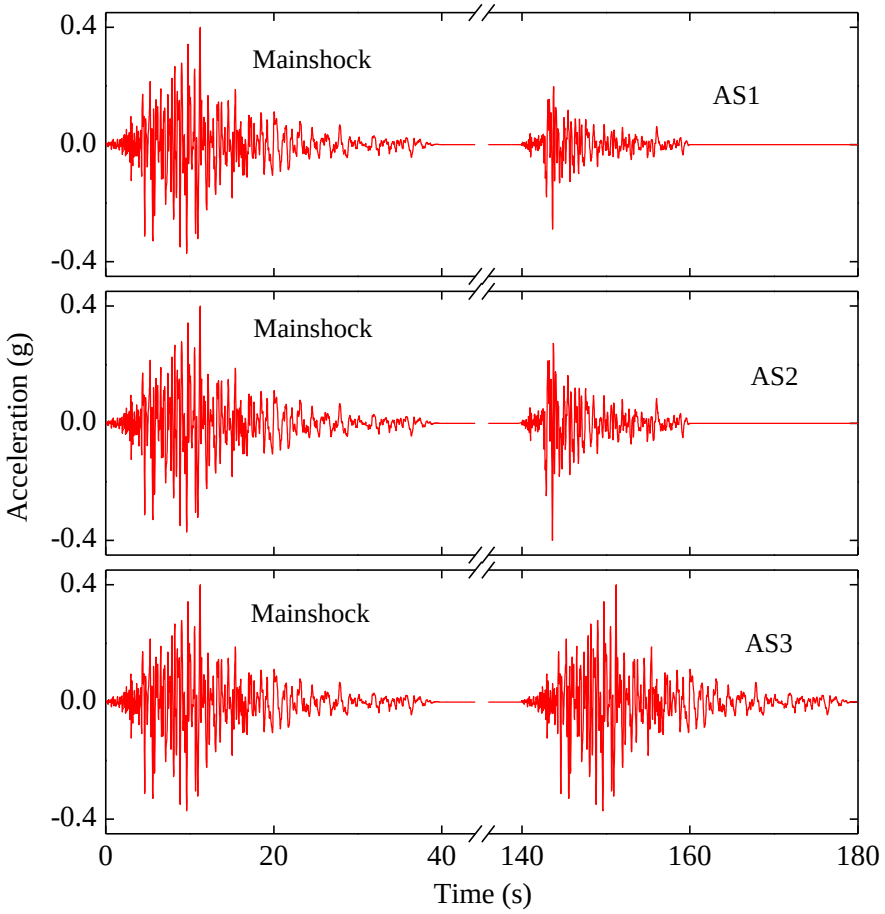

Figure 5.1. Acceleration time histories of applied ground motions.

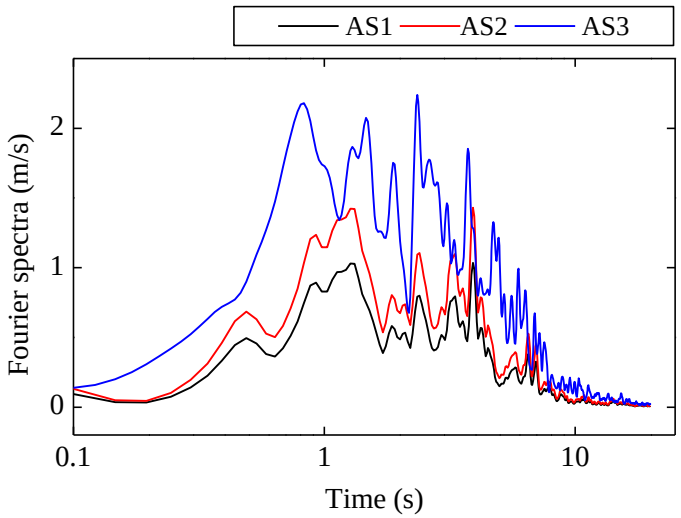

Figure 5.2. Fourier spectra of aftershocks of applied ground motions.

Table 5.1 Ground motion characteristics.

Ground motions	Peak acceleration of input motion (g)		Duration of input motion	
	Mainshock	Aftershock	Mainshock	Aftershock
GM1	0.4	0.2	40 s	20 s
GM2		0.4		20 s
GM3		0.4		40 s

different aftershock (Figure 5.1). Figure 5.2 and Table 5.1 show the Fourier spectra and the properties of ground motions, respectively.

5.2 Computational results during mainshock

During the computational simulations, excess pore water pressures were monitored for the locations, indicated by prefix "P*" as shown in Fig. 4.11. These locations were selected to represent different stress states: (1) under the toe of the embankment where static shear stress exists; and (2) under the center of embankment where large effective stress exists. The crest settlements were monitored at LV1 and LV2 locations and displacement at free field was sampled at PM1 location. At these key locations, computed excess pore water pressures, settlement, and strain responses will be compared for different foundation cases.

5.2.1 Excess pore water pressure responses

The time histories of excess pore water pressure ratios at different depths below the embankment center, embankment toe, and free field region during the mainshock are shown in Figs 5.3-5.5, respectively. It can be seen that the r_u values are largest at the free field and toe region and lowest below the embankment throughout the shaking. The generation of pore water during the initial stage of shaking, i.e, until 10 s is nearly the same for all the foundations. At all depths, excess pore water pressure first gradually increases until 10 sec and rapidly increases at 12 s which might be due to application of high intensity acceleration and also due to the dissipation of pore water from the underlying soil.

At the depth of 7.15 m, i.e., at P1, P2, and P3, the r_u values are found to be nearly the same except for model UG, where the value is lower during the entire shaking. In Model NHG2 and CG, the presence of upper silty layer at the depth of 1.2 m causes the trapping of pore water, ultimately increasing the pore water pressure beneath the silty layer. As a result, r_u values are larger at P4 in Models NHG2 and CG. On the other hand, the presence of the relatively impermeable layer restricts the transmission of pore water through it. Thus, the excess pore water pressure above the silty layer in Models NHG2 and CG is completely due to the generation of pore water from the soil above silty layer rather than the

combination of pore water dissipated from the underlying layers, which leads to the lower ru values. However in Models NHG1 and UG, the responses of ru values look similar. However, a remarkable difference in EPWP ratio was observed at a shallow depth of 0.75 m after 12 s. For instance, at P7 which is below the embankment, ru value raised from -0.5 to 0.3 between 12-15 s in non-homogeneous foundation grounds. However, ru value raised from -0.2 to 0.2 between 12-15 s at P7 in uniform foundation ground. During dynamic excitation, sand below the embankment showed a tendency for cyclic dilation in the form of lower ru values in uniform foundation ground.

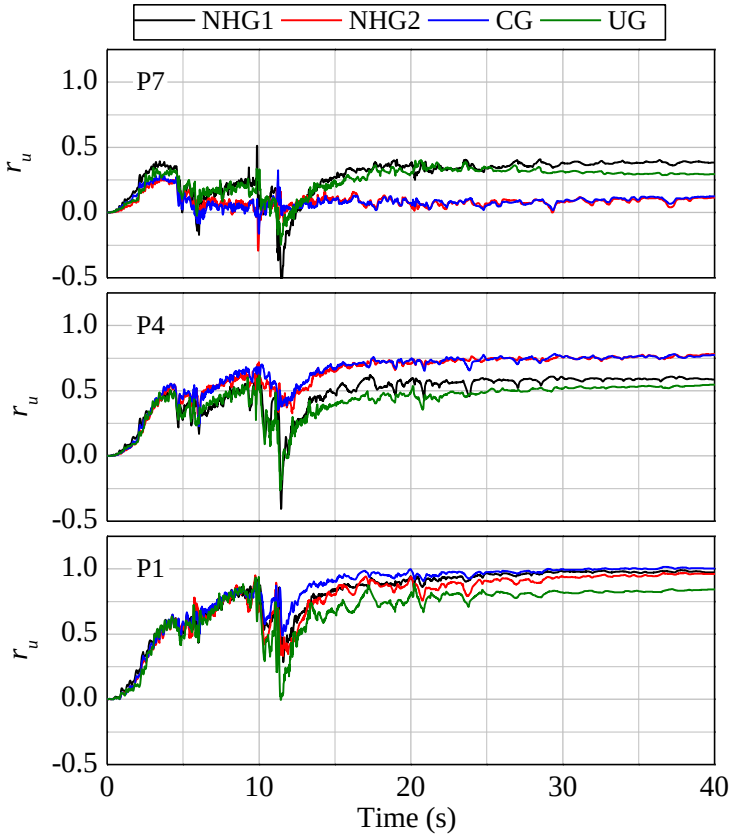

Figure 5.3. Time histories of excess pore water pressure ratio at different depths below the embankment center during mainshock.

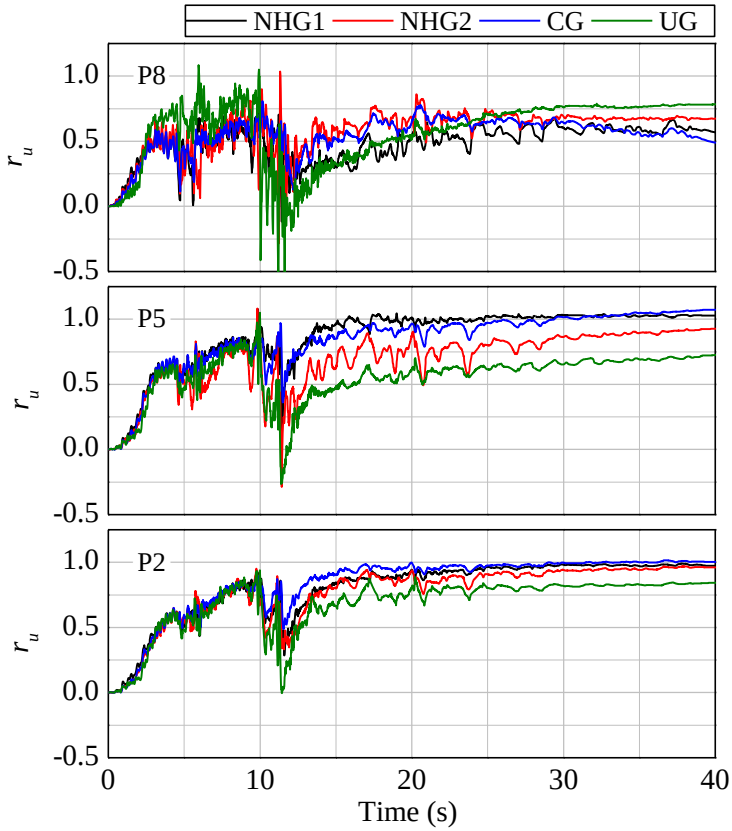

Figure 5.4. Time histories of excess pore water pressure ratio at different depths below the embankment toe during mainshock.

5.2.2 Displacement responses

The most governing factor which describes the performance of embankment during earthquakes is the movement of the embankment and its settlement. The prediction of earthquake-induced deformations of the soil structures is the major factor to design seismically safe structures and implement the appropriate mitigation measures. The final deformations obtained by the deformed finite element mesh after completion of excess pore water dissipation for non-homogeneous and uniform foundation grounds are shown in Fig. 5.6, where the scale factor is 2.5. The time histories of displacement at the crest, center, crest edge, and free field is shown in Fig. 5.7. The embankment crest settled a total of 0.35 m in non-homogeneous and continuous layered ground and about 0.25 m in uniform ground. The large settlements at the central part caused the heaving of about 0.2 m and 0.1 m at the free field region (3 m away from the left boundary) in non-homogeneous and uniform foundation grounds, respectively.

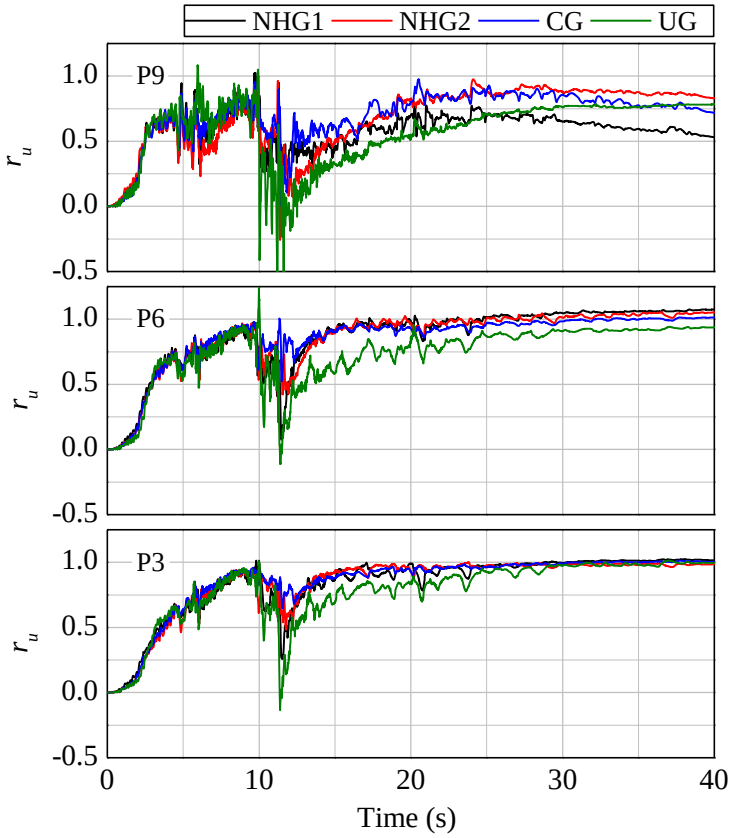

Figure 5.5. Time histories of excess pore water pressure ratio at different depths in the free field region during mainshock.

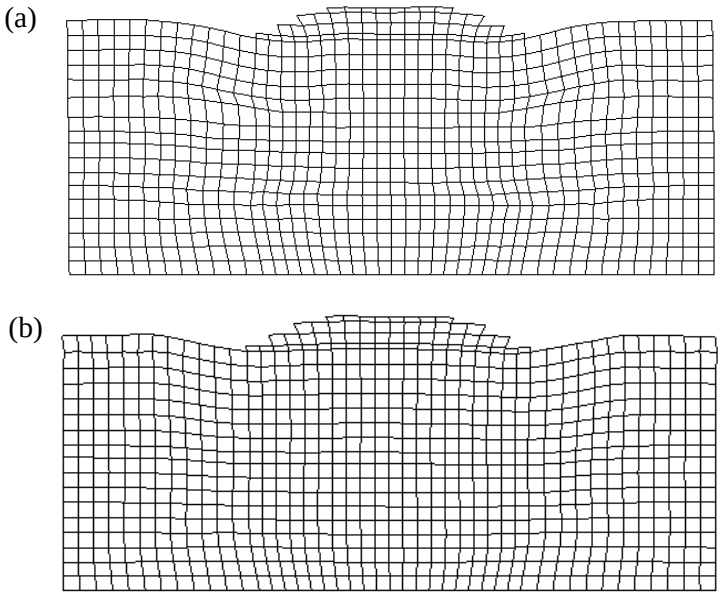

Figure 5.6. Deformed finite element mesh at t = 40 s: (a) Model NHG and (b) Model UG.

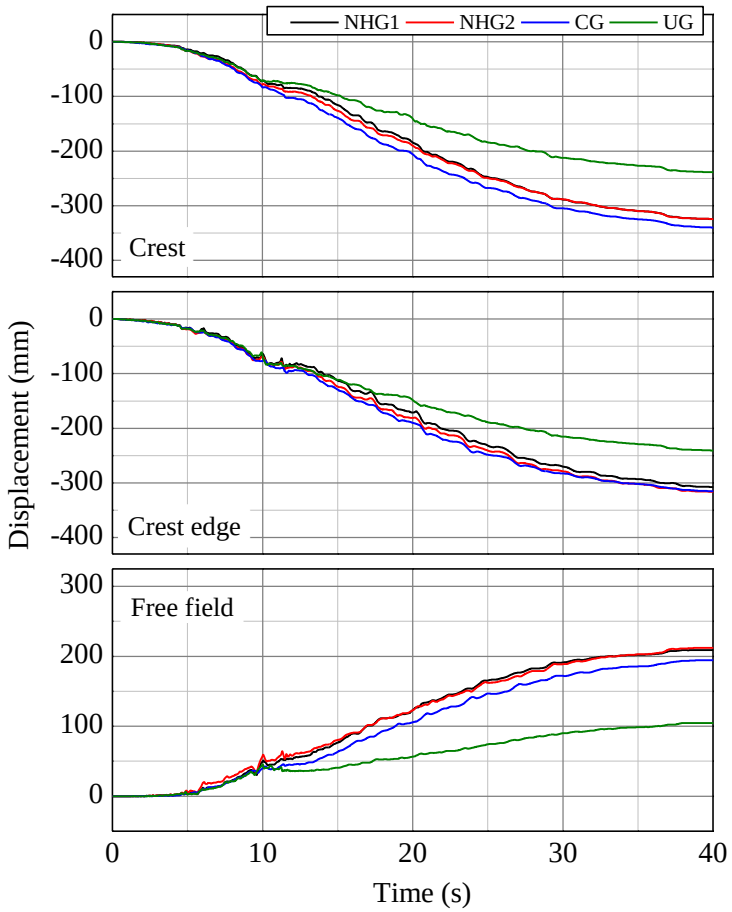

Figure 5.7. Displacement time histories at the crest center, crest edge and free field during mainshock.

respectively. Lateral deformation in the foundation soil below the embankment was found to attain its maximum near the embankment toe. The accumulation of lateral tensile strain might have caused the lateral deformation of foundation ground.

The r_u values at different depths under the embankment toe and free field region are found to be significantly smaller for Model UG. For instance, under the toe region at P5 and P8, and in the free field region at P6 and P9, the r_u values could not reach the value equal to 1 during shaking. However, the r_u values under the toe region and free field nearly approach to 1, which signified the soil has completely liquefied at the free field region, reflecting the associated loss of soil stiffness and strength under the toe region and free field region in non-homogeneous and continuous layered ground. However, the lower r_u values at free field region of uniform ground suggested that soil has not yet completely liquefied. The lower r_u values at the free field region manifested the associated decreased tendency for lateral deformation in uniform foundation ground. The liquefaction of soil in the free field and toe region might have reduced the confinement of the soil below the embankment and might have allowed the lateral stretching of the soil below the embankment towards the free field.

Under nearly undrained condition, this tensile strain mechanism suppressed the increase of excess pore water pressure in the soil below the embankment.

5.2.3 Horizontal and vertical strain responses

Figure 5.8 displays the horizontal and vertical strain isochrones in the centerline of embankment. The compressive strain is represented by positive value. The horizontal and vertical strains look similar during the early seconds of shaking, i.e., at 10 s for all the models. Nonetheless, the trapping of pore water at the lower silty sand layer in Model NHG1 and at the upper silty layer in Model NHG2 caused the larger horizontal tensile strain after 10 s in Model NHG1. Moreover, the horizontal tensile strain is also larger at shallow depths, i.e., at the discontinuity region after 10 s in Model NHG. However, the horizontal tensile strain remains nearly the same for different time at shallow depths in Model UG. The pore water is forced to drain through the permeable region below the embankment at the upper silty layer due to the relatively less permeable silty sand layers in the free field zone. Dissipation of pore water is concentrated at the discontinuity region below the center of embankment, as the upper silty sand layers restricts the vertical transmission. This might have attributed to the large amount of deformation during 10-30 s. This might have increased the sand compaction and also the migration of underlying foundation soil toward the free field was noted. This causes the vertical settlement of about 210 mm between 10-30 s in non-homogenous foundation ground and that of about 110 mm in uniform foundation ground. This was the remarkable difference observed in the displacement during first shaking. The settlement occurs along with the initiation of earthquake loading and generation of EPWP, concluding that the drainage of water from soil mass takes place even during the shaking (Maharjan & Takahashi 2013a). This caused the larger vertical settlement and the ground surface was observed to heave upward by 0.2 m, whereas the total heave was 0.1 m in uniform ground foundation.

5.2.4 Shear strain responses

Figure 5.9 shows the contour of shear strain at 40 s for all the model foundation. The pore water was accumulated beneath the silty sand layer as the silty sand layer acted as the barrier for vertical dissipation of excess pore water pressure. As a result, formation of dilation zone beneath the low permeability silty layer might occur, isolating the silty layer and the lateral deformation was observed at the bottom of the silty sand layer. Shear strain amplitudes were larger at the bottom of the silty sand layer as seen in Models NHG1, NHG2, and CG. The larger r_u values at the toe region due to combine effect of pore water generation due to shaking and dissipation through the underlying soil layer, increases the shear strain at the toe region in non-homogeneous foundation. This might have further contributed to the lateral stretching of foundation soil towards the free field. Moreover, the shear strain below the embankment was larger in non-homogeneous foundation grounds.

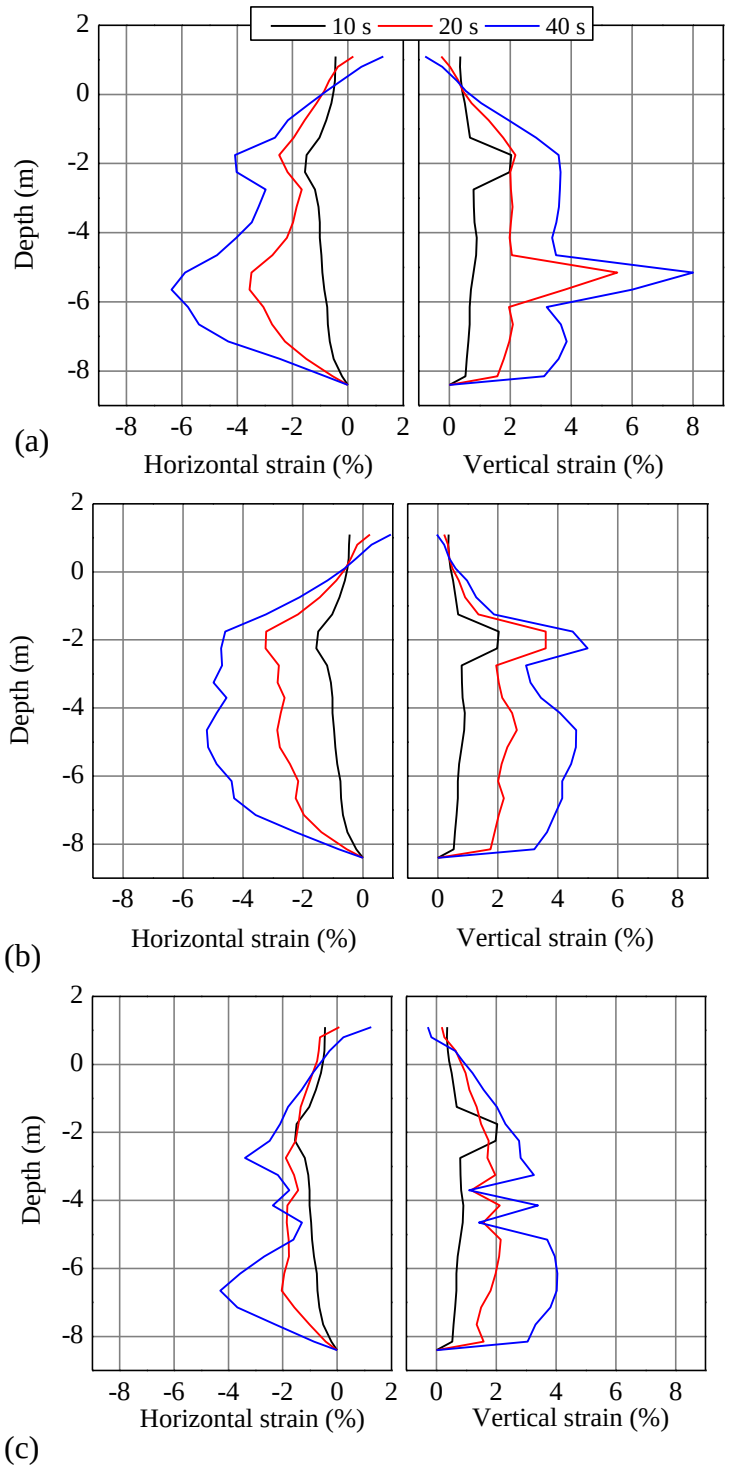

Figure 5.8. Horizontal and vertical isochrones at the centerline: (a) Model NHG, (b) Model NHG2, and (c) Model UG.

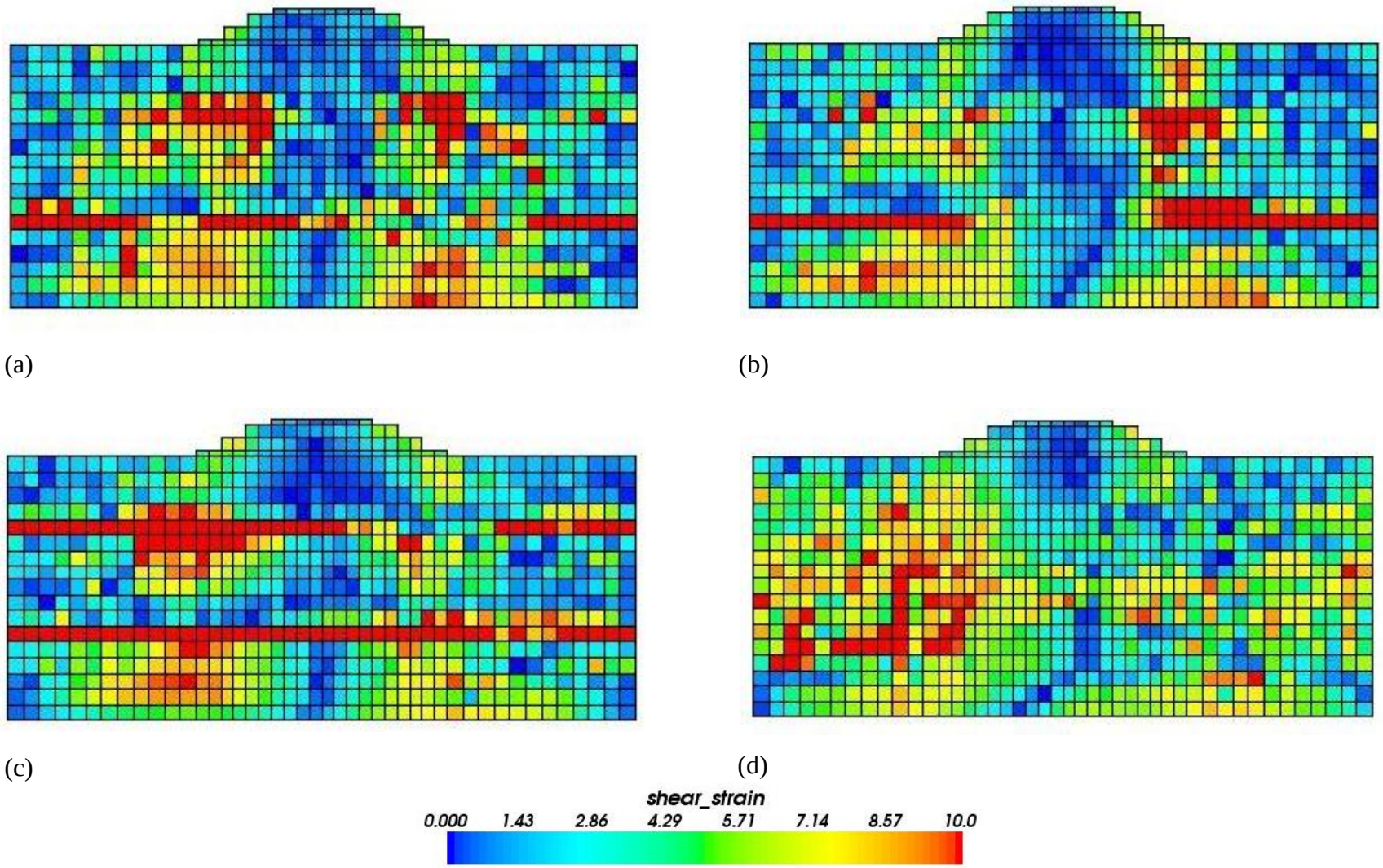

Figure 5.9. Shear strain contours at 40 s: (a) NHG1, (b) NHG2, (c) CG, and (d) UG.

5.3 Responses during aftershocks

5.3.1 Excess pore water pressure responses

Figures 5.10 and 5.11 show the time histories of excess pore water pressure ratio at the depth of 3.65 m and 0.75 m during the input motions 1 and 3. During the application of small aftershock, AS1 the excess pore water pressure does not change, rather maintains nearly the same value as that observed before the mainshock at the depth of 3.65 m. However, during the application of aftershock of higher intensity, AS3 the r_u values decreases initially but a significant rise in excess pore water pressure ratio is observed at 150 s in all the model foundation grounds. Nonetheless, the increase in excess pore water pressure is found to be very smaller in Model UG as shown in Fig 5.11(a). Moreover at shallow depth, i.e., at 0.75 m the r_u values are found to be significantly larger at P8 and P9 in Model UG as soon as the mainshock stops; before the application of aftershocks AS1 and AS3 (Fig. 5.10(b) and 5.11(b)). This is due to the dissipation of pore water from the underlying foundation. Model UG, being a uniform ground consisting only of Toyoura sand of higher permeability is accompanied by progressive dissipation of excess pore water pressure within shorter period of time. This causes the excess pore water pressure to be larger near the toe and free field region at shallow depth as soon as the mainshock stops. Moreover, r_u rapidly decreased at P8 and P9 after mainshock shaking, as they lay above the upper silty sand layer where the dissipation of pore water was not allowed. However, no changes in excess pore water pressure is observed during the application of small and big aftershock at P8 and P9 in Model UG. While the excess pore water pressure increases in all the model foundation except Model UG at P8 and P9 irrespective of the intensity of input motions applied.

5.3.2 Displacement responses

Figure 5.12 and 5.13 present the time histories of displacement at embankment crest, toe and free field region. Figure 5.14 compares the total amount of crest settlement in each model foundation during AS1, AS2, and AS3. The increase in excess pore water pressure due to the aftershocks re-liquefy the soil under the toe and free field region. Crest settlement during aftershocks was found to larger in non-homogeneous foundations compared to uniform foundation. For instance, an additional crest settlement of 75 mm and 110 mm was observed during AS1 in Model UG and NHG2, respectively. Moreover, the crest settlement in non-homogeneous foundation was more pronounced compared to Model UG during high intensity aftershock, AS3. The crest settled about 290 mm in Model NHG2 due to AS3, while the settlement was about 175 mm in Model UG. Also, the dissipation of pore water was concentrated at the discontinuous region in non-homogeneous foundation, making the dissipation time longer. The dissipation of EPWP and displacement continued until 1000 s in non-homogeneous foundation and completely ceased at 400 s in uniform foundation.

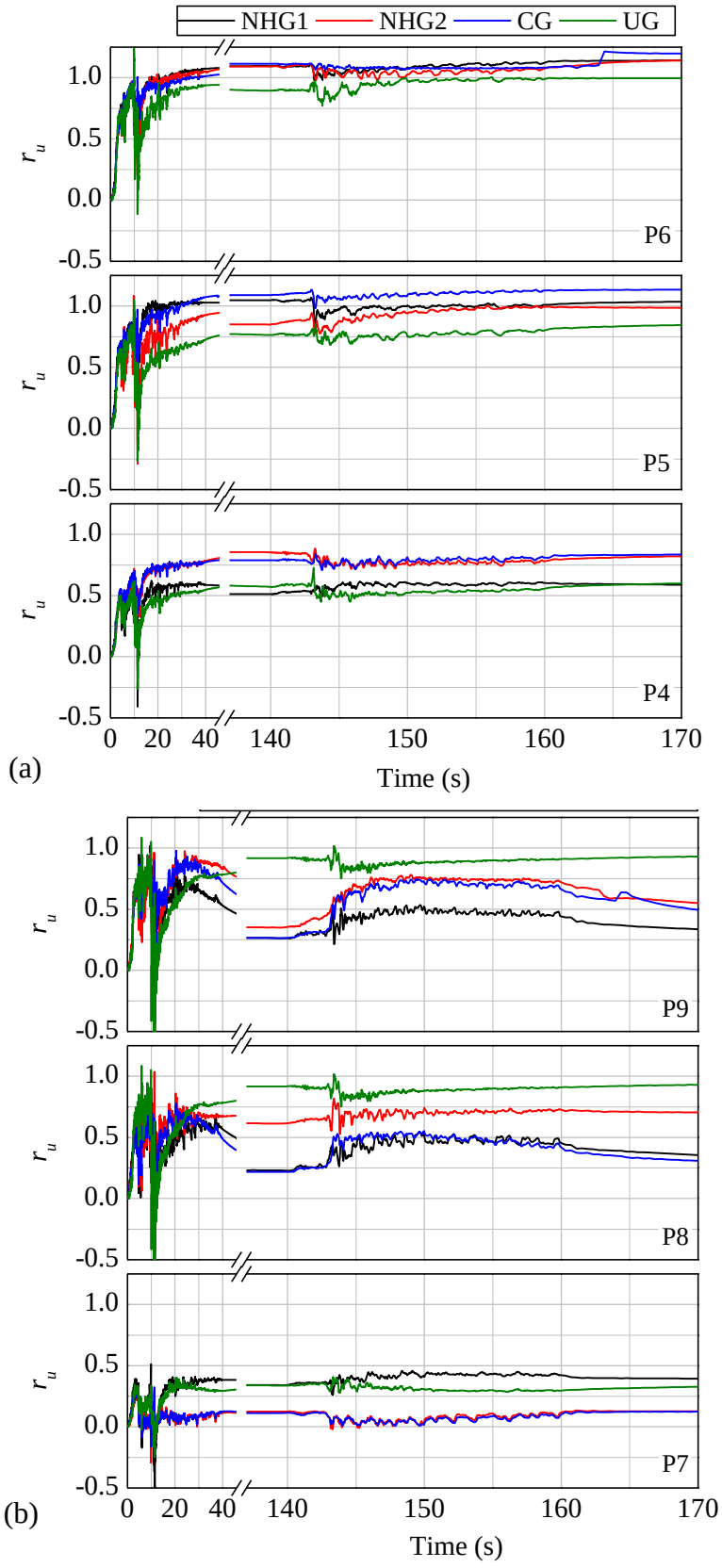

Figure 5.10. Time histories of excess pore water pressure ratio during input ground motion 1: (a) At depth of 3.65 m and (b) At depth of 0.75 m.

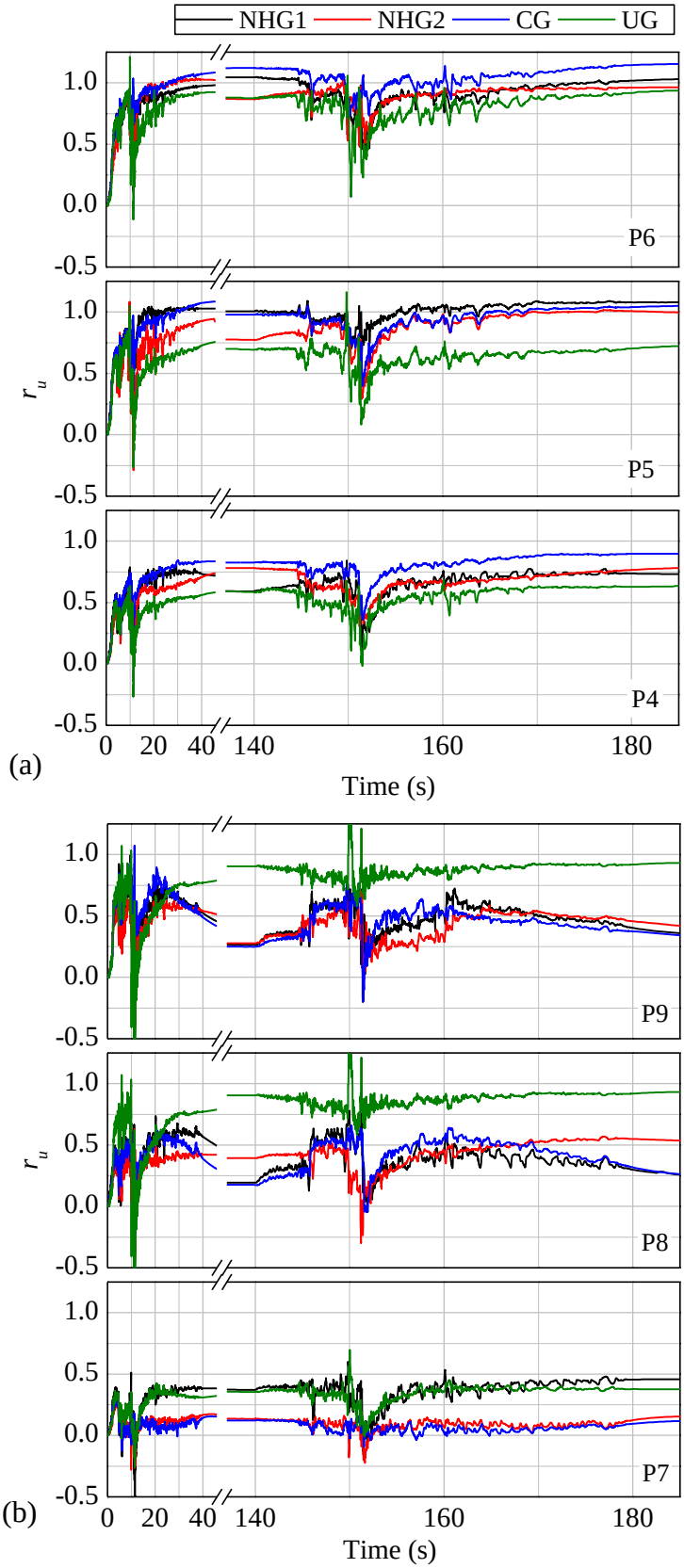

Figure 5.11. Time histories of excess pore water pressure ratio during input ground motion 3: (a) At depth of 3.65 m and (b) At depth of 0.75 m.

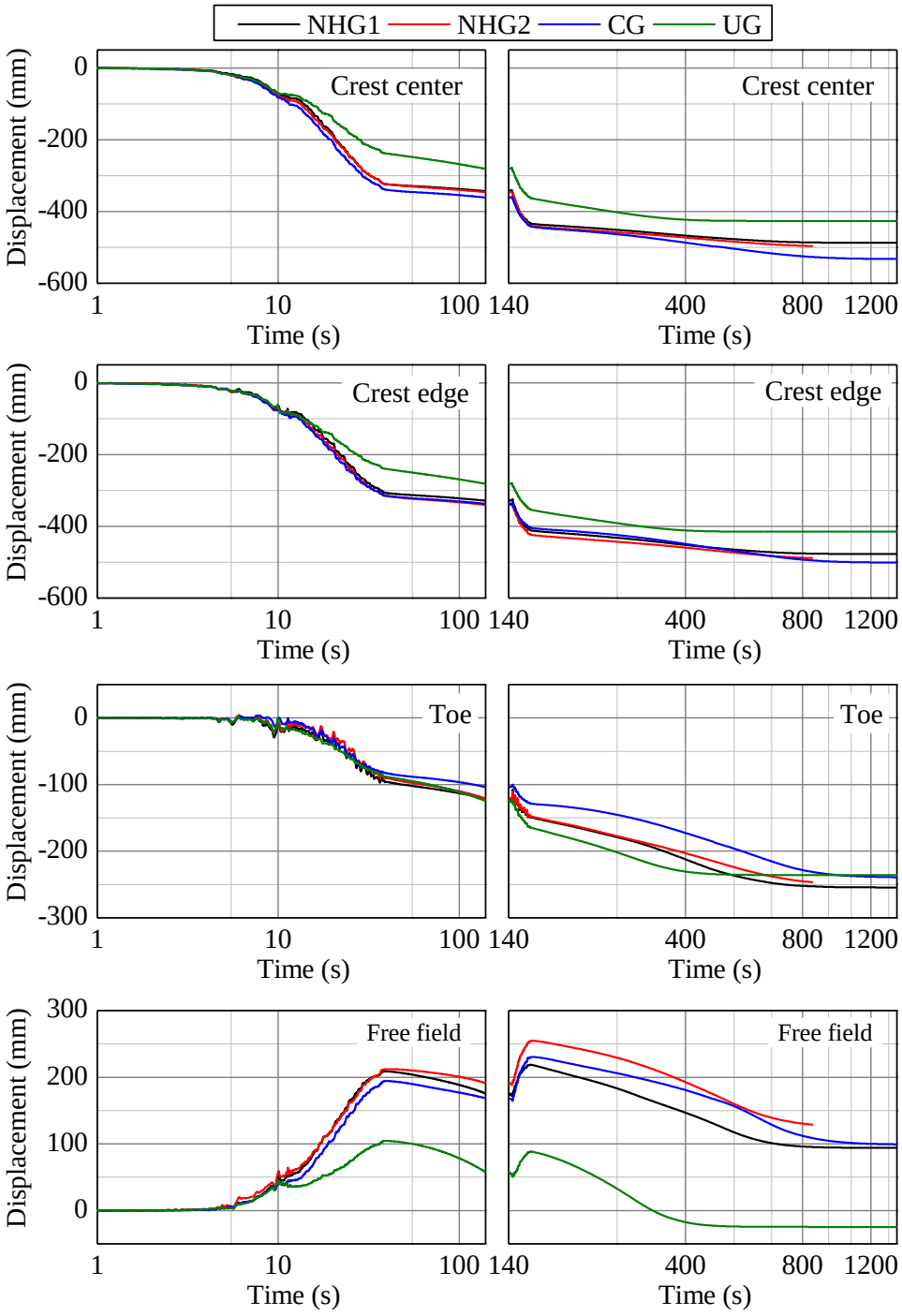

Figure 5.12. Displacement time histories during input ground motion 1.

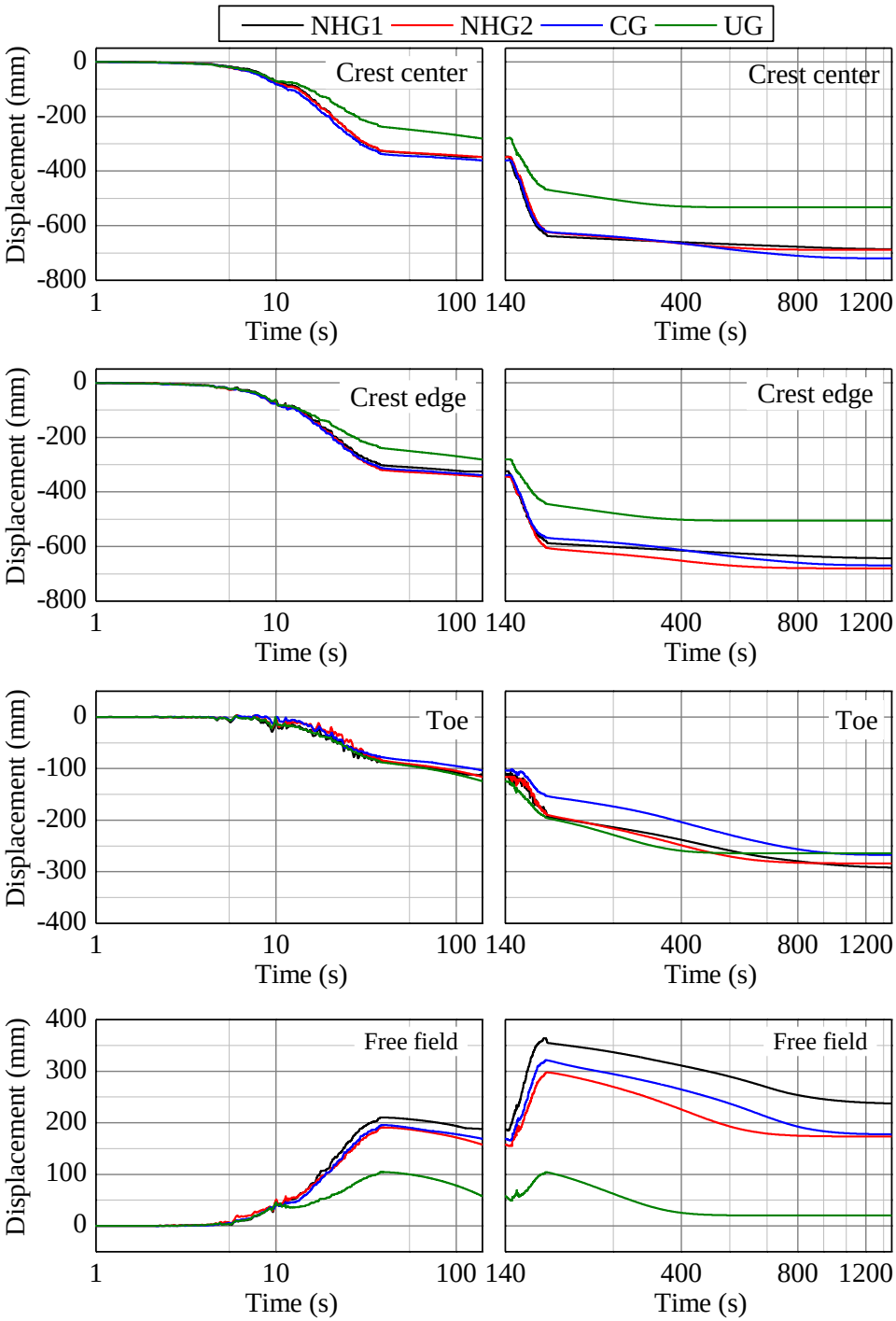

Figure 5.13. Displacement time histories during input ground motion 3.

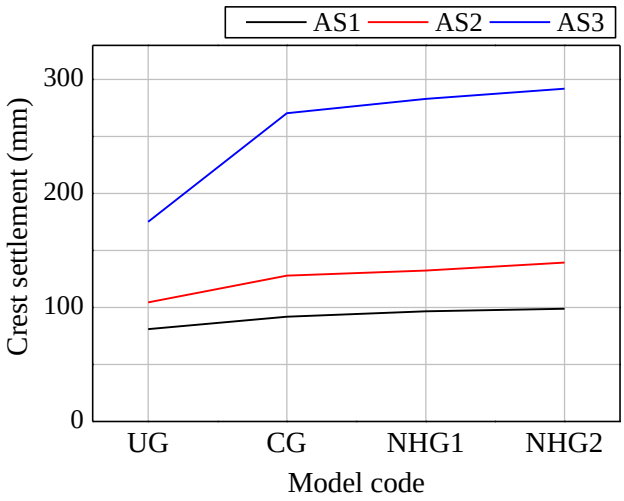

Figure 5.14. Crest settlement during different aftershocks.

The dissipation of excess pore water pressure became the dominant mechanism after seismic loading as the pore pressure generation ceased the supply of new mass of water, which is manifested as settlement. During the dissipation of pore water through the discontinuity region below the embankment to the ground surface, the consolidation of liquefied sand continued causing additional settlement. The amount of crest settlement due to the dissipation of pore water was about 85 mm in non-homogeneous and about 55 mm in uniform ground. Similarly the amount of heave and settlement at toe were also larger in non-homogeneous ground.

5.3.3 Strain responses

Figure 5.15 presents the isochrones of horizontal and vertical strain during aftershocks AS2 and AS3 in Model NHG1. The compressive strain is represented by positive value. Both horizontal and vertical strain increases with time at all the depths. The trapping of pore water at the lower silty sand layer in Model NHG1 caused the larger horizontal tensile strain as shown in Fig. 5.15. This increases the shear stain at the bottom of silty sand layer as shown in Fig. 5.16 (a). The pore water was accumulated beneath the silty sand layer as the silty sand layer acted as the barrier for vertical dissipation of excess pore water pressure. As a result, formation of dilation zone beneath the low permeability silty layer might occur, isolating the silty layer and shear strain gets accumulated. As a result, the lateral deformation was observed at the bottom of the silty sand layer. However, the horizontal and vertical strain was significantly larger for aftershock AS3, compared to AS1. Similarly, the horizontal strain and shear strain are extensively larger at shallow depths. i.e., at the discontinuous region for AS3 (Fig. 5.15 and 5.16).

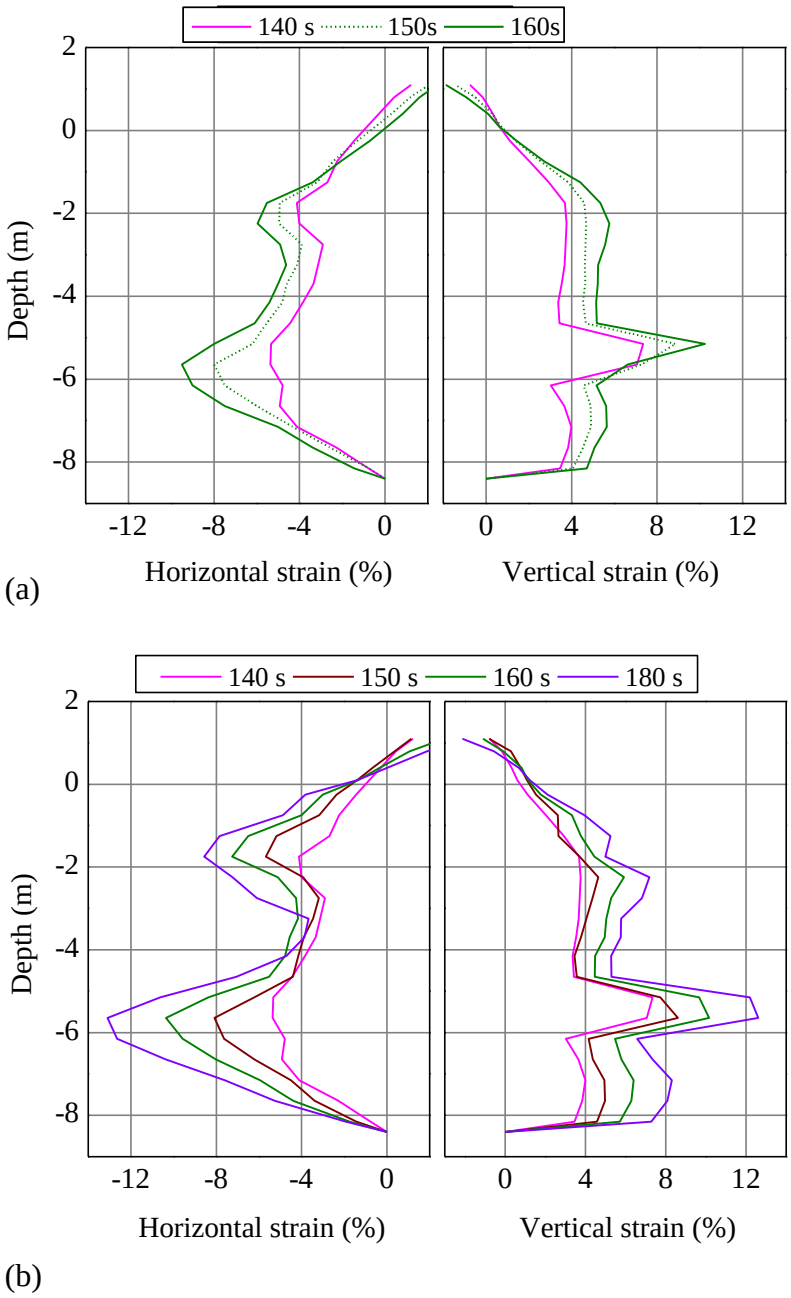

Figure 5.15. Horizontal and vertical strain isochrones: (a) During AS2 and (b) AS3.

5.4 Primary factors of settlement

The primary factors that contributes to the crest settlement of embankment are: (i) shear deformation of embankment, (ii) lateral deformation of foundation layer, and (iii) contractive volume change of soil below embankment, assuming the volume change of embankment due to shaking to be negligible, as no slope failure of the embankments were detected, as depicted in Fig. 5.17 The volume change of embankment is derived from the

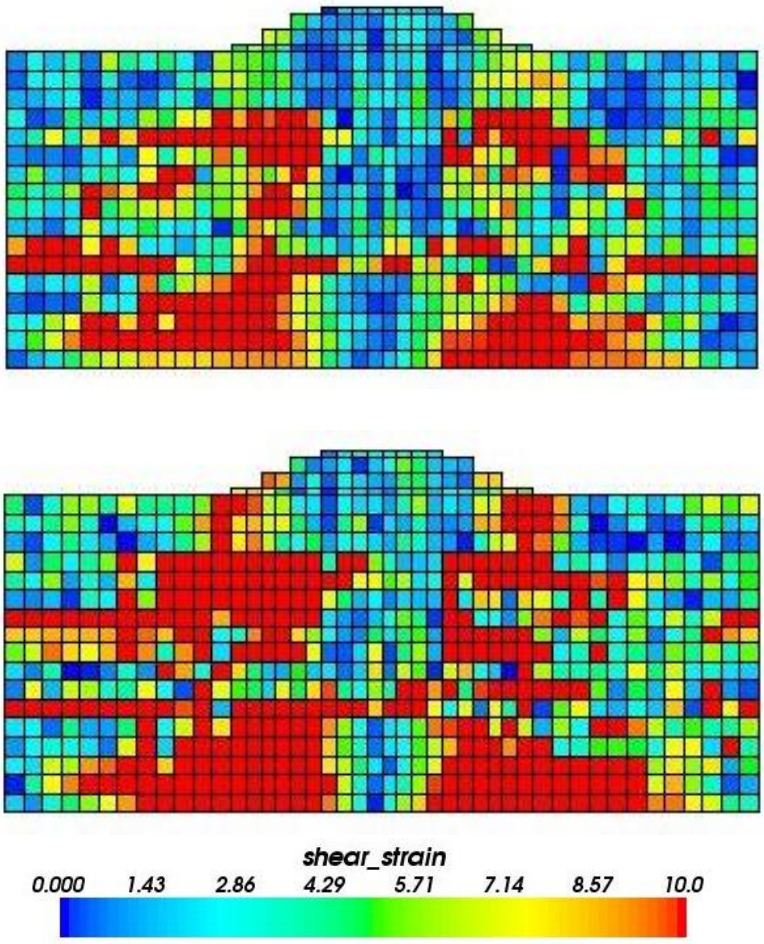

Figure 5.16. Shear strain contour in Model NHG1: (a) At the end of aftershock AS1 and (b) At the end of aftershock AS3.

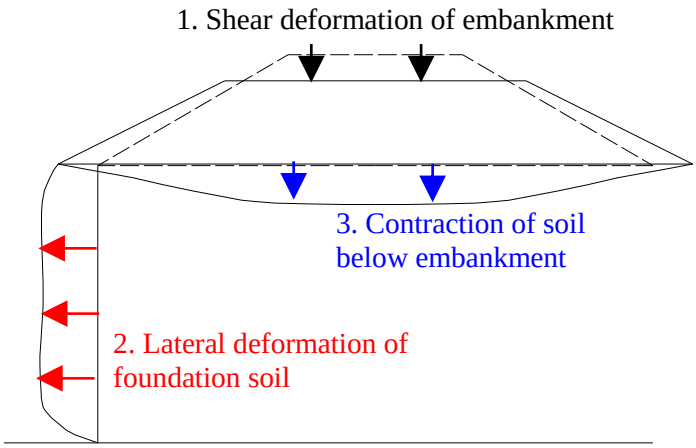

Figure 5.17. Primary factors of crest settlement.

vertical volumetric strain of embankment, which is found to be negligible. The shear deformation of embankment is expressed as the product of horizontal strain of embankment base and its height, assuming the vertical strain at the top of embankment becomes equal to the horizontal strain at the embankment base. The crest settlement due to lateral deformation of foundation soil is expressed as the area of lateral deformation divided by the width of embankment base and that due to volume change of foundation soil is expressed as the change in area of foundation below the embankment divided by the width of embankment base.

The amount of crest settlement caused by each factors for all the model cases during the application of input motions GM1 and GM3, is presented in Figs. 5.18 and 5.19, respectively. For each time period, the settlement caused by lateral flow of foundation soil is dominant and larger in all the cases. However, at the end of mainshock, i.e., at 40 s, the settlement due to lateral spreading is larger in Model CG, compared to Models NHG1 and NHG2. Nevertheless, the settlement due to lateral spreading increases and is found to be larger in non-homogeneous foundation, i.e., Models NHG1 and NHG2 at the end of aftershocks AS1 (at 140 s of GM1) and AS3 (at 160s of GM3), as shown in Figs. 5.18 and

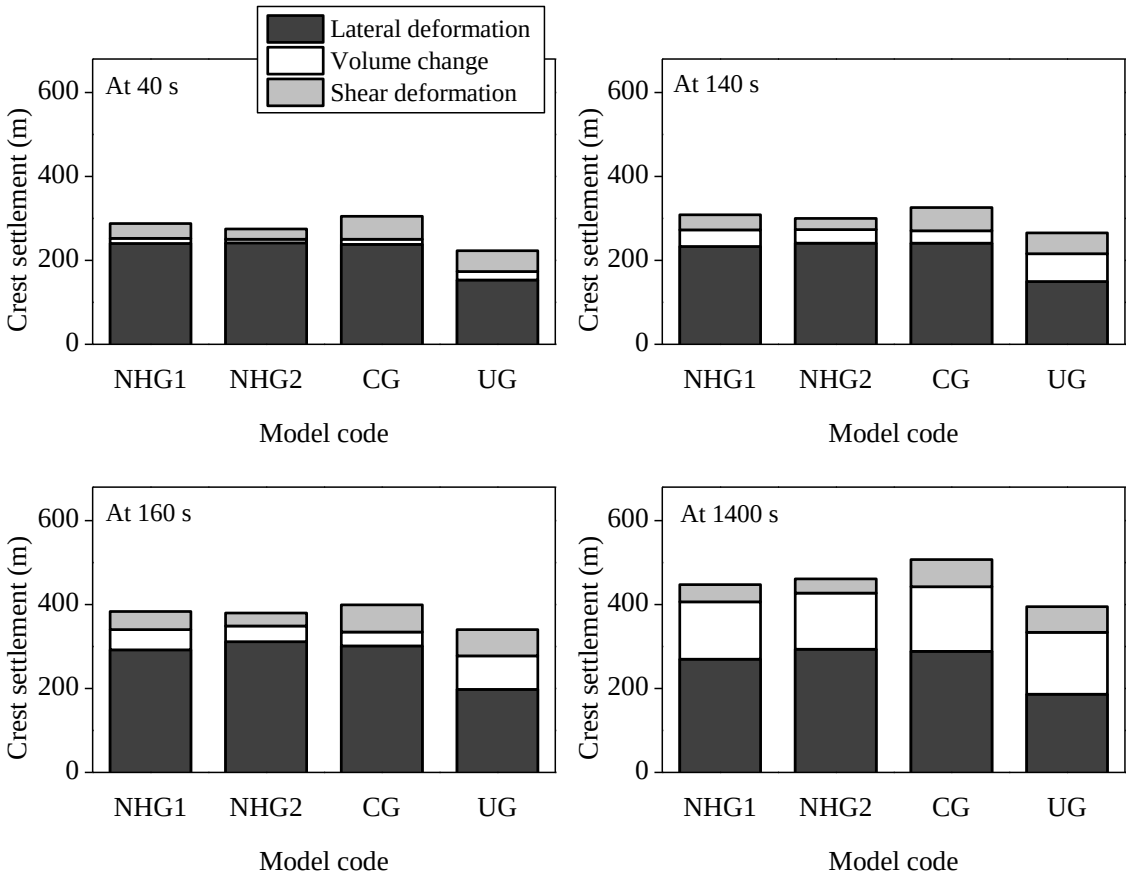

Figure 5.18. Primary factors of crest settlement at different time period during input motion 1 (GM1).

5.19. The crest settlement due to volume contraction of soil below the embankment is found to be significantly smaller during the mainshock in all the models. However, the settlement due to volume compression is somewhat larger to some extent in Model UG during aftershocks, which might be due to the rapid dissipation of pore water, leading to the contraction of the soil skeleton.

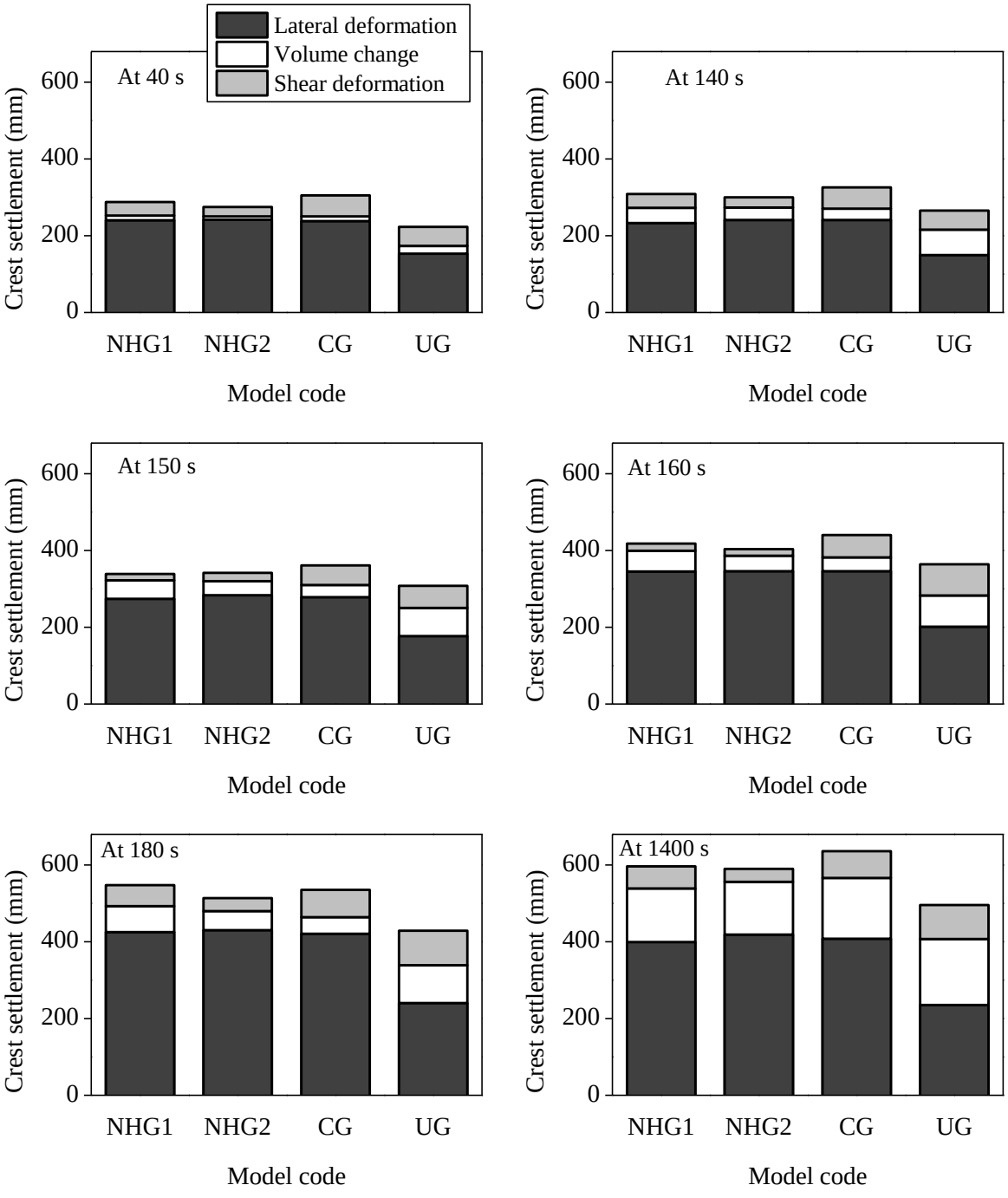

Figure 5.19. Primary factors of crest settlement at different time period during input motion 3 (GM3).

5.5 Uniform ground foundation with silty sand layer

Previous studies has investigated the soils prone to liquefaction and case histories indicated that silty soils containing non-plastic silts and gravel are susceptible to liquefaction (Bolton et al., 1985; Thevanayagam and Martin, 2002). Despite apparent differences when compared against each other, liquefaction resistance of sand and silty sands is similar which is affected by grain contact density. At the same void ratio, cyclic strength of silty sand decreases with an increase in silt content. Beyond a transition silty content (about 20-30%), the trend reverses and the strength increases with further increase in silt content. Hence, it becomes prudent to carry out the numerical analysis to understand the behavior of embankments on uniform ground foundation consisting of silty sand only which consists of 25-30% fine particles and hydraulic conductivity of $2x10^{-5}$ m/s. Figure 5.20 shows the finite element discretization of the model represented as 'Model UG_silty sand'.

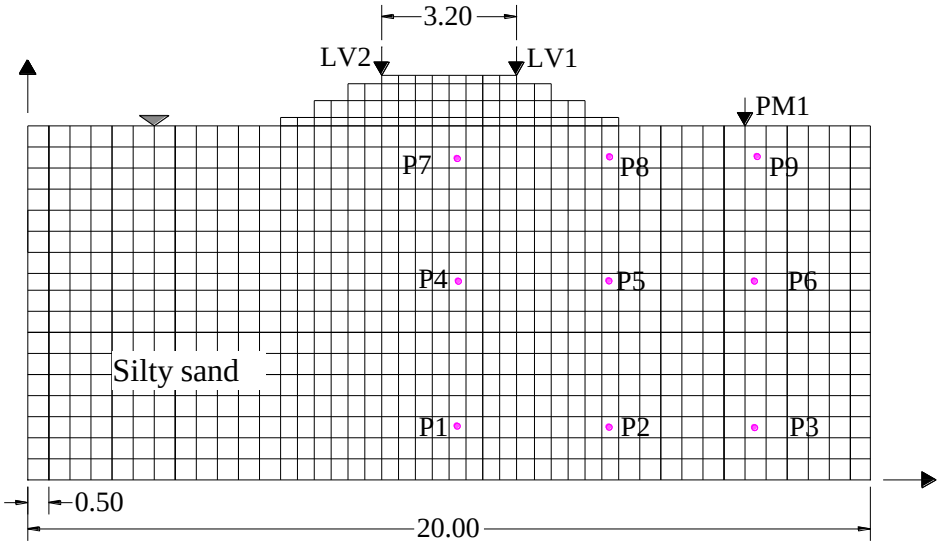

Figure 5.20. Finite element discretization of Model UG_silty sand.

Figures 5.21 and 5.23 present the time histories of excess pore water pressure ratios, r_u at different locations below the embankment and below the free field region as indicated in Fig. 5.20. The generation of excess pore water is found to be slightly different in contrast to that in sand as observed in other tests (Models UG, CG, NHG1 and NHG2). In Models UG, CG, NHG1 and NHG2, the excess pore water pressure generates during the early stage of shaking and decreases during 10-12 s of shaking which might be due to the dissipation of pore water followed by further increase in Δu. However, the Δu continuously keeps increasing during early stage of shaking (0-15 s). The lower permeability of silty sand makes the rate of pore pressure dissipation slower compared to that in sand, thus keeping the excess pore water pressure ratio larger. Nevertheless, the difference in the generation of excess pore water pressure might also be attributed due to the lower liquefaction strength characteristics

of silty sand. The r_u values at the free field region (at P3, P6, and P9) are nearly equal to 1 during shaking, which are significantly larger compared to that in other tests (Models UG, CG, NHG1 and NHG2). This larger r_u values cause liquefaction of soil at the free field region, decreasing the confining stress of soil below the foundation. This allows the large amount of foundation soil to stretch/laterally spread away towards the free field region, causing a larger crest settlement in Model UG_silty sand as shown in Fig. 5.22. Moreover, the larger tensile strain mechanism during undrained condition prevents the generation of Δu under the center of embankment, leading to the lower r_u values. The r_u values are significanlty lower even at the bottom strata compared to that in other tests ((Models UG, CG, NHG1 and NHG2, Fig. 5.21), indicating the larger lateral outflow of foundation soil towards the free field. It is noted that the larger settlement in Model UG_silty sand is not solely due to the high compressibility of silty sand. Nevertheless, the slightly lower liquefaction resistance and the less permeability of silty sand contribute to the larger deformation of embankment. This corroborates the findings from the previous study which has concluded that the cyclic strength of silty sand decreases with an increase in silt content (upto 30%).

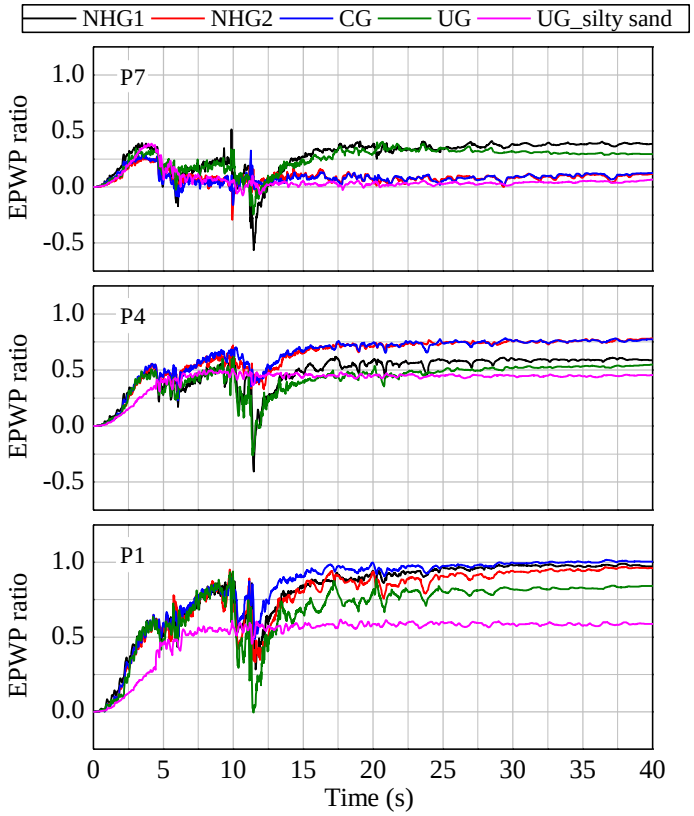

Figure 5.21. Time histories of excess pore water pressure ratio below the center of embankment at different locations.

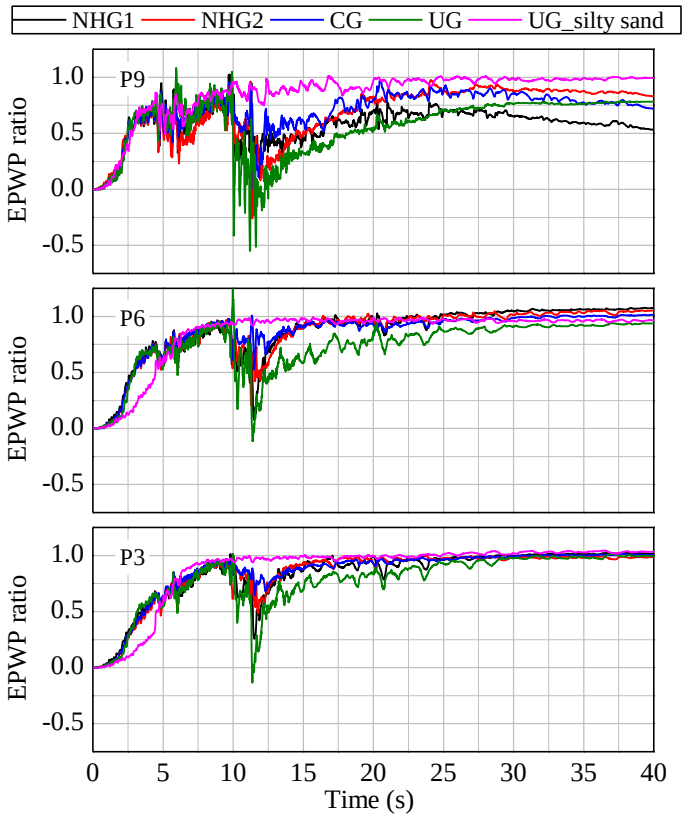

Figure 5.22. Time histories of excess pore water pressure ratio below the free field region at different locations.

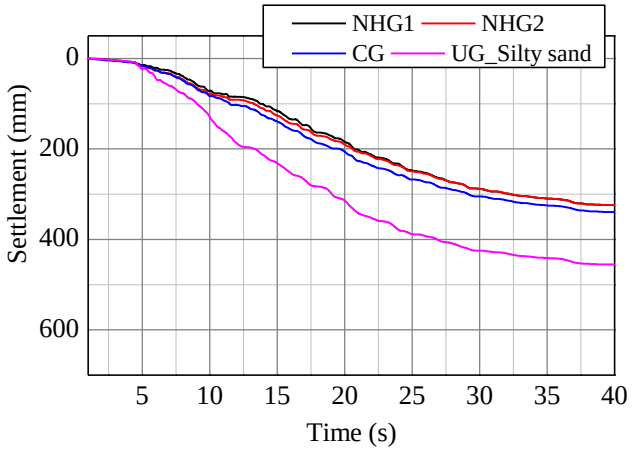

Figure 5.23. Settlement time histories at the crest center.

This analysis was conducted to examine the seismic behavior of embankment on uniform ground consisting of silty sand only in terms of excess pore water pressure and displacement responses. Nonetheless, the real soil profile is never uniform, consisting of only soil of less permeability, like silty sand and silts. Considering the uniform foundation

consisting of only sand underestimates the actual deformation of embankment while designing the soil structures. On the other hand, the deformation is overestimated while designing the soil structures when the uniform foundation consisting of silty sand only is considered, increasing the cost of the project. Thus, for the performance based design of soil structures, the real soil profile consisting of many sublayers of soil with discontinuous low permeability layers should be accounted for.

5.6 Summary and conclusions

After the verification and validation of the numerical tool approached, the numerical model was applied to study the earthquake liquefaction-induced deformation of embankments under various ground motions consisting of aftershocks of different characteristics. The realistic earthquake ground motion recorded during 1994 Northridge earthquake, consisting of mainshock and aftershock was applied to the embankment resting on different liquefiable foundation ground: non-homogeneous liquefiable foundation, continuous layered foundation and uniform foundation. Aftershocks consisting of varying duration and peak ground acceleration were applied before the major dissipation of excess pore water pressure, where the quite period between mainshock and aftershock was 100 s. It was determined that the lateral deformation attributed to be the dominant factor for the deformation of embankment in all the foundations. Nonetheless, the lateral spreading was found to be larger in non-homogeneous and continuous layered foundation, inducing larger crest settlement. The application of three different aftershocks suggested that the deformation of embankment was more pronounced in embankment on non-homogeneous foundation during the application of longer duration aftershocks compared to that on uniform foundation.

Chapter 6

Effects of non-homogeneity in the liquefaction-induced deformation of embankments

After conducting a rigorous analysis on liquefaction-induced deformation of embankments resting on different foundations, it was concluded that the embankments resting on non-homogeneous foundation suffered severe damage during earthquakes compared to the uniform foundation. Hence, it becomes essential to investigate the effects of non-homogeneity on the deformation of embankments. This chapter presents parametric studies of embankments on non-homogeneous liquefiable foundation by changing the position of non-homogeneity. The analysis and computation results of the different cases are compared to determine the critical position of non-homogeneity.

6.1 Embankments on non-homogeneous foundation

Most of the embankments rest on the non-homogeneous liquefiable soil profile, which consists of thin layers of discontinuous low permeability layers like silty sand or clay. In our previous study (Maharjan and Takahashi, 2013a; 2013b) we conducted centrifuge model tests and numerical analyses to investigate the liquefaction mechanism in leveled non-homogeneous soil deposits. It was revealed that more excess pore water pressure (Δu) remains for a longer period of time at discontinuous region in non-homogeneous soil deposits compared with the continuous layered and uniform soil deposits, manifesting a larger settlement at the corresponding part causing non-uniform settlements. Further experimental and numerical studies were carried out to investigate the liquefaction-induced deformation of embankments resting on non-homogeneous foundation (Maharjan and Takahashi, 2014a, b). It was found out that the embankment resting on non-homogeneous soil deposits suffer more damage, where the discontinuity lies below the center of embankment compared to the uniform sand foundation.

Nonetheless, the stratification of non-homogeneous foundation is complex and the discontinuity in low-permeability layer may lie at any location below the embankment. Hence, the need to understand the effects of position of non-homogeneity on the deformation of embankment, is apparent. The determination of critical position and location of non-homogeneity in non-homogeneous foundation is the realistic approach for the safety

design of embankments. Thus, it becomes prudent to understand the effects of sequential ground motion on the deformation of embankment lying on different non-homogeneous liquefiable foundations.

6.2 Parametric studies

6.2.1 Finite element model setup

From the experimental and numerical results, it is found that the embankment resting on non-homogeneous soil deposits suffer more damage compared to the uniform sand foundation of the same relative density. Moreover, the numerical results agreed well with experimental results, validating the numerical model used. Nonetheless, the discontinuity may lie at any position below the embankment. So it is prudent to carry out the parametric studies to determine the critical position of non-homogeneity by using numerical analysis.

Parametric studies were carried out by changing the position of non-homogeneity. Figure 6.1 shows the general layout of the model configuration with embankment width of B and X_d is the distance between the center of embankment to the center of length of discontinuity. The length of discontinuity in silty layer at a depth of one-fifth of the embankment width (1.5 m) is the crest width of embankment (3.2 m). The position of non-homogeneity varies from the discontinuity lying exactly below the center of embankment to the toe of embankment. A total of seven cases were analyzed by changing the value of X_d . The value of X_d /B changes from 0 to 0.7 as shown in Table 6.1.

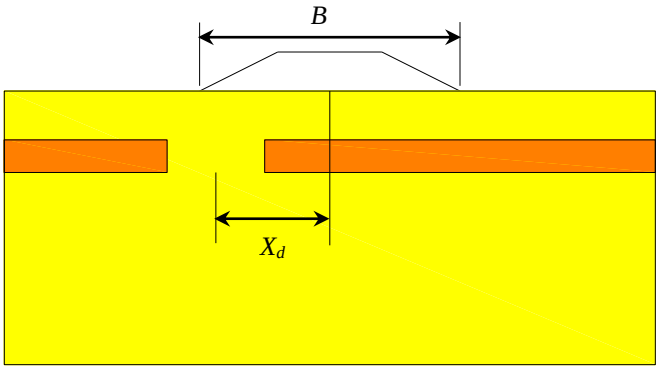

Figure 6.1. General layout of model.

Figure 6.2 shows the finite element discretization of models NHG1, NHG3, NHG5, and NHG7. Discontinuity lies exactly below the center of embankment in NHG1. The position of discontinuity is changed towards the left embankment toe in each model configuration. In model NHG5, the discontinuity lies partly below the free field and partly below the embankment toe, while the discontinuity lies completely below the free field

region in model NHG7. The sequential ground motion consisting of mainshock and aftershock, recorded at the Moorpark-Fire station (EW component) during 1994 Northridge earthquake (PEER. 2013), normalized to maximum PGA equal to 0.4 g for mainshock was applied along the base (Fig. 6.3).

Table 6.1. Model configurations.

Models	B	X_d	X_d/B
NHG1	8	0	0
NHG2	8	0.8	0.1
NHG3	8	1.6	0.2
NHG4	8	2.4	0.3
NHG5	8	3.6	0.45
NHG6	8	4.5	0.56
NHG7	8	5.5	0.69

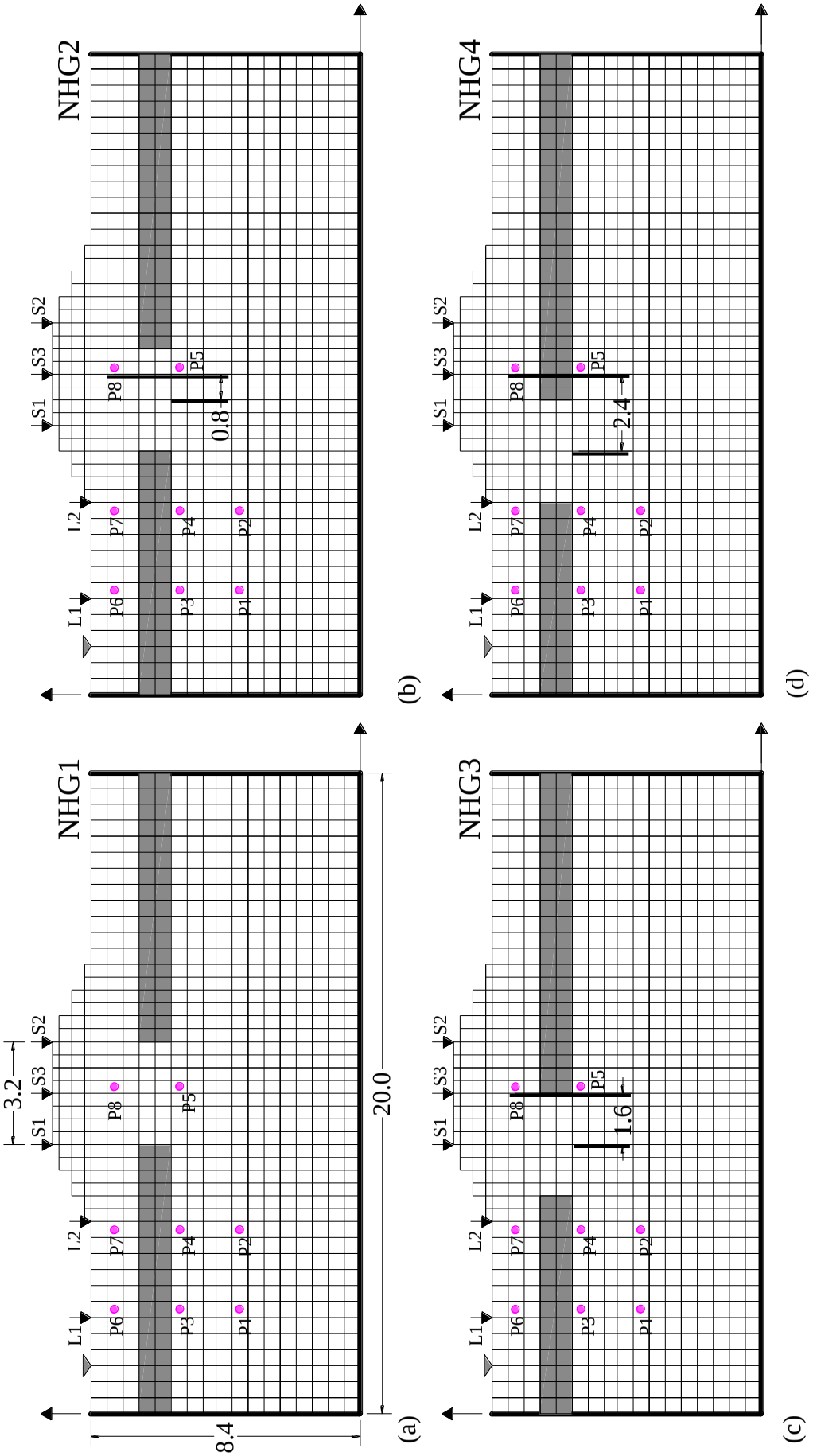
NHG1
NHG2
NHG3
NHG4
S1
S2
S3
L1
L2
P1
P2
P3
P4
P5
P6
P7
P8
3.2
20.0
8.4
0.8
2.4
1.6
(a)
(b)
(c)
(d)

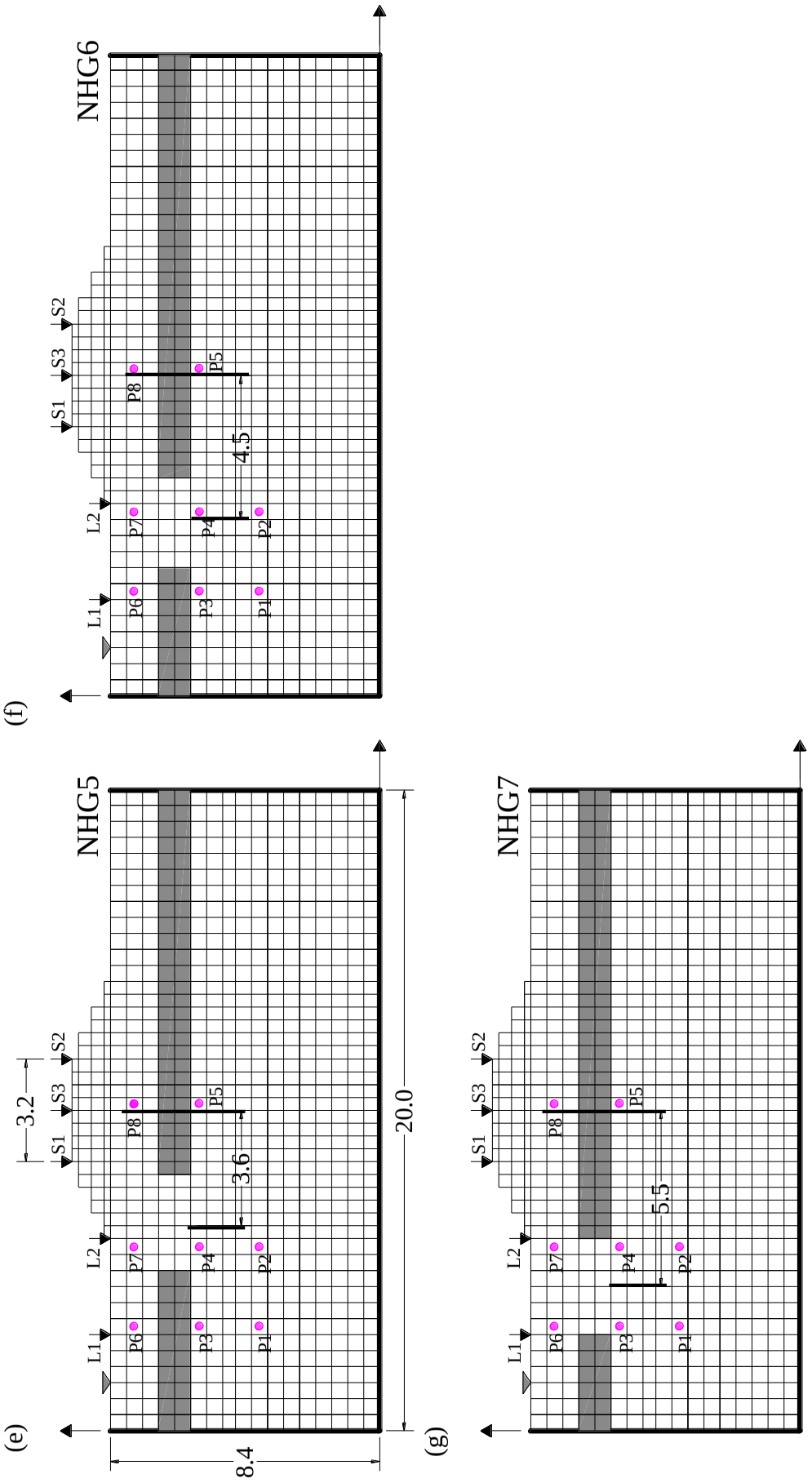

Figure 6.2. Finite element discretization of all the models for parametric studies.

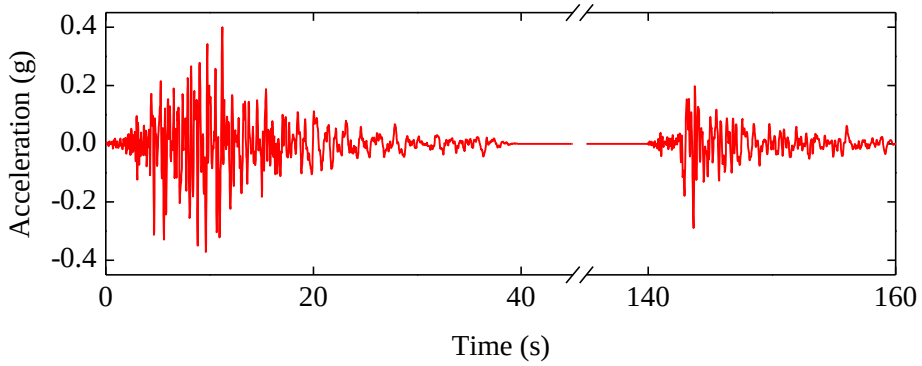

Figure 6.3. Input acceleration time history.

6.2.2 Numerical modeling procedure

Two dimensional finite element analyses were conducted under the plain strain condition (Takahashi, 2002). The constitutive model, extended sub-loading surface model proposed by Hashiguchi and Chen (1998), was adopted for the soil layers. The material parameters of the soil layers are listed in Table 4.1. Toyoura sand is used as liquefiable sand and Silica sand No. 8 is used to create the non-homogeneity in the foundation as the permeability of Silica sand No. 8 is ten times less that that of Toyoura sand, signifying relatively impermeable layer. The liquefaction resistance curve for Toyoura sand and Silica sand No. 8 are illustrated in Fig 4.1. The liquefaction resistance curve is a relation between the ratio of the cyclic shear stress to the initial confining stress and the number of loading cycles required to cause shear strain of 5% in the double amplitude. The soil model used, could not properly simulate the flat curves which causes the simulated values of cyclic stress ratio for both Toyoura sand and Silica sand No. 8 larger than those obtained from laboratory test results at the smaller number of loading cycles. However, the simulated values are closer to those obtained in the laboratory for larger number of loading cycles. In order to obtain the numerical solution, the differential equations were integrated along time. System damping was represented by stiffness- proportional damping, and the damping ratio used was 1% in the first mode of the free vibration of the system. All the models were modeled using four-node quadrilateral elements using one-point intergration together with a classical hourglass control technique (Flanagan and Belytschko, 1981). A periodic boundary was considered to simulate the flexible boundary at the ends of both sides. Nodes at the both side ends were allowed to move freely in vertical directions.

6.3 Computational results and discussion

During the computational simulations, excess pore water pressure and stress-strain responses were monitored for the locations, indicated by prefix “P*” as shown in Fig. 6.1. These locations were selected to represent different stress states: (1) under the toe of the embankment where static shear stress exists; and (2) under the center of embankment where

large effective stress exists. The crest settlement and lateral displacement were monitored at the locations, indicated by prefix "S*"and "L*", respectively as presented in Fig. 6.1. At these key locations, computed excess pore water pressures, settlement, and lateral displacements will be compared for different model cases.

6.3.1 Excess pore water pressure responses

When the excess pore water pressure, reaches a value equal to the initial vertical effective stress, i.e., excess pore water pressure ratio, r_u approaches unity, $\left(r_u = \Delta u / \sigma'\right)$ liquefaction occurs. The r_u values were largest at the free field and toe region and lowest below the embankment throughout the shaking. The primary factor which causes the deformation of embankment is the liquefaction under the toe and free field region. Figures 6.4-6.5 presents the time histories of excess pore water pressure ratios at different sampled locations. It can be seen in Fig. 6.4, that the r_u is significantly larger under the toe region (at P7) for the cases where the discontinuity lies below the toe region during mainshock at shallow depth. Moreover, the r_u values below the toe region are also pronounced for the cases where the discontinuity lies below the toe region during aftershock as well. The larger r_u values at the

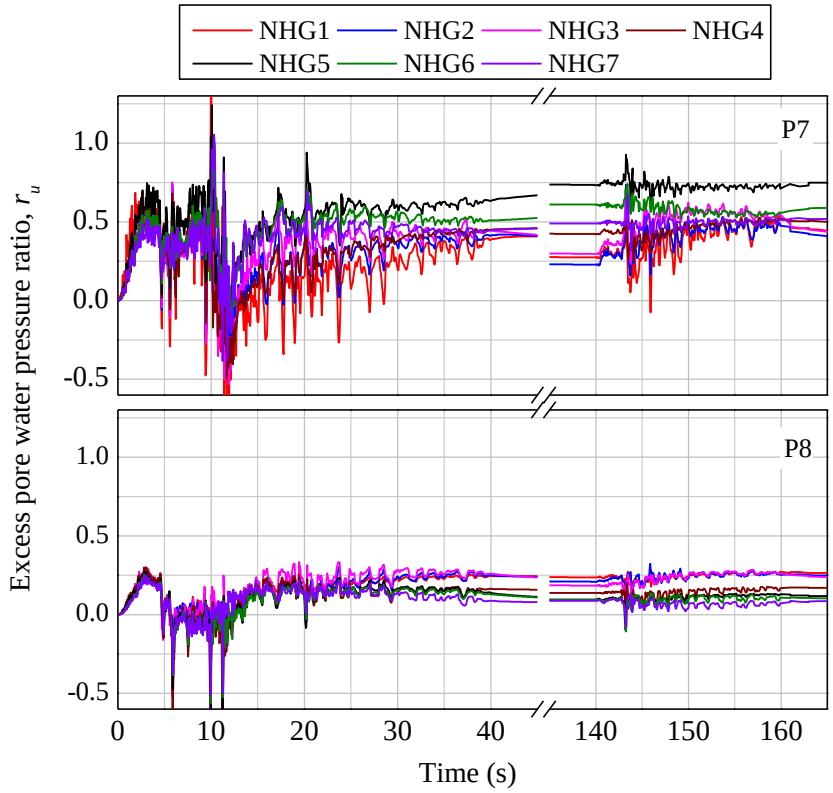

Figure 6.4. Time histories of excess pore water pressure ratio, r_u at P7, under the toe and P8, under the embankment.

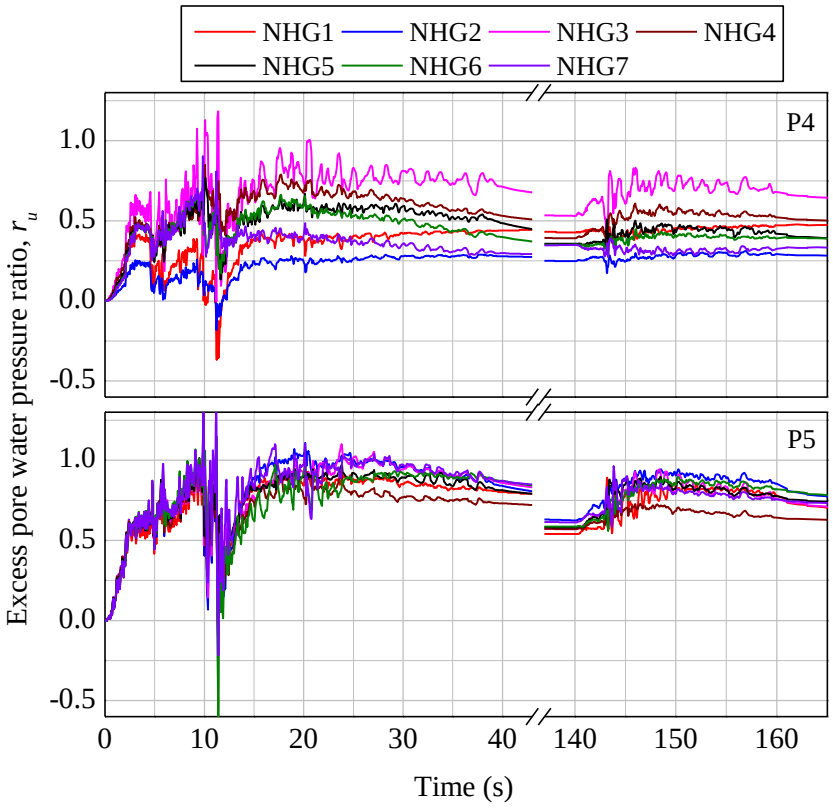

Figure 6.5. Time histories of excess pore water pressure ratio, r_u at P4, under the toe and P5, under the embankment.

toe region for the cases where the discontinuity lies below the embankment toe is due to the combine effect of pore water generation due to shaking and dissipation through the underlying soil layer. However, when the discontinuity lies below the center of embankment, the silt below the toe and free field region restricts the upward flow of pore water. In that case, the excess pore water pressure under the toe region is solely due to the generation of pore water above the silty layer, causing lower r_u values at P7 as in NHG1. The liquefaction in free field and toe region in the form of larger r_u might have reduced the confinement of the soil below the embankment. This might have allowed the lateral stretching of the foundation soil below the embankment towards the free field, inducing larger deformation of embankments. However, the r_u is observed to be larger under the toe region below the silty layer (at P4) for NHG3 and NHG4.

Furthermore, the r_u values are larger below the embankment when the discontinuity lies below the embankment centerline (Fig. 6.4(b)). The presence of discontinuity under the embankment center concentrates the dissipation of pore water below the center. This makes the r_u values slightly larger for the cases where the discontinuity lies closer to the embankment center and lower r_u values at the toe portion. However, the values are not large enough to cause liquefaction. The soil under the center of embankment does not liquefy in

all the cases. Under nearly undrained conditions, the tensile strain mechanism suppressed the increase of excess pore water pressure in the soil below the embankment, which causes the response under the embankment center to be more or less the same in all the cases, signifying the liquefaction at free field and toe region as the major factor for the deformation of embankments.

6.3.2 Displacement responses

Figure 6.6 presents the horizontal displacement at free field (L1) and toe region (L2). The horizontal displacement at both free field and toe region is larger for the cases where the discontinuity lies below the toe and free field region compare to the cases where the discontinuity lies below the center of embankment during both mainshock and aftershock. Moreover, the horizontal displacement is more pronounced during aftershock for the cases where the discontinuity lies below the embankment toe (Fig. 6.6). Figure 6.7 shows the settlement time histories at the crest edges (S1 and S2) and crest center (S3). Figure 6.8 presents the settlement profile of embankment crest after the mainshock and aftershock.

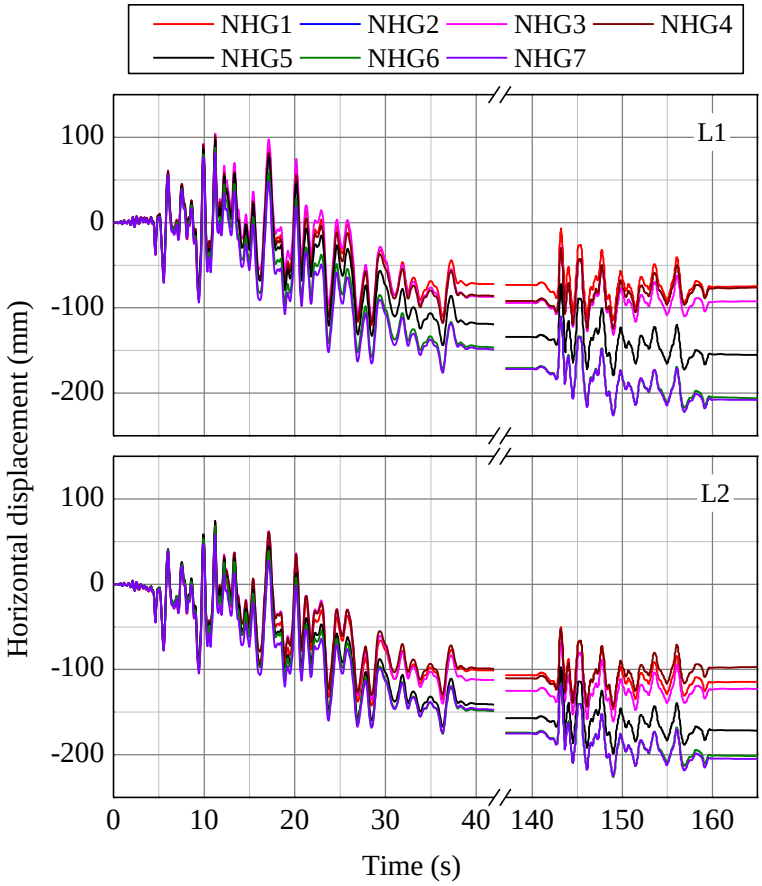

Figure 6.6. Time histories of horizontal displacement: (a) At free field and (b) At toe.

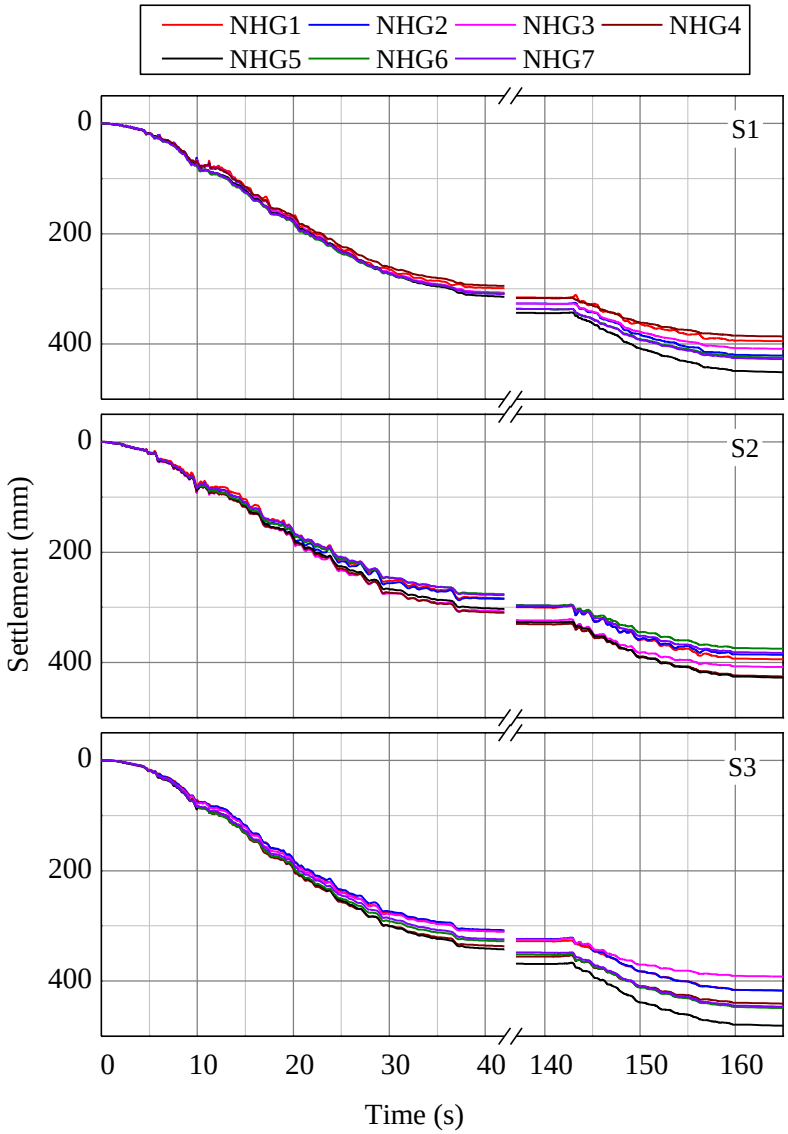

Figure 6.7. Settlement time histories at the crest: (a) At the left edge and (b) At the right edge; and (c) At the center.

Larger settlement is induced at center of embankment crest after mainshock for the cases where the discontinuity lie below the embankment toe (NHG5-NHG7, Figs. 6.7 and 6.8). Furthermore, the difference in settlement is more significant during aftershock. For instance, in cases NHG5-NHG7, the crest settlement at the left crest, S1 is larger than that at the right crest, S2. Also, the embankment crest settled more for the cases where the discontinuity lies below the embankment toe at the end of aftershock.

Moreover, the presence of discontinuity below the left part of embankment induces the larger crest settlement at left part compared to the right part, leading to the non-uniform settlement in cases NHG5-7(Fig. 6.8). However, the differential settlement is more severe

for NHG6 and NHG7, although the amount of settlement is less than that observed in NHG5. The liquefaction near the toe and free field region at the left part reduces the lateral restraint of soil underneath the embankment, inducing larger outflow of foundation soil towards the left side, which finally causes larger deformation at the left portion of embankment for the cases where the discontinuity lies below the toe portion. Nonetheless, the crest settlement at S1, S2, and S3 appears to be nearly the same in NHG1, revealing the uniform settlement, where the discontinuity lies exactly below the embankment center forming a symmetric foundation ground (Figs. 6.7 and 6.8). The settlement is found to be larger at the right side than that at left side in NHG3 and NHG4, in contrast to NHG5-7. The presence of discontinuity region below the embankment crest and slope does not cause liquefaction around discontinuous region and also below the toe region. However, the shear strain below the silty layer is found to be larger at the right side than that at the left side, inducing larger settlement at the right side of embankment in NHG3 and NHG4 (Fig. 6.8).

Figure 6.9 compares the amount of settlement occurred at crest with respect to embankment height for different values of X_d/B. The crest settled about 27% and 40% of embankment height when X_d/B=0.45, i.e., Model NHG5 at the end of mainshock and aftershock, respectively. The amount of crest settled is found to be minimum when the value of X_d/B is minimum, and maximum when the value is 0.45.

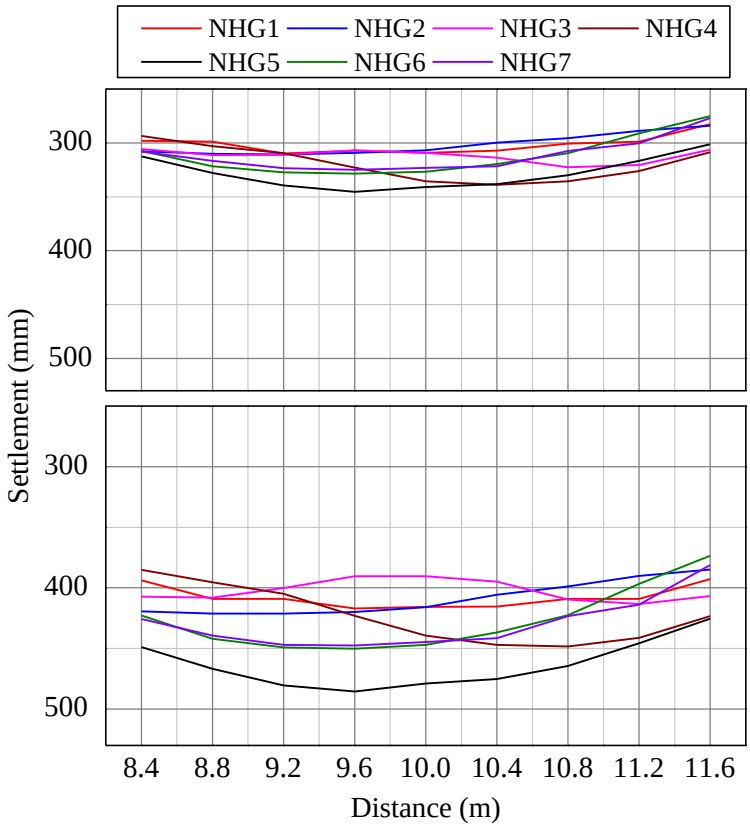

Figure 6.8. Soil profile of embankment crest of all the models: (a) After mainshock and (b) After aftershock.

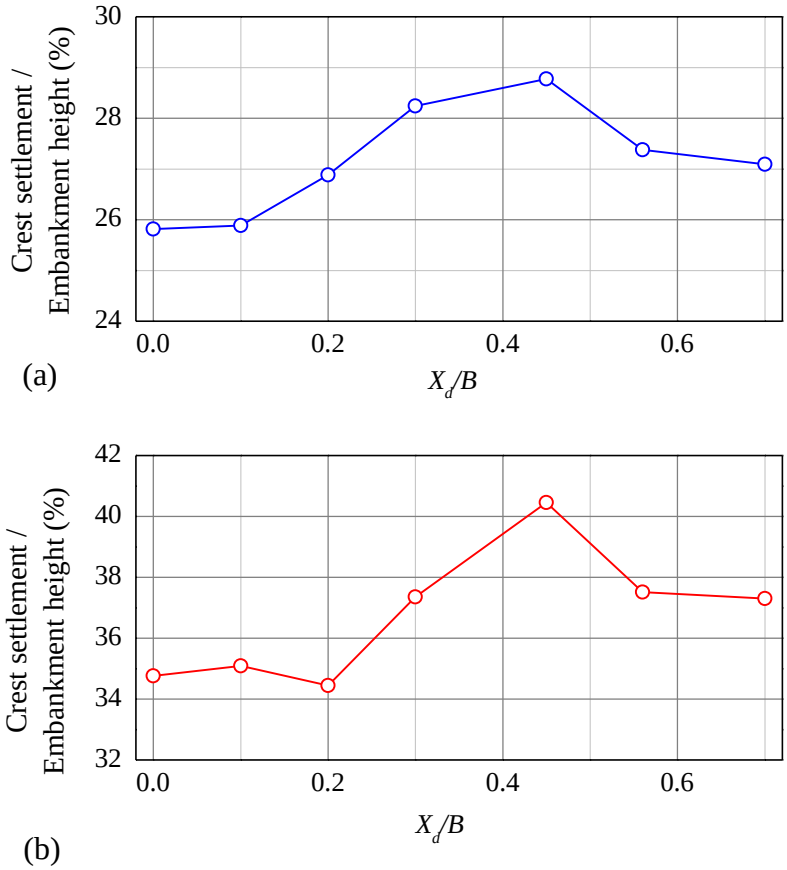

Figure 6.9. Maximum crest settlement with respect to embankment height (a) At the end of mainshock and (b) At the end of aftershock.

6.3.3 Stress-strain responses

Figure 6.10 shows the horizontal and vertical strain isochrones for different time period for Models NHG1, NHG5, and NHG7. The strains are found to be larger in NHG5 and NHG7 at the beginning of shaking, i.e., at 10 s. The trapping of pore water beneath the silty sand layer, below the embankment centerline, increases the horizontal strain in Models NHG5 and NHG7. Moreover, the larger horizontal strain was attained below the silty sand layer as the shaking duration increased. For instance, at 40 s the horizontal strain increases continuously until the depth of 2.5 m in Model NHG5. The liquefaction of soil in the free field and toe region might have allowed the lateral stretching of the foundation soil below the embankment towards the free field in the left side, thus increasing the horizontal strain in Model NHG5. However, in Model NHG7 the free field region was totally liquefied instead of toe part, thus suppressing the lateral stretching of the foundation soil below the center of embankment. This causes the reduction in horizontal strain in NHG7.

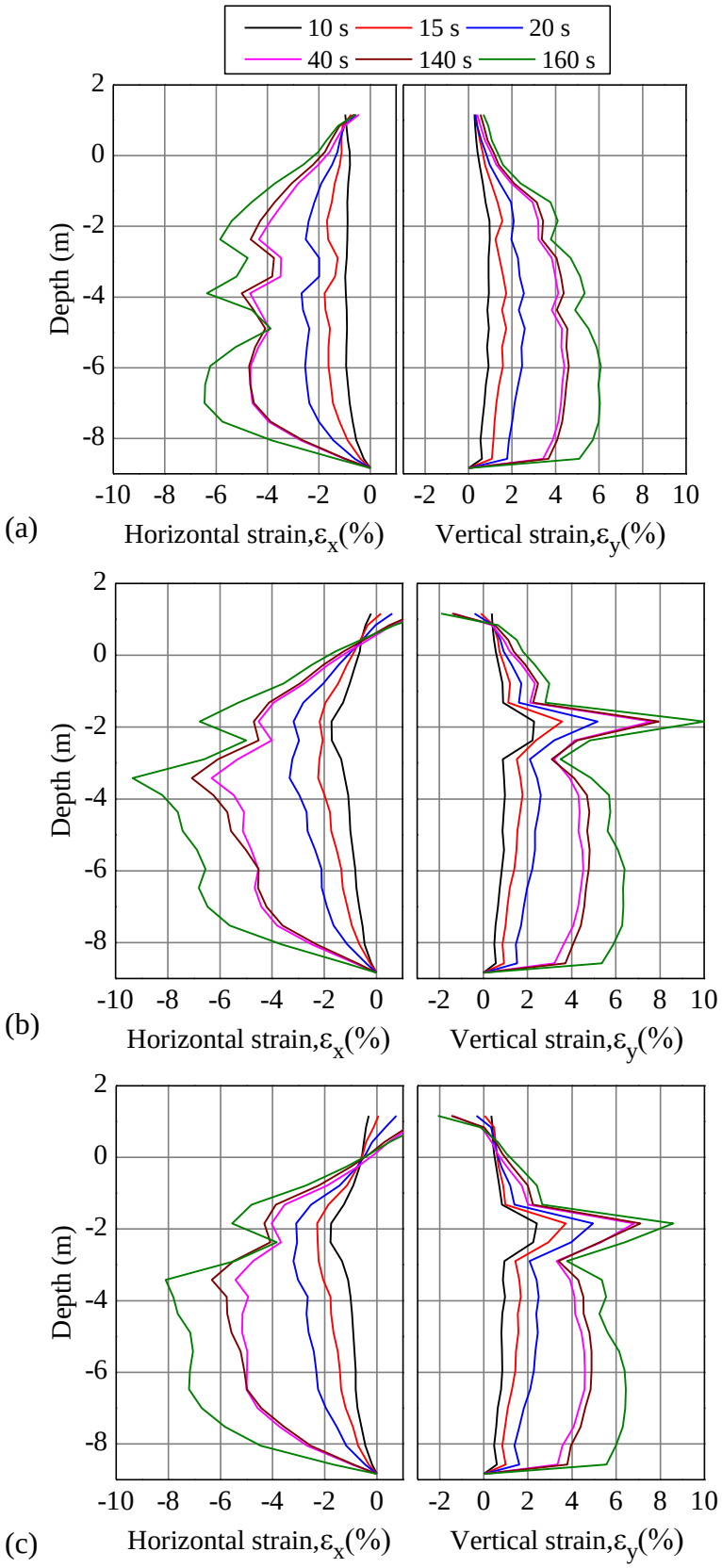

Figure 6.10. Horizontal and vertical isochrones: (a) NHG1, (b) NHG5, and (c) NHG7.

Figures 6.11 and 6.12 compare the computed shear stress-strain responses at toe (at P4) and free field region (at P1) for cases NHG1, NHG5, and NHG7, respectively. The deformation in the cases where discontinuity lies below the embankment toe, i.e., NHG5 and NHG7, was associated with a large permanent lateral shear strain of about 10% under the toe, which clearly shows the mechanism of cycle-by-cycle shear strain accumulation and gradual loss of shear strength (Fig. 6.11). However, the smaller lateral deformation for the cases where the discontinuity lies below the embankment center is associated with lower shear strain accumulation. Similarly, the accumulated shear strain is also larger in NHG5 at free field region compared to NHG1, where the discontinuity is exactly below the center of embankment (Fig. 6.12).

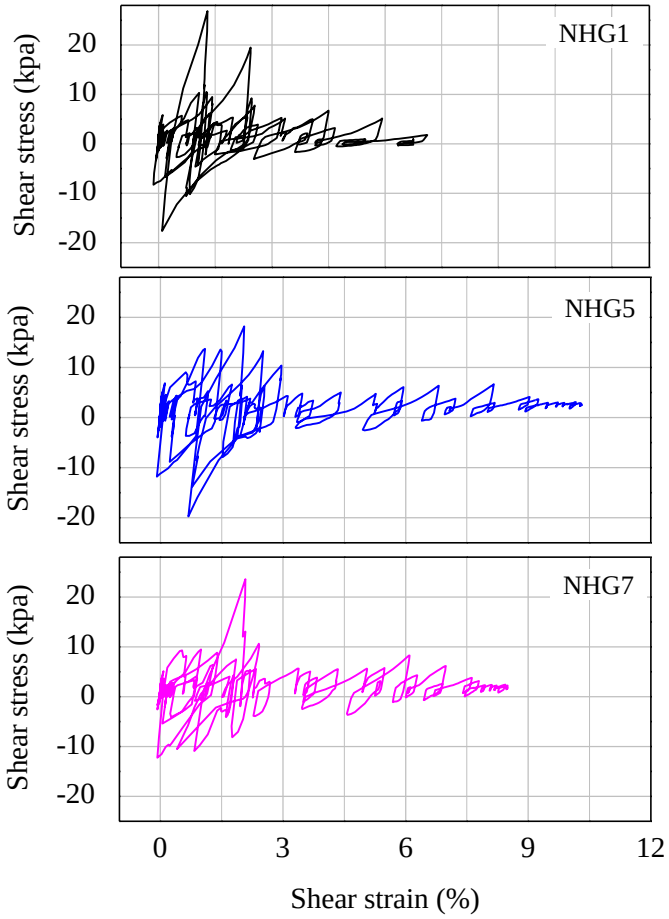

Figure 6.11. Computed shear stress-strain histories under the embankment toe at P4.

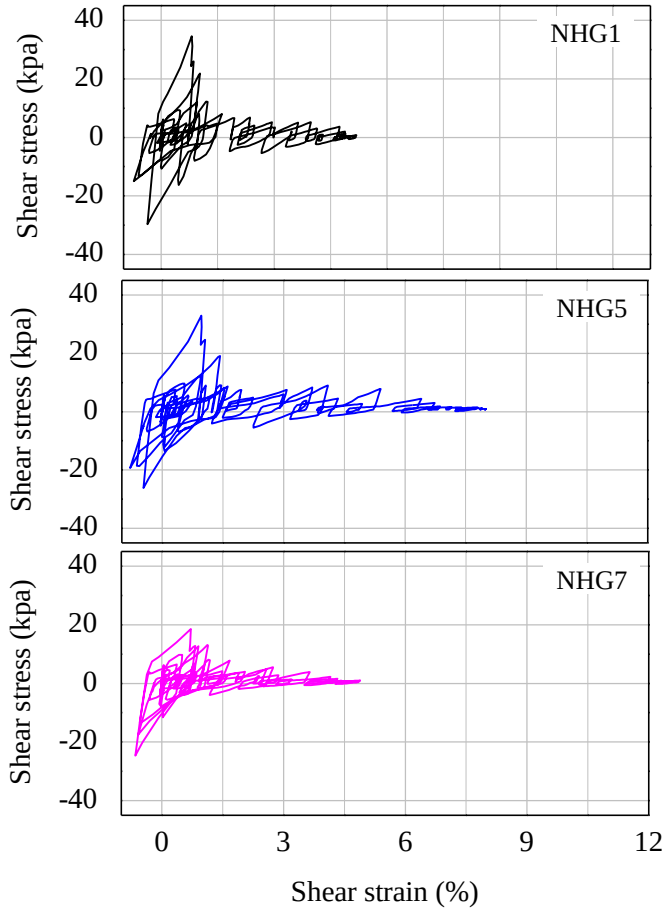

Figure 6.12. Computed shear stress-strain histories under the embankment toe at P1.

6.4 Impact of lower less permeable layer

It was determined from the preceding section that larger deformation occurred in embankments for the cases where the discontinuity lay below the embankment toe. The preceding section only investigates the foundation consisting of one layer of discontinuous less permeable layer located at the depth of 1.5 m. However, the effect of less permeable layers located at the bottom strata is of prime concern as well. Many studies have pointed out that the location of less permeable layer at the bottom depth does not cause any effect on the deformation of super structures. Nevertheless, it becomes worth to carry out the computational analysis by considering less permeable layer at the bottom strata of foundation. Here, the lower less permeable layer comprising of continuous less permeable layer (NHG5'' and NHG'') and discontinuous less permeable layer with the discontinuity below the center of embankment (NHG5' and NHG6') are considered (Figure 6.13).

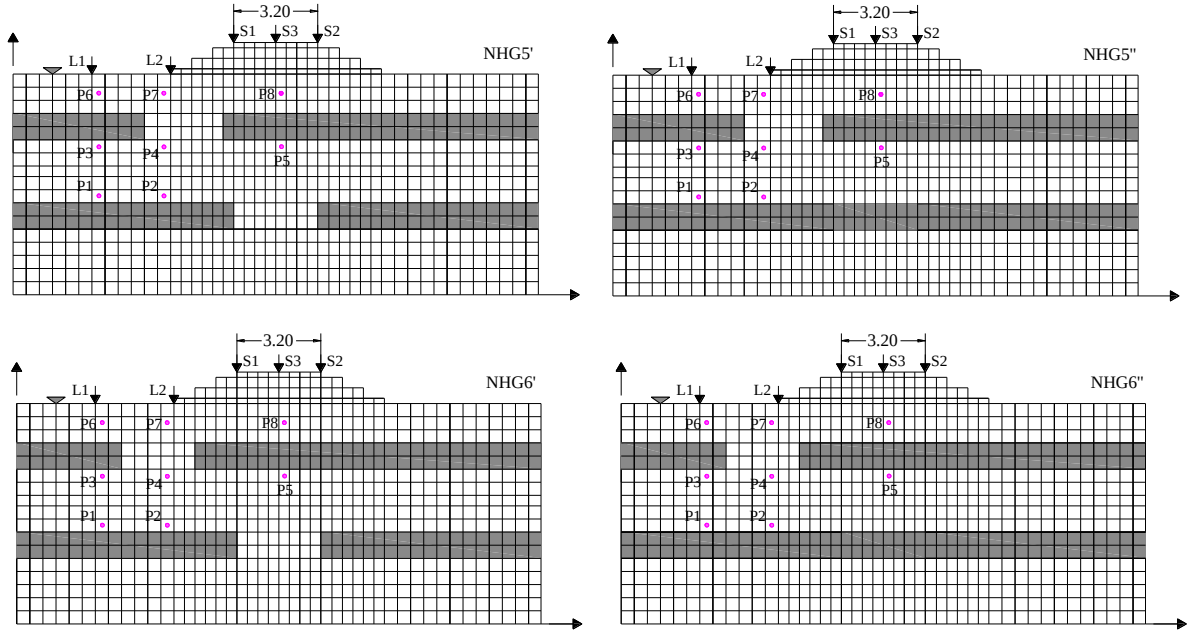

Figure 6.13. Finite element discretization of models consisting of lower less permeable layer.

Figure 6.14 compares the time histories of excess pore water pressure at P7 and P8 during shaking for Models NHG5, NHG6, NHG5', and NG6'. It can be seen that r_u values are still larger during mainshock and aftershock at P7 and P8 in Models NHG5 and NHG6 compared to NHG5' and NHG6', respectively. The trapping or accumulation of pore water beneath the lower silty sand layer in Models NHG5' and NHG6'delays the dissipation of pore water to the soils at shallow depths. As a results, excess pore water pressure is dominantly reduced at the shallow depths in the models consisting of lower less permeable layers. Figure 6.15 shows the deformed shape of Models NHG5, NHG5', and NHG5'' at the end of aftershock (i.e., 160 s). The liquefaction of soil at the free field and toe region at the shallow depth decreases the soil confinement of foundation soil below the embankment in Model NHG5. This allows the lateral outflow of foundation soil towards the free field as shown in Fig. 6.15 (a). Moreover, the trapping of pore water beneath the upper less permeable layer induces the shear deformation underneath it, which lies below the center of embankment. However, in Models NHG5' and NHG5'', shear deformation occurs beneath the lower silty sand layer and no lateral outflow of foundation soil towards the free field is observed above the lower silty sand layer (Fig. 6.15 (a) and (b)). Moreover, no shear deformation is induced below the upper silty sand layer in Model NHG5' and NHG5'', despite being less permeable, which contributes to the less amount of deformation of embankments. Figure 6.16 comapres the crest settlement time histories at different locations. During mainshock, the crest settlement is found to be slightly lower in Model NHG5. However, the dissipation of pore water from the underlying layers gradually increases the pore water pressure at the shallow depths, increasing the lateral stretching of foundation soil towards free field. As a result, larger crest settlement is induced in Model NHG5 during the

quite period (40-140 s) and during aftershock.

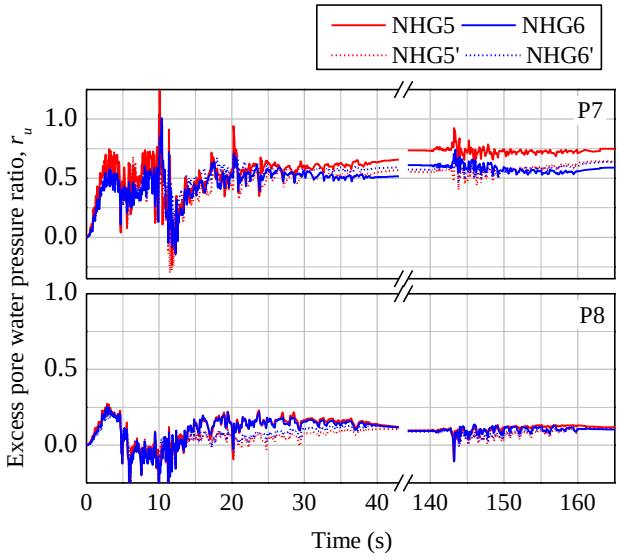

Figure 6.14. Time histories of excess pore water pressure ratio at P7 and P8.

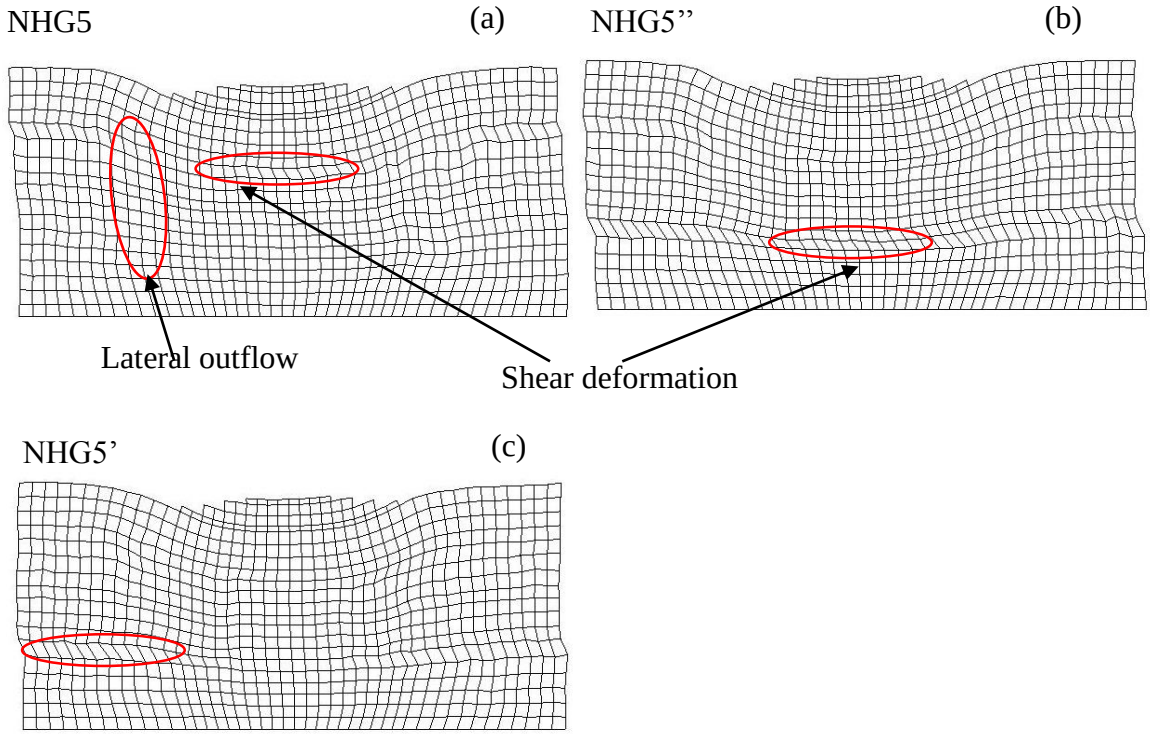

Figure 6.15. Deformed shape at the end of aftershock (at 160 s): (a) Model NHG5, (b) Model NHG5', and (c) Model NHG''.

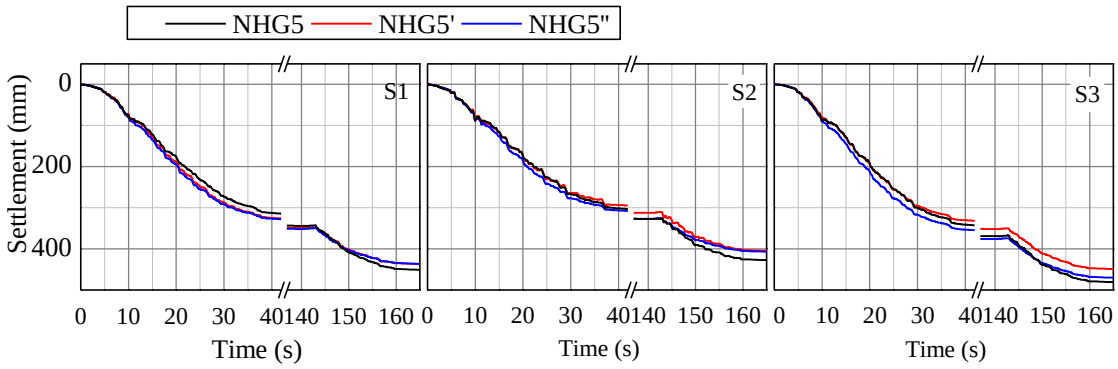

Figure 6.16. Time histories of crest settlement at different locations.

6.5 Determination of critical location of non-homogeneity

The liquefaction occurs with the larger r_u values at the toe region for the cases where the discontinuity lies below the embankment toe. However, when the discontinuity lies below the center of embankment, the silt below the toe and free field region restricts the upward flow of pore water. In that case, the excess pore water pressure under the toe region is solely due to the generation of pore water above the silty layer, causing lower r_u values for the cases where discontinuity lies below the center of embankment. Despite the presence of discontinuity at the center of embankment, the soil under the embankment never liquefies. In fact, the r_u values seem to be more or less the same for all the cases under the center of embankment. The liquefaction in free field and toe region in the form of larger r_u might have reduced the confinement of the soil below the embankment. This might have allowed the lateral stretching of the foundation soil below the embankment towards the free field, inducing larger deformation of embankments. Under nearly undrained conditions, the tensile strain mechanism suppressed the increase of excess pore water pressure in the soil below the embankment, which causes the response under the embankment center to be more or less the same in all the cases, signifying the liquefaction at free field and toe region as the major factor for the deformation of embankments. Thus, the cases of non-homogeneity, where the discontinuity lies under the embankment toe, the deformation is more severe and the position attains the critical position of non-homogeneity.

6.6 Summary and conclusions

The parametric studies showed that larger excess pore water pressure ratio were found below the toe region for the cases where the discontinuity lay below the embankment toe. This caused the liquefaction of soil at the free field and toe region, which decreased the confining stress of foundation soil below the embankment. This may have allowed the lateral stretching of the soil below the embankment towards the free field, leading to the larger

lateral deformation in the free field and toe region for the cases where discontinuity lay below the embankment toe. Hence, the outflow of foundation soil below the embankment towards the free field region ultimately increased the deformation of embankment. Moreover, the deformation of embankment was found to be more pronounced during aftershock for the cases where the discontinuity lay below the embankment toe than that for the cases where the discontinuity lay below the center of embankment. Furthermore, the crest settlement was found to be even and uniform when the discontinuity lay exactly below the center of embankment. However, uneven settlements occurred at the embankment crest when the discontinuity was located at the position other than the center of embankment.

Chapter 7
Conclusions and recommendations

Accounting for geological non-uniformities are very hard to evaluate but this study modeled the features of actual liquefiable soil profiles with discontinuous low permeability layers to provide new insights into the drainage path for dissipation of excess pore water pressure in various ground conditions and compared the liquefaction-induced deformation of embankments on different foundations. To this end, a series of dynamic centrifuge tests were conducted on saturated uniform, continuous silt interlayered sand, and discontinuous silt interlayered sand, referred as non-homogeneous soil profile specimens. Tests were also conducted with embankments on different foundation grounds. Finite element analyses were also carried out to simulate the experimentally observed behavior and to conduct parametric studies for generalization of the findings of the study.

The modeling of liquefaction in the field is complicated due to the various uncertainties in stratigraphic details and geological non-uniformities. It is impossible to model the real soil profile to be exactly the same considering all the geological non-uniformities and taking into account the uncertainties and various soil properties. Attempts have been made to model the multi-layered soil profile consisting of discontinuous thin layers of low permeability based on observations of several damage sites during the last earthquakes to improve the ability to account for them in practice. Valuable insights are gained for the modeling of liquefaction in the field consisting of discontinuous impermeable layer that can affect the influence of shear localizations, void redistributions, and dissipations of excess pore water pressure. The findings of the study are expected to assist the analysis and design of super structures lying on non-homogeneous liquefiable soils. This study modeled the multi-layered soil profile consisting of discontinuous thin layers of low permeability based on observations of several damage sites during recent earthquakes to improve the ability to account for them in practice. The work presented in this study provides new insights into the dissipation of excess pore water pressure and the potential causes of non-uniform settlements in realistic non-homogeneous soil deposits. The test results would be useful in the development of design guidelines, as well as in the calibration of numerical procedures.

7.1 Conclusions

7.1.1 Conclusions based on Chapter 2: Liquefaction-induced settlement and pore water migration in non-homogeneous soil deposits

Here the conclusions are drawn based on the investigation of liquefaction mechanism in non-homogeneous soil deposits by conducting dynamic centrifuge model tests. In particular, two model tests were conducted on non-homogenous soil deposits, where non-homogeneity was incorporated by including periodically distributed discontinuous silty sand patches with lower permeability than the surrounding soil. For comparison purposes, tests were also conducted on a model for continuous layered soil deposit and a model for uniform soil deposit. This study was focused on modeling of realistic liquefiable soil profile with discontinuous low permeability layers to properly simulate the generation, redistribution, and dissipation of excess pore water pressure during and after shaking. The conclusions are:

1. It was found that, in non-homogeneous soil deposits, the pore water was trapped beneath or within less permeable silty sand patches due to the local migration of pore water and difference in permeabilities of the soils, restricting its upward movement.
2. The pore water finds a path to drain from the high pore pressure region to the low pressure region, which reveals that the presence of the discontinuous less permeable layer can have substantial effects on the pore pressure dissipation mechanism and drainage.
3. The presence of discontinuity of higher permeability in the less permeable soil layer concentrates the dissipation of excess pore water pressure mainly through the discontinuity region, increasing the rate and total time of dissipation after shaking, inducing the larger settlement in the discontinuity region.
4. Excess pore water pressure was accumulated for a longer period of time after shaking in non-homogeneous soil deposits compared with the uniform and continuous layered soil deposits, especially at shallow depths. The settlement induced by seepage at the surface above the discontinuity part was found to be larger than that above the silty sand layer, resulting in non-uniform settlements.

7.1.2 Conclusions based on Chapter 3: Deformation of earthen embankments on non-homogeneous soil deposits under sequential ground motions

Here the conclusions were drawn based on a series of dynamic centrifuge tests performed to investigate the seismic performance of earthen embankments resting on various liquefiable foundations. The liquefiable foundations include a uniform sand foundation, a multi-layered sand/silty sand foundation, and a non-homogeneous multi-layered discontinuous sand/silty sand foundation. The effects of repeated earthquake ground motions in the deformation of embankments were also studied by applying mainshock-aftershock sequential ground motions. The work presented in this chapter modeled the

features of actual liquefiable soil profiles with discontinuous low permeability layers to provide new insights into the liquefaction-induced deformation of embankments on different foundations. The conclusions are:

1. Clear shear straining was observed in the foundation and the embankments appeared to have settled into the foundation in all tests. The accumulation of pore water beneath the low permeability silty sand layer induced large shear strain below the silty sand layer, resulting lateral spreading and excessive settlement in non-homogeneous foundation.
2. In the non-homogeneous foundation, the dissipation of pore water from the underlying layer was concentrated at the discontinuous region below the embankment, inducing the larger excess pore water pressure ratios.
3. No massive failures were observed in the embankments, but the overall deformation was still very large in the non-homogeneous foundation. Severe deformation patterns in the form of cracking, lateral spreading and slumping were observed.
4. It was found that the sequential ground motions have a significant effect on the accumulated deformation of embankments. Moreover, the effects of aftershocks were more pronounced in the non-homogeneous liquefiable foundations, leading to the post-liquefaction delayed settlement.

7.1.3 Conclusions based on Chapter 4: Numerical analysis of liquefaction in non-homogeneous soil deposits and Chapter 5: Effects of aftershock on deformation of embankments

Confidence in ability of the numerical tool, for the realistic behavior on embankments and saturated soils during dynamic loading events, relies heavily on proper verification and validation. In this chapter, the computational simulations were presented for a series of centrifuge tests conducted to investigate the liquefaction mechanism of non-homogeneous soils deposits and to understand the liquefaction-induced deformation of embankments on non-homogeneous liquefiable foundations. The realistic earthquake ground motion recorded during 1994 Northridge earthquake, consisting of mainshock and aftershock was applied to the embankment resting on different liquefiable foundation ground. The conclusions are:

1. The numerical model used was also verified and validated using the experimental data.
2. Analyses have emulated the centrifuge model tests and can give important insight into both the behavior of embankments during mainshock and aftershock resting on different foundations. In all cases, computed excess pore water pressure responses were in good agreement with the recorded counterparts. Computed displacement responses were also realistic in pattern and amplitude. However, significant discrepancies existed between the computed and recorded acceleration responses. The computed one showed a large amount of amplification at the shallow depth.
3. It was determined that the lateral deformation attributed to be the dominant factor for the deformation of embankment in all the foundations. Nonetheless, the lateral spreading was found to be larger in non-homogeneous and continuous layered foundation, inducing larger crest settlement.

4. The application of three different aftershocks suggested that the deformation of embankment was more pronounced for the aftershocks of longer duration.

7.1.4 Conclusions based on Chapter 6: Effects of non-homogeneity in the liquefaction-induced deformation of embankments

Here, the conclusions are drawn based on the parametric studies of embankments on non-homogeneous liquefiable foundation by changing the position of non-homogeneity. The conclusions are:

1. The parametric studies showed that larger excess pore water pressure ratio were found below the toe region for the cases where the discontinuity lay below the embankment toe. This caused the liquefaction of soil at the free field and toe region, which decreased the confining stress of foundation soil below the embankment.
2. The liquefaction of soil at the free field and toe region may have allowed the lateral stretching of the soil below the embankment towards the free field, leading to the larger lateral deformation in the free field and toe region for the cases where discontinuity lay below the embankment toe. Hence, the outflow of foundation soil below the embankment towards the free field region ultimately increased the deformation of embankment.
3. The deformation of embankment was found to be more pronounced during aftershock for the cases where the discontinuity lay below the embankment toe than that for the cases where the discontinuity lay below the center of embankment.
4. The crest settlement was found to be even and uniform when the discontinuity lay exactly below the center of embankment. However, uneven settlements occurred at the embankment crest when the discontinuity was located at the position other than the center of embankment.

7.2 Recommendations for future research

The natural soil profile is complex and accounting for the stratigraphic details and geological non-uniformities is not certain. However, understanding the liquefaction mechanism of real soil profile incorporating the geological non-uniformities and its consequences on the soil-structures is indeed the most important aspect regardless of the less attention paid by the researchers. This study has determined that the discontinuous low-permeability layers present in liquefiable soil has significant effect on the soil-structures lying on such foundation. In addition, it has been found out that the effect is more significant when the discontinuities lie below the toe of soil structures. No design guidelines has developed yet incorporating these aspects. Implementing this findings in practice is yet another important concern as determining the discontinuities in low permeability and weak layers is difficult task. At present, the cross section of soil profile is determined based on

few bore holes data and available geological data. This method is not well enough to obtain the detail cross section of soil profile consisting of all the discontinuities, which might sometime miss the important layers or discontinuities. No technique has been developed so far to examine the detail information of soil profile. Moreover, the geophysical technique which can explore the physical properties of subsurface, along with the anomalies can be applied to detect the presence and position of various soil layers including weak and discontinuities. In addition, subsurface exploration with the cone penetration testing truck (Sounding test) which employs sensors that are pushed into the ground to infer the properties of soils and pore fluids, can also be used to detect the position of discontinuities (U.S. Geological Survey, 2013). This method can map out the vertical and lateral extent of stratigraphic layers. Further detail research and survey technique should be carried out which can determine the soil stratification over wide range at low cost. A technique or a technology should be developed to capture the high resolution image of the subsurface. As soon as the detection of discontinuities of low permeability layers becomes possible, the findings of study can be implemented in real practice, which can prove to be the novel factor to be considered while designing soil structures.

Apart from developing a technique to capture the detail high resolution image of subsurface, following are some additional recommendations for further studies.

1. Methods to mitigate the liquefaction-induced deformation of embankments on non-homogeneous foundations should proposed and investigated.
2. More detail non-uniformities can be considered for the further study which can represent the more stratigraphic details.
3. Design guidelines should be developed to construct the embankments on non-homogeneous ground.

References

Adalier, K. (1998). "Foundation liquefaction countermeasures for earth embankments". *Journal of Geotechnical and Geoenvironmental Engineering*, Vol. 124, No. pp. 500.

Adalier, K. & Aydingun, O. (2003). "Numerical analysis of seismically induced liquefaction in earth embankment foundations. Part II. Application of remedial measures". *Canadian Geotechnical Journal*, Vol. 40, No. 4, pp. 766-779.

Adalier, K. & Elgamal, A. (2004). "Mitigation of liquefaction and associated ground deformations by stone columns". *Engineering Geology*, Vol. 72, No. 3-4, pp. 275-291.

Adalier, K. & Elgamal, A. W. (2002). "Seismic response of adjacent dense and loose saturated sand columns". *Soil Dynamics and Earthquake Engineering*, Vol. 22, No. 2, pp. 115-127.

Adalier, K., Elgamal, A. W. & Martin, G. R. (1998). "Foundation liquefaction countermeasures for earth embankments". *Journal of Geotechnical and Geoenvironmental Engineering*, Vol. 124, No. 6, pp. 500-517.

Adalier, K. & Sharp, M. K. (2004). "Embankment dam on liquefiable foundation-dynamic behavior and densification remediation". *Journal of Geotechnical and Geoenvironmental Engineering*, Vol. 130, No. 11, pp. 1214-1224.

Amini, F. & Sama, K. M. (1999). "Behavior of stratified sand–silt–gravel composites under seismic liquefaction conditions". *Soil Dynamics and Earthquake Engineering*, Vol. 18, pp. 445-455.

Arulanandan, K. & Scott, R. F. (1994). *Verification of numerical procedures for the analysis of soil liquefaction problems*, Routledge.

ASTM (2013). "Standard practice for classification of soils for Engineering purposes (Unified Soil Classification System)". *Designation: D2487 - 11*.

Atkinson, J. (2007). *The mechanics of soils and foundations*, London and New York, Taylor and Francis.

Aydingun, O. & Adalier, K. (2003). "Numerical analysis of seismically induced liquefaction in earth embankment foundations. Part I. Benchmark model". *Canadian*

Geotechnical Journal, Vol. 40, No. 4, pp. 753-765.

Balakrishnan, A. (2000). *Liquefaction remediation at a bridge site*. PhD dissertation, University of California, Davis.

Balakrishnan, A. & Kutter, B. L. (1999). "Settlement, sliding, and liquefaction remediation of layered soil". *Journal of Geotechnical and Geoenvironmental Engineering*, Vol. 125, No. 11, pp. 968-978.

Beaty, M. H. & Byrne, P. M. (2011). *UBCSAND constitutive model version 904aR*.

Been, K. & Jefferies, M. G. (1985). "A state parameter for sands". *Geotechnique*, Vol. 35, No. 2, pp. 99-112.

Bolton, S. H., Tokimatsu, K., Harder, L. F. & Chung, R. M. (1985). "Influence of SPT procedures in soil liquefaction resistance evaluations". *Journal of Geotechnical Engineering*, Vol. 111, No. 12, pp. 1425-1445.

Boulanger, R. W. (2003). "Relating K α to relative state parameter index". *Journal of Geotechnical and Geoenvironmental Engineering*, Vol. 129, No. 8, pp. 770-773.

Boulanger, R. W. & Seed, R. B. (1995). "Liquefaction of sand under bidirectional monotonic and cyclic loading". *Journal of Geotechnical Engineering*, Vol. 121, No. 12, pp. 870-878.

Boulanger, R. W., Seed, R. B., Chan, C. K., Seed, H. B. & Sousa, J. B. (1991). *Liquefaction behavior of saturated sands under uni-directional and bi-directional monotonic and cyclic simple shear loading*, University of California, Berkeley.

Boulanger, R. W. & Truman, S. P. (1996). "Void redistribution in sand under post-earthquake loading". *Canadian Geotechnical Journal*, Vol. 33, No. 5, pp. 829-834.

Boulanger, R. W. & Ziotopoulou, K. (2012). *A sand plasticity model for earthquake engineering applications*, Center for Geotechnical Modeling, Department of Civil and Environmental Engineering, University of California, Davis, CA.

Boulanger, R. W. & Ziotopoulou, K. (2013). "Formulation of a sand plasticity plane-strain model for earthquake engineering applications". *Soil Dynamics and Earthquake Engineering*, Vol. 53, pp. 254-267.

Brennan, A. & Madabhushi, S. (2005). "Liquefaction and drainage in stratified soil". *Journal of Geotechnical and Geoenvironmental Engineering*, Vol. 131, pp. 876-885.

Brennan, A. J., Thusyanthan, N. I. & Madabhushi, S. P. G. (2005). "Evaluation of shear modulus and damping in dynamic centrifuge tests". *Journal of Geotechnical and Geoenvironmental Engineering*, Vol. 131, No. 12, pp. 1488-1497.

Byrne, P. M., Park, S. S., Beaty, M., Sharp, M., Gonzalez, L. & Abdoun, T. (2004).

"Numerical modeling of liquefaction and comparison with centrifuge tests". *Canadian Geotechnical Journal,* Vol. 41, No. 2, pp. 193-211.

Chakrabortty, P. & Popescu, R. (2012). "Numerical simulation of centrifuge tests on homogeneous and heterogeneous soil models". *Computers and Geotechnics,* Vol. 41, pp. 95-105.

Chakrabortty, P., Popescu, R., Philips, R. & Dief, H. (2008). "Liquefaction of heterogeneous soil: centrifuge study" *Proceedings of International Association for Computer Methods and Advances in Geomechanics,* pp. 1389-1396.

Dafalias, Y. F. & Manzari, M. T. (2004). "Simple plasticity sand model accounting for fabric change effects". *Journal of Engineering mechanics,* Vol. 130, No. 6, pp. 622-634.

Davis, R. O. & Berrill, J. B. (1998). "Rational approximation of stress and strain based on downhole acceleration measurements". *International Journal for Numerical and Analytical Methods in Geomechanics,* Vol. 22, No. 8, pp. 603-619.

Davis, R. O. & Berrill, J. B. (2001). "Pore Pressure and Dissipated Energy inEarthquakes—Field Verification". *Journal of Geotechnical and Geoenvironmental Engineering,* Vol. 127, No. 3, pp. 269-274.

Dobry, R. & Abdoun, T. (1998). "Post-triggering response of liquefied sand in the free field and near foundations" *Proceedings ASCE 1998 Specialty Conference on Geotechnical Earthquake Engineering and Soil Dynamics,* ASCE, pp. 270-300.

Dobry, R. & Liu, L. (1992). "Centrifuge modeling of soil liquefaction" *Tenth World Conference on Earthquake Engineering,* pp. 6801-6809.

Dobry, R., Taboada, V. & Liu, L. (1995). "Centrifuge modeling of liquefaction effects during earthquakes" *Proceedings 1st International Conference on Earthquake Geotechnical Engineering,* Rotterdam, The Netherlands, Balkema, pp. 129-162.

EERI (2011). *Geotechnical Effects of the Mw 9.0 Tohoku, Japan, Earthquake of March 11, 2011*.

Elgamal, A., Yang, Z. H., Lai, T., Kutter, B. L. & Wilson, D. W. (2005). "Dynamic response of saturated dense sand in laminated centrifuge container". *Journal of Geotechnical and Geoenvironmental Engineering,* Vol. 131, No. 5, pp. 598-609.

Elgamal, A., Zeghal, M. & Parra, E. (1996a). "Liquefaction of reclaimed island in Kobe, Japan". *Journal of Geotechnical Engineering,* Vol. 122, No. 1, pp. 39-49.

Elgamal, A. W., Zeghal, M., Taboda, V. & Dobry, R. (1996b). "Analysis of site liquefaction and lateral spreading using centrifuge testing records". *Soils and Foundations,* Vol. 36, No. 2, pp. 111-121.

Fiegel, G. L. & Kutter, B. L. (1994). "Liquefaction mechanism for layered soils". *Journal*

of Geotechnical Engineering, Vol. 120, No. 4, pp. 737-755.

Flanagan, D. P. & Belytschko, T. (1981). "A uniform strain hexahedron and quadrilateral with orthogonal hourglass control". *International Journal for Numerical Methods in Engineering,* Vol. 17, No. 5, pp. 679-706.

GEER (2011). *Quick Report 2: Preliminary Observations of Levee Performance and Damage following the March 11, 2011 Tohoku Offshore Earthquake, Japan*.

Ghosh, B., Klar, A. & Madabhushi, S. P. G. (2005). "Modification of site response in presence of localised soft layer". *Journal of Earthquake Engineering,* Vol. 9, No. 6, pp. 855-876.

Harder, L. F. & Boulanger, R. W. (1997). "Application of Kσ and Kα correction factors" *NCEER Workshop on Evaluation of Liquefaction Resistance of Soils*.

Hashiguchi, K. & Chen, Z. P. (1998). "Elastoplastic constitutive equation of soils with the subloading surface and the rotational hardening". *International Journal for Numerical and Analytical Methods in Geomechanics,* Vol. 22, No. 3, pp. 197-227.

Idriss, I. M. & Boulanger, R. W. (2003). "Estimating Kα for use in evaluating cyclic resistance of sloping ground" *Eighth U.S.-Japan Workshop on Earthquake Resistant Design of Lifeline Facilities and Countermeasures Against Liquefaction*, Technical Report MCEER-03-0003, Multidisciplinary Center for Earthquake Engineering Research, pp.

Ishihara, K. & Cubrinovski, M. (1998). "Problems associated with liquefaction and lateral spreading during earthquakes". *Geotechnical Earthquake Engineering and Soil Dynamics III,* Vol. 75, No. 1, pp. 301-312.

Ishihara, K. & Koga, Y. (1981). "Case studies of liquefaction in 1964 Niigata Earthquake". *Soils and Foundations,* Vol. 21, No. 3, pp. 35.

Ishihara, K. & Towhata, I. (1983). "Effects of rotation of principal stress firections on cyclic response of sand" *Constitutive Laws for Engineering Materials; Theory and Application: Proceedings of the International Conference Held in Tucson, Arizona, January 10-14, 1983,* University of Arizona, pp. 203.

Ishihara, K. & Yamazaki, F. (1980). "Cyclic simple shear tests on saturated sand in multi-directional loading". *Soils and Foundations,* Vol. 20, No. 1, pp. 45-59.

Ishihara, K. & Yoshimine, M. (1992). "Evaluation of settlements in sand deposits following liquefaction during earthquakes". *Soils and Foundations,* Vol. 32, No. 1, pp. 173-188.

Kamai, R. & Boulanger, R. W. (2011). *Liquefaction-Induced Shear Strain Localization Processes in Layered Soil Profiles.* PhD dissertation, University of California, Davis.

Kawakami, F. & Asada, A. (1966). "Damage to the ground and earth structures by the Niigata earthquake of June 16, 1964". *Soils and Foundations,* Vol. 6, No. 1, pp. 14-30.

Kimura, T., Takemura, J., Hiro-Oka, A., Okamura, M. & Matsuda, T. (1997). "Countermeasures against liquefaction of sand deposits with structures" *Proceedings of the 1st International Conference on Earthquake Geotechnical Engineering. Edited by K. Ishihara. AA Balkema, Rotterdam, The Netherlands*, pp. 1203-1224.

Kishida, H. (1966). "Damage to reinforced concrete buildings in Niigata City with special reference to foundation engineering". *Soils and foundations,* Vol. 6, No. 1, pp. 71-88.

Koga, Y. & Matsuo, O. (1990). "Shaking table tests of embankments resting on liquefiable sandy ground". *Soils and Foundations,* Vol. 30, No. 4, pp. 162-174.

Kokusho, T. (1999). "Water film in liquefied sand and its effect on lateral spread". *Journal of Geotechnical and Geoenvironmental Engineering,* Vol. 125, No. 10, pp. 817-826.

Kokusho, T. (2000). "Mechanism for water film generation and lateral flow in liquefied sand layer". *Soils and Foundations,* Vol. 40, No. 5, pp. 99-111.

Kokusho, T. & Fujita, K. (2002). "Site investigations for involvement of water films in lateral flow in liquefied ground". *Journal of Geotechnical and Geoenvironmental Engineering,* Vol. 128, No. 11, pp. 917-925.

Kokusho, T. & Kojima, T. (2002). "Mechanism for postliquefaction water film generation in layered sand". *Journal of Geotechnical and Geoenvironmental Engineering,* Vol. 128, No. 2, pp. 129-137.

Kramer, S. L. (1996). *Geotechnical earthquake engineering,* Upper Saddle River, NJ, Prentice Hall.

Kulasingam, R., Malvick, E. J., Boulanger, R. W. & Kutter, B. L. (2004). "Strength loss and localization at silt interlayers in slopes of liquefied sand". *Journal of Geotechnical and Geoenvironmental Engineering,* Vol. 130, No. 11, pp. 1192-1202.

Liu, H. & Qiao, T. (1984a). "Liquefaction potential of saturated sand deposits underlying foundation of structure" *Proceedings of the 8th World Conference on Earthquake Engineering,* San Francisco, pp. 21-28.

Liu, H. & Qiao, T. (1984b). "Liquefaction potential of saturated sand deposits underlying foundation of structure" *Eighth World Conference on Earthquake Engineering,* San Francisco, pp. 199-206.

Lu, X. B. & Cui, P. (2010). "A study on water film in saturated sand". *International Journal of Sediment Research,* Vol. 25, No. 3, pp. 221-232.

Maharjan, M. & Takahashi, A. (2013a). "Centrifuge model tests on liquefaction-induced settlement and pore water migration in non-homogeneous soil deposits". *Soil Dynamics and Earthquake Engineering,* Vol. 55, pp. 161-169.

Maharjan, M. & Takahashi, A. (2013b). "Effects of non-homogeneity on liquefaction in stratified soil deposits" *Proceeding of Tenth International Conference for Urban Earthquake Engineering,* Tokyo, Japan, pp. 483-492.

Maharjan, M. & Takahashi, A. (2014a). "Liquefaction-induced deformation of earthen embankments on non-homogeneous soil deposits under sequential ground motions". *Soil Dynamics and Earthquake Engineering,* Vol. 66, pp. 113-124.

Maharjan, M. & Takahashi, A. (2014b). "Numerical simulation of liquefaction-induced deformation of embankments on non-homogeneous foundation" *Numerical Methods in Geotechnical Engineering,* Delft, The Netherlands, Taylor & Francis Group.

Malvick, E. J., Kutter, B. L. & Boulanger, R. W. (2008a). "Postshaking shear strain localization in a centrifuge model of a saturated sand slope". *Journal of Geotechnical and Geoenvironmental Engineering,* Vol. 134, No. 2, pp. 164-174.

Malvick, E. J., Kutter, B. L. & Boulanger, R. W. (2008b). "Postshaking shear strain localization in a centrifuge model of a saturated sand slope". *Journal of Geotechnical and Geoenvironmental Engineering,* Vol. 134, pp. 164-174.

Marcuson, W. L. & Silver, M. L. (1987). "Shake-Proof Dams". *Civil Engineering—ASCE,* Vol. 57, No. 12, pp. 44-47.

Matsuo, O. (1996). "Damage to river dikes". *Soils and Foundations,* Vol. Jan, pp. 235-240.

MCEER (2007). *Major Peruvian & Chilean Earthquakes of the 20th Century*, University at Buffalo, The state University of New York.

Meneses-Loja, J., Ishihara, K. & Towhata, I. (1998). "Effects of superimposing cyclic shear stress on the undrained behavior of saturated sand under monotonic loading". *Soils and foundations,* Vol. 38, No. 4, pp. 115-127.

Miura, N. (1975). "Effect of water on the behavior of a quartz-rich sand under high stresses". *Soils and Foundations,* Vol. 15, No. 4, pp. 1-12.

Naesgaard, E., Byrne, P., Seid-Karbasi, M. & Park, S. (2005). "Modeling flow liquefaction, its mitigation, and comparison with centrifuge tests", *Proceedings, performance based design in earthquake geotechnical engineering: concepts and research, geotechnical earthquake engineering satellite conference,* Osaka, Japan, pp. 95-102.

National Research Council, B. (1985). *Liquefaction of soils during earthquakes*, National Academy Press.

Oka, F., Tsai, P., Kimoto, S. & Kato, R. (2012). "Damage patterns of river embankments due to the 2011 off the Pacific Coast of Tohoku earthquake and a numerical modeling of the deformation of river embankments with a clayey subsoil layer". *Soils and Foundations,* Vol. 52, No. 5, pp. 890-909.

Okamura, M., Abdoun, T. H., Dobry, R., Sharp, M. K. & Taboda, V. M. (2001). "Effects of sand permeability and weak aftershocks on earthquake-induced lateral spreading". *Soils and Foundations,* Vol. 41, No. 6, pp. 63-77.

Okamura, M. & Matsuo, O. (2002). "Effects of remedial measures for mitigating embankment settlement due to foundation liquefaction". *International Journal of Physical Modelling in Geotechnics,* Vol. 2, No. 2, pp. 1-12.

Osterberg, J. O. (1957). "Influence values for vertical stresses in semi-infinite mass due to embankment loading" *Proceedings of the 4th International Conference on Soil Mechanics and Foundation Engineering*, London, pp. 393-396.

Port and Airport Research Institute. (1997). *Handbook on liquefaction remediation of reclaimed land*.

PEER. 2013. *Pacific Earthquake Engineering Research (PEER) Center: Ground motion database* [Online].

Popescu, R., Prevost, J. H., Deodatis, G. & Chakrabortty, P. (2006). "Dynamics of nonlinear porous media with applications to soil liquefaction". *Soil Dynamics and Earthquake Engineering,* Vol. 26, No. 6-7, pp. 648-665.

Sasaki, Y., Towhata, I., Miyamoto, K., Shirato, M., Narita, A., Sasaki, T. & Sako, S. (2012). "Reconnaissance report on damage in and around river levees caused by the 2011 off the Pacific coast of Tohoku earthquake". *Soils and Foundations,* Vol. 52, No. 5, pp. 1016-1032.

Schofield, A. N. (1981). "Dynamic and earthquake geotechnical centrifuge modelling" *Proceedings, International Conference on Recent Advances in Geotechnical Earthquake Engineering and Soil Dynamics*, Missouri, USA, pp. 1081-1100.

Scott, R. (1986). "Solidification and consolidation of a liquefied sand column". *Soils and Foundations,* Vol. 26, No. 4, pp. 23-31.

Scott, R. & Zuckerman, K. (1972). "Sandblows and liquefaction in the Great Alaska Earthquake of 1964", Engineering publication, Washington DC,. *National Academy of Sciences*, pp. 170-189.

Seed, H. B. (1968). "Landslides during earthquakes due to liquefaction". *Journal of Soil Mechanics & Foundations Div,* Vol. 94, No. 5, pp. 1055-1123.

Seed, H. B. (1981). "Earthquake-resistant design of earth dams" *First International Conference on Recent Advances in Geotechnical earthquake Engineering and Soil*

Dynamics (1981: April 26-May 3; St. Louis, Missouri), Missouri S&T (formerly the University of Missouri--Rolla).

Seid-Karbasi, M. & Byrne, P. M. (2007). "Seismic liquefaction, lateral spreading, and flow slides: a numerical investigation into void redistribution". *Canadian Geotechnical Journal*, Vol. 44, No. 7, pp. 873-890.

Sento, N., Kazama, M., Uzuoka, R., Ohmura, H. & Ishimaru, M. (2004). "Possibility of postliquefaction flow failure due to seepage". *Journal of Geotechnical and Geoenvironmental Engineering*, Vol. 130, pp. 707.

Shahir, H., Pak, A., Taiebat, M. & Jeremić, B. (2012). "Evaluation of variation of permeability in liquefiable soil under earthquake loading". *Computers and Geotechnics*, Vol. 40, pp. 74-88.

Shamoto, Y., Zhang, J. M. & Goto, S. (1997). "Mechanism of large post-liquefaction deformation in saturated sand". *Soils and Foundations*, Vol. 37, No. 2, pp. 71-80.

Sharp, M. K. & Adalier, K. (2006). "Seismic response of earth dam with varying depth of liquefiable foundation layer". *Soil Dynamics and Earthquake Engineering*, Vol. 26, No. 11, pp. 1028-1037.

Taiebat, M., Jeremic, B., Dafalias, Y. F., Kaynia, A. M. & Cheng, Z. (2010). "Propagation of seismic waves through liquefied soils". *Soil Dynamics and Earthquake Engineering*, Vol. 30, No. 4, pp. 236-257.

Takahashi, A. (2002). *Soil-pile interaction in liquefaction-induced lateral spreading of soils*. PhD dissertation, Tokyo Institute of Technology.

Takahashi, A. (2004). *Development of data acquisition program for digital oscilloscope*, Imperial College, London.

Takemura, J., Kondoh, M., Esaki, T., Kouda, M. & Kusakabe, O. (1999). "Centrifuge model tests on double propped wall excavation in soft clay". *Soils and Foundations*, Vol. 39, No. 3, pp. 75-87.

Tani, S. (1991). "Consideration of earthquake damage to earth dam for irrigation in Japan" *Proceedings of 2nd Intl. Conf. on Recent Advances in Geotechnical Earthquake Engineering and Soil Dynamics*, Missouri, USA, pp. 1137-1142.

Tatsuoka, F., Goto, S. & Sakamoto, M. (1986a). "Effects of some factors on strength and deformation characteristics of sand at low pressures". *Soils and foundations*, Vol. 26, No. 1, pp. 105-114.

Tatsuoka, F., Ochi, K., Fujii, S. & Okamoto, M. (1986b). "Cyclic undrained triaxial and torsional shear strength of sands for different sample preparation methods". *Soils and Foundations*, Vol. 26, No. 3, pp. 23-41.

Taylor, R. N. (1995). *Geotechnical centrifuge technology,* London, Blackie Academic and Professional.

Thevanayagam, S. & Martin, G. R. (2002). "Liquefaction in silty soils—screening and remediation issues". *Soil Dynamics and Earthquake Engineering,* Vol. 22, No. 9, pp. 1035-1042.

Tohumcu Özener, P., Özaydın, K. & Berilgen, M. M. (2008). "Investigation of liquefaction and pore water pressure development in layered sands". *Bulletin of Earthquake Engineering,* Vol. 7, No. 1, pp. 199-219.

Towhata, I., Yasuda, S., Ohtomo, K. & Yamada, K. (1988). "Experimental studies on liquefaction induced permanent ground displacement" *Proceedings. 1st Japan-US Workshop on Liquefaction, Large Ground Deformation and Their Effects on Lifeline Facilities* pp. 81-92.

Tsukamo, Y. & Ishihara, K. (2010). "Analysis of settlement of soil deposits following liquefaction during earthquakes". *Soils and Foundations,* Vol. 50, No. 3, pp. 399-411.

University of Washington. 2000. *http://www.ce.washington.edu/~liquefaction/html/what/what1.html* [Online].

U. S. Geological Survey. (2013). *Subsurface exploration with the cone penetration testing truck* [Online].

Vaid, Y. P. & Chern, J. C. (1985). "Cyclic and monotonic undrained response of saturated sands" *Advances in the art of testing soils under cyclic conditions,* ASCE Annual Convention, Detroit, pp. 120-147.

Vaid, Y. P. & Finn, W. D. L. (1979). "Static shear and liquefaction potential". *Journal of Geotechnical and Geoenvironmental Engineering,* Vol. ASCE(105), pp. 1223-1246.

Vaid, Y. P. & Thomas, J. (1995). "Liquefaction and postliquefaction behavior of sand". *Journal of Geotechnical Engineering,* Vol. 121, No. 2, pp. 163-173.

Wang, Z. L., Dafalias, Y. F. & Shen, C. K. (1990). "Bounding surface hypoplasticity model for sand". *Journal of Engineering mechanics,* Vol. 116, No. 5, pp. 983-1001.

Xia, Z.-F., Ye, G.-L., Wang, J.-H., Ye, B. & Zhang, F. (2010). "Fully coupled numerical analysis of repeated shake-consolidation process of earth embankment on liquefiable foundation". *Soil Dynamics and Earthquake Engineering,* Vol. 30, No. 11, pp. 1309-1318.

Yang, Z. & Elgamal, A. (2002). "Influence of permeability on liquefaction-induced shear deformation". *Journal of Engineering Mechanics,* Vol. 128, No. 7, pp. 720-729.

Yang, Z. & Elgamal, A. (2003). "Application of unconstrained optimization and sensitivity

analysis to calibration of a soil constitutive model". *International Journal for Numerical and Analytical Methods in Geomechanics,* Vol. 27, No. 15, pp. 1277-1297.

Yang, Z., Elgamal, A. & Parra, E. (2003). "Computational model for cyclic mobility and associated shear deformation". *Journal of Geotechnical and Geoenvironmental Engineering,* Vol. 129, No. 12, pp. 1119-1127.

Ye, B., Ye, G., Zhang, F. & Yashima, A. (2007). "Experiment and numerical simulation of repeated liquefaction-consolidation of sand". *Soils and Foundations,* Vol. 47, No. 3, pp. 547-558.

Yoshida, N. & Finn, W. D. L. (2000). "Simulation of liquefaction beneath an impermeable surface layer". *Soil Dynamics and Earthquake Engineering,* Vol. 19, No. 5, pp. 333-338.

Yoshida, N., Masanori, K., Masuda, T. & Finn, W. D. L. (1987). "Behavior of sand after liquefaction". *Technical report,* Vol. 1.

Zeghal, M., Elgamal, A. W., Zeng, X. W. & Arulmoli, K. (1999). "Mechanism of liquefaction response in sand-silt dynamic centrifuge tests". *Soil Dynamics and Earthquake Engineering,* Vol. 18, No. 1, pp. 71-85.

Zhang, S., Wang, G. & Sa, W. (2013). "Damage evaluation of concrete gravity dams under mainshock–aftershock seismic sequences". *Soil Dynamics and Earthquake Engineering,* Vol. 50, pp. 16-27.

Ziotopoulou, K. & Boulanger, R. W. (2013). "Calibration and implementation of a sand plasticity plane-strain model for earthquake engineering applications". *Soil Dynamics and Earthquake Engineering,* Vol. 53, pp. 268-280.

Appendix A
Back analysis of instrumental array

A.1 Introduction

Back analyses of accelerometer array data from the field or physical models to define the stress-strain response of the soil has been found useful by many researchers in the past studies (Koga and Matsuo, 1990; Elgamal et al., 1996ba; Elgamal et al., 1996ab; Zeghal et al., 1999; Elgamal et al., 2005; Brennan et al., 2005; Davis and Berrill, 2001, 1998). The stress-strain calculated from the back analyses can be utilized to identify the stiffness, damping of the saturated soil deposits. (Koga and Matsuo, 1990) derived stress strain loops in 1 g shaking table models to describe liquefaction effects. Davis and Berrill (1998) provided an accurate approximation of determining stress and strain, based in instrumental records. Zeghal et al. (1999); Adalier and Elgamal (2002) employed the recorded lateral accelerations to evaluate shear stress and strain histories at different elevations within the soil systems. Brennan et al. (2005) evaluated the shear modulus and shear degradation curves for a dry sand, saturated sand, soft clay from the acceleration histories obtained from centrifuge tests.

The back analysis techniques compared herein assume a 1D shear-beam response with upward propagation of shear waves. Other forms of waves such as surface waves or P-waves reflecting off the container walls are assumed to be largely negligible. Figure 2.3 is a schematic representation of a 1D soil column, divided into elements of soil between every two adjacent accelerometers, also referred to as ‘nodes’ and pore pressure transducers are implanted between two accelerometers, forming a vertical array. Hence, among all the centrifuge tests conducted in laminar box, the transducers are located as mentioned above. The derivation of shear strain requires integrating the accelerations twice in time to obtain displacements, followed by differentiation of the displacements in space to obtain shear strains. The differentiation of displacement data at discrete points has been performed using different numerical methods. Zeghal and Elgamal (1994) and Zeghal et al. (1995) used piece-wise linear interpolation, whereas Davis and Berrill (1998, 2001) used a cosine chain similarly to conducting a Fourier transform of the displacement profile. In this study the method proposed by Zeghal et al. (1999) is used to calculate the shear stress and shear strain from the accelerations recorded.

A.2 Calculation of shear stresses

Shear stresses are calculated at the centers of each element (midpoints between accelerometers), as indicated in Fig. A.1, by the summation of the horizontal inertia forces of the soil above that point. Accelerations are assumed to vary linearly between accelerometers.

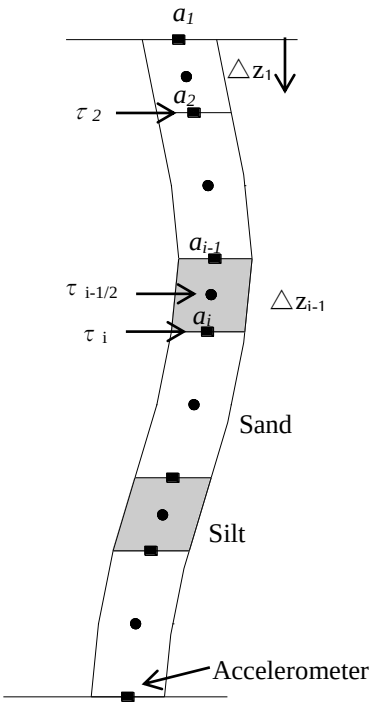

Figure A.1. Schematic of 1D shear beam model and stress-strain sampling locations (as of Model 2 and 4).

The governing equations for determining shear stress is

$$\frac{\partial \tau}{\partial z} = \rho \ddot{u}, \text{ with boundary conditions u(h,t)} = \mathrm{u}_g(t), \text{ and } \tau(0,t) = 0 \qquad \text{(A.1)}$$

in which t is time, z is depth coordinate, $\tau = \tau(z,t)$ is lateral shear stress, $\ddot{u} = u(z,t)$ is absolute lateral acceleration, u=u(z,t) is absolute lateral displacement, $u_g(t)$ is input base lateral displacement, $\rho = \rho(z)$ is mass density, h is total depth of soil stratum

The shear stress at the surface is zero, and thus the shear stresses at the first two elements are determined as by integrating the equation of motion and using the surface stress-free boundary condition (Eq. 1), shear stress at any level z within the ground is expressed as:

$$\tau(z,t) = \int_0^z \rho \ddot{u}(\xi,t)\mathrm{d}\xi \qquad \text{(A.2)}$$

The shear stresses at levels z_i and $(z_{i-1}+z_i)/2$ may be expressed by Eq. 2 as (Fig. A.1):

$$\tau_i(t)=\tau_{i-1}(t)+\rho_{i-1}\frac{\ddot{u}_{i-1}+\ddot{u}_i}{2}\Delta z_{u-1},\quad i=2,3,.... \tag{A.3}$$

$$\tau_{i-1/2}(t)=\tau_{i-1}(t)+\rho_{i-1}\frac{3\ddot{u}_{i-1}+\ddot{u}_i}{8}\Delta z_{u-1},\quad i=2,3,.... \tag{A.4}$$

In which the subscripts i and $(i-1/2)$ refer to levels z_i (of the ith accelerometer) and $(z_{i-1}+z_i)/2$ (halfway between accelerometer *(i-1)* and *i)* respectively, $\ddot{u}_i=\ddot{u}(z,t)$, ρ_{i-1} is the average mass density for the soil layer between levels z_{i-1} and z_i, and Δz_i is the spacing interval as shown in Fig. A.1

A.3 Calculation of shear strains

Shear strains are computed as the derivative of the soil displacements with depth. The displacements are evaluated by double-integration of the accelerations histories. Before integration, the acceleration time histories are filtered to eliminate the frequencies that are not within the sensor's bandwidth. Filtering was performed in the frequency domain using 7th-order Butterworth high-pass and low-pass filters with corner frequencies of 0.3 Hz and 10 Hz, respectively, based on the signal-to-noise characteristics of the recorded accelerations and knowledge of the instrumentation/data acquisition system's characteristics. A corresponding set of second order accurate shear strains at levels z_i and $(z_{i-1}+z_i)/2$ may be expressed as

$$\gamma_i(t)=\frac{1}{\Delta z_{i-1}+\Delta z_i}\left((u_{i+1}-u_i)\frac{\Delta z_{i-1}}{\Delta z_i}+(u_i-u_{i-1})\frac{\Delta z_i}{\Delta z_{i-1}}\right),\quad i=2,3,... \tag{A.5}$$

$$\gamma_{i-1/2}(t)=\frac{u_i-u_{i-1}}{\Delta z_{i-1}},\quad i=2,3,... \tag{A.6}$$

in which $u_i=u(z_i,t)$ is displacement evaluated from double integration of the acceleration histories.

A.4 Analysis results and observations

The acceleration histories recorded during the centrifuge model tests were employed in Eqs. A.3-A.6 to obtain shear stress and shear strain time histories at different depths, as shown in Figs. A.2-A.5. Stress-strain curves obtained from the time histories of shear stress and shear strain are shown in Figs. A.6-A.9.

Very large strains are observed during 12-15 sec of loading in the silt layer in Model 2-4 (Figs. A.6-A.9). The shear strain is more larger in Model 2 and 4 compared to that in Model 3. The presence of the continuous relatively impermeable silt layer acts as a barrier to retard the escape of the pore water. This causes an accumulation of pore water beneath the silt layer, causing a large shear strain. The continuous silt layer could completely trap the pore water, leading to a larger shear strain than in Model 2. The shear strain sharply increases during 12-15 sec, indicating the onset of liquefaction. After the initial liquefaction, the soil responses are characterized by cycles of large strains and small stresses, reducing the stiffness of the soil (Figs. A.5-A.9). However, the shear strains at the lower most strata are comparatively smaller and the shear stresses are comparatively larger. All the hysteresis stress-strain lops indicate softening with increase in number of cycles.

Figure A.10 shows the effective stress paths at different locations for all the model tests. The vertical effective stress is computed by Eq. A.7.

$$\sigma_v^{'} = \sigma_{vo}^{'} - \Delta u \qquad \text{(A.7)}$$

Where Δu = excess pore water pressure ratio

$\sigma_{vo}^{'}$ =Vertical effective confining stress

In Model 1, the whole soil column attains zero effective stress state, indicating the total liquefaction in the soil column. In Model 2-4, the soil does not attain zero effective stress state at the lower most strata, while the rest attains zero effective stress state. During the first few cycles, the shear stress increases and soon decreases along with the diminution of effective vertical stress.

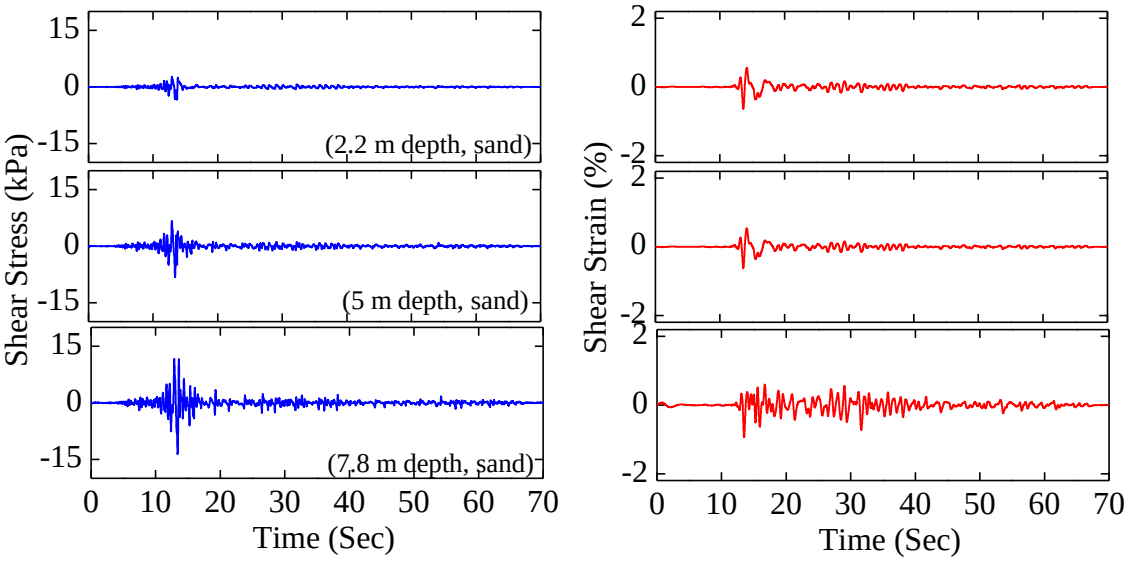

Figure A.2. Shear stress and shear strain time histories at 2.2, 5.0, and 7.8 m depths for Model 1.

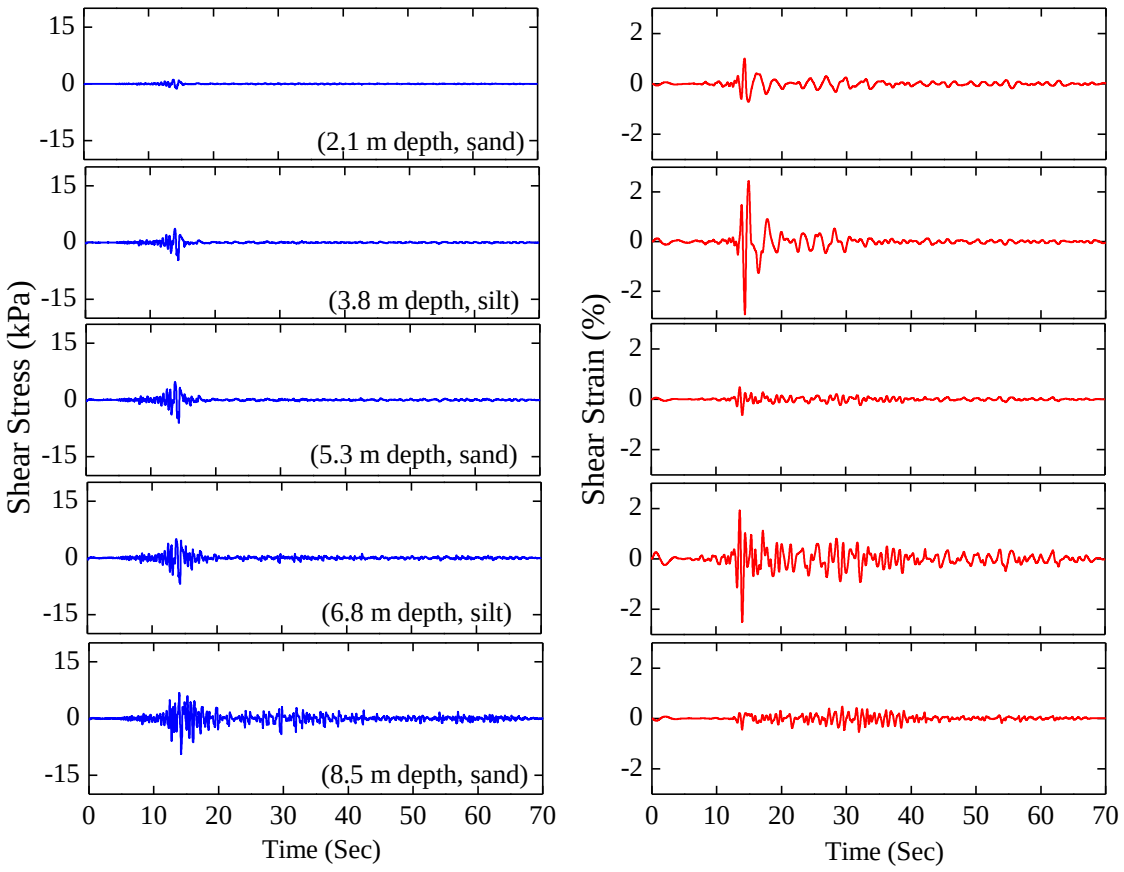

Figure A.3. Shear stress and shear strain time histories at 2.1, 3.75, 5.3, 6.8, and 8.5 m depths for Model 2.

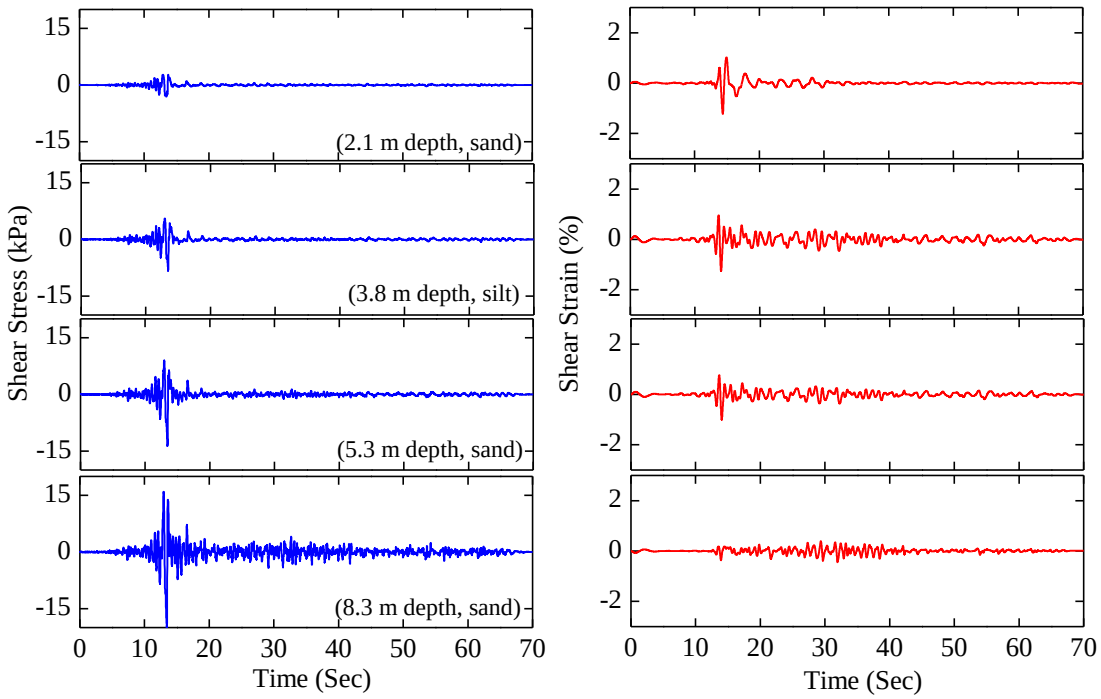

Figure A.4. Shear stress and shear strain time histories at 2.1, 3.8, 5.3, and 8.3 m depths for Model 3.

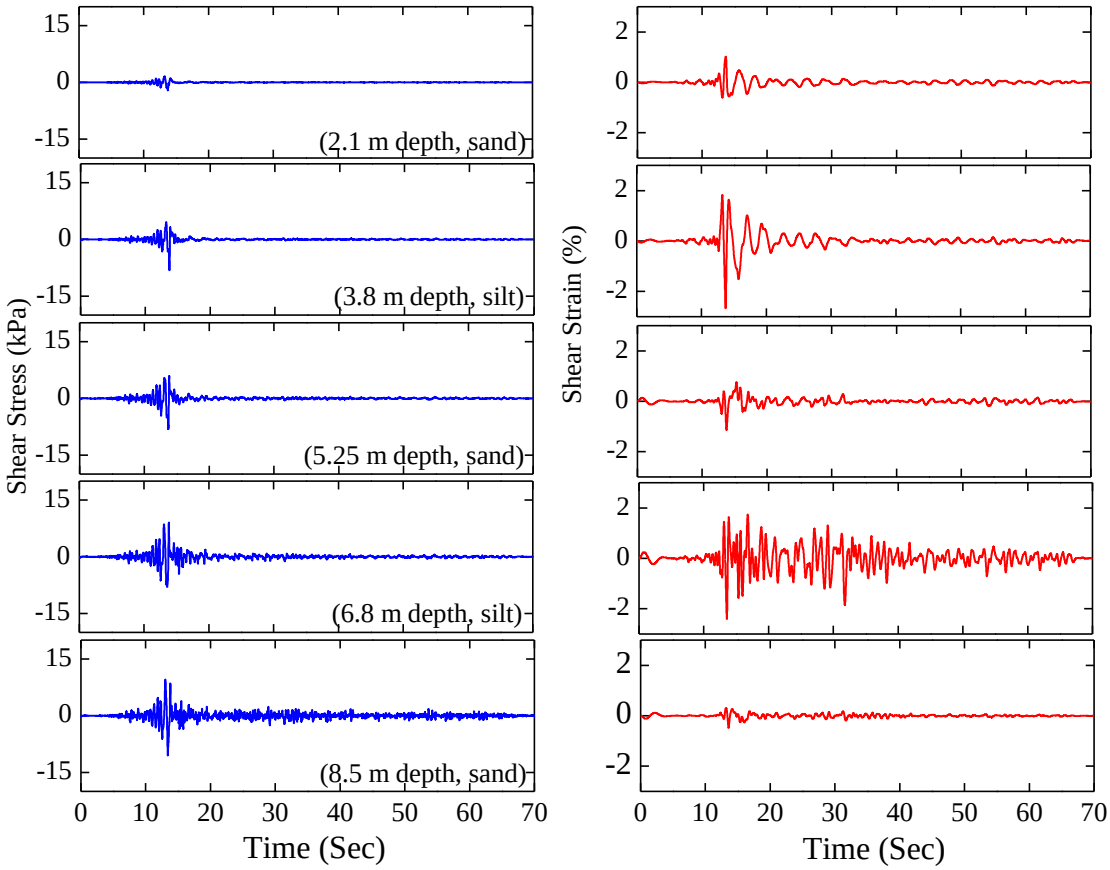

Figure A.5. Shear stress and shear strain time histories at 2.1, 3.8, 5.3, 6.8, and 8.3 m depths for Model 4.

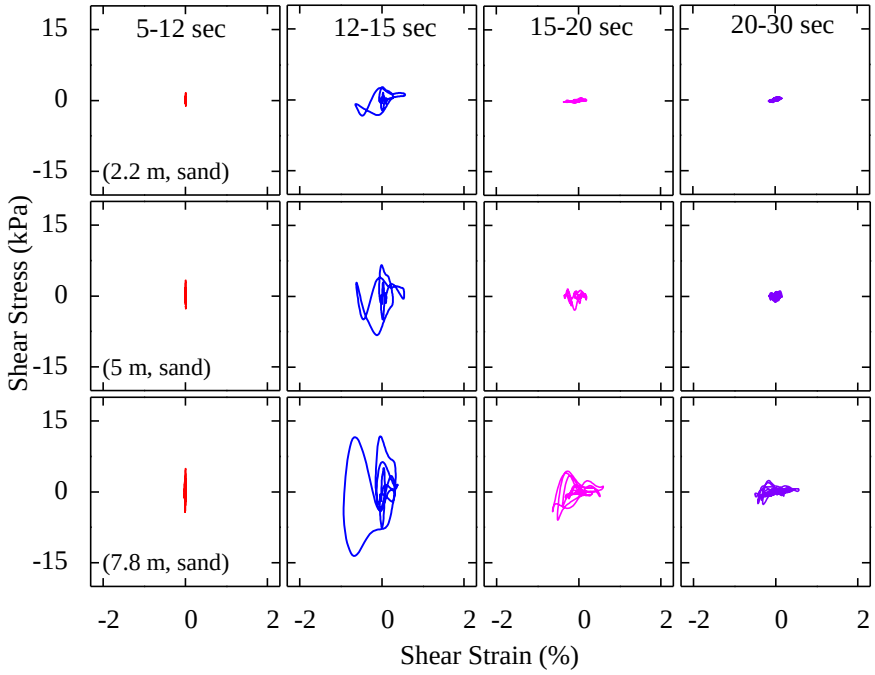

Figure A.6. Shear stress-strain relationships at 2.2, 5.0, and 7.8 m in Model 1.

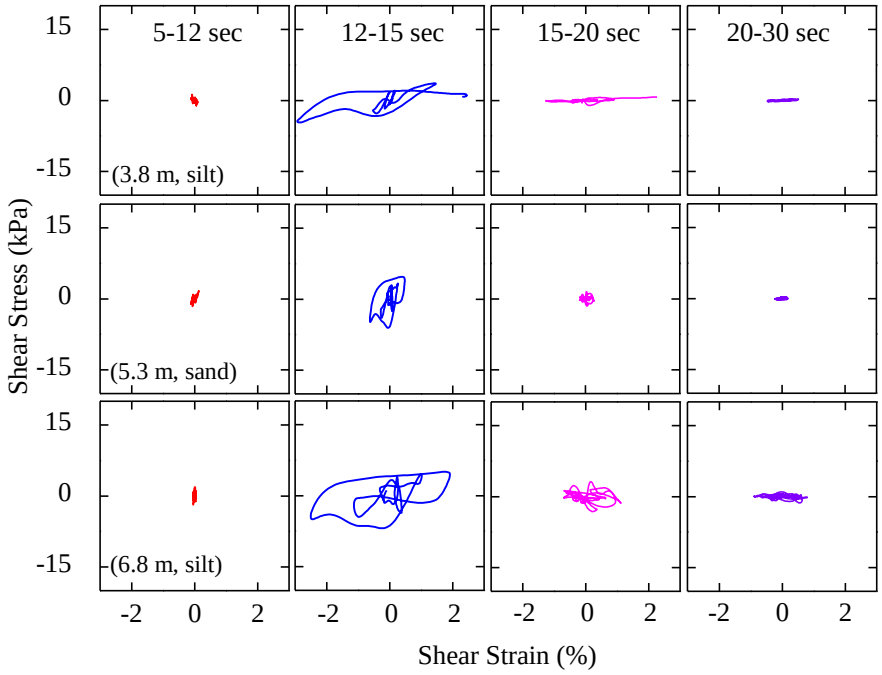

Figure A.7. Shear stress-strain relationships at 3.8, 5.3, and 6.8 m in Model 2.

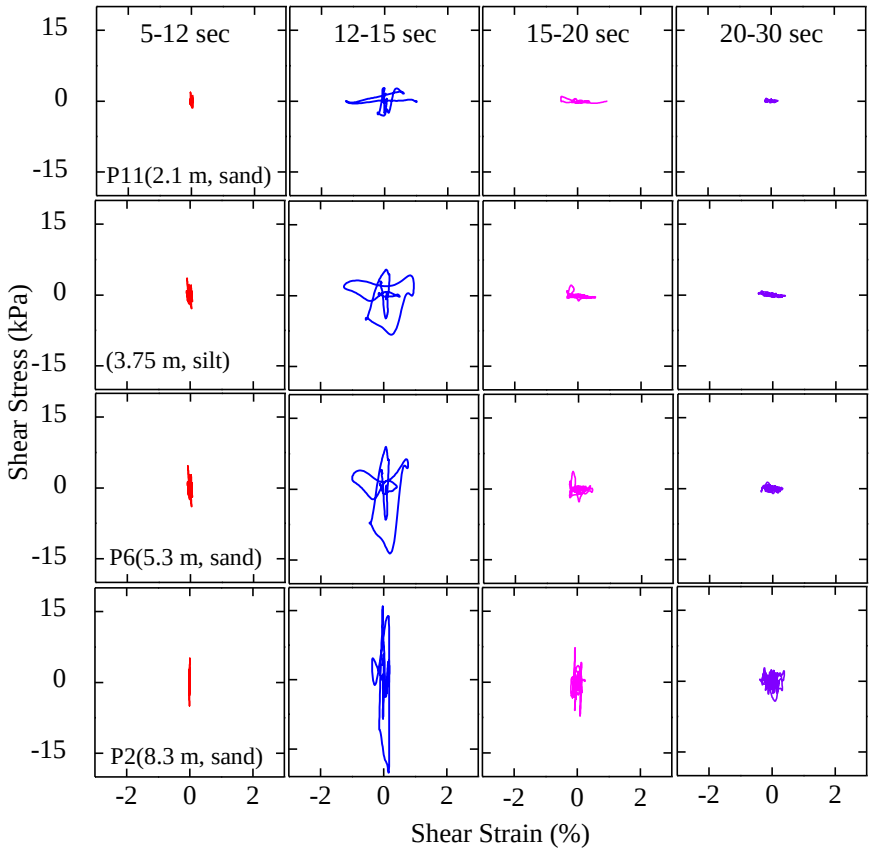

Figure A.8. Shear stress-strain relationships at 2.1, 3.8, 5.3, and 8.3 m in Model 3.

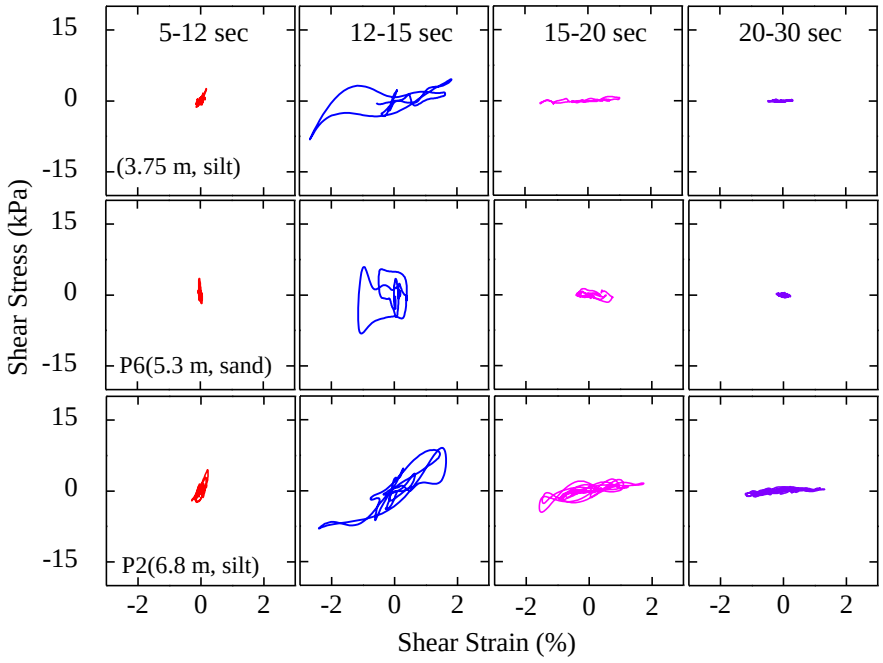

Figure A.9. Shear stress-strain relationships at 3.8, 5.3, and 6.8 m in Model 4.

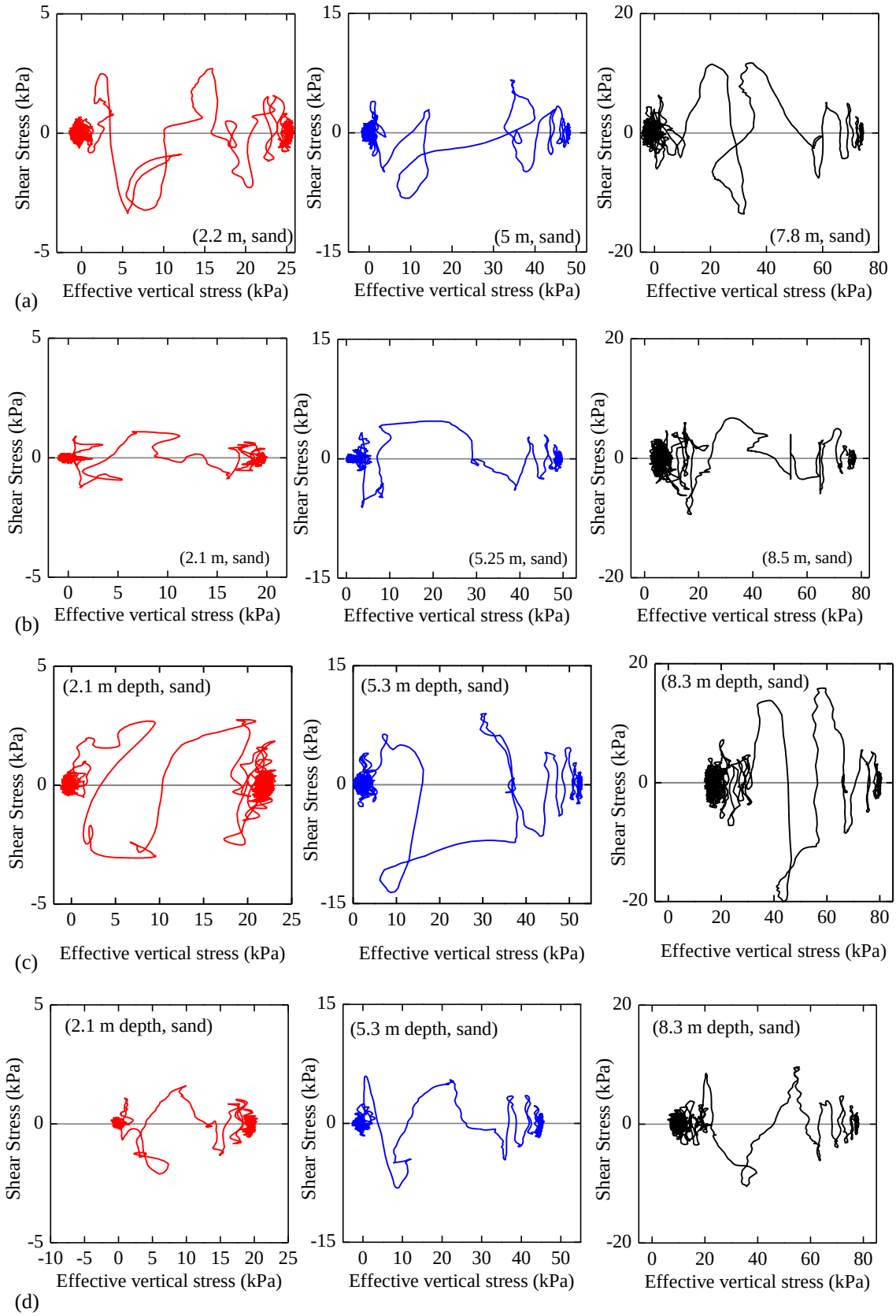

Figure A.10. Effective stress paths: (a) Model 1; (b) Model 2; (c) Model 3; and (d) Model 4.

A.5 Back analyses for calculation of shear wave velocity

The acceleration time histories recorded by the accelerometer during experiment are employed to calculate the shear wave velocity. The time lag between the input wave and received wave can be used to compute the shear wave velocity as

$$\text{Shear wave velocity, } v = \frac{\Delta h}{\Delta t}$$

where, Δh is the depth between the input wave and the point at which the wave is received and Δt is the time lag between the input wave and received wave.

The first arrival time can be calculated by using cross-correlation function (Takahashi, 2004). Cross-correlation is a measure of similarity of two waveforms as a function of a time-lag applied to one of them..

Figure A.11 shows the shear wave velocity profiles for all the model tests for different time windows. In all the tests, before the onset of liquefaction, the shear wave velocity is significantly larger. As soon as liquefaction occurs during 12-15 s, the shear wave velocity drastically decreases, indicating the degradation of stiffness and strength of the soil. During the entire shaking, i.e. until 70 sec, the computed shear wave velocity for all the tests is quite smaller. No increment in shear wave velocity is observed until 70 sec, indicating that the soil is fully liquefied during the entire shaking period.

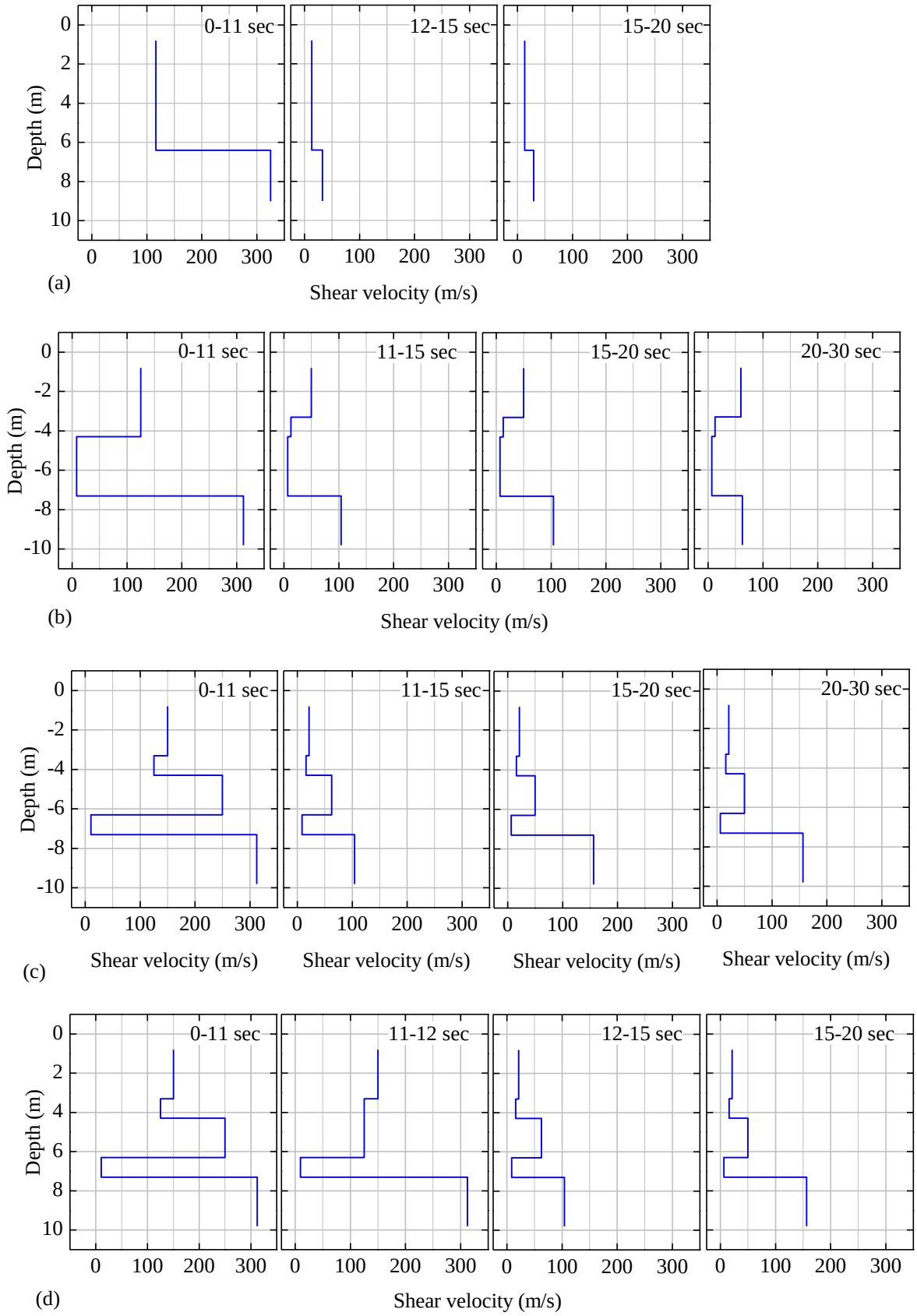

Figure A.11. Shear wave velocity profile: (a) Model 1; (b) Model 2; (c) Model 3; and (d) Model 4.

A.6 Summary and conclusions

Shear stress and shear strain can be back calculated by employing the acceleration time histories recorded during the centrifuge tests. The recorded acceleration time histories can also be employed for the back calculating the shear wave velocity. The stress-strain hysteresis loop obtained from the shear stress and shear strain could provide insight to predict the stiffness and strength of the liquefied soil. In order to achieve the appropriate the instruments should be densely placed in an array, which is not possible in the small scale centrifuge tests.

Appendix B
Geotechnical centrifuge modeling

B.1 Geotechnical centrifuge modeling

Modeling of geotechnical earthquake problems in centrifuge has significantly grown since last few decades as it enables the study and analysis of design problems (Taylor, 1995). Physical modeling replicates the properties, dimension and in situ stresses change with depth, i.e. stress history of the prototype scale. The technique involves testing scale models in the increased g environment of a geotechnical centrifuge. A geotechnical centrifuge is used to conduct model tests to study geotechnical problems such as the strength, stiffness and capacity of foundations for bridges and buildings, settlement of embankments, stability of slopes, earth retaining structures, tunnel stability and seawalls. The centrifuge may be useful for scale modeling of any large-scale nonlinear problem for which gravity is a primary driving force. The VELCAS project showed the effectiveness of centrifuge tests for studying the liquefaction in cohesionless soil during seismic events (Arulanandan and Scott, 1994).

Geotechnical materials such as soil and rock have nonlinear mechanical properties that depend on the effective confining stress and stress history. The centrifuge applies an increased "gravitational" acceleration to physical models in order to produce identical self-weight stresses in the model and prototype. The one to one scaling of stress enhances the similarity of geotechnical models and makes it possible to obtain accurate data to help solve complex problems such as earthquake-induced liquefaction, soil-structure interaction and underground transport of pollutants such as dense non-aqueous phase liquids. Centrifuge model testing provides data to improve our understanding of basic mechanisms of deformation and failure and provides benchmarks useful for verification of numerical models.

Large Earthquakes are infrequent and unrepeatable but they can be devastating. All of these factors make it difficult to obtain the required data to study their effects by post-earthquake field investigations. Instrumentation of full scale structures is expensive to maintain over the large periods of time that may elapse between major temblors, and the instrumentation may not be placed in the most scientifically useful locations. Centrifuge modeling is a valuable tool for studying the effects of ground shaking on critical structures without risking the safety of the public.

B.2 Scaling laws

The scaling laws described by (Schofield, 1981) for dynamic centrifuge modeling is summarized in Table B.1. The main principle in centrifuge modeling is that a 1/N scale model placed at the end of a centrifuge arm subjected to a gravitational acceleration of N g will feel the same stresses as the prototype. For instance, if a ground surface of 50 m depth has to be modeled the 1 m deep model container is filled with soil, placed on the end of a centrifuge and subject to a centrifugal acceleration of 50 g. The pressures and stresses are increased by a factor of 50. So, the vertical stress at the base of the model container is equivalent to the vertical stress at a depth of 50 m below the ground surface on earth. Thus the 1 m deep model represents 50 m of prototype soil. The reason for the centrifuge is to enable small scale models to feel the same stresses as a full scale prototype. The stress would be 50 times smaller if it is measure under gravity. The scaling laws allow stresses and strains in model and prototype structures to be identical and hence true prototype behavior is observed in the model (Fig. B.1).

Table B.1. Scaling Laws.

Parameter	Ratio of model to prototype
Length	1/N
Area	$1/N^2$
Volume	$1/N^3$
Velocity	1
Acceleration	N
Frequency	N
Stress	1
Strain	1
Force	$1/N^2$
Time (dynamic)	1/N
Time (Consolidation)	$1/N^2$

B.3 The Tokyo Tech Mark III Centrifuge

The Tokyo Tech Mark III centrifuge (Takemura et al., 1999) was used for all the tests Fig. B.1. The centrifuge is a beam type centrifuge having a pair of parallel arms which holds platform on which the model container and a weight for counterbalance are mounted as shown in Fig. B.2. The radius of rotation is 2.45 m, which is the distance from the rotating shaft to the platform base. The surface of the swinging platform is always normal to the resultant of the centrifugal acceleration, and earth's gravity. Specifications of the centrifuge are summarized in Table B.2.

For data acquisition, two types of signal transmission methods are used. One is classical electrical slip rings. Transducers are connected to the slip rings through a junction box and signals are transferred to amplifiers on the laboratory floor. The other type is an optical rotary joint. Transducers are connected to signal conditioners on the centrifuge. Analog signals from the transducers are amplified there and then are converted to digital signals by A/D converters. Gains and the other conditions of the signal conditioners can be controlled by a PC on the lab floor. The digital signals are transferred to the PC on the lab floor through the optical rotary joint.

A hydraulic rotary joint with maximum pressure of 20.5MPa mounted on the centrifuge is used for charging and discharging oil to the centrifuge during spinning of the centrifuge. A big hydraulic accumulator is mounted on the centrifuge to satisfy the required flow rate of the pressurized oil for the high performance 1D shaker.

Table B.2. Specifications of the Tokyo Tech Mark III Centrifuge.

Radius	Platform radius	2.45 m
	Effective radius	2.0-2.2 m
Platform Dimensions	Width	0.9 m
	Depth	0.9 m
	Maximum height	0.97 m
Capacity	Maximum payload	50g.ton
	Maximum number of rotation	300 rpm
	Maximum payload at 80g	600 kg
Electrical slip rings	For instrumentation	72 channels
	For operation	20 channels
Rotary joint	Working pressure for air and water	1 Mpa
	Working pressure for oil	21 Mpa
	Wireless LAN	64 channels

Figure B.1. Tokyo Tech Mark III Centrifuge.

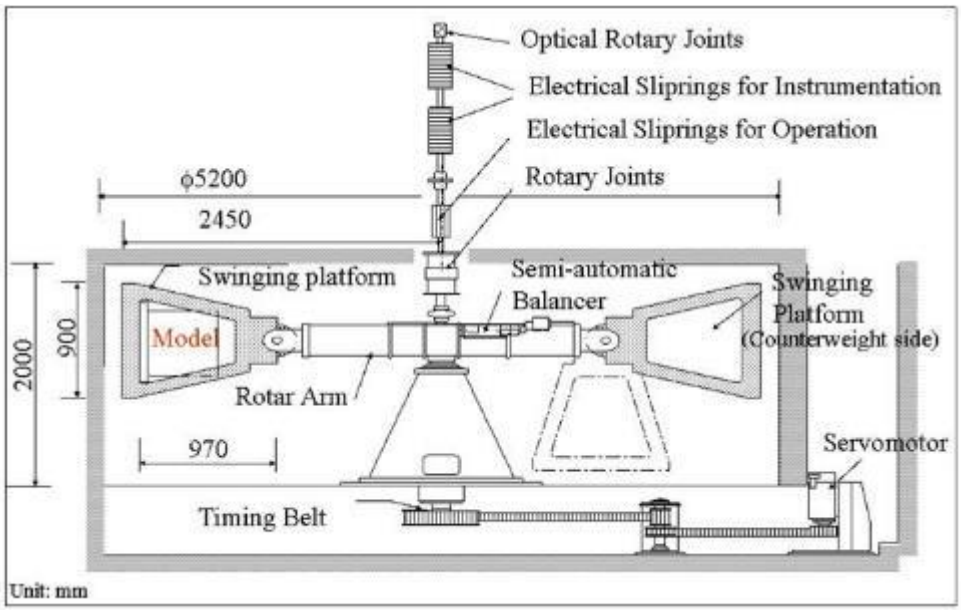

Figure B.2. Sectional view of the Tokyo Tech Mark III Centrifuge.

Appendix C
Material parameters of soil

C.1 Material parameters

The material parameters used in the constitutive model proposed by Hashiguchi and Chen (1998) are listed in Table C.1. The parameters of λ and κ can be determined from the isotropic normal consolidation and swelling curves. G or ν may be determined from the shear modulus obtained by some element tests. ϕ_{d} can be determined by phase transformation line in the undrained test. β_{ij0} can be determined by a stress path of anisotropic consolidation, i.e., the coefficient of earth pressure at rest. $F_0/(-\sigma_{\mathrm{m0}})$ represents an over consolidation ratio, where $p_0 \equiv -\sigma_{m0}$. The other parameters i.e. μ, ϕ, u_1, m_1, b_r, ϕ_b, c and s_{ij0} can be determined by trial and error so that the parameters can be fitted into the element tests.

The material parameters of Toyoura sand has been calculated by trial and error method and are shown in Table C.1. The details involved in determining the values are summarized in next section:

Table C.1. Parameters for Toyoura sand of D_R=50%.

G	e_0	κ	λ	ν	ϕ	ϕ_d	μ
2.65*	0.79*	0.0013*	0.0072*	0.33*	40°	25°*	1.0
ϕ_b	b_r	u_1	m_1	c	β_{ij0}	$F_0/(-\sigma_{m0})$	s_{ij0}
30°	100	4.0	1.0*	30.0	$\dfrac{\sigma_{ij0}-\sigma_{m0}\delta_{ij}^{\ *}}{(-\sigma_{m0})}$	1.2	$0.2\sigma_{ij0}$

The values marked with an asterisk were fixed throughout the parametric study.

The slope of the normal consolidation line and swelling line is determined from the typical isotropic consolidation test results on Toyoura sand by Miura (1975) (Fig.C.1). The poisson's ratio, ν and phase transformation angle, ϕ_{d} are determined from element tests and

are normally taken as 0.33 and 25^o respectively.

The typical stress path and stress-strain relationship of undrained cyclic triaxial tests for isotropically consolidated sand, obtained in the laboratory (Ishihara and Towhata, 1983) is presented in Fig. C.2 and the results obtained for the same condition as carried out by Ishihara and Towhata (1983) computed from the numerical analysis is presented in Fig. C.3. The soil parameters shown in Table C.2 are used in the analysis. The stress path obtained from experiment and computation looked more or less similar, however. the laboratory test result shows the continuous increase in axial strain with shear stress in extension side when the stress path shows a cyclic mobility. However, the calculated axial strain locks up with the close loops of stress-strain curve. The material parameters for the relative stress ratio, *m* is considered constant for simplicity in this study. The calculated stress paths are similar to those in the laboratory, however some differences can be observed in the stress-strain curves between the calculated and the laboratory test results.

The cyclic triaxial tests were conducted to examine the undrained behavior of the sand. The soil sample was isotropically or anisotropically consolidated under a mean confining pressure of 98 kPa, and then a cyclic axial stress was applied.

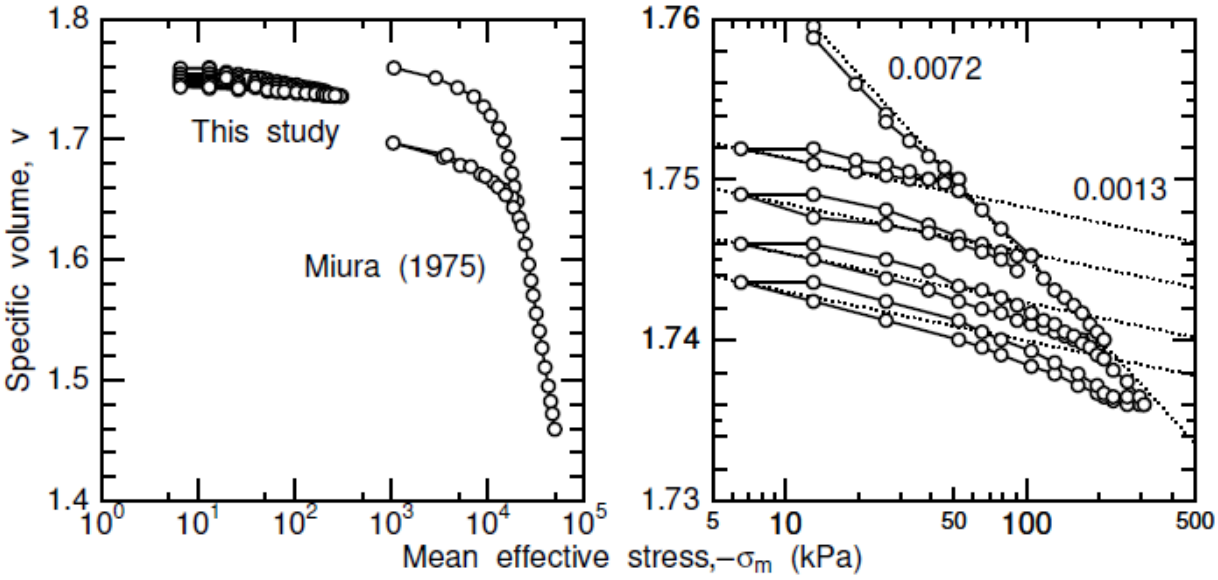

Figure C.1. Typical isotropic consolidation test results on Toyoura sand together with test results by Miura (1975) in v-$ln(-\sigma_m)$ space.

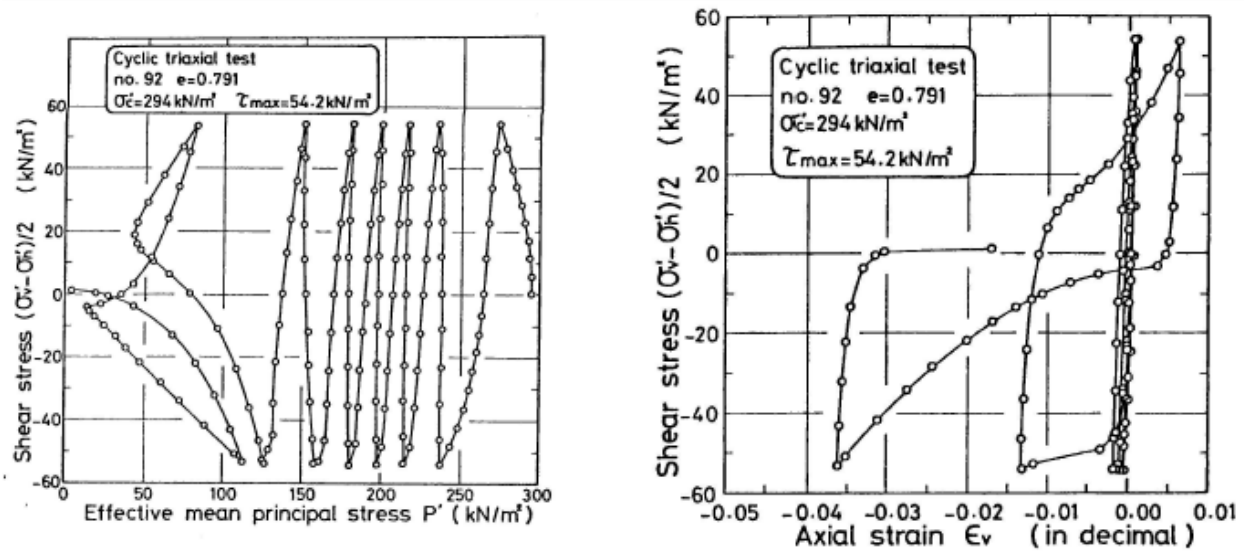

Figure C.2. Typical stress path and stress-strain relation in undrained cyclic triaxial test for isotropically consolidated sand in laboratory (Ishihara and Towhata, 1983).

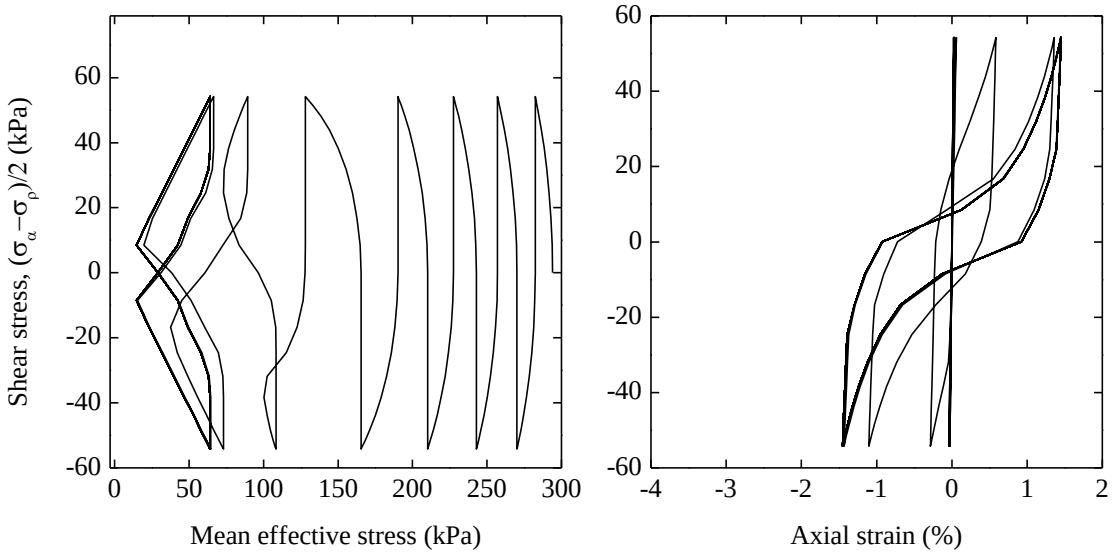

Figure C.3. Typical stress path and stress-strain relation in undrained cyclic triaxial test for isotropically consolidated sand in numerical analysis.

C.2 Sensitivity of material parameters

The other material parameters has to be fitted into the results of element tests by trial and error. Following section shows stress paths and stress-strain relationships obtained by changing each parameter during trial and error method, involved in determining the material parameters.

1. Isotropic hardening/softening, μ (Fig. C.4)

The parameter μ contributes to the plastic shear strain to the isotropic hardening/softening of the soil. When the value of μ is very smaller, i.e., 0.2, the soil does not reach failure. However, for the larger μ value, the isotropic hardening/softening largely depends on the plastic shear strain. As a results, the stress-strain relation shows rapid hardening and softening and the stress path approaches the origin of the stress space

2. Ratio of size of the subloading surface to that of the normal yield surface, u_1 (Fig C.5)

The shape of the stress-strain curve of the soil after the stress path has crossed the phase transformation line is basically affected by parameter $u_{1.}$ .The smaller value of u_1 makes the subloading surface smaller as the ratio of the size of the subloading surface to that of the normal yield surface decreases. Thus, it easily makes the stress path approach to the origin when cyclic mobility occurs.

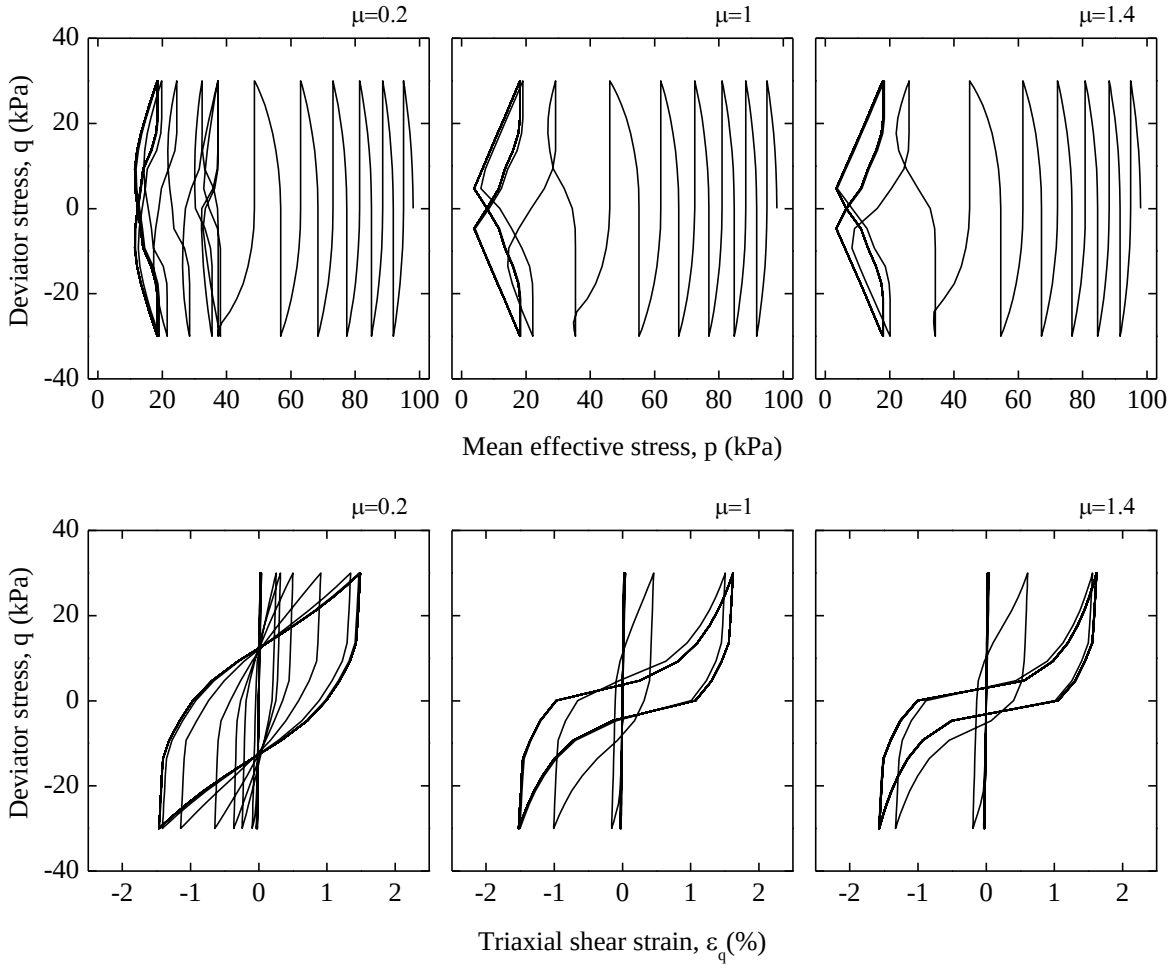

Figure C.4. 'μ' variation effect on behavior of isotropically consolidated soil in undrained cyclic triaxial test.

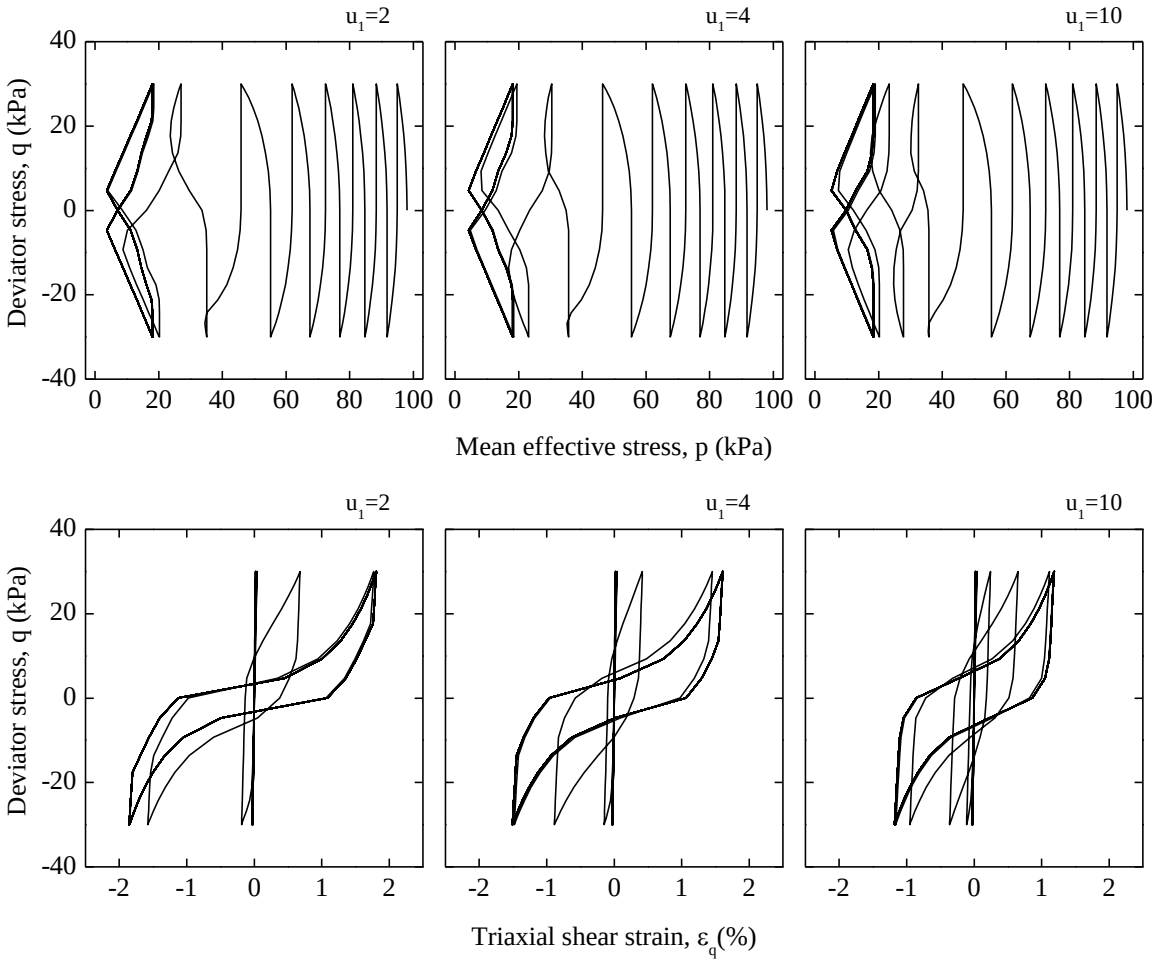

Figure C.5. 'u_1' variation effect on behavior of isotropically consolidated soil in undrained cyclic triaxial test.

3. Movement of similarity center of the normal yield surface and the suboading surface, *c* (Fig. C.6)

The shape of the stress-strain curve of the soil after the stress path has crossed the phase transformation line is basically affected by parameter *c*. The larger *c* makes the velocity of the similarity center of the surface larger, causing the faster movement of the similarity center than the hardening and rotation of the normal yield surface. This shows the similar trend of stress path of smaller value of u_1. Moreover, the stress-strain relation comes to show rapid hardening/softening and smaller hysteretic damping when the parameters u_1 becomes larger or when the parameter *c* becomes smaller.

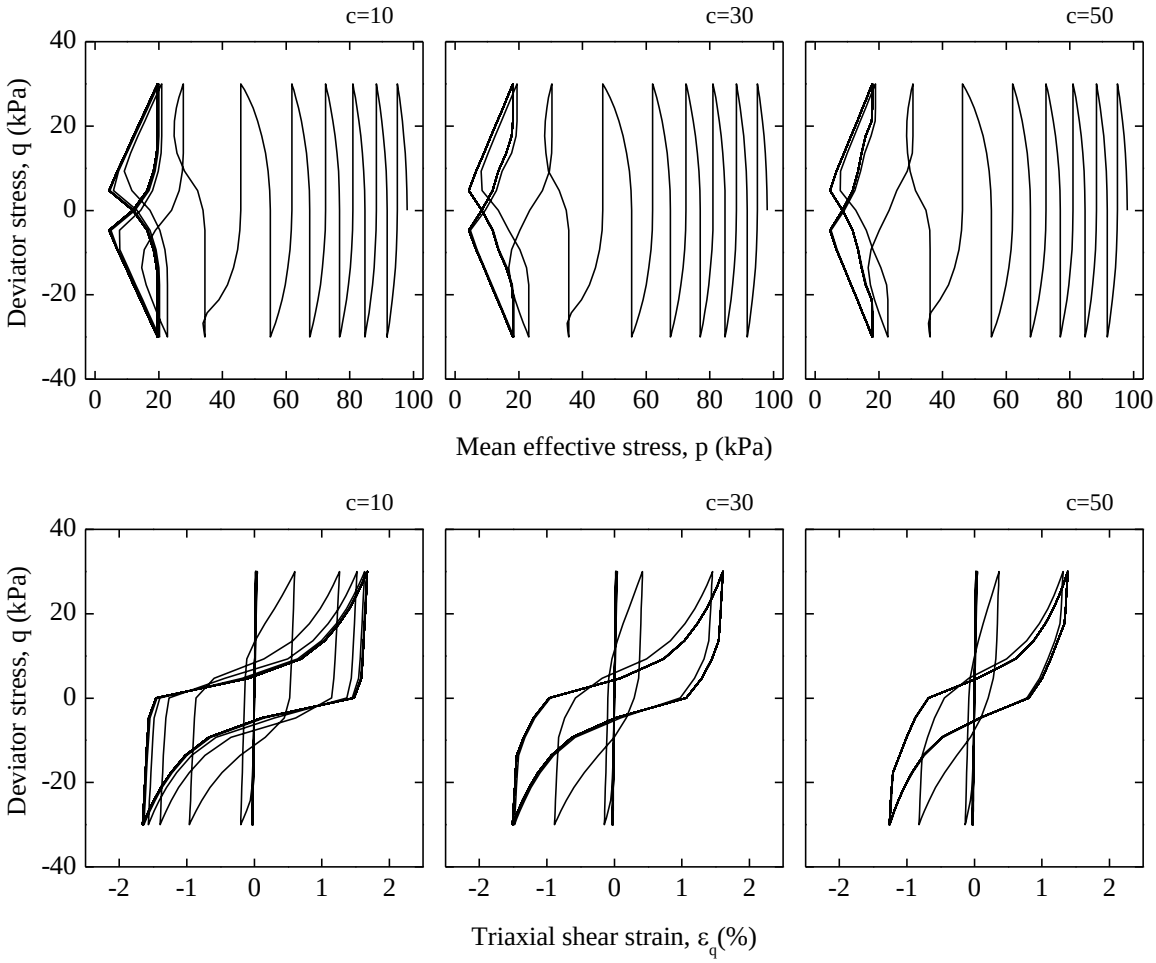

Figure C.6. '*c*' variation effect on behavior of isotropically consolidated soil in undrained cyclic triaxial test.

4. Rotational hardening: b_r and ϕ_b (Figs. C.7 and C.8)

The behavior of the subloading surface and the normal yield surface is affected by the parameters b_r and ϕ_b after the stress path crosses the phase transformation line. When the parameters b_r and ϕ_b are smaller, the stress-strain relation shows the rapid hardening and softening and smaller hysteretic damping.

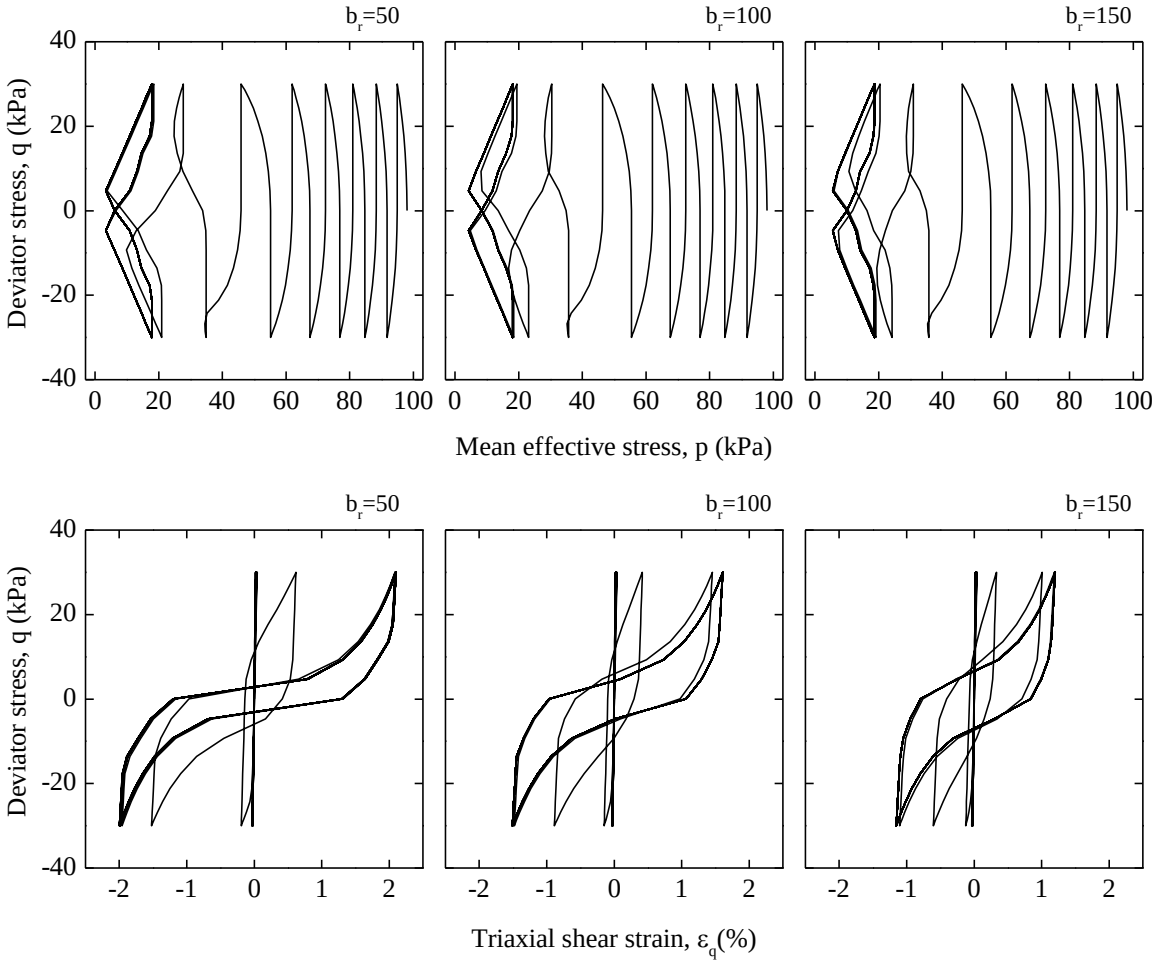

Figure C.7. 'b_r' variation effect on behavior of isotropically consolidated soil in undrained cyclic triaxial test.

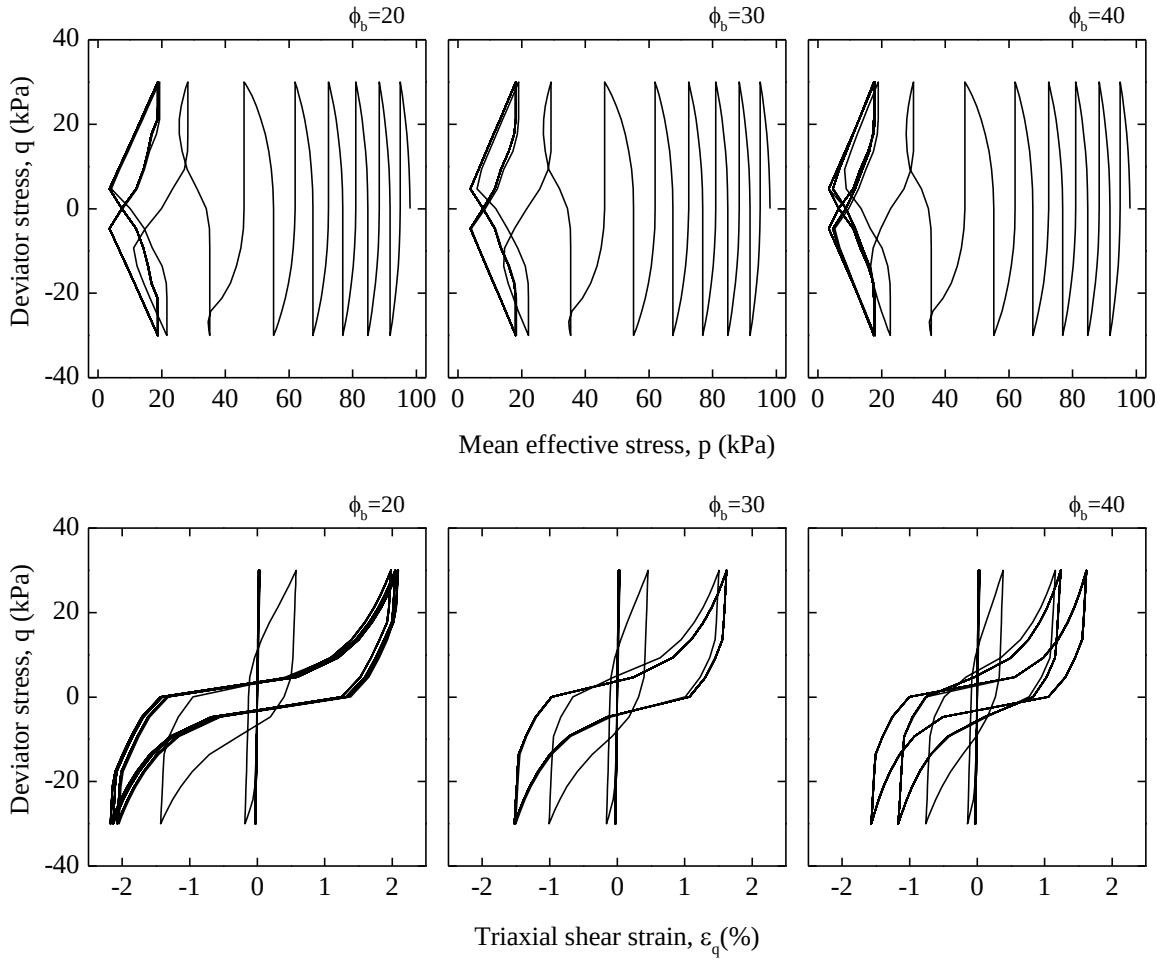

Figure C.8. 'ϕ_b' variation effect on behavior of isotropically consolidated soil in undrained cyclic triaxial test.

5. Shape of the normal yield surface and the subloading surface, ϕ (Fig. C.9)

The faster generation of excess pore water pressure takes place before the cyclic mobility reducing the liquefaction resistance when the ϕ value is smaller. Howevere, the larger ϕ causes the increase in liquefaction resistance. The failure of soil largely depend upon the value of ϕ since the critical state surface if a function of ϕ. Thus the parameter ϕ should be carefully determined for the better evaluation.

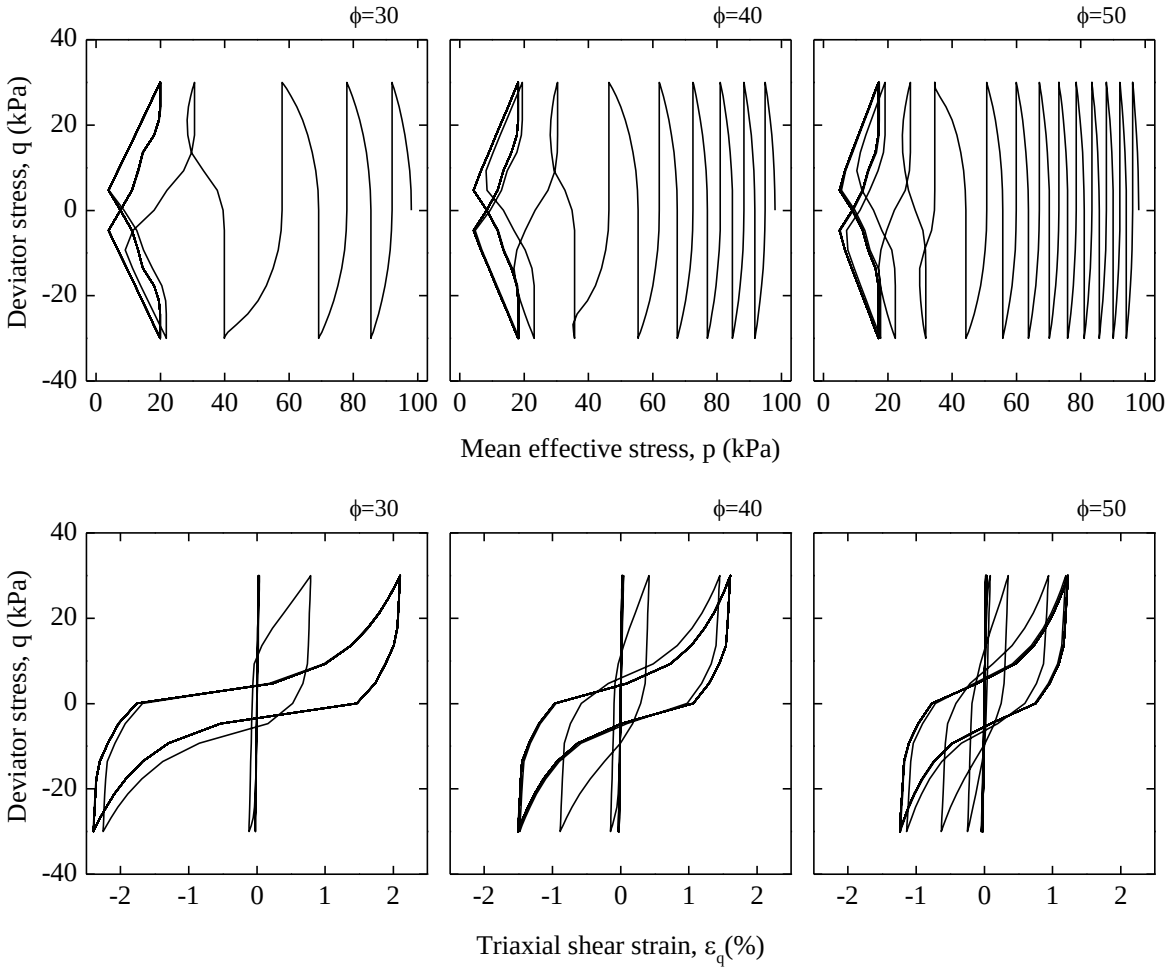

Figure C.9. 'ϕ' variation effect on behavior of isotropically consolidated soil in undrained cyclic triaxial test.

6. Initial location of the similarity center, s_0 (Fig. C.10)

The stress path and the stress-strain relations at the beginning of the cyclic loadings and during the cyclic mobility are essentially the same, irrespective of the initial location of the similarity center. However, the stress path rapidly approaches the origin of the stress space in the case of the larger s_{ij0}/σ_{ij0}, while it gradually approaches the origin in the case of smaller s_{ij0}/σ_{ij0} after the start of the normal yield surface rotation. This is the important parameter which affects the development of excess pore water pressure before the cyclic mobility. Thus the initial location of the similarity center should be carefully determined in order to fit the liquefaction resistance to the laboratory test results.

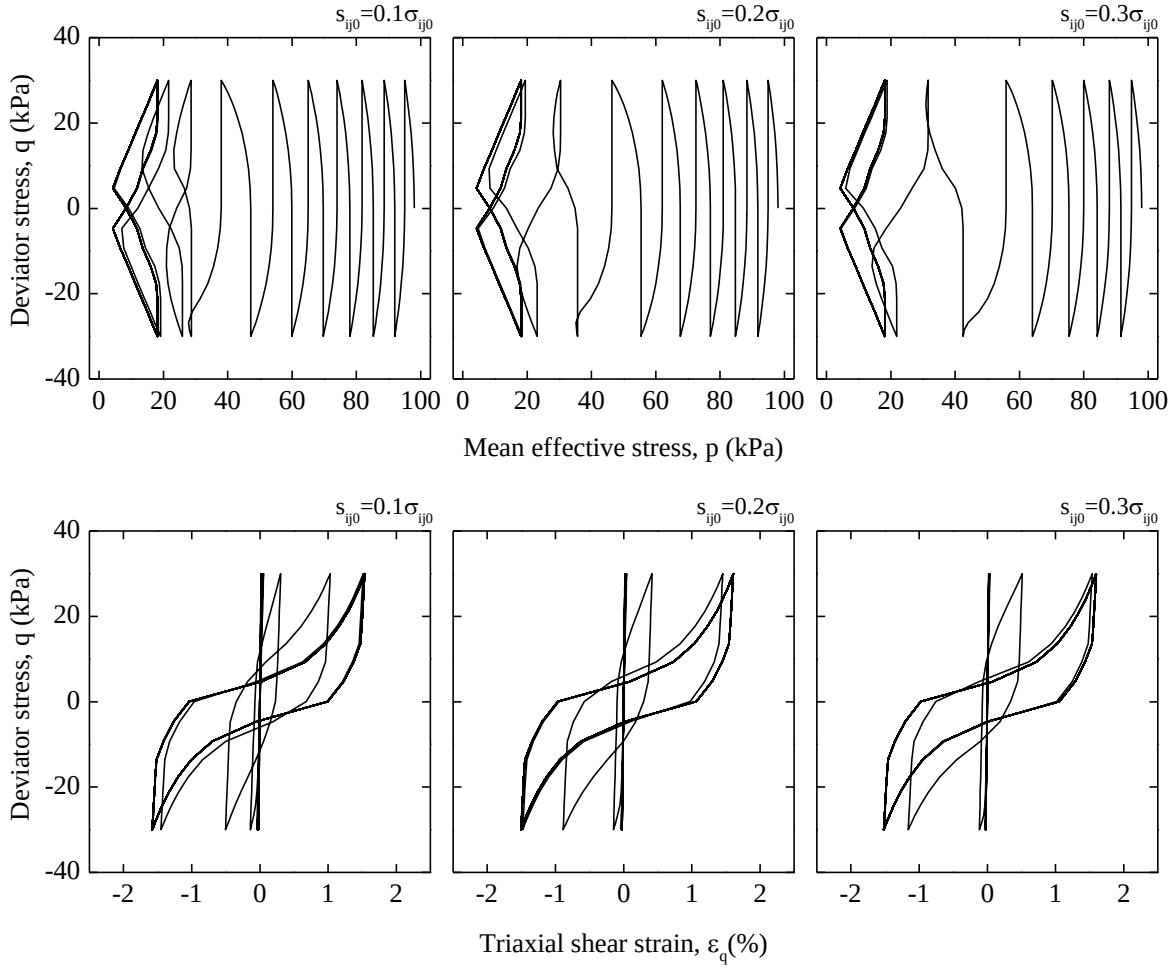

Figure C.10. 's_0' variation effect on behavior of isotropically consolidated soil in undrained cyclic triaxial test.

7. Overconsolidation ratio, F_0 (Fig. C.11)

The increase in parameter F causes a decrease in the ratio of the size of the subloading surface to that of the normal yield surface, R with the cyclic loading at the beginning of the cyclic loadings. However, the stress path ceases to move towards the origin of the stress space immediately after the normal yield surface rotation starts.

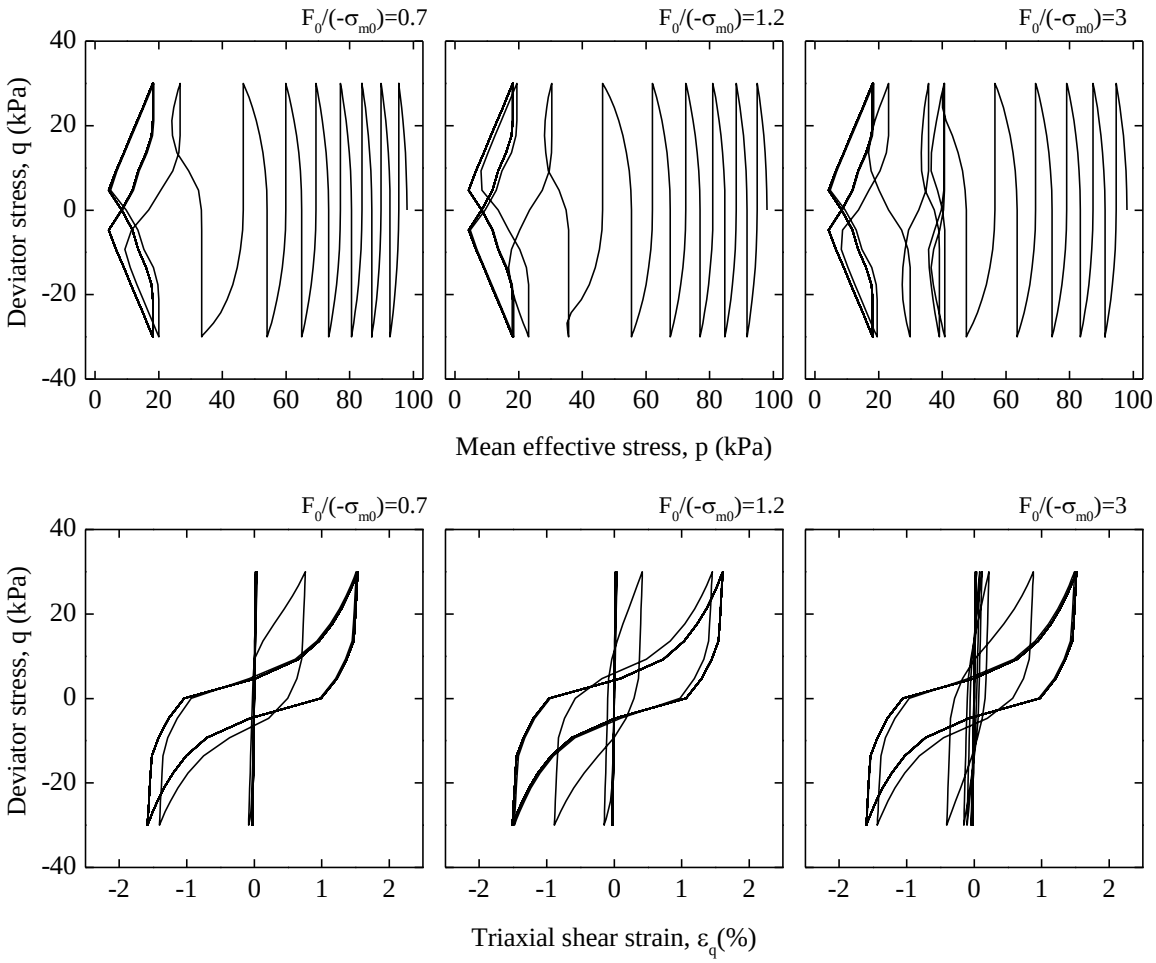

Figure C.11. 'F_0' variation effect on behavior of isotropically consolidated soil in undrained cyclic triaxial test.

Appendix D
Constitutive modeling of liquefaction effects in sloping ground

Accurate prediction of the cyclic mobility behavior associated with the undrained cyclic loading of sand under a nonzero static shear stress ratio can be important for numerically simulating earthquake-induced deformations of slopes. Experimental studies on the deformation of clean sands under undrained cyclic direct simple shear loading show a progressive accumulation of shear strains both under a zero and a non-zero static shear stress ratio which represent level and sloping ground conditions, respectively. Single element numerical simulations of undrained cyclic loading using a number of constitutive models show that they all have certain limitations and that the effect of sloping ground conditions is particularly difficult to simulate for many of the models. This chapter presents example results from undrained cyclic direct simple shear tests on clean sands under zero and nonzero static shear stress ratio conditions, reviews findings from past experimental studies for these types of loading conditions, and presents examples of the performance of selected constitutive models in modeling the observed experimental results.

D.1 Introduction

Numerical simulations of the seismic response of geotechnical structures affected by liquefaction represent the synthesis of individual responses of all the elements comprising the structure. For example, the seismic response of a geotechnical structure like the earth dam schematically illustrated in Fig. D.1 will need to account for strata or zones of sand ranging from very loose to dense under a wide range of confining stresses, initial static shear stresses, drainage conditions, and dynamic loads. Successful numerical simulations of earthquake-induced deformations for these types of geotechnical structures need constitutive models that can reasonably approximate the responses that liquefiable soils exhibit under all of these loading conditions.

An understanding of the response of liquefiable soils under sloping ground conditions can play an important role in a nonlinear deformation analysis (NDA) of a slope or embankment. There is a large body of experimental data describing the elemental behavior of sands under such loading conditions. The presence of a slope is represented in

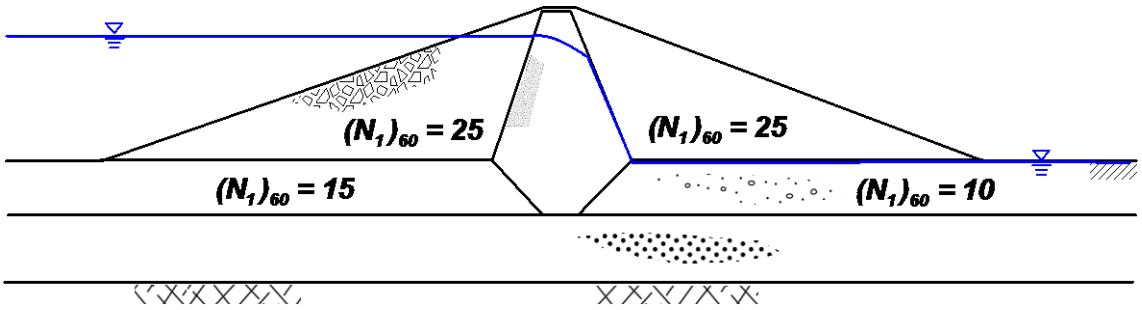

Figure D.1. Cross-section of an earth dam illustrating the wide range of density, saturation, and stress conditions that may need to be modeled.

such tests by a static shear stress ratio α (= τ_s / σ'_{vc}) which is the ratio of static shear stress to the effective consolidation stress on the plane of interest.

The cyclic resistance ratio (*CRR*) of a liquefiable soil is affected by the presence of static shear stresses, such as exist within slopes or embankment dams, but the available case history data are not sufficient to empirically quantify this effect. Seed (1981) introduced the K_α correction factor which describes the observed experimental effects of α on *CRR*:

$$K_a = \frac{CRR_a}{CRR_{a=0}} \qquad (1)$$

where CRR_α is the *CRR* value for a given value of α and $CRR_{\alpha=0}$ is the *CRR* value when $\alpha = 0$. Over the years, experimental data have been compiled that form a basis for understanding the aforementioned phenomena and serving as a guide for calibration of constitutive models.

The purpose of this chapter is to examine some issues pertinent to the modeling of liquefaction effects under sloping ground conditions. Results of cyclic undrained direct simple shear laboratory tests under both level and sloping ground conditions are described, followed by an examination of existing liquefaction correlations that are commonly used in practice to account for the effects of sloping ground on the cyclic resistance ratio of sands. The results of single-element numerical simulations under undrained cyclic direct simple shear conditions with selected constitutive models are presented. It is illustrated that all models have limitations. Finally, it is concluded that the recognition and understanding of such limitations through single-element simulations replicating the field conditions are essential for fostering improvements and increasing confidence in the use of NDAs for evaluating the seismic performance of geotechnical structures affected by liquefaction.

D.2 Experimental results for clean sand

The undrained cyclic loading response of saturated sand under level and sloping ground conditions is illustrated by some example test results with and without a static shear stress ratio respectively, followed by a summary of the general trends observed in the literature and summarized in design relationships based on the cumulative body of data.

D.2.1 Undrained cyclic loading behavior for level ground conditions ($\alpha = 0$)

The effect of a zero initial static shear stress ($\alpha = 0$) on the undrained cyclic direct simple shear (DSS) loading response of saturated sand is illustrated by the test results for Nevada sand shown in Fig. D.2. The specimen of dry pluviated Nevada sand had a relative density D_R = 50 % and was consolidated to a vertical effective stress of σ'_{vc} =100 kPa. The applied cyclic stress ratio (*CSR*) was about 0.10 which means that the horizontal shear stress τ was symmetrically cycling around 0 kPa (-10 kPa to 10 kPa) under undrained conditions. The induced excess pore water pressure ratio r_u (as depicted through the stress path in Fig.D. 2) increased quickly in the first few loading cycles and eventually reached peak values of 100% (mean effective stress p' = 0). The stress-strain loops, also shown in Fig. D.2, exhibit the continuous accumulation of shear strains commonly referred to as cyclic mobility.

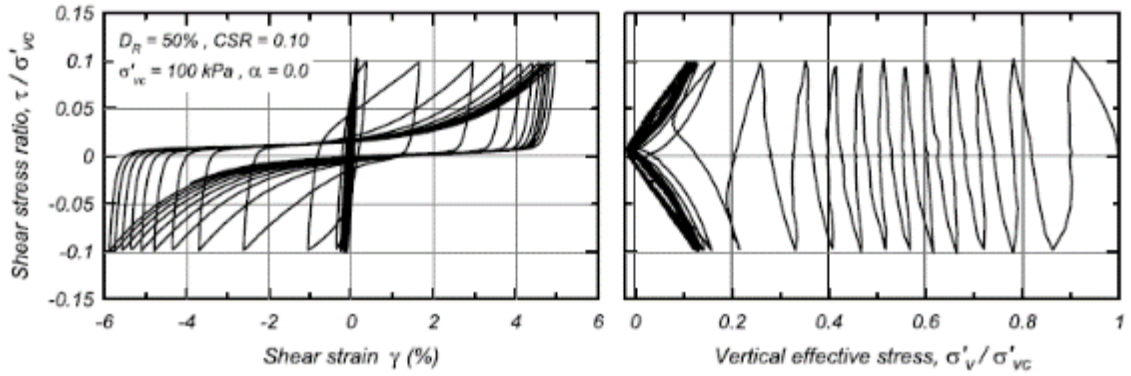

Figure D.2. Stress-strain loop and stress path for undrained cyclic direct simple shear test on Nevada Sand under a vertical effective stress of σ'_{vc} = 100 kPa and a zero initial static shear stress (α = 0) that corresponds to level ground conditions.

D.2.2 Undrained cyclic loading behavior for sloping ground conditions ($\alpha > 0$)

The effect of an initial static shear stress ($\alpha > 0$) on the undrained cyclic DSS loading behavior of saturated sand is illustrated by the test results for Nevada sand shown in Fig. D.3. The specimen of dry pluviated Nevada sand had a D_R = 45 % and was consolidated at σ'_{vc} =100 kPa with τ_s = 10 kPa so that α = 0.10. The applied *CSR* was 0.08 which means that

τ was always positive (about 2 kPa – 18 kPa) and did not reverse over the zero shear stress axis. The induced r_u increased quickly in the first few loading cycles and then increased slowly with each subsequent cycle of loading but was always less than 100% so that p' (and σ'_v) never became zero. This is illustrated in Fig. D.3 together with the continuous accumulation of shear strains in the direction of the static shear stress.

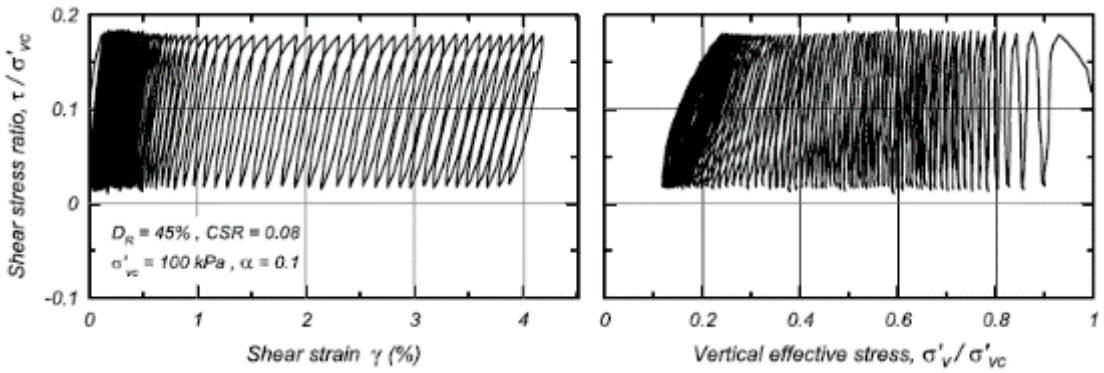

Figure D.3. Stress-strain loop and stress path for undrained cyclic direct simple shear test on Nevada Sand under a vertical effective stress of σ'_{vc} = 100 kPa and an initial static shear stress ratio α = 0.1 that corresponds to sloping ground conditions.

D.2.3 General trends and design relationships

Since Seed (1981) introduced the K_α correction factor for describing the effects of α on *CRR*, numerous researchers have studied this phenomenon using cyclic triaxial, cyclic simple shear, torsional shear, and torsional ring shear devices. These studies have shown that K_α depends on D_R and confining stress, which together reflect the state of the sand in relation to its critical state (e.g., (Been and Jefferies, 1985)). In addition, K_α depends on the failure criteria that are used to define *CRR* and depends somewhat on the laboratory test device, with DSS preferred over triaxial loading because it more closely approximates the in-situ rotation of principal stress directions expected during earthquake shaking (Harder and Boulanger, 1997).

Experimental results on a range of sands at confining stresses less than about 300 kPa showed that *CRR* (for some strain failure criterion) would decrease with increasing α for loose sands and increase with increasing α for dense sands. The general trends of K_α observed from results for sands tested at confining stresses less than about 300 kPa are summarized in Fig. D.4a for three ranges of D_R (Harder and Boulanger, 1997). For sands tested across a broader range of confining stresses, (Boulanger, 2003b), based on tests by (Boulanger et al., 1991; Vaid and Finn, 1979; Vaid and Chern, 1985), showed that the trends were better related to some measure of state, such as the relative state parameter index ξ_R as

shown in Fig. D.4b. In both cases, the trends observed are similar in that K_α increases with increasing α for dense sands ($D_R \approx 55 - 70\%$ or $\xi_R << 0$), while it decreases with increasing α for loose sands ($D_R \approx 35\%$ or $\xi_R > 0$). The results shown in Fig. D.4 were determined using a failure criterion of 3% single-amplitude shear strain to define the *CRR* values; the r_u's in sand reach their limiting value at this level of shear strain and thus generally are not expected to increase with further increases in the maximum shear strains.

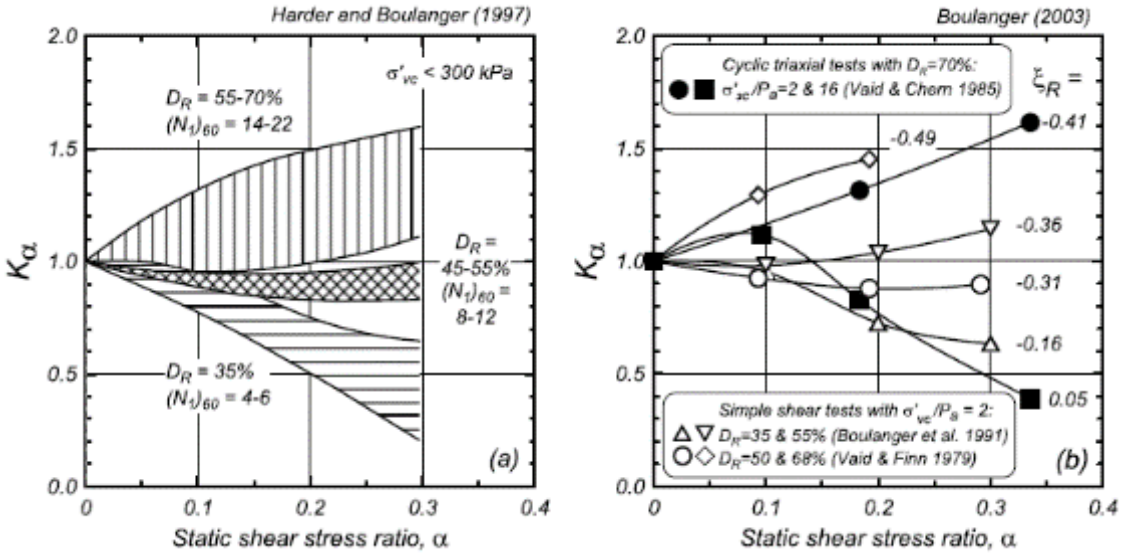

Figure D.4. Experimental trends between *CRR* and α depicted in terms of K_α relationships: (a) for sands at different D_R's and $\sigma'_{vc} < 300$ kPa (Harder and Boulanger, 1997), and (b) for sands at different relative state parameter index, ξ_R, values (Boulanger, 2003a).

D.3 Constitutive models and numerical simulations

The evaluations of NDA models against physical model tests and case histories involving liquefaction have shown that realistic simulations of the dynamic response of many types of structures can only be obtained using more advanced constitutive models that can approximate behaviors such as cyclic mobility. Such constitutive models need to be calibrated and validated using single-element simulations for the types of loading paths that are expected to be important (i.e. α conditions herein).

Several advanced constitutive models (Hashiguchi and Chen, 1998), Pressure-Dependent-Multi-Yield Surface model by Yang et al. (2003), UBCSAND by Byrne et al. (2004) and Beaty and Byrne (2011), Dafalias and Manzari (2004), Boulanger and Ziotopoulou (2012, 2013) and Wang et al. (1990) were evaluated for their ability to simulate

the aforementioned cyclic loading behaviors under level and sloping ground using single-element DSS numerical simulations. Examples of these simulations are illustrated herein and evaluated against the extensive body of experimental based correlations that were presented in Fig. D.4. The objective was to evaluate the ability of each constitutive model to produce results that are within the range of responses that have been observed experimentally for similar soils and conditions.

D.3.1 Cyclic response for level ground conditions ($\alpha = 0$)

The first step was performing single-element DSS simulations to obtain the stress-strain responses under the reference case of level ground conditions ($\alpha = 0$). Particularly important is the accumulation of shear strains (cyclic mobility) which can be shown to differ amongst different constitutive models.

Some models stop accumulating shear strains (locking-up) after reaching r_u = 100% (or some limiting r_u value close to 100%) when there is no static shear stress ratio ($\alpha = 0$) such that the stress cycles are applied symmetrically. Examples of locking and non-locking cyclic stress-strain responses are shown in Fig. D.5 for two related constitutive models; the first model (Dafalias and Manzari, 2004) locks up at shear strains of about 0.3% (Fig. D.5a)

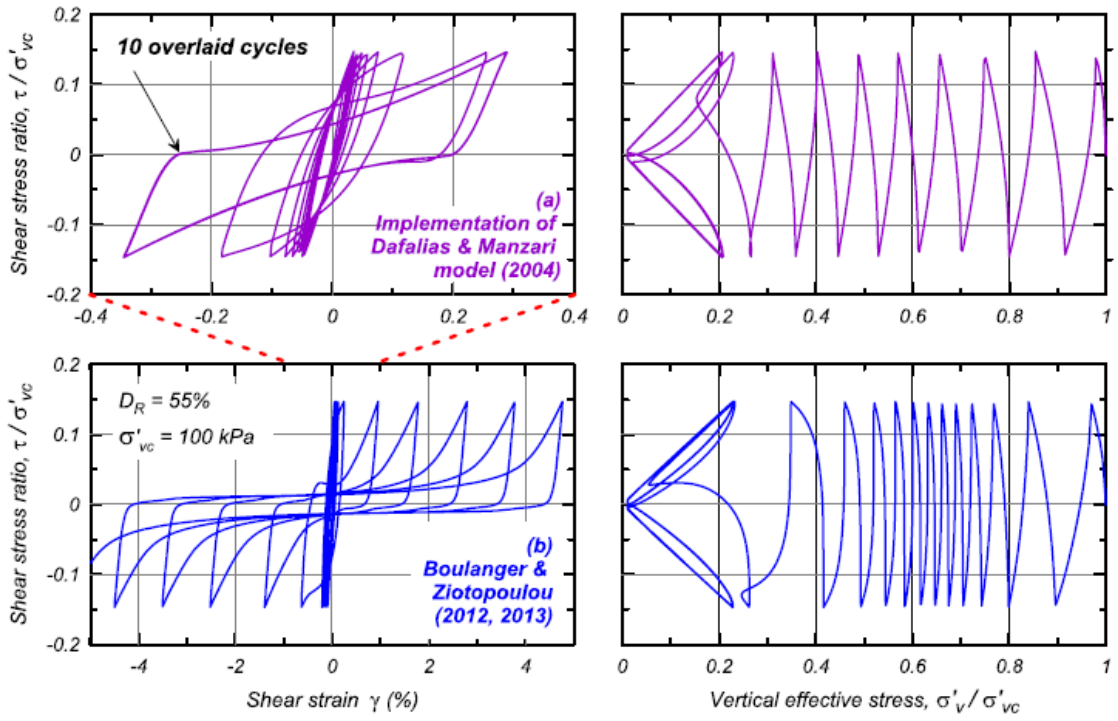

Figure D.5. Stress-strain responses from single-element simulations of undrained cyclic direct simple shear: (a) using an implementation of the Dafalias and Manzari model [12], and (b) using the model by Boulanger and Ziotopoulou (2012, 2013).

whereas the second model (Boulanger and Ziotopoulou (2012, 2013), (Ziotopoulou and Boulanger, 2013) is able to progressively accumulate shear strains after $r_u \approx 100\%$ first occurs (Fig. D.5b). This can affect the definition of "triggering" depending on the constitutive model being used. Thus, a triggering criterion for the simulations may need to be based on r_u for a model that locks up, or on a failure strain amplitude (e.g., a maximum single amplitude shear strain of 3%) for a model that does not. Note that the second model was based on the framework of the first, with modifications to the functional forms of the constitutive equations being necessary to improve this and other features of behavior (Boulanger and Ziotopoulou (2012, 2013).

The ability of a constitutive model to predict some progressive accumulation of shear strains for $\alpha = 0$ conditions, as observed in experimental results (Fig. D.2), may or may not be important for a specific NDA application. Nonetheless, it is essential that an analyst be aware of any such limitations as part of performing an NDA or interpreting its results.

D.3.2 Cyclic response for sloping ground conditions ($\alpha > 0$)

Similar to the evaluation of the cyclic response of a constitutive model under level ground conditions, single-element DSS simulations should be performed to obtain the stress-strain responses under sloping ground conditions. Fig. D.6 illustrates such responses for two constitutive models under a static shear stress ratio of $\alpha = 0.2$.

Simulated stress-strain responses for DSS loading of sand with $D_R = 55\%$, $\sigma'_{vc} = 100$ kPa, and $\alpha = 0.2$ are shown for the model by Yang et al. (2003) in Fig. 6a and the model by Boulanger and Ziotopoulou (2012, 2013) in Fig. 6b. The stress paths are both reasonable, showing that $r_u = 100\%$ ($p' = 0$) cannot be reached for these dense of critical sands when the cyclic loading is insufficient to cause a full shear stress reversal ($CSR < \alpha$). The peak r_u values for the two models differ because of their differences in unloading behaviors, with the peak r_u values being about 0.75 for the Yang et al. model and about 0.87 for the Boulanger and Ziotopoulou model as can be seen through the two stress paths in Fig. C.6. This constitutes a notable difference in the amount of shed p'. Both models accumulate shear strains in the direction of the τ_s (Yang et al. model up to 6%, Boulanger and Ziotopoulou model up to 10%), consistent with experimental observations, but at different rates per cycle of loading.

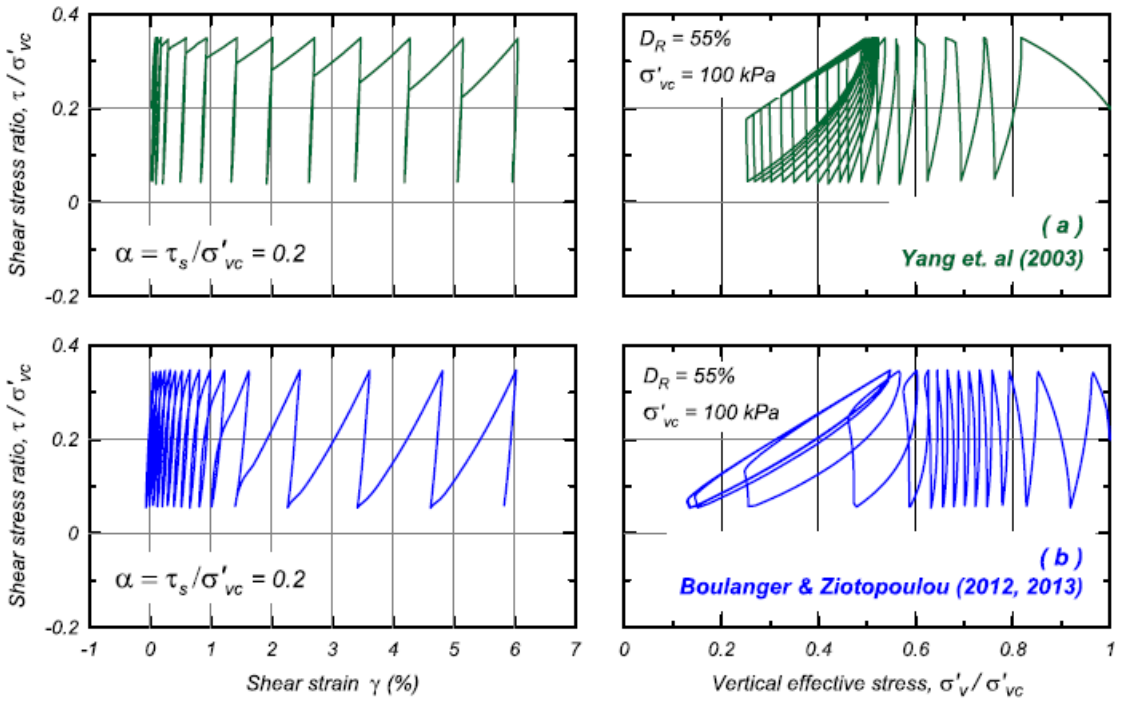

Figure D.6. Single-element responses for undrained cyclic DSS loading on sand at D_R = 55%, σ'_{vc} = 100 kPa, and α = 0.2 simulated using: (a) PDMY model by Yang et al. (2003), and (b) PM4Sand model by Boulanger and Ziotopoulou (2012, 2013).

D.4 Simulation trends for sloping ground conditions

The trends in simulation results obtained using different constitutive models were expressed in terms of their equivalent K_α factors, as illustrated by the following examples. Single-element DSS simulations using the models by Yang et. al (2003) and Boulanger and Ziotopoulou (2012, 2013) were repeated for D_R = 35, 55, and 75% with σ'_{vc} = 100 kPa to define the effect of α on *CRR* for a range of D_R's. The *CRR* values were determined for a shear strain failure criterion of 3%. The results are presented in terms of equivalent K_α values in Fig. D.7a for the Yang et al. (2003) model and Fig. D.7b for the Boulanger and Ziotopoulou (2012, 2013) model. The simulated behaviors deviate significantly from the trends observed experimentally (Fig. D.4), with neither model being able to reasonably reproduce the observed increases in *CRR* with increasing α for D_R = 75% or decreases in *CRR* with increasing α for D_R = 35%.

Single-element simulations using two versions of the UBCSAND model were presented by Beaty and Byrne (2011) to illustrate the improvements in responses obtained with their newer version. The equivalent K_α values obtained using the older version 904a, as shown Fig. 8a, deviated greatly from the experimentally observed results in Fig. D.4. The

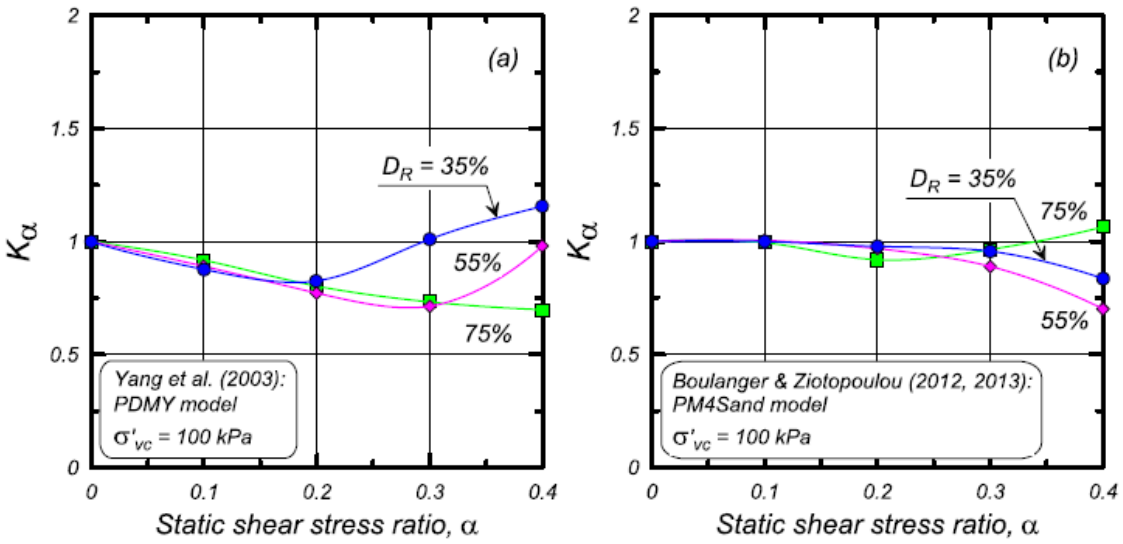

Figure D.7. Single-element simulation results for undrained cyclic DSS loading using: (a) PDMY model by Yang et al. (2003) and (b) PM4Sand model by Boulanger and Ziotopoulou (2012, 2013).

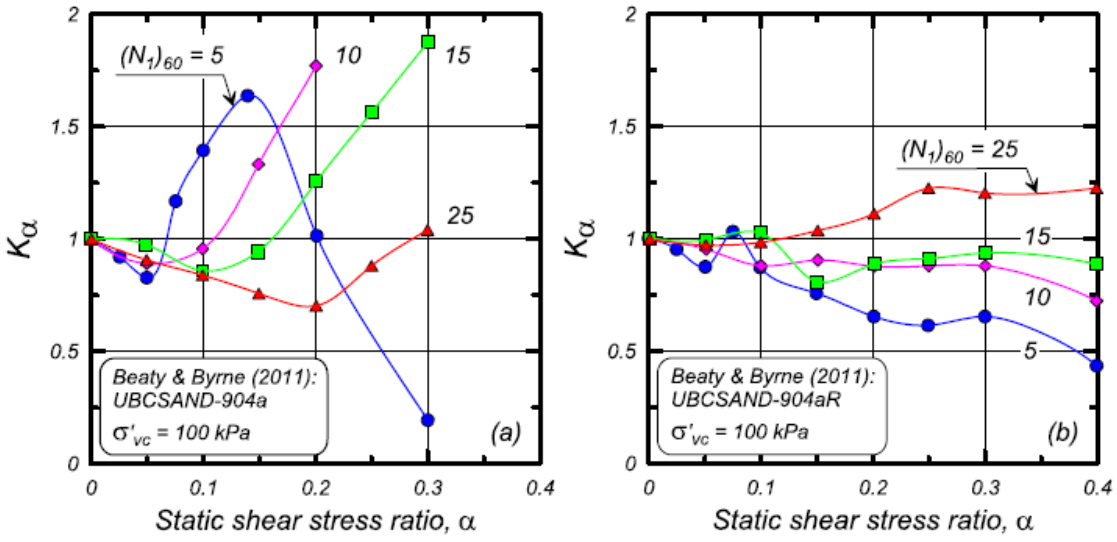

Figure D.8. Single-element simulation results for undrained cyclic DSS loading using two versions of UBCSAND: (a) version 904a and (b) 904aR (Beaty and Byrne (2011)).

results obtained with this model included significant kinks in the trends and an almost inverted trend for the sands at $(N_1)_{60}$ values of 10, 15, and 25 (i.e., the curves shift lower with increasing denseness). In contrast, the results obtained using the newer version 904aR,

as shown in Fig. D.8b, are in reasonable agreement with the experimentally observed trends of Fig. D.4. It is noteworthy that Beaty and Byrne (2011) identified the limitations in the 904a version during a project involving the seismic analysis of an embankment dam, which provides an early example of this particular aspect of model validation. The K_α behavior was a critical item at this dam due to the relative magnitudes of the static shear stress and cyclic shear stress ratios. They used the findings of that study to guide model improvements which resulted in their 904aR version. As a side note, it must be pointed out that for models such as UBCSAND that are periodically updated and modified, it is clearly necessary to document both the model name and version when performing an analysis.

D.5 Summary and conclusions

The examination of a number of constitutive models for liquefiable soils showed that all models present some limitations in replicating the full range of liquefaction behaviors observed in the lab and that the simulation of K_α effects is one of the more difficult challenges for many constitutive models. These limitations can be particularly important in nonlinear deformation analyses of problems involving liquefiable soils under sloping ground conditions. For example, the ability of a constitutive model to produce responses similar to the experimentally observed K_α responses (Fig. 4) is important for dams because α values are often in the range of 0.1 to 0.3 under both the upstream and downstream shells of a dam. For this reason, it is particularly important that single-element simulations be used to demonstrate a constitutive model's behavior under these types of loading conditions as part of any NDA study for a dam.

A constitutive model's ability to approximate liquefaction behavior across a range of seismic hazard levels (e.g., different shaking intensities and durations) and in-situ stress conditions (e.g., different overburden stresses and initial static shear stress ratios) can be important for avoiding bias in numerical simulations for performance-based evaluations of geotechnical structures. In practice, it is important to evaluate any constitutive model's ability to approximate the range of behaviors important to a structure's performance. This is usually accomplished by comparing simulated responses to a set of applicable design correlations, empirical relationships and available experimental data. The present chapter illustrated such a comparison for one specific aspect of behavior for selected constitutive models. The critical examination of constitutive models for liquefiable soils is necessary for identifying weaknesses, fostering improvements, and increasing confidence in their use for evaluating the seismic performance of geotechnical structures affected by liquefaction.